AN ABSTRACT OF THE DISSERTATION OF

Lulu Zhang for the degree of Doctor of Philosophy in Chemistry presented on October 31, 2018.

Title: Innovative Bioanalytical Tools & Methods for Combinatorial Non-Coding RNA Analysis.

Abstract approved: _____

Sean M. Burrows

Recently researchers have discovered that groups of small non-coding RNAs (ncRNAs) play regulatory roles in gene expression and participate in various biological processes.[1–4] For example, pathogenesis of many diseases[3], cell cycle regulation[4], and signaling pathways[5]. Intracellular and live cell imaging of small ncRNA groups will reveal their relative expression levels and provide unparalleled detail on spatial and temporal heterogeneities within a single cell. The ability to measure heterogeneities will help define cell types and cell states for differentiating cell populations.[6] Having analytical tools that reveal heterogeneities among cell populations will provide unique insights on the physiological changes and processes (*e.g.* aging and apoptosis) of each cell and how the cells work together to maintain homeostasis or drive disease progression.

To profile small ncRNAs expression, one popular analytical tool is known as programmable molecular logic sensors.[7] Relying on nucleic acids, a natural building block[8], molecular logic sensors are constructed for computing what groups of small ncRNAs are in a cell. As a model system to design innovative molecular logic sensors around, I picked microRNAs. MicroRNAs (miRs) are small non-coding single-stranded RNAs that are approximately 22 nucleotides in length.[9] The roles of miRs are to regulate gene expression, mainly post-transcriptionally, during messenger-RNA translation.[10]

Current nucleic-acid-based *in situ* sensors that are capable of revealing a cells miR pattern suffer from 1) low multiplexing ability (up to two miR inputs per sensor), 2) poor selectivity, and 3) false signals due to sensor degradation by nucleases[11]. Therefore, I conducted research to design, characterize, optimize, and apply two different designs of logic sensors to overcome some of the bottlenecks facing current *in situ* sensors. My research in the field of molecular logic centered

around contributing innovative designs and establishing design principles for constructing nanodevices. The term "AND" means the sensor's signal only turns ON when all miR inputs are present.

My first logic sensor design[12], published in *Nanoscale*, is called a nano-assembly logic gate (NALG). My contribution to the molecular logic field is a unique multi-hairpin motif designed. The purpose the multi-hairpin motif was to improve input number (multiplexing ability), selectivity, and robustness to false signal generation. Furthermore, the motif's design will serve as the base building block for a modular design for scaling up the multiplexing ability. NALG was designed for three miRs: miR27a, miR96, and miR182. The signal transduction mechanism of NALG was based on Förster Resonance Energy Transfer (FRET) enhancement. The results showed that NALG had: (1) low nanomolar (nM) limits of detection (LOD), (2) selectivity against off-analyte cocktails (sequence similariaty ranged from 13% to 27%), (3) no false-positive signal from nuclease degradation, and (4) the ability to respond to three miRs in a matrix mimicking the cellular environment (*i.e.* crude MCF-7 cell lysate). However, NALG needed refinement to improve its ability to differentiate input numbers because it showed signal response in the presence of two out of three miRs.

In order to reduce NALG's signal response from two miRs, I studied how to fine-tune the multi-hairpin motif to better resist biochemical and biophysical interactions with two miRs. The manuscript for this work is currently under review at *Analytical Chemistry.* Three new motif types were developed based on the original motif. The motif designs were assessed based on the following design metrics: (1) the location of the inputs' complementary sequence, (2) the predicted number of Hydrogen-bonds formed in the motif, (3) the predicted change in thermodynamic values of the motif after the addition of the inputs, and (4) the predicted molarity percentage of motif forming complex with different numbers of inputs (two versus three). We measured the fluorescence response from these motifs in the presence of inputs and discovered gaps between the predicted and experimental results. Our findings provide a noteworthy improvement to the design process of molecular logic sensors for measurement science.

To overcome the limitations in the first logic sensor (NALG) design and applying what I learned about the design process, I came up with an innovative design that I call: autowalk AND logic operator (AALO). AALO was designed for a three-miR combination: miR27a, miR24, and miR210. Different from current nucleic-acid-based sensors that recognize analyte miRs through a

single toehold-mediated strand displacement reaction (TMSDR), AALO relies on a cascading (five-step) TMSDRs. The cascading TMSDRs mechanism exposes one toehold per step to initiate successive TMSDRs. The toehold (~3-6 nucleotides sequence) in the gate strand initiates binding with an incoming strand and subsequently displaces a pre-bound strand from the gate. Such a recognition mechanism requires the presence of all miR inputs to complete the cascading process and achieve signal change. AALO's lower signal change in the presence of two miRs (19% from AALO compared to 53% from NALG) means that AALO's recognition mechasim was able lower the false response from incomplete miR combinations. The five-step TMSDRs were thus able to improve the logic sensors' differentiating-input-number ability. Compared to NALG, AALO showed increased selectivity against off-analyte miRs with sequence similiarity ranging from 41% to 95%. We have prelimitary data that shows AALO was transfected into the cell line HEK 293T through nucleofection.

Reference:

(1) Jabri, E. Non-Coding RNA: Small, but in Control. *Nat. Rev. Mol. Cell Biol.* **2005**, *6*, 361.

(2) Kaikkonen, M. U.; Lam, M. T. Y.; Glass, C. K. Non-Coding RNAs as Regulators of Gene Expression and Epigenetics. *Cardiovasc. Res.* **2011**, *90* (3), 430–440.

(3) Esteller, M. Non-Coding RNAs in Human Disease. *Nat. Rev. Genet.* **2011**, *12*, 861.

(4) Lal, A.; Navarro, F.; Maher, C. A.; Maliszewski, L. E.; Yan, N.; O'Day, E.; Chowdhury, D.; Dykxhoorn, D. M.; Tsai, P.; Hofmann, O.; et al. MiR-24 Inhibits Cell Proliferation by Targeting E2F2, MYC, and Other Cell-Cycle Genes via Binding to "Seedless" 3′UTR MicroRNA Recognition Elements. *Mol. Cell* **2009**, *35* (5), 610–625.

(5) Loayza-Puch, F.; Yoshida, Y.; Matsuzaki, T.; Takahashi, C.; Kitayama, H.; Noda, M. Hypoxia and RAS-Signaling Pathways Converge on, and Cooperatively Downregulate, the RECK Tumor-Suppressor Protein through MicroRNAs. *Oncogene* **2010**, *29* (18), 2638–2648.

(6) Trapnell, C. Defining Cell Types and States with Single-Cell Genomics. *Genome Res.* **2015**, *25* (10), 1491–1498.

(7) Hemphill, J.; Deiters, A. DNA Computation in Mammalian Cells: MicroRNA Logic Operations. *J. Am. Chem. Soc.* **2013**, *135* (28), 10512–10518.

(8) Tagore, S.; Bhattacharya, S. DNA Computation: Applications and Perspectives. *J. Proteomics Bioinform.* **2010**, *03* (07).

(9) He, L.; Hannon, G. J. MicroRNAs: Small RNAs with a Big Role in Gene Regulation. *Nat. Rev. Genet.* **2004**, *5* (7), 522–531.

(10) Bartel, D. P. MicroRNAs: Genomics, Biogenesis, Mechanism, and Function. *cell* **2004**, *116* (2), 281–297.

(11) Chen, A. K.; Behlke, M. A.; Tsourkas, A. Avoiding False-Positive Signals with Nuclease-Vulnerable Molecular Beacons in Single Living Cells. *Nucleic Acids Res.* **2007**, *35* (16), e105–e105.

(12) Zhang, L.; Bluhm, A. M.; Chen, K.-J.; Larkey, N. E.; Burrows, S. M. Performance of Nano-Assembly Logic Gates with a DNA Multi-Hairpin Motif. *Nanoscale* **2017**, *9* (4), 1709–1720.

Innovative Bioanalytical Tools & Methods for Combinatorial Non-Coding RNA Analysis

by
Lulu Zhang

A DISSERTATION

submitted to

Oregon State University

in partial fulfillment of
the requirements for the
degree of

Doctor of Philosophy

Presented October 31, 2018
Commencement June 2019

Doctor of Philosophy dissertation of Lulu Zhang presented on October 31, 2018

APPROVED:

Major Professor, representing Chemistry

Head of the Department of Chemistry

Dean of the Graduate School

I understand that my dissertation will become part of the permanent collection of Oregon State University libraries. My signature below authorizes release of my dissertation to any reader upon request.

Lulu Zhang, Author

ACKNOWLEDGEMENTS

First I would like to thank my advisor Dr. Sean M. Burrows for his guidance, support, and contribution. Sean taught me almost everything I know about spectroscopy. I appreciated the research discussion in the office, the hands-on demonstration in the lab, and the encourage of presentation in the conference. Over the past 5 years, Sean has guided and assisted me to develop a deeper understanding of being a scientist.

I would like to thank my other graduate committee members for their insightful advice: Dr. Colin Johnson, Dr. Staci Simonich, Dr. Siva Kolluri, Dr. Dipankar Koley, Dr. Christopher Beaudry, and Dr. David McIntyre. I would like to thank Dr. Colin Johnson for his expertizing suggestions on cell fixation. I would like to thank Dr. Staci Simonich and Dr. Dipankar Koley for their brilliant advice on presenting scientific projects to the public audience. I would like to thank Dr. Siva Kolluri for helping me on my cellular transfection experiments, giving me the access to his lab, and giving HEK 293T cell lines as a gift. I would like to thank Dr. Christopher Beaudry for willing to substitute for Dr. Dipankar Koley and attending my final thesis defense.

I would like to thank Dr. Weihong Qiu for allowing me to use the TIRF microscope and the postdoctoral scholar, Dr. Kuo-Fu Tseng, for his training on the usage of the TIRF microscope for cellular imaging. I would like to thank Martin Pearce, a graduate student from Dr. Siva Kolluri's research group, for training me to use the nucleofector for delivering the DNA samples into HEK 293T cells. I would like to thank Dr. Chrissa Kioussi for allowing me to use the electroporator. Vera C. Lattier, a graduate student from Dr. Chrissa Kioussi's research group, sharing their brilliant suggestions on cellular transfection and imaging work, and patient assistance of training on the usage of the instruments.

I thank all the amazing people I have worked with from the Department of Chemistry at OSU: Dr. Chris Pastorek, Dr. Neal Sleszynski, Dr. Kristin Ziebart, Margie Haak, Paula Weiss, and Kristi Edwards.

I would like to thank my lab mates Nicholas Larkey, Kyle Almlie, Lixia Zhou, Kuan-Jen Chen, Annie Bluhm, Susmitha Matlapudi, Shan Lansing, Jake Ramsey, Victoria Tran, Cori Brucks, Sophia Le, Natasha Smith, and Chen Ng. The lab became a much interesting place with your presence. I especially thank Dr. Nicholas Larkey. He is not only my previous lab mate and

roommate, but also one of my best friend. Thank you Nick for inspiring suggestions in research, encouragement in the scientific outreach events, and amusing company to enjoy food and movies.

I would like to thank my lovely family, Suiyuan, Jianlan, Xianfan, Luqiong, and Ke. You have always been so supportive and caring. Especially my younger brother Xianfan has been encouraging and helping me. And good luck for him seeking his master degree in Mechanical Engineering at OSU. I love you all.

I would also like to thank my American family Ben Slothower and Melody Slothower for helping me settle down in Corvallis five years ago. Their kindness has been warming me all the time.

Kelly Boonloed, Tony Anukul Boonloed, Partha Sheet, Fisher Yu Xi have been four of my best friends during my time here in Corvallis. I thank them for making my graduate life more amusing and exciting. I would also like to thank all my other friends in Corvallis for being there for me.

To my undergraduate advisors, Dr. Shiming Wang and Dr. Kestas G. Bendinskas, without your help I would not be able to make it to graduate school. Thank you so much.

I would also like to thank the Bruce Graham Memorial Scholarship Fund, Milton Harris Summer Fellowship, and Graduate student travel award for supporting my research.

CONTRIBUTION OF AUTHORS

Chapter 2. Sean M. Burrows contributed in part to the preparation and review of this manuscript. Annie Bluhm, Kuan-Jen Chen, and Nicholas Larkey all performed some experiments for the manuscript.

Chapter 3. Sean M. Burrows contributed in part to the preparation and review of this manuscript. Annie Bluhm and Dr. Kuo-Fu Tseng all performed experiments for the manuscript.

Chapter 4. Sean M. Burrows contributed in part to the preparation and review of this manuscript. Susmitha Matlapudi and Annie Bluhm all performed experiments for the manuscript.

TABLE OF CONTENTS

Page

TABLE OF CONTENTS (Continued)

Page

LIST OF FIGURES

LIST OF FIGURES (Continued)

Figure Page

LIST OF TABLES

Table Page

Innovative Bioanalytical Tools & Methods for Combinatorial Non-Coding RNA Analysis

Chapter 1.

Introduction

1.1 Current Technology for small non-coding RNA Analysis

Once thought to be "junk RNAs" are now emerging as critical sculptors of cell biology. One exciting class of "junk RNAs" are small non-protein-coding RNAs (ncRNAs). Small ncRNAs exhibit functional roles in regulating gene expression[1–4] and participating in a diverse set of physiological processes[5–7] as well as the pathogenesis of many diseases[8–12]. Cell based assays for small ncRNAs are in demand for monitoring the change in their expressional patterns, such as the relative expression levels and the spatial and temporal heterogeneities. The ability to measure heterogeneities will help define cell types and cell states for differentiating cell populations.[13] Having molecular analysis tools that reveal heterogeneities among cell populations will provide unique insights on the physiological changes and processes (*i.e.* aging) of each cell and how these cells work together to maintain homeostasis or drive disease progression. However, most of current techniques were not built for small ncRNAs due to their features including the small physical size, sequence similarity, low abundance, or complexity of expressional patterns (combinations of multiple molecules more relevant than any one molecule alone). *As a model system to develop innovative molecular analysis tools for small non-coding RNAs around, my thesis will focus on microRNAs (miRs)*.[14] For details about miR biogenesis and specific disease-associated miR combinations see Section 1.2 below.

MicroRNAs are emerging as the interesting analytes because we are only beginning to learn about the biological significance of their spatiotemporal localization in live cells and differential combinatorial expression between normal and diseased cells.[15–19] By analyzing miR patterns in whole cells, we will be able to better understand how miRs shape cell biology and advance miR biomarkers discovery. Therefore, scientists need innovative molecular analysis tools and methods to monitor intracellular miR patterns.[20] Furthermore, as miR biomarker discovery progresses, having the analytical technology ready will be crucial to support discovery efforts and disease diagnostics.[12,21] Although miR is the model system to assess the analytical values of the

tools and methods presented herein, my contributions will be broadly applicable to any small ncRNA, other short oligonucleotides, and possibly small molecules.

Intracellular multiplex analysis is critical to identifying temporal and spatial heterogeneities in small ncRNA expression within a single cell and/or among cell populations. However, due to small ncRNA's short length, low expression level, and sequence similarity, current analytical approaches are not directly applicable for intracellular multiplex small ncRNA analysis. Current analytical approaches can be classified as *in vitro* and *intracellular (or in situ)*. *In vitro* methods include: a) microarrays[22,23], b) quantitative reverse transcription polymerase chain reaction (qRT-PCR)[24–26], and c) next-generation sequencing[27]. Current *in situ* analytical tools for fixed and live cell analysis or tissue imaging rely mainly on nucleic acids as natural building blocks to construct programmable analysis devices[28–37] including: a) Fluorescence *In-Situ* Hybridization (FISH[38,39], including multiplexed error-robust FISH[40–42]), b) Smartflares®[43], c) molecular beacons (MBs)[44,45], and logic gates[46–48]. I will briefly discuss the benefits and challenges of *in vitro* and *in situ* methods when they are adapted to intracellular analysis of short oligonucleotides (*e.g.* miR). Tables 1.1 and 1.2 highlight some of the challenges facing both *in vitro* and *in situ* methods for small oligonucleotide analysis that I will address in my thesis.

Table 1.1 Challenges facing *in vitro* analytical methods for short miR profiling.

In vitro analytical methods	Challenges
Common limitations for all *in vitro* analytical methods discussed here	-Due to RNA extraction, *in vitro* analytical methods cannot visualize spatial changes of miR patterns in cells and tissues -Loss of information on cell-to-cell variability in expression due to RNA typical pooling prior to analysis
qRT-PCR	-No common sequence (*e.g.* poly(A) tail) as a binding site for universal primers -miRs sequence is too short to bind for traditional primers -Low selectivity to different miRs with similar sequence
Microarray	-Poor sensitivity to low levels of miRs -Poor correlation between microarray- and qRT-PCR-based miR expression have been reported
Next-generation sequencing	-Require complicated computational systems for data analysis and interpretation -Cannot compare miR expression from different samples with high variance

Table 1.2 Challenges facing *in situ* analytical methods for short miR profiling.

In situ analytical methods	Challenges
Fluorescence in situ hybridization (FISH)	-Cannot detect miRs in live cells or tissues -miRs lost from multiple washing steps – requires extra chemicals to avoid loss from washing, but introduces possibility of fixing probe to off-analyte -Challenging probe design due to short length of miRs -Often require extra signal amplification step thus increasing time-to-result -Poor selectivity as a result of unspecific binding with endogenous mRNA and off-analyte miRs – requires expensive chemical modification to address this problem and often the chemical modification is not sufficient.
Smartflare®	-Susceptible to false signals from nuclease degradation during biological analysis due to the transduction mechanism relying on the disruption of a quencher-fluorophore pair -Low throughput for the maximum limit of two to four miRs
Molecular beacons	-Like Smartflares® susceptible to false signals from nuclease degradation -Poor selectivity for miRs with similar sequences[1] -Low throughput for only handling one miR input per sensor
Logic gates	-Many logic gates rely on the disruption of a quencher-fluorophore pair, thus susceptible to false signals from nuclease degradation during biological analysis -Low throughput for the maximum of two miRs per logic gate

1.1.1 Analytical tools for *in vitro* analysis

In vitro approaches for miR profiling require extracting total RNA from biological samples. However, total RNA extraction is susceptible to the loss of detailed information in regard to miRs' spatial and temporal expression within the cell and in sub-cellular compartments.[49] Another down side to most *in vitro* methods is the fact that RNA among many cells are pooled together prior to analysis.[50,51] Such pooling of RNA loses information on cell-to-cell heterogeneity as it pertains to the miR patterns making up the cells.

After total RNA extraction, analyte miRs are reversely transcribed, and then amplified through quantitative polymerase chain reaction (Figure 1.1a). Unlike mRNAs, mature miRs lack common sequence (*e.g.* a poly(A) tail) as a binding site for universal primers and are too short (~22 nucleotides) to bind to traditional primers. Therefore, in order to profile miR expression with qRT-PCR, analyte miRs either require a stem-loop primer for the reverse transcription, or an *E.coli* poly(A) polymerase to add a poly(A) tail for both reverse transcription and PCR.

The amplification products can be detected in real-time by oligonucleotide probes (e.g. TaqMan® probes) or intercalating dyes (SYBR® Green I). A TaqMan® probe is labeled with a fluorescent reporter dyes at 5-prime end, and a quencher dye at 3-prime end. During PCR, TaqMan® probe hybridizes to a prime site in the analyte sequence (reverse transcribed products) and then is cleaved by Taq DNA polymerase as the primer is extended (Figure 1.1a). The cleavage

separates the fluorophore from the quencher leading to the increase in fluorescence. The fluorescence increase is proportional to the number of probe cleavage cycles, thus allowing for quantitative analysis of RNAs. "SYBR® Green I" can also be used for real-time detection of PCR as its fluorescence signal increases when bound to the increasing double-stranded DNA amplicon. Working with either TaqMan® probes or intercalating dyes, qRT-PCR has the potential to detect low concentration of RNAs from samples such as plasma and serum[52,53] through amplification. However, applying qRT-PCR to analyze shorter RNAs is problematic because off-analyte miRs with similar sequences to the analtyte miRs are susceptible to being amplified during PCR. Thus qRT-PCR has poor sequence selectivity when it comes to small ncRNAs.

Microarrays (Figure 1.1b) rely on a surface-bound hybridization-based assay for analyzing large numbers of RNA in parallel. After total RNA extraction, analyte RNAs are reverse transcribed to the complementary DNA (cDNA). Then these cDNAs are immobilized on a slide or on beads to act as capture probe. A T4 RNA ligase connects each RNA molecule to nucleotides that contain a fluorophore at the 3'end. After the ligation process, the fluorophore labeled RNAs are introduced to the slide or beads containing capture probes. Any RNAs that are complementary to the cDNAs are captured and will not be removed by the subsequent surface washing steps. The fluorescent signal is then measured to determine the relative amounts of RNA from two or more samples (*e.g.* control vs. treatment). Compared to the other *in vitro* approaches discussed, microarrays are less expensive.[54] However, microarray techniques are limited in their sensitivity especially for measuring low levels of RNAs.[54] The reason microarray technology suffer from sensitivity issues is because RNAs are diluted when pooled for analysis. In addition, microarrays cannot determine the absolute quantity of analyte RNAs and the results normally require validation by other methods, such as RT-qPCR.[54,55] Furthermore, some cancer-related studies have reported a relatively poor correlation between microarray- and qRT-PCR-based miR expression.[56,57]

Next-generation sequencing (Figure 1.1c) enriches the low levels RNA through size-selection methods (*e.g.* gel electrophoresis[24]). Similar to the reverse transcription step in RT-qPCR, enriched analyte RNAs are reverse transcribed creating a cDNA library. The ends of cDNAs are then ligated with adapters (short artificial DNA oligonucleotides) in order to affix these cDNAs to a solid phase (*e.g.* IIIumina platform), or to beads for emulsion PCR (Roche and ABI platform) for sequence reading. The major advantage of next-generation sequencing for miR assays is the ability to discover novel miRs.[56] However, these novel miRs need further verification through

experiments.[54] Compared to RT-qPCR, next-generation sequencing costs more and require complicated computational systems for data analysis and interpretation.[54] Such technique can only quantifies the relative abundance of miRs in a specific sample based on the ratio of the sequence-reads number for a given miR to the total sequence-reads number for that sample. However, due to the possibility of high variances between different samples, it is not reliable to compare miR expression from these samples.[54]

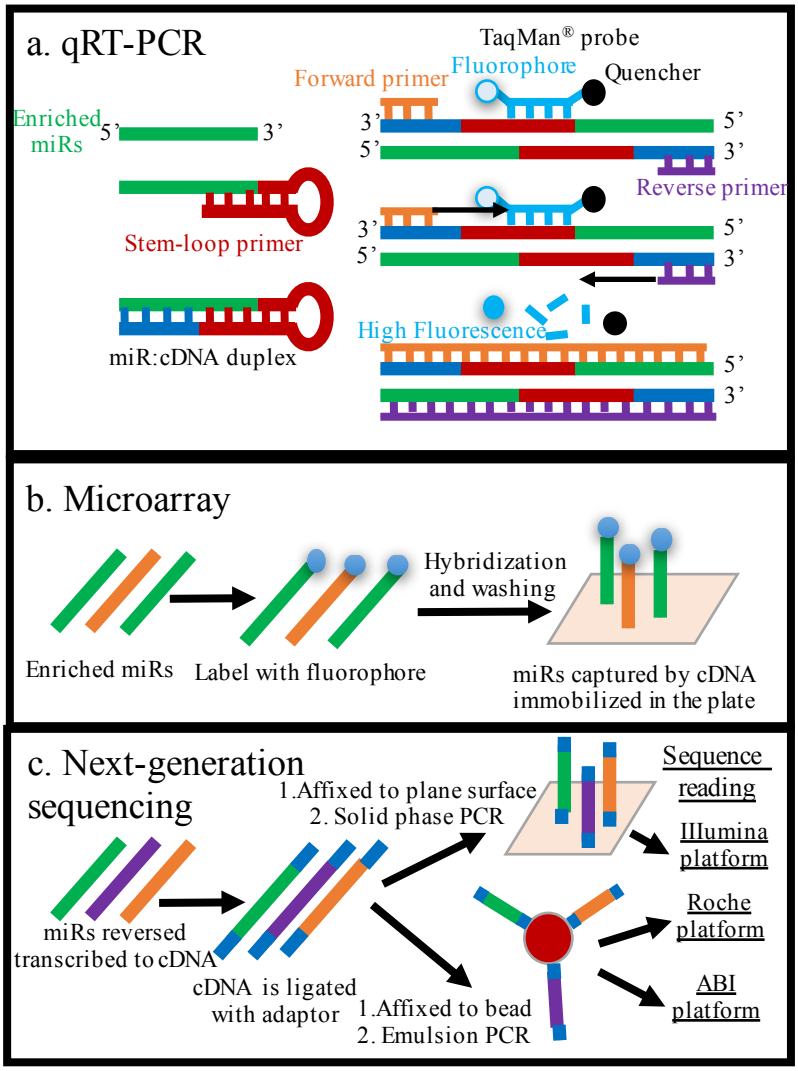

Figure 1.1 *In vitro* miRNA profiling approaches: (a) qRT-PCR, (b) microarray, (c) next-generation sequencing.[54]

1.1.2 Analytical tools for *Intracellular (in situ)* analysis

In situ analysis allows for visualizing where analytes spatially distributed as well as differentiating cell types and subtypes based on their miR patterns. One predominate i*n situ* method

is Fluorescence *In-Situ* Hybridization (FISH, Figure 1.2a). FISH is a well-developed method for nucleic acid analysis. FISH relies on fluorescently-labeled probes that are transfected into the sample and bind analyte nucleic acids through base-pairing. Since the fluorescently labeled FISH probes always generate signal, the biological samples (cells or tissues) require fixation and permeabilization to allow for rinsing of unbound probes.[56] After several washing steps only the fully complementary probe-analyte complexes are left behind inside the fixed samples. Potential secondary labeling may be needed for signal amplification before these cells or tissues are imaged through fluorescence microscopy. As discussed earlier, FISH can only be used on fixed cells and tissues, making live cell analysis unobtainable. In addition, FISH struggles with other limitations when applied to miR due to their small sized and low abundance. These limitations include (1) loss of miRs from multiple washing steps[56], (2) challenging probe design due to short analyte miR[56], (3) sometimes require extra signal amplification step such as Tyramide Signal Amplification (TSA^{TM})[58,59], and (4) poor selectivity as a result of unspecific binding with endogenous mRNA and off-analyte miRs[42]. Developed from standard FISH, multiplexed error-robust FISH (MERFISH) enables multiple probes to simultaneously measure hundreds of nucleic acids analytes in a single cell.[40] However, the increased number of probes increases the number of hybridization rounds, which significantly increases time-to-result.[40] Furthermore, MERFISH suffers from all the same limitations that standard FISH, making the approach challenging for intracellular miR pattern analysis.[60,61]

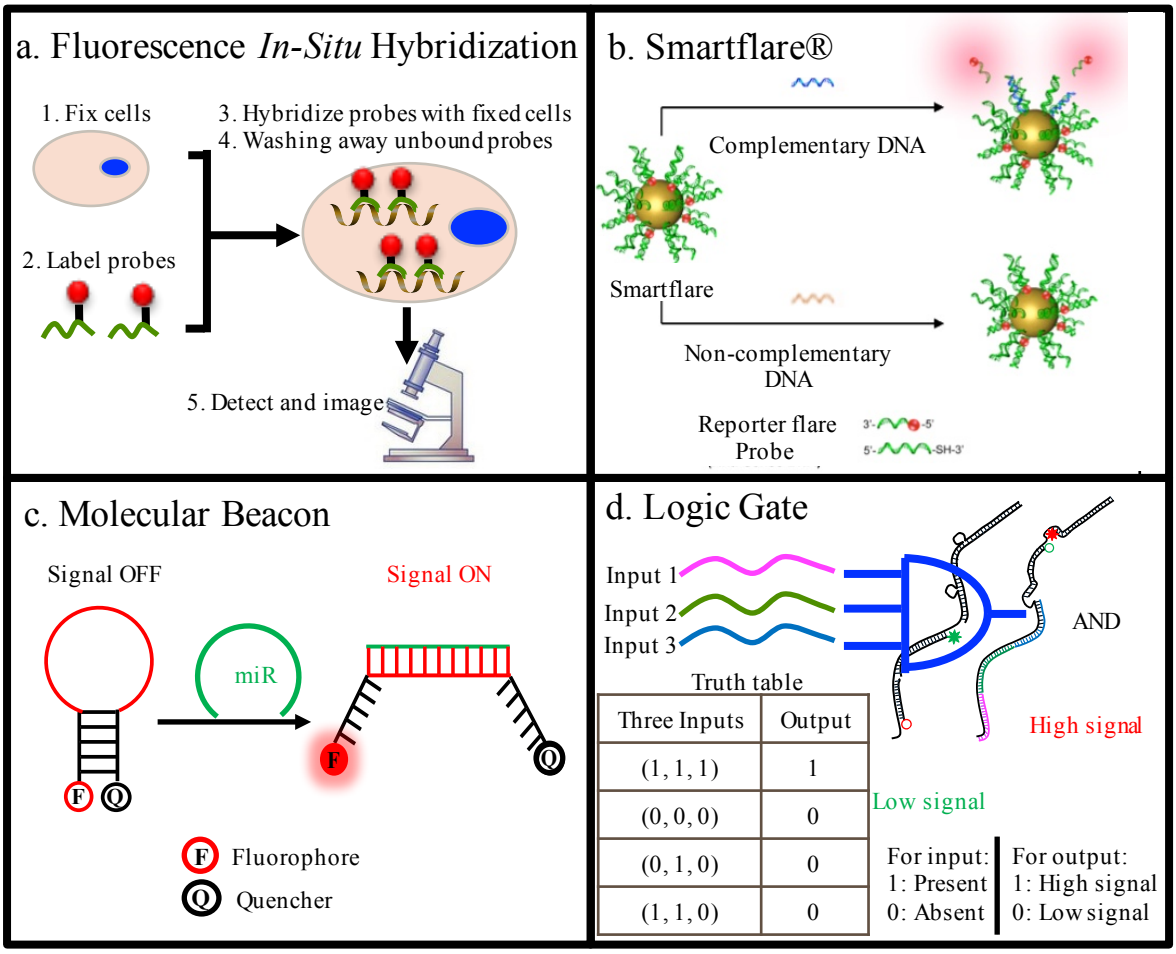

Figure 1.2 *In situ* analytical methods for RNA analysis: (a) Fluorescence *In-Situ* Hybridization (FISH)[62], (b) Smartflare®[63], (c) Molecular Beacon (MB)[64], (c) AND Logic Gate (*e.g.* my developed autowalk AND logic operator in Chapter 4).

One popular tool for live cell molecular analysis is a Smartflare® (Figure 1.2b). Smartflare®s consist of a 'spherical nucleic acid' (SNA) conjugate with partially double-stranded oligonucleotides bound to a gold nanoparticle. The partially double-stranded oligonucleotide consists of a capture strand and a dye-labeled "flare" strand. The capture strand is designed to bind to analyte nucleic acids via a process known as toehold-mediated strand displacement.[65–67] In this process the capture strand has a few bases exposed, known as a toehold, to initiate binding with analyte nucleic acids. The strand displacement reaction displaces the reporter strand from the capture strand. Without analyte, the dye-labeled reporter strand stays on the gold nanoparticle and exhibits quenched fluorescence. With analyte present, the reporter strands get displaced and the fluorescent signal is increased. The transduction signal of Smartflares® relies on the disrupting a quencher (gold nanoparticle)-fluorophore pair. Unfortunately, such transduction mechanisms are

susceptible to false signals from nuclease degradation during cellular and tissue imaging. Furthermore, Smartflare®s were not designed for the small size of miR.

Molecular beacons (MB, Figure 1.2c) allow for both *in vitro* analysis[45] and *in situ* cellular imaging of nucleic acids.[44,68] Molecular beacons are single-stranded nucleic acids with stem-loop structure. Typically they are labeled with a fluorophore on one end and a quencher on the other end. In the absence of complementary analyte oligonucleotides, the fluorophore is close to the quencher creating low fluorescent signal (known as signal OFF). In the presence of complementary analyte oligonucleotides, the analyte binds to the loop of MB to disrupt the stem, therefore separating the dye from the quencher. As a result, the fluorescent signal is increased (known as signal "ON"). Since the transduction mechanism relies on the displacement of the fluorophore from the quencher, it is prone to false signals due to nuclease degradation of MBs.[68] As for miR analysis, other disadvantages of MBs include the low selectivity for miRs with similar sequences[69] and low throughput (only one miR input per sensor). Thus, the low throughput for MBs combined with spectral cross-talk from multiple dyes restricts simultaneous multiplexing in single cells to 4 miRs.[70]

In addition to the gold particles[71,72] employed in Smartflare®, alternative nanoparticles such as silver nanoclusters (AgNC)[73], quantum dots (QDs)[74], carbon nanotubes[75], polymer dots (PDs)[76], upconverting nanoparticles (UCNPs)[77] have been reported to serve as signal transducer and work with nucleic-acid-based probes (*e.g.* molecular beacons) for sensing nucleic acids. However, the safety of these nanoparticles (*e.g.* Cd for QDs) in biological studies and applications is still unclear so far and needs further study. Therefore, instead of applying these transducers for nucleic acids analysis, organic fluorophores (FAM and ATTO633) were selected to label nucleic-acid-based sensors for signal transduction.

1.1.3 Nucleic-acid-based logic gates

In order to make progress in the multiplex small ncRNA analysis, nucleic-acid-based logic gates (Figure 1.2d) are emerging. So-called molecular logic implements one or multiple Boolean logic functions (AND, OR, and NOT). Logic gates[65] usually consist of two nucleic acid strands: (1) a gate strand and (2) an output strand. The biomolecules of interest are referred as the input strands. The gate strand is typically designed to be more complementary to the input than to the output strands[78]. In order to report on the interaction between the gates and inputs, output strands

are often labelled with fluorescent dyes and thus are also known as reporter strands.

To advance molecular logic analysis in terms of intracellular multiplex analysis of small nucleic acids, I focused on AND molecular logic. AND logic means the logic gate only responds to a specific pattern of small nucleic acids. The recognition mechanism relies on a toehold-mediated strand displacement reaction (TMSDR) that facilitates the release of the output strand as the input strands bind the gate. Recall that a toehold is a small exposed segment of DNA (~ 3-6 nucleotides long) in the gate strand that helps the input intimate binding and subsequent TMSDR.[79–81] Strand displacement refers to a thermodynamically driven process whereby inputs outcompete outputs to bind the gate strand through more complementary base-pairing interactions. The thermodynamic values (*e.g.* Gibbs energy) of the gate-input and gate-output complex can be predicted from open-source web servers such as DINAMelt[82,83] and NUPACK[84]. The displacement of the output strands result in a detectable signal change. Various transduction mechanisms for output signal generation have been reported such as fluorescent-based[65,74,85], electrochemical-based[86,87], photoelectrochemical-based[86], and chemiluminescent-based[88]. The two logic gates that I designed rely on Förster resonance energy transfer (FRET) for signal generation. We will discuss FRET more in Section 1.1.4.

1.1.4 FRET-based transduction mechanism

Building off work by Bao[64] for mRNA analysis tools, I adapted and applied the distance-sensitive Förster resonance energy transfer (FRET) process as the transduction mechanism. By monitoring the FRET signal changes, I investigated the interaction between the molecular logic gates and miR inputs. FRET is a photo-physical phenomenon that occurs when an excited donor fluorophore transfers energy to a nearby acceptor fluorophore (typical distance is 1 – 10 nm) through a nonradioactive dipole-dipole interaction.[89,90] The efficiency of the energy transfer between the donor and acceptor depends on: (1) their distance (inversely proportional to the sixth power of the separation distance), (2) the extent of spectral overlap between the dyes, (3) the relative orientation of each dye's transition moment (higher efficiency the more parallel they are to each other), and (4) the fluorescence lifetime of the donor must be long enough to allow FRET to occur (i.e. $t_{fluorescence} >>> t_{FRET}$). Spectral overlap refers to the overlap between the donor's emission spectrum and the acceptor's absorption or excitation spectrum.

1.1.5 Development of AND logic gates

My thesis will describe the work I did and contributed to the field of molecular logic design. I focused on advancing logic gate technologies for multiplex analysis of small ncRNA through the development of two innovative logic gates. The logic gates rely on a toehold-mediated strand displacement reaction as the recognition mechanism. To address the low throughput of current *in situ* analytical tools, I innovated the nanostructure of current logic sensors to expand input numbers. As we know the expression patterns of multiple miRs are often more informative of the biology, than any one miR.[91,92] Compared to most published logic devices only for one or two inputs, my logic nanosensors are able to sense three inputs. The ability to sense one more input is powerful when three-input logic gates are used as building blocks to develop logic circuits. For example, a logic circuit combined by four of three-input logic gates is able to expand input number up to tens.[70] Such logic circuit is able to detect four more inputs than a circuit built upon two-input logic gates.

To address the sensor's susceptibility to false-positive signal from nuclease degradation, both AND logic gates relied on Föster Resonance Energy Transfer as the transduction mechanism. No false-positive signals were observed from studies exposing the nanosensors to enzymes (DNAse I). These findings confirm the FRET design methods addressed false-positive signal susceptibility.

After reading the literature and attending symposia in the field, I was inspired to combine what I learned about toehold and strand displacement reaction to create this new design, autowalk AND logic gate (AALO). AALO relies on a cascading toehold-mediated strand displacement reaction to inhibit recognition process until all analyte biomolecules are present. Thus recognition mechanism allows AALO to better differentiate a complete from an incomplete combinations of biomolecules thus improving its differentiating-input-number ability.

In Chapter 2 "Performance of nano-assembly logic gates with a DNA multi-hairpin motif", I will present my first logic sensor design for multiplex analysis of small ncRNA.[85] As a model small ncRNA system to design and test the logic sensor in this chapter, I chose three miRs: miR27a, miR96, and miR182. To the best of my knowledge, the nano-assembly logic gate (NALG) was the first enzyme-free and label-free (analyte miRs do not need to be labeled) AND logic gate that accept three miR inputs per gate. Chapter 2 demonstrates that NALG achieves a detection limit of nanomolar-range to a combination three miR inputs, (2) is selective against off-analyte cocktails

(sequence similariaty ranged from 13% to 27%), (3) avoids false-positive signal from nuclease degradation, and (4) is able to respond to three miRs in a matrix mimicking the cellular environment (*i.e.* crude MCF-7 cell lysate).

However, NALG did not act as a strict AND logic gate for three inputs because it showed signal responses when two miR inputs were present. Such similar signal response to a complete and incomplete combination of miRs resulted in a low differentiating-input-number ability for NALG. In order to improve the differentiating-input-number ability of NALG, I focused on the multi-hairpin motif because in NALG, motif was the key part to accommodate the inputs and change the signal. I hypothesized that modifying the motif would improve its differentiating-input-number ability.

To test my hypothesis, in Chapter 3 "Structural and thermodynamic principles influencing nanoscale molecular-logic-based measurement systems", I present design metrics to fine-tune the multi-hairpin motif in order to improve its differentiating-input-number ability. The design metrics include *in silico* thermodynamic factors (*e.g.* Gibbs energy and melting points) and structural features (the locations of the binding sites for inputs). The differentiating-input-number ability of these motifs are predicted from open-resource web servers and compared to the experimental results. In this chapter, I will highlight agreement and disagreement between the theoretical and experimental signal response of the motif in the presence of two versus three inputs.

Chapter 4 "Molecular logic nanosensor with cascading-toeholds for error-robust small RNA combinatorial analysis", presents my second logic gate design for three miRs: miR27a, miR24, miR210. The recognition and transduction mechanism of autowalk AND logic operator replies on a cascading toehold-initiated strand displacement reaction and signal increase from Föster Resonance Energy Transfer. Compared to NALG, AALO showed critical improvements in (1) the selectivity against off-analyte miRs with up to 95% sequence similarity to analyte miRs, and (2) the differentiating-input-number ability at distinguishing two miRs from three miRs by enlarging their signal difference from 47% (seen in NALG) to 80%.

Chapter 5 summarizes all the research I have done on the logic sensor design for multiplexing miRs analysis. This chapter will outline the challenges and future directions of my logic sensors.

1.2 RNA Biology

Not all DNA genes are transcribed to protein-coding mRNA, many are transcribed to non-coding RNAs (ncRNAs) that do not encode proteins.[93] These ncRNAs are found to fulfill regulatory functions in cells.[94] Regulatory ncRNAs include but are not limited to long non-coding RNAs (lncRNAs), microRNAs (miRs), piwi-interacting RNAs (piRNSs), and small interfering RNAs (siRNAs).[95] Regulatory ncRNAs have been postulated to regulate gene expression by a variety of mechanisms, at various times, and at various expression levels. Examples of regulatory roles include: (1) transcription, (2) post-transcriptional processing, and (3) translation.[93,96,97] Most regulatory ncRNAs exhibit conserved expression patterns in a subcellular-[98], cellular-[99,100], and tissue-specific[101,102] manner. The temporal and spatial expression of regulatory ncRNAs have been discovered in diverse biological processes, such as (1) cell cycle regulation[103], (2) apoptosis[4], aging[7], (3) cell fate decisions[104], and (4) different signaling pathways[105]. In addition, changes in intracellular expression patterns of regulatory ncRNAs have been observed during the pathogenesis of many diseased cells[106,107], such as cancer cells[15,108–111].

As a model system to design small ncRNA analysis technology around I will focus on microRNAs (miRs). Because of their temporal and spatial heterogeneities in their cellular expression, miRs are gaining attention. However, due to their cell and tissue specific nature, short length, sequence similarity, and coordinate regulation of mRNA and other genetic biomolecules, innovative cell-based analytical tools are in demand. Moreover, innovative tools are required to provide unique insights on the physiological changes and processes of cells and tissues.

1.2.1 MicroRNA: characteristics, bio-function, and biogenesis

MicroRNAs (miRs) are one class of small ncRNA that have gained recent attention. They are characterized by their short length of approximately 18 to 24 nucleotides and low expression level ranging from femtomolar (fM) to nanomolar (nM).[14] Typically, miRs post-transcriptionally regulate messenger-RNA (mRNA) expression through base-pairing by interacting with its 3'-untranslated regions (UTRs). As a result, miRs inhibit protein synthesis by either repressing mRNA ranslation, promoting mRNA deadenylation, or inducing mRNA decay.[112] In addition to the classical mechanism (discussed more detail below), miRs have been observed to target promoter region in the DNA[2,96] and activate translation[112] to induce gene expression.

MicroRNAs represent an important analyte because the precise roles they play in biology

are still being elucidated.[103,104] Additionally, they are emerging as potential biomarkers or therapeutic tools to diagnose and treat diseases, respectively.[21,113,114] The expression pattern of miRs has been found to be conserved within healthy cells but changed in different states of cell cycle and in diseased cells.[115] The dysregulation of miR expression (either up- or down-regulated) have been observed in various cancers such as breast[109,116–119], lung[111,120,121], and ovarian[122]. For example, White *et al.* discovered that the mRNA transcripts of a putative tumor suppressor (FOXO1) was coordinately regulated by a group of miRs in breast cancer cells.[117] Besides cancer, miR-associated regulation has been found in many other diseases such as immunological diseases[123], cardiovascular diseases[124], and neurological diseases[125].

Figure 1.3 depicts the biogenesis of miRs.[14,20] RNA polymerase II transcribes most miR genes to primary precursor miRs (pri-miRs, 500-3000 bases) that are folded into a hairpin-loop structure containing the mature miR sequences. Pri-miRs are processed down to ~70-nucleotide precursor miRs (pre-miR) by Drosha (an RNase III enzyme) and DGCR8/Parsha (a double–stranded RNA-binding domain protein) in the nucleus. An alternative miR biogenesis pathway produce pre-miRs from short introns (mirtrons) via splicing and debranching, thereby circumventing the Drosha-DGCR8 pathway.[126] Finally, pre-miRs are transported out of the nucleus and into the cytoplasm by the export factor Exportin-5.

Once in the cytoplasm, pre-miRs are cleaved by Dicer (another RNase III enzyme), with its co-factor transactivation-responsive RNA-binding protein (TRBP), to produce an ~22-base-pair double-stranded duplex (miR/miR*). An additional pre-miR processing step is observed in mammals where argonaute 2 (AGO2) supports Dicer by cleaving pre-miRs (12 nts in 3' end) thus forming an intermediate referred as argo2-cleaved precursor miR (ac-pre-miR).[127]

The final stage of miR biogenesis involves an RNA-induced silencing complex (RISC) that contains Argonaute (Ago2), Dicer, and TRBP. RISC preferentially binds to the mature/guide strand. The mature/guide strand generally is the one that has less stable base-paired 5-prime end in the miR/miR* duplex.[112] The other strand (passenger/anti-sense strand, miR*) is preferentially released and degraded. However, many miR* strands are being found to be well-conserved and demonstrate regulatory capacity.[128,129] Most mammalian miRs from miR-RISC bind imperfectly to 3' untranslated region (3'-UTR) of their target mRNA. As a result, the target mRNAs are transnationally repressed, deadenylated, or degraded.[14] Most plant miRs were found to target either the coding regions or 3'-UTRs of mRNA through nearly perfect base-pairing, therefore activating

the endonuclease activity of RISC to cleave and further degrade mRNA.[130–132]

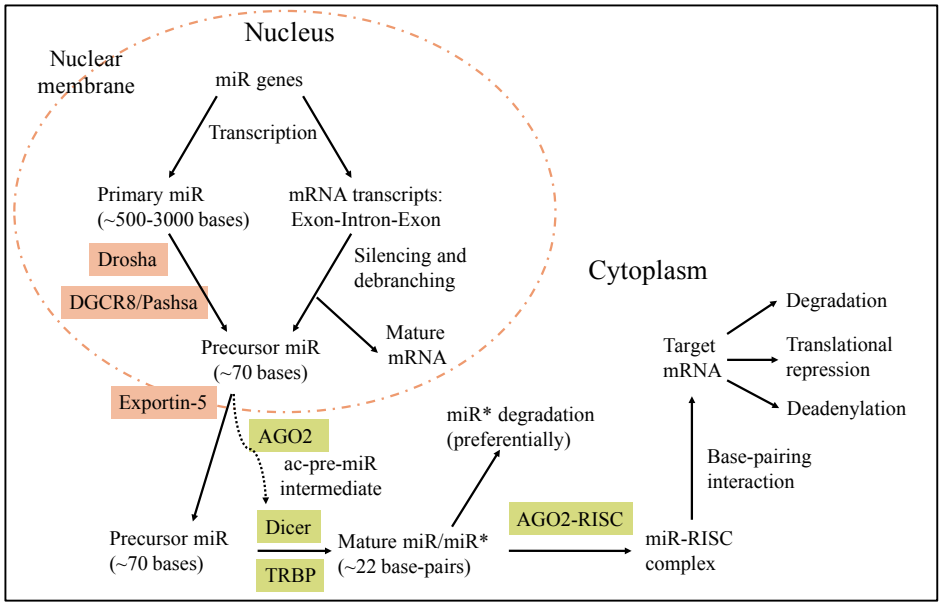

Figure 1.3 MicroRNA biogenesis.[112] Large pri-miRs are transcribed from miR genes, then processed in the nucleus by Drosha and DGCR8 into ~70-nucleotides pre-miR. A non-canonical pathway reveals some pre-miRs are produced from short introns (mirtrons) via splicing and debranching. Pre-miRs are transported to the cytoplasm by Exportin-5. Then the pre-miRs are cleaved by Dicer with its co-factor TRBP to produce the mature miR/miR* duplex (~ 22 base-pairs). An additional pre-miR processing step is observed in mammals where argonaute 2 (AGO2) supports Dicer to cleave the pre-miR thus forming an intermediate (ac-pre-miR). The guide miR is preferentially loaded into Ago2-containing RNA-induced silencing complex (RISC), whereas the anti-sense strand miR* is preferentially degraded. The guide strand (miR) in miR-RISC targets mRNA transcripts by base-paring interactions. The guide strand (miR) anneals to the target mRNA with either imperfect (in most animals) or nearly perfect base-paring (in most plants) resulting in either degradation, deadenylation, or transcriptional repression of target mRNA.

1.2.2 Disease-associated microRNA patterns as model systems

Often miR coordinately work in groups to control target gene expression in a cell- and tissue-specific manner.[117,133–135] The temporal and spatial heterogeneities in miR expression patterns are related to diverse physiological processes and pathogenesis of diseases. Thus, miR patterns may someday become valuable biomarkers or therapeutic tools.[16,20,21,136] However, as reported in a recent review article on miR analysis[70], the available tools are insufficient to support research to understand miR biology and discover biomarkers. Thus, measuring the temporal and spatial expression changes of a cell's, or tissue's miR landscape will help (1) reveal miRs' yet to be discovered regulatory functions, (2) distinguish cell subtypes based on differential miR profiles, (3) gain insight on miR-based cellular regulation pathways, and (4) one day diagnose the onset of disease. For these reasons, scientist need innovative molecular analysis tools to fulfill these research demands and enable unprecedented molecular analysis of cell and tissue specific miR

patterns.

To develop such molecular tools, we selected two disease-associated miR patterns as model systems. For Chapter 2, I chose a group of three breast cancer relevant miRs: miR27a, miR96, and miR182 (Table 1.3). I picked these miRs because White and coworkers found that three over-expressed miRs (miR27a, miR96, and miR182) coordinately work as a group to suppress the translation of Forkhead Box O1 (FOXO1) mRNA in MCF-7 breast cancer cells.[117] **White's work exemplifies the literature precedence for the need to perform intracellular combinatorial miR analysis.**

Another biologically relevant miR profile is that of hypoxia-regulated miRs (HRMs).[111,116,137] Hypoxia is the deficiency of the oxygen content in a biotic environment.[138] Hypoxia evokes cellular responses to maintain and develop cells through the coordinated regulation of many genes.[19,105,111,116] However, it is not fully understood how the expression profiles of HRM change to adapt to hypoxia, and consequently effect the synthesis of cellular proteins involved in proliferation and growth of the cell.[139] HRMs are of interest for combinatorial miR analysis because there is much to be learned in regard to their biological roles and how they shape cell biology under hypoxic conditions. Therefore, a set of three hypoxia-regulated miRs were chosen for the second sensor design (Chapter 4). These miRs are hsa-miR-210-3p[140], hsa-miR-24-3p[4], hsa-miR-27a-3p[9] (Table 1.3). These miRs were selected because they were found to be over-expressed in MCF-7 breast cancer cells after being cultured in a hypoxic environment for approximately 24 hours.[138]

Table 1.3 Sequences for disease-associated miRs of interest to design and test logic sensors. HSA (*homo sapiens*) is human-derived miR sequence. The 3p and 5p indicate the corresponding 3-prime and 5-prime ends of the double-stranded miR duplex (miR/miR*).

MicroRNA name	Sequence (5' to 3')
hsa-miRNA-182-5p (miR182)	UUUGGCAAUGGUAGAACUCACACU
hsa-miRNA-96-5p (miR96)	UUUGGCACUAGCACAUUUUUGCU
hsa-miRNA-27a-3p (miR27a)	UUCACAGUGGCUAAGUUCCGC
hsa-miRNA-210-3p (miR210)	CUGUGCGUGUGACAGCGGCUGA
hsa-miRNA-24-3p (miR24)	UGGCUCAGUUCAGCAGGAACAG

1.3 Cellular Imaging under Single- and Multi-Photon Light Sources

The two logic sensors I developed can work with both single-photon and multi-photon light

sources. Multi-photon light source has some unique advantages over single-photon sources in biological applications. Different from single-photon excitation, the multi-photon absorption or excitation process requires multiple photons to arrive at a molecule 'simultaneously' (within ~0.5 fs). As such, multi-photon excitation only occurs at the focal point rather than in the entire excitation cone of light as is the case for single-photon excitation, therefore reducing out-of-focus background noise.[75] The lower scattering arises from the fact that most multi-photon sources rely on near-infrared wavelengths (NIR 700–1 400 nm). Compared to single-photon microscopy, multi-photon microscopy shows advantages including: (1) lower photodamage, (2) lower photobleaching, and (3) reduced light scattering resulting leading to lower background noise and deeper penetration into biological samples.[141,142]

The future goal of my research is to apply *in situ* FRET-based logic gates for intracellular imaging of small ncRNAs with single- and multi-photon microscopy. Combining logic gates with imaging techniques will reveal expressional heterogeneities among cell populations in tissues and tissue mimics. In doing so the technology I contribute will help better understand small ncRNA biology in the future.

1.4 References

(1) Rinn, J. L.; Kertesz, M.; Wang, J. K.; Squazzo, S. L.; Xu, X.; Brugmann, S. A.; Goodnough, L. H.; Helms, J. A.; Farnham, P. J.; Segal, E.; et al. Functional Demarcation of Active and Silent Chromatin Domains in Human HOX Loci by Noncoding RNAs. *Cell* **2007**, *129* (7), 1311–1323.

(2) Kim, D. H.; Saetrom, P.; Snove, O.; Rossi, J. J. MicroRNA-Directed Transcriptional Gene Silencing in Mammalian Cells. *Proc. Natl. Acad. Sci.* **2008**, *105* (42), 16230–16235.

(3) Chen, Z.; Li, Y.; Huang, P.; Luthra, R. Hypoxia-Regulated MicroRNA-210 Modulates Mitochondrial Function and Decreases ISCU and COX10 Expression. *Oncogene* **2010**, *29*, 4362–4368.

(4) Srivastava, N.; Manvati, S.; Srivastava, A.; Pal, R.; Kalaiarasan, P.; Chattopadhyay, S.; Gochhait, S.; Dua, R.; Bamezai, R. N. MiR-24-2 Controls H2AFX Expression Regardless of Gene Copy Number Alteration and Induces Apoptosis by Targeting Antiapoptotic Gene BCL-2: A Potential for Therapeutic Intervention. *Breast Cancer Res.* **2011**, *13* (2), 1.

(5) Abrahante, J. E.; Daul, A. L.; Li, M.; Volk, M. L.; Tennessen, J. M.; Miller, E. A.; Rougvie, A. E. The Caenorhabditis Elegans Hunchback-like Gene Lin-57/Hbl-1 Controls Developmental Time and Is Regulated by MicroRNAs. *Dev. Cell* **2003**, *4* (5), 625–637.

(6) Blackshaw, S.; Harpavat, S.; Trimarchi, J.; Cai, L.; Huang, H.; Kuo, W. P.; Weber, G.; Lee, K.; Fraioli, R. E.; Cho, S.-H.; et al. Genomic Analysis of Mouse Retinal Development. *PLoS Biol.* **2004**, *2* (9), e247.

(7) Smith-Vikos, T.; Slack, F. J. MicroRNAs and Their Roles in Aging. *J. Cell Sci.* **2012**, *125* (1), 7–17.

(8) Croce, C. M. Causes and Consequences of MicroRNA Dysregulation in Cancer. *Nat. Rev. Genet.* **2009**, *10* (10), 704–714.

(9) Mertens-Talcott, S. U.; Chintharlapalli, S.; Li, X.; Safe, S. The Oncogenic MicroRNA-27a Targets Genes That Regulate Specificity Protein Transcription Factors and the G2-M Checkpoint in MDA-MB-231 Breast Cancer Cells. *Cancer Res.* **2007**, *67* (22), 11001–11011.

(10) Faghihi, M. A.; Modarresi, F.; Khalil, A. M.; Wood, D. E.; Sahagan, B. G.; Morgan, T. E.; Finch, C. E.; St. Laurent III, G.; Kenny, P. J.; Wahlestedt, C. Expression of a Noncoding RNA Is Elevated in Alzheimer's Disease and Drives Rapid Feed-Forward Regulation of β-Secretase. *Nat. Med.* **2008**, *14* (7), 723–730.

(11) Romaine, S. P. R.; Tomaszewski, M.; Condorelli, G.; Samani, N. J. MicroRNAs in Cardiovascular Disease: An Introduction for Clinicians. *Heart* **2015**, *101* (12), 921–928.
(12) da Silva Oliveira, K. C.; Thomaz Araújo, T. M.; Albuquerque, C. I.; Barata, G. A.; Gigek, C. O.; Leal, M. F.; Wisnieski, F.; Rodrigues Mello Junior, F. A.; Khayat, A. S.; de Assumpção, P. P.; et al. Role of MiRNAs and Their Potential to Be Useful as Diagnostic and Prognostic Biomarkers in Gastric Cancer. *World J. Gastroenterol.* **2016**, *22* (35), 7951.
(13) Trapnell, C. Defining Cell Types and States with Single-Cell Genomics. *Genome Res.* **2015**, *25* (10), 1491–1498.
(14) Bartel, D. P. MicroRNAs: Genomics, Biogenesis, Mechanism, and Function. *cell* **2004**, *116* (2), 281–297.
(15) Reis, E. M.; Nakaya, H. I.; Louro, R.; Canavez, F. C.; Flatschart, Á. V. F.; Almeida, G. T.; Egidio, C. M.; Paquola, A. C.; Machado, A. A.; Festa, F.; et al. Antisense Intronic Non-Coding RNA Levels Correlate to the Degree of Tumor Differentiation in Prostate Cancer. *Oncogene* **2004**, *23* (39), 6684–6692.
(16) Bloomston, M.; Frankel, W. L.; Petrocca, F.; Volinia, S.; Alder, H.; Hagan, J. P.; Liu, C.-G.; Bhatt, D.; Taccioli, C.; Croce, C. M. MicroRNA Expression Patterns to Differentiate Pancreatic Adenocarcinoma from Normal Pancreas and Chronic Pancreatitis. *Jama* **2007**, *297* (17), 1901–1908.
(17) Bockmeyer, C. L.; Christgen, M.; Müller, M.; Fischer, S.; Ahrens, P.; Länger, F.; Kreipe, H.; Lehmann, U. MicroRNA Profiles of Healthy Basal and Luminal Mammary Epithelial Cells Are Distinct and Reflected in Different Breast Cancer Subtypes. *Breast Cancer Res. Treat.* **2011**, *130* (3), 735–745.
(18) Chiang, C.-H.; Hou, M.-F.; Hung, W.-C. Up-Regulation of MiR-182 by β-Catenin in Breast Cancer Increases Tumorigenicity and Invasiveness by Targeting the Matrix Metalloproteinase Inhibitor RECK. *Biochim. Biophys. Acta BBA - Gen. Subj.* **2013**, *1830* (4), 3067–3076.
(19) Rupaimoole, R.; Ivan, C.; Yang, D.; Gharpure, K. M.; Wu, S. Y.; Pecot, C. V.; Previs, R. A.; Nagaraja, A. S.; Armaiz-Pena, G. N.; McGuire, M.; et al. Hypoxia-Upregulated MicroRNA-630 Targets Dicer, Leading to Increased Tumor Progression. *Oncogene* **2016**, *35* (33), 4312–4320.
(20) Hui, A.; How, C.; Ito, E.; Liu, F.-F. Micro-RNAs as Diagnostic or Prognostic Markers in Human Epithelial Malignancies. *BMC Cancer* **2011**, *11* (1), 1.
(21) Paranjape, T.; Slack, F. J.; Weidhaas, J. B. MicroRNAs: Tools for Cancer Diagnostics. *Gut* **2009**, *58* (11), 1546–1554.
(22) Liu, H.-H.; Tian, X.; Li, Y.-J.; Wu, C.-A.; Zheng, C.-C. Microarray-Based Analysis of Stress-Regulated MicroRNAs in Arabidopsis Thaliana. *RNA* **2008**, *14* (5), 836–843.
(23) Abell, J. L.; Driskell, J. D.; Dluhy, R. A.; Tripp, R. A.; Zhao, Y.-P. Fabrication and Characterization of a Multiwell Array SERS Chip with Biological Applications. *Biosens. Bioelectron.* **2009**, *24* (12), 3663–3670.
(24) Mitchell, P. S.; Parkin, R. K.; Kroh, E. M.; Fritz, B. R.; Wyman, S. K.; Pogosova-Agadjanyan, E. L.; Peterson, A.; Noteboom, J.; O'Briant, K. C.; Allen, A.; et al. Circulating MicroRNAs as Stable Blood-Based Markers for Cancer Detection. *Proc. Natl. Acad. Sci.* **2008**, *105* (30), 10513–10518.
(25) Becker, C.; Hammerle-Fickinger, A.; Riedmaier, I.; Pfaffl, M. W. MRNA and MicroRNA Quality Control for RT-QPCR Analysis. *Methods* **2010**, *50* (4), 237–243.
(26) Heegaard, N. H. H.; Schetter, A. J.; Welsh, J. A.; Yoneda, M.; Bowman, E. D.; Harris, C. C. Circulating Micro-RNA Expression Profiles in Early Stage Nonsmall Cell Lung Cancer. *Int. J. Cancer* **2012**, *130* (6), 1378–1386.
(27) Wang, Z.; Gerstein, M.; Snyder, M. RNA-Seq: A Revolutionary Tool for Transcriptomics. *Nat. Rev. Genet.* **2009**, *10* (1), 57–63.
(28) Seeman, N. C. Nucleic Acid Junctions and Lattices. *J. Theor. Biol.* **1982**, *99* (2), 237–247.
(29) Adleman, L. Molecular Computation of Solutions to Combinatorial Problems. *Science* **1994**, *266* (5187), 1021-1024.
(30) Rothemund, P. W. K.; Papadakis, N.; Winfree, E. Algorithmic Self-Assembly of DNA Sierpinski Triangles. *PLoS Biol.* **2004**, *2* (12), e424.
(31) Seelig, G.; Soloveichik, D.; Zhang, D. Y.; Winfree, E. Enzyme-Free Nucleic Acid Logic Circuits. *Science* **2006**, *314* (5805), 1585–1588.
(32) Couny, F.; Benabid, F.; Roberts, P. J.; Light, P. S.; Raymer, M. G. Generation and Photonic Guidance of Multi-Octave Optical-Frequency Combs. *Science* **2007**, *318* (5853), 1118–1121.
(33) Frezza, B. M.; Cockroft, S. L.; Ghadiri, M. R. Modular Multi-Level Circuits from Immobilized DNA-Based Logic Gates. *J. Am. Chem. Soc.* **2007**, *129* (48), 14875–14879.
(34) Lubrich, D.; Lin, J.; Yan, J. A Contractile DNA Machine. *Angew. Chem. Int. Ed.* **2008**, *47* (37), 7026–7028.

(35) Goodman, R. P.; Heilemann, M.; Doose, S.; Erben, C. M.; Kapanidis, A. N.; Turberfield, A. J. Reconfigurable, Braced, Three-Dimensional DNA Nanostructures. *Nat. Nanotechnol.* **2008**, *3* (2), 93–96.
(36) Chen, X.; Ellington, A. D. Shaping up Nucleic Acid Computation. *Curr. Opin. Biotechnol.* **2010**, *21* (4), 392–400.
(37) He, H.-Z.; Chan, D. S.-H.; Leung, C.-H.; Ma, D.-L. G-Quadruplexes for Luminescent Sensing and Logic Gates. *Nucleic Acids Res.* **2013**, *41* (8), 4345–4359.
(38) Lagendijk, A. K.; Moulton, J. D.; Bakkers, J. Revealing Details: Whole Mount MicroRNA in Situ Hybridization Protocol for Zebrafish Embryos and Adult Tissues. *Biol. Open* **2012**, *1* (6), 566–569.
(39) Markey, F. B.; Ruezinsky, W.; Tyagi, S.; Batish, M. Fusion FISH Imaging: Single-Molecule Detection of Gene Fusion Transcripts In Situ. *PLoS ONE* **2014**, *9* (3), e93488.
(40) Chen, K. H.; Boettiger, A. N.; Moffitt, J. R.; Wang, S.; Zhuang, X. Spatially Resolved, Highly Multiplexed RNA Profiling in Single Cells. *Science* **2015**, *348* (6233), aaa6090–aaa6090.
(41) Moffitt, J. R.; Zhuang, X. RNA Imaging with Multiplexed Error Robust Fluorescence in Situ Hybridization. **2016**, 42.
(42) Moffitt, J. R.; Hao, J.; Bambah-Mukku, D.; Lu, T.; Dulac, C.; Zhuang, X. High-Performance Multiplexed Fluorescence in Situ Hybridization in Culture and Tissue with Matrix Imprinting and Clearing. *Proc. Natl. Acad. Sci.* **2016**, *113* (50), 14456–14461.
(43) Prigodich, A. E.; Randeria, P. S.; Briley, W. E.; Kim, N. J.; Daniel, W. L.; Giljohann, D. A.; Mirkin, C. A. Multiplexed Nanoflares: MRNA Detection in Live Cells. *Anal. Chem.* **2012**, *84* (4), 2062–2066.
(44) Kang, W. J.; Cho, Y. L.; Chae, J. R.; Lee, J. D.; Choi, K.-J.; Kim. Molecular Beacon-Based Bioimaging of Multiple MicroRNAs during Myogenesis. *Biomaterials* **2011**, *32* (7), 1915–1922.
(45) Baker, M. B.; Bao, G.; Searles, C. D. In Vitro Quantification of Specific MicroRNA Using Molecular Beacons. *Nucleic Acids Res.* **2012**, *40* (2), e13–e13.
(46) Buck, A. H.; Campbell, C. J.; Dickinson, P.; Mountford, C. P.; Stoquert, H. C.; Terry, J. G.; Evans, S. A. G.; Keane, L. M.; Su, T.-J.; Mount, A. R.; et al. DNA Nanoswitch as a Biosensor. *Anal. Chem.* **2007**, *79* (12), 4724–4728.
(47) Chen, A. K.; Davydenko, O.; Behlke, M. A.; Tsourkas, A. Ratiometric Bimolecular Beacons for the Sensitive Detection of RNA in Single Living Cells. *Nucleic Acids Res.* **2010**, *38* (14), e148–e148.
(48) Fan, D.; Zhu, J.; Zhai, Q.; Wang, E.; Dong, S. Cascade DNA Logic Device Programmed Ratiometric DNA Analysis and Logic Devices Based on a Fluorescent Dual-Signal Probe of a G-Quadruplex DNAzyme. *Chem Commun* **2016**, *52* (19), 3766–3769.
(49) Johnson, B. N.; Mutharasan, R. Biosensor-Based MicroRNA Detection: Techniques, Design, Performance, and Challenges. *The Analyst* **2014**, *139* (7), 1576.
(50) Barad, O.; Meiri, E.; Avniel, A.; Aharonov, R.; Barzilai, A.; Bentwich, I.; Einav, U.; Gilad, S.; Hurban, P.; Karov, Y.; et al. MicroRNA Expression Detected by Oligonucleotide Microarrays: System Establishment and Expression Profiling in Human Tissues. *Genome Res.* **2004**, *14* (12), 2486–2494.
(51) Benes, V.; Castoldi, M. Expression Profiling of MicroRNA Using Real-Time Quantitative PCR, How to Use It and What Is Available. *Methods* **2010**, *50* (4), 244–249.
(52) Arroyo, J. D.; Chevillet, J. R.; Kroh, E. M.; Ruf, I. K.; Pritchard, C. C.; Gibson, D. F.; Mitchell, P. S.; Bennett, C. F.; Pogosova-Agadjanyan, E. L.; Stirewalt, D. L.; et al. Argonaute2 Complexes Carry a Population of Circulating MicroRNAs Independent of Vesicles in Human Plasma. *Proc. Natl. Acad. Sci.* **2011**, *108* (12), 5003–5008.
(53) Pritchard, C. C.; Kroh, E.; Wood, B.; Arroyo, J. D.; Dougherty, K. J.; Miyaji, M. M.; Tait, J. F.; Tewari, M. Blood Cell Origin of Circulating MicroRNAs: A Cautionary Note for Cancer Biomarker Studies. *Cancer Prev. Res. (Phila. Pa.)* **2012**, *5* (3), 492–497.
(54) Pritchard, C. C.; Cheng, H. H.; Tewari, M. MicroRNA Profiling: Approaches and Considerations. *Nat. Rev. Genet.* **2012**, *13* (5), 358–369.
(55) Hanna, J.; Wimberly, H.; Kumar, S.; Slack, F.; Agarwal, S.; Rimm, D. Quantitative Analysis of MicroRNAs in Tissue Microarrays by in Situ Hybridization. *BioTechniques* **2012**, *52* (4).
(56) Koshiol, J.; Wang, E.; Zhao, Y.; Marincola, F.; Landi, M. T. Strengths and Limitations of Laboratory Procedures for MicroRNA Detection. *Cancer Epidemiol. Biomarkers Prev.* **2010**, *19* (4), 907–911.
(57) Avissar, M.; Christensen, B. C.; Kelsey, K. T.; Marsit, C. J. MicroRNA Expression Ratio Is Predictive of Head and Neck Squamous Cell Carcinoma. *Clin. Cancer Res.* **2009**, *15* (8), 2850–2855.
(58) Nhuber, W. S.; Fuchs, B.; Juretschko, S.; Amann, R. Improved Sensitivity of Whole-Cell Hybridization by the Combination of Horseradish Peroxidase-Labeled Oligonucleotides and Tyramide Signal Amplification. *APPL Env. MICROBIOL* **1997**, *63*, 6.

(59) Silahtaroglu, A. N.; Nolting, D.; Dyrskjøt, L.; Berezikov, E.; Møller, M.; Tommerup, N.; Kauppinen, S. Detection of MicroRNAs in Frozen Tissue Sections by Fluorescence in Situ Hybridization Using Locked Nucleic Acid Probes and Tyramide Signal Amplification. *Nat. Protoc.* **2007**, *2*, 2520.

(60) Chen, K. H.; Boettiger, A. N.; Moffitt, J. R.; Wang, S.; Zhuang, X. Spatially Resolved, Highly Multiplexed RNA Profiling in Single Cells. *Science* **2015**, *348* (6233), aaa6090–aaa6090.

(61) Moffitt, J. R.; Hao, J.; Bambah-Mukku, D.; Lu, T.; Dulac, C.; Zhuang, X. High-Performance Multiplexed Fluorescence in Situ Hybridization in Culture and Tissue with Matrix Imprinting and Clearing. *Proc. Natl. Acad. Sci.* **2016**, *113* (50), 14456–14461.

(62) Moffitt, J. R.; Hao, J.; Bambah-Mukku, D.; Lu, T.; Dulac, C.; Zhuang, X. High-Performance Multiplexed Fluorescence in Situ Hybridization in Culture and Tissue with Matrix Imprinting and Clearing. *Proc. Natl. Acad. Sci.* **2016**, *113* (50), 14456–14461.

(63) Chinen, A. B.; Guan, C. M.; Ferrer, J. R.; Barnaby, S. N.; Merkel, T. J.; Mirkin, C. A. Nanoparticle Probes for the Detection of Cancer Biomarkers, Cells, and Tissues by Fluorescence. *Chem. Rev.* **2015**, *115* (19), 10530–10574.

(64) Tsourkas, A.; Behlke, M. A.; Xu, Y.; Bao, G. Spectroscopic Features of Dual Fluorescence/Luminescence Resonance Energy-Transfer Molecular Beacons. *Anal. Chem.* **2003**, *75* (15), 3697–3703.

(65) Hemphill, J.; Deiters, A. DNA Computation in Mammalian Cells: MicroRNA Logic Operations. *J. Am. Chem. Soc.* **2013**, *135* (28), 10512–10518.

(66) Wang, D.; Fu, Y.; Yan, J.; Zhao, B.; Dai, B.; Chao, J.; Liu, H.; He, D.; Zhang, Y.; Fan, C.; et al. Molecular Logic Gates on DNA Origami Nanostructures for MicroRNA Diagnostics. *Anal. Chem.* **2014**, *86* (4), 1932–1936.

(67) Cheglakov, Z.; Cronin, T. M.; He, C.; Weizmann, Y. Live Cell MicroRNA Imaging Using Cascade Hybridization Reaction. *J. Am. Chem. Soc.* **2015**, *137* (19), 6116–6119.

(68) Chen, A. K.; Behlke, M. A.; Tsourkas, A. Avoiding False-Positive Signals with Nuclease-Vulnerable Molecular Beacons in Single Living Cells. *Nucleic Acids Res.* **2007**, *35* (16), e105–e105.

(69) Almlie, C. K.; Larkey, N. E.; Burrows, S. M. Fluorescent MicroRNA Biosensors: A Comparison of Signal Generation to Quenching. *Anal Methods* **2015**, *7* (17), 7296–7310.

(70) Graybill, R. M.; Bailey, R. C. Emerging Biosensing Approaches for MicroRNA Analysis. *Anal. Chem.* **2016**, *88* (1), 431–450.

(71) Thaxton, C. S.; Georganopoulou, D. G.; Mirkin, C. A. Gold Nanoparticle Probes for the Detection of Nucleic Acid Targets. *Clin. Chim. Acta* **2006**, *363* (1–2), 120–126.

(72) Yang, W.-J.; Li, X.-B.; Li, Y.-Y.; Zhao, L.-F.; He, W.-L.; Gao, Y.-Q.; Wan, Y.-J.; Xia, W.; Chen, T.; Zheng, H.; et al. Quantification of MicroRNA by Gold Nanoparticle Probes. *Anal. Biochem.* **2008**, *376* (2), 183–188.

(73) Yeh, H.-C.; Sharma, J.; Shih, I.-M.; Vu, D. M.; Martinez, J. S.; Werner, J. H. A Fluorescence Light-Up Ag Nanocluster Probe That Discriminates Single-Nucleotide Variants by Emission Color. *J. Am. Chem. Soc.* **2012**, *134* (28), 11550–11558.

(74) Miao, P.; Tang, Y.; Wang, B.; Meng, F. Near-Infrared Ag2S Quantum Dots-Based DNA Logic Gate Platform for MiRNA Diagnostics. *Anal. Chem.* **2016**, *88* (15), 7567–7573.

(75) Cao, H.; Liu, S.; Tu, W.; Bao, J.; Dai, Z. A Carbon Nanotube/Quantum Dot Based Photoelectrochemical Biosensing Platform for the Direct Detection of MicroRNAs. *Chem Commun* **2014**, *50* (87), 13315–13318.

(76) Zhang, W.; Sun, H.; Yin, S.; Chang, J.; Li, Y.; Guo, X.; Yuan, Z. Bright Red-Emitting Polymer Dots for Specific Cellular Imaging. *J. Mater. Sci.* **2015**, *50* (16), 5571–5577.

(77) Mao, L.; Lu, Z.; He, N.; Zhang, L.; Deng, Y.; Duan, D. A New Method for Improving the Accuracy of MiRNA Detection with NaYF4:Yb,Er Upconversion Nanoparticles. *Sci. China Chem.* **2017**, *60* (1), 157–162.

(78) Teichmann, M.; Kopperger, E.; Simmel, F. C. Robustness of Localized DNA Strand Displacement Cascades. *ACS Nano* **2014**, *8* (8), 8487–8496.

(79) Zhang, D. Y.; Seelig, G. Dynamic DNA Nanotechnology Using Strand-Displacement Reactions. *Nat. Chem.* **2011**, *3* (2), 103–113.

(80) Wu, P.; Tu, Y.; Qian, Y.; Zhang, H.; Cai, C. DNA Strand-Displacement-Induced Fluorescence Enhancement for Highly Sensitive and Selective Assay of Multiple MicroRNA in Cancer Cells. *Chem Commun* **2014**, *50* (8), 1012–1014.

(81) Larkey, N. E.; Almlie, C. K.; Tran, V.; Egan, M.; Burrows, S. M. Detection of MiRNA Using a Double-Strand Displacement Biosensor with a Self-Complementary Fluorescent Reporter. *Anal. Chem.* **2014**, *86* (3), 1853–1863.

(82) Markham, N. R.; Zuker, M. DINAMelt Web Server for Nucleic Acid Melting Prediction. *Nucleic Acids Res.* **2005**, *33* (Web Server), W577–W581.
(83) Markham, N. R.; Zuker, M. *UNAFold: Software for Nucleic Acid Folding and Hybridization*; Humana Press, Totowa, NJ; Vol. II.
(84) Zadeh, J. N.; Steenberg, C. D.; Bois, J. S.; Wolfe, B. R.; Pierce, M. B.; Khan, A. R.; Dirks, R. M.; Pierce, N. A. NUPACK: Analysis and Design of Nucleic Acid Systems. *J. Comput. Chem.* **2011**, *32* (1), 170–173.
(85) Zhang, L.; Bluhm, A. M.; Chen, K.-J.; Larkey, N. E.; Burrows, S. M. Performance of Nano-Assembly Logic Gates with a DNA Multi-Hairpin Motif. *Nanoscale* **2017**, *9* (4), 1709–1720.
(86) Ge, L.; Wang, W.; Sun, X.; Hou, T.; Li, F. Versatile and Programmable DNA Logic Gates on Universal and Label-Free Homogeneous Electrochemical Platform. *Anal. Chem.* **2016**, *88* (19), 9691–9698.
(87) Yu, S.; Wang, Y.; Jiang, L.-P.; Bi, S.; Zhu, J.-J. Cascade Amplification-Mediated In Situ Hot-Spot Assembly for MicroRNA Detection and Molecular Logic Gate Operations. *Anal Chem* **2018**, *90* (7), 4544–4551.
(88) Bi, S.; Zhang, J.; Hao, S.; Ding, C.; Zhang, S. Exponential Amplification for Chemiluminescence Resonance Energy Transfer Detection of MicroRNA in Real Samples Based on a Cross-Catalyst Strand-Displacement Network. *Anal. Chem.* **2011**, *83* (10), 3696–3702.
(89) Marras, S. A.; Kramer, F. R.; Tyagi, S. Efficiencies of Fluorescence Resonance Energy Transfer and Contact-Mediated Quenching in Oligonucleotide Probes. *Nucleic Acids Res.* **2002**, *30* (21), e122–e122.
(90) Hussain, S. A. An Introduction to Fluorescence Resonance Energy Transfer (FRET). *ArXiv Prepr. ArXiv09081815* **2009**.
(91) Graybill, R. M.; Bailey, R. C. Emerging Biosensing Approaches for MicroRNA Analysis. *Anal. Chem.* **2016**, *88* (1), 431–450.
(92) Guttilla, I. K.; White, B. A. Coordinate Regulation of FOXO1 by MiR-27a, MiR-96, and MiR-182 in Breast Cancer Cells. *J. Biol. Chem.* **2009**, *284* (35), 23204–23216.
(93) Amaral, P. P.; John S. Mattick. Noncoding RNA in Development. *Mamm. Genome* **2008**, *19* (7–8), 454–492.
(94) Choudhuri, S. Small Noncoding RNAs: Biogenesis, Function, and Emerging Significance in Toxicology. *J. Biochem. Mol. Toxicol.* **2010**, *24* (3), 195–216.
(95) Mattick, J. S.; Makunin, I. V. Non-Coding RNA. *Hum. Mol. Genet.* **2006**, *15* (suppl_1), R17–R29.
(96) Place, R. F.; Li, L.-C.; Pookot, D.; Noonan, E. J.; Dahiya, R. MicroRNA-373 Induces Expression of Genes with Complementary Promoter Sequences. *Proc. Natl. Acad. Sci.* **2008**, *105* (5), 1608–1613.
(97) Khalil, A. M.; Guttman, M.; Huarte, M.; Garber, M.; Raj, A.; Rivea Morales, D.; Thomas, K.; Presser, A.; Bernstein, B. E.; van Oudenaarden, A.; et al. Many Human Large Intergenic Noncoding RNAs Associate with Chromatin-Modifying Complexes and Affect Gene Expression. *Proc. Natl. Acad. Sci.* **2009**, *106* (28), 11667–11672.
(98) Mercer, T. R.; Dinger, M. E.; Sunkin, S. M.; Mehler, M. F.; Mattick, J. S. Specific Expression of Long Noncoding RNAs in the Mouse Brain. *Proc. Natl. Acad. Sci.* **2008**, *105* (2), 716–721.
(99) Furuno, M.; Pang, K. C.; Ninomiya, N.; Fukuda, S.; Frith, M. C.; Bult, C.; Kai, C.; Kawai, J.; Carninci, P.; Hayashizaki, Y.; et al. Clusters of Internally Primed Transcripts Reveal Novel Long Noncoding RNAs. *PLoS Genet.* **2006**, *2* (4), e37.
(100) Kapranov, P. Large-Scale Transcriptional Activity in Chromosomes 21 and 22. *Science* **2002**, *296* (5569), 916–919.
(101) Nakaya, H. I.; Amaral, P. P.; Louro, R.; Lopes, A.; Fachel, A. A.; Moreira, Y. B.; El-Jundi, T. A.; da Silva, A. M.; Reis, E. M.; Verjovski-Almeida, S. Genome Mapping and Expression Analyses of Human Intronic Noncoding RNAs Reveal Tissue-Specific Patterns and Enrichment in Genes Related to Regulation of Transcription. *Genome Biol.* **2007**, *8* (3), R43.
(102) Ravasi, T. Experimental Validation of the Regulated Expression of Large Numbers of Non-Coding RNAs from the Mouse Genome. *Genome Res.* **2005**, *16* (1), 11–19.
(103) Carleton, M.; Cleary, M. A.; Linsley, P. S. MicroRNAs and Cell Cycle Regulation. *Cell Cycle* **2007**, *6* (17), 2127–2132.
(104) Ivey, K. N.; Srivastava, D. MicroRNAs as Regulators of Differentiation and Cell Fate Decisions. *Cell Stem Cell* **2010**, *7* (1), 36–41.
(105) Loayza-Puch, F.; Yoshida, Y.; Matsuzaki, T.; Takahashi, C.; Kitayama, H.; Noda, M. Hypoxia and RAS-Signaling Pathways Converge on, and Cooperatively Downregulate, the RECK Tumor-Suppressor Protein through MicroRNAs. *Oncogene* **2010**, *29* (18), 2638–2648.
(106) Esteller, M. Non-Coding RNAs in Human Disease. *Nat. Rev. Genet.* **2011**, *12*, 861.

(107) Kumar, V.; Westra, H.-J.; Karjalainen, J.; Zhernakova, D. V.; Esko, T.; Hrdlickova, B.; Almeida, R.; Zhernakova, A.; Reinmaa, E.; Võsa, U.; et al. Human Disease-Associated Genetic Variation Impacts Large Intergenic Non-Coding RNA Expression. *PLoS Genet.* **2013**, *9* (1), e1003201.

(108) Reis, E. M.; Ojopi, E. P. B.; Alberto, F. L.; Rahal, P.; Tsukumo, F.; Mancini, U. M.; Guimarães, G. S.; Thompson, G. M. A.; Camacho, C.; Miracca, E.; et al. Large-Scale Transcriptome Analyses Reveal New Genetic Marker Candidates of Head, Neck, and Thyroid Cancer. *Cancer Res.* **2005**, *65* (5), 1693–1699.

(109) Iorio, M. V.; Ferracin, M.; Liu, C.-G.; Veronese, A.; Spizzo, R.; Sabbioni, S.; Magri, E.; Pedriali, M.; Fabbri, M.; Campiglio, M.; et al. MicroRNA Gene Expression Deregulation in Human Breast Cancer. *Cancer Res.* **2005**, *65* (16), 7065–7070.

(110) Perez, D. S.; Hoage, T. R.; Pritchett, J. R.; Ducharme-Smith, A. L.; Halling, M. L.; Ganapathiraju, S. C.; Streng, P. S.; Smith, D. I. Long, Abundantly Expressed Non-Coding Transcripts Are Altered in Cancer. *Hum. Mol. Genet.* **2008**, *17* (5), 642–655.

(111) Krutilina, R.; Sun, W.; Sethuraman, A.; Brown, M.; Seagroves, T. N.; Pfeffer, L. M.; Ignatova, T.; Fan, M. MicroRNA-18a Inhibits Hypoxia-Inducible Factor 1α Activity and Lung Metastasis in Basal Breast Cancers. *Breast Cancer Res.* **2014**, *16* (4), 1.

(112) Krol, J.; Loedige, I.; Filipowicz, W. The Widespread Regulation of MicroRNA Biogenesis, Function and Decay. *Nat. Rev. Genet.* **2010**, *11* (9), 597–610.

(113) Yang, N.; Coukos, G.; Zhang, L. MicroRNA Epigenetic Alterations in Human Cancer: One Step Forward in Diagnosis and Treatment. *Int. J. Cancer* **2007**, *122* (5), 963–968.

(114) Mousa, S. Biosensors: The New Wave in Cancer Diagnosis. *Nanotechnol. Sci. Appl.* **2010**, 1.

(115) Mogilyansky, E.; Rigoutsos, I. The MiR-17/92 Cluster: A Comprehensive Update on Its Genomics, Genetics, Functions and Increasingly Important and Numerous Roles in Health and Disease. *Cell Death Differ.* **2013**, *20* (12), 1603–1614.

(116) Camps, C.; Buffa, F. M.; Colella, S.; Moore, J.; Sotiriou, C.; Sheldon, H.; Harris, A. L.; Gleadle, J. M.; Ragoussis, J. Hsa-MiR-210 Is Induced by Hypoxia and Is an Independent Prognostic Factor in Breast Cancer. *Clin. Cancer Res.* **2008**, *14* (5), 1340–1348.

(117) Guttilla, I. K.; White, B. A. Coordinate Regulation of FOXO1 by MiR-27a, MiR-96, and MiR-182 in Breast Cancer Cells. *J. Biol. Chem.* **2009**, *284* (35), 23204–23216.

(118) Corcoran, C.; Friel, A. M.; Duffy, M. J.; Crown, J.; O'Driscoll, L. Intracellular and Extracellular MicroRNAs in Breast Cancer. *Clin. Chem.* **2011**, *57* (1), 18–32.

(119) Gilkes, D. M.; Semenza, G. L. Role of Hypoxia-Inducible Factors in Breast Cancer Metastasis. *Future Oncol.* **2013**, *9* (11), 1623–1636.

(120) Hald, S. M.; Bremnes, R. M.; Al-Shibli, K.; Al-Saad, S.; Andersen, S.; Stenvold, H.; Busund, L.-T.; Donnem, T. CD4/CD8 Co-Expression Shows Independent Prognostic Impact in Resected Non-Small Cell Lung Cancer Patients Treated with Adjuvant Radiotherapy. *Lung Cancer* **2013**, *80* (2), 209–215.

(121) Eilertsen, M.; Andersen, S.; Al-Saad, S.; Richardsen, E.; Stenvold, H.; Hald, S. M.; Al-Shibli, K.; Donnem, T.; Busund, L.-T.; Bremnes, R. M. Positive Prognostic Impact of MiR-210 in Non-Small Cell Lung Cancer. *Lung Cancer* **2014**, *83* (2), 272–278.

(122) Resnick, K. E.; Alder, H.; Hagan, J. P.; Richardson, D. L.; Croce, C. M.; Cohn, D. E. The Detection of Differentially Expressed MicroRNAs from the Serum of Ovarian Cancer Patients Using a Novel Real-Time PCR Platform. *Gynecol. Oncol.* **2009**, *112* (1), 55–59.

(123) O'Connell, R. M.; Rao, D. S.; Baltimore, D. MicroRNA Regulation of Inflammatory Responses. *Annu. Rev. Immunol.* **2012**, *30* (1), 295–312.

(124) Semenza, G. L. TranscriptionalRegulation by Hypoxia-InducibleFactor I Molecular Mechanisms of Oxygen Homeostasis. *Trends Cardiovasc. Med.* **1996**, *6* (5), 151–157.

(125) Lai, N.; Dong, Q.; Ding, H.; Miao, Z.; Lin, Y. MicroRNA-210 Overexpression Predicts Poorer Prognosis in Glioma Patients. *J. Clin. Neurosci.* **2014**, *21* (5), 755–760.

(126) Westholm, J. O.; Lai, E. C. Mirtrons: MicroRNA Biogenesis via Splicing. *Biochimie* **2011**, *93* (11), 1897–1904.

(127) Diederichs, S.; Haber, D. A. Dual Role for Argonautes in MicroRNA Processing and Posttranscriptional Regulation of MicroRNA Expression. *Cell* **2007**, *131* (6), 1097–1108.

(128) Okamura, K.; Phillips, M. D.; Tyler, D. M.; Duan, H.; Chou, Y.; Lai, E. C. The Regulatory Activity of MicroRNA* Species Has Substantial Influence on MicroRNA and 3′ UTR Evolution. *Nat. Struct. Mol. Biol.* **2008**, *15* (4), 354–363.

(129) Yang, J.-S.; Phillips, M. D.; Betel, D.; Mu, P.; Ventura, A.; Siepel, A. C.; Chen, K. C.; Lai, E. C. Widespread Regulatory Activity of Vertebrate MicroRNA* Species. *RNA* **2011**, *17* (2), 312–326.

(130) Rhoades, M. W.; Reinhart, B. J.; Lim, L. P.; Burge, C. B.; Bartel, B.; Bartel, D. P. Prediction of Plant MicroRNA Targets. *Cell* **2002**, *110* (4), 513–520.
(131) Llave, C. Cleavage of Scarecrow-like MRNA Targets Directed by a Class of Arabidopsis MiRNA. *Science* **2002**, *297* (5589), 2053–2056.
(132) Chen, X. A MicroRNA as a Translational Repressor of APETALA2 in Arabidopsis Flower Development. *Science* **2004**, *303* (5666), 2022–2025.
(133) Krek, A.; Grün, D.; Poy, M. N.; Wolf, R.; Rosenberg, L.; Epstein, E. J.; MacMenamin, P.; da Piedade, I.; Gunsalus, K. C.; Stoffel, M.; et al. Combinatorial MicroRNA Target Predictions. *Nat. Genet.* **2005**, *37* (5), 495–500.
(134) Kalsotra, A.; Wang, K.; Li, P. F.; Cooper, T. A. MicroRNAs Coordinate an Alternative Splicing Network during Mouse Postnatal Heart Development. *Genes Dev.* **2010**, *24* (7), 653–658.
(135) Wang, J.; Haubrock, M.; Cao, K.-M.; Hua, X.; Zhang, C.-Y.; Wingender, E.; Li, J. Regulatory Coordination of Clustered MicroRNAs Based on MicroRNA-Transcription Factor Regulatory Network. *BMC Syst. Biol.* **2011**, *5* (1), 199.
(136) Calin, G. A.; Sevignani, C.; Dumitru, C. D.; Hyslop, T.; Noch, E.; Yendamuri, S.; Shimizu, M.; Rattan, S.; Bullrich, F.; Negrini, M.; et al. Human MicroRNA Genes Are Frequently Located at Fragile Sites and Genomic Regions Involved in Cancers. *Proc. Natl. Acad. Sci.* **2004**, *101* (9), 2999–3004.
(137) Camps, C.; Saini, H. K.; Mole, D. R.; Choudhry, H.; Reczko, M.; Guerra-Assunção, J. A.; Tian, Y.-M.; Buffa, F. M.; Harris, A. L.; Hatzigeorgiou, A. G.; et al. Integrated Analysis of MicroRNA and MRNA Expression and Association with HIF Binding Reveals the Complexity of MicroRNA Expression Regulation under Hypoxia. *Mol. Cancer* **2014**, *13* (1), 1.
(138) Kulshreshtha, R.; Ferracin, M.; Wojcik, S. E.; Garzon, R.; Alder, H.; Agosto-Perez, F. J.; Davuluri, R.; Liu, C.-G.; Croce, C. M.; Negrini, M.; et al. A MicroRNA Signature of Hypoxia. *Mol. Cell. Biol.* **2007**, *27* (5), 1859–1867.
(139) Harris, A. L. HYPOXIA — A KEY REGULATORY FACTOR IN TUMOUR GROWTH. *Nat. Rev. Cancer* **2002**, *2* (1), 38–47.
(140) Crosby, M. E.; Kulshreshtha, R.; Ivan, M.; Glazer, P. M. MicroRNA Regulation of DNA Repair Gene Expression in Hypoxic Stress. *Cancer Res.* **2009**, *69* (3), 1221–1229.
(141) Denk, W.; Strickler, J. H.; Webb, W. W.; others. Two-Photon Laser Scanning Fluorescence Microscopy. *Science* **1990**, *248* (4951), 73–76.
(142) helmchen, F.; Denk, W. Deep Tissue Two-Photon Microscope. *Nat. Methods* **2005**, *2* (12), 932–940.

Chapter 2.

Performance of nano-assembly logic gates with a DNA multi-hairpin motif

Lulu Zhang, Annie M. Bluhm,‡ Kuan-Jen Chen,‡ Nicholas E. Larkey‡ and Sean M. Burrows

Nanoscale
Royal Society of Chemistry (RSC) USA: 1050 Connecticut Ave NW, Suite 500 Washington DC 20036
2017, *9*, 1709–1720. *DOI: 10.1039/c6nr07814a.*
‡These authors contributed equally.

2.1 Abstract

DNA nano-assemblies have far-reaching implications for molecular computers. Boolean logic gates made from DNA respond to specific combinations of chemical or molecular inputs. In complex samples an assortment of other chemicals and molecules may interfere with the gate's recognition and response mechanisms. For logic gates to accept an increasing number of inputs, while maintaining selectivity, their design must only respond when specific input combinations are available simultaneously. Here we present proof-of-principle for a fluorescent-based nano-assembly logic gate for three inputs. Central to the gate's design is a multi-hairpin motif that distinguishes it from other works in this area. The multi-hairpin motif facilitates a larger and increasing number of inputs and a place to generate FRET-based signal enhancement. We will show the nano-assembly logic gate worked in aqueous buffer and in crude MCF-7 cell lysate. We will demonstrate the gate's selectivity against off-analyte cocktails. Finally, multi-hairpin motifs with different chemical and physical properties were evaluated to test their logic capabilities. Future work will demonstrate the gate's ability to visually identify specific combinations of oligonucleotides called small non-coding RNAs (ncRNAs) in cells. This nano-assembly logic gate for small ncRNA has far reaching cellular computation and single-cell analysis applicability. The gate can be used for basic cellular analysis, computing and observing the unique molecular expression patterns in tumor microenvironments, and advancing the field of therapeutics.

2.2 Introduction

Small non-coding RNAs (ncRNAs) include: (1) microRNAs, (2) small interfering RNAs, and (3) piwi-interacting RNAs. These RNA often work in groups to fine-tune protein translation of many genes.[1] RNAseq and quantitative-real-time-polymerase chain reaction (qRT-PCR) have identified several small ncRNAs that are key at various stages of cell growth and in many diseases.[2-4] However, to validate RNAseq data and advance the accuracy in regard to the biological role of small ncRNA groups, proper *in situ* analytical tools are needed to visualize these groups in cells and tissues.[5,6] Furthermore, *in situ* analysis provides a method to distinguish the sub-cell types based on the specific small ncRNA profiles.[7] To address those needs we present the proof-of principle nano-assembly logic gate that is selective for combinations of small ncRNAs. The logic gate here was designed to perform "AND" logic. The word "AND" means the gate's output response will only occur when all three inputs are present.

For this proof-of-principle study, microRNAs (miRs) were the selected analyte due to their discovery as a potential marker to understand and diagnose diseases. miRs are between 18 to 24 nucleotides long.[8-11] They typically work in unique groups to post-transcriptionally regulate messenger RNA (mRNA) transcripts.[12-14] In general, miR regulates mRNA by interacting with 3′ untranslated regions (UTRs), ultimately prohibiting protein synthesis.[15-18] In cancer, miRs become either over-expressed or under-expressed, showing a tumor- associated miR signature.[19-22] Thus, miRs are emerging as a class of biomarkers to learn about the underlying mechanisms of cancer processes.[23-26] They also hold potential for early detection and a gauge of the aggressiveness of cancers.[27-31]

Since miRs usually work in groups and in a cell-specific manner, logic analysis fulfills the need of responding to these groups because the gate will indicate if multiple miRs are present. As a cancer-relevant model system to design the nano-assembly logic gate around we chose the concerted regulation of the Forkhead Box O1 (FOXO1) transcription factor's mRNA by three miRs.[32] White and coworkers showed coordinate suppression of FOXO1 mRNA by miR27a, miR96, and miR182 in MCF-7 cells.[33] FOXO1 belongs to the family of transcription factors (TFs) called FOXO.[34,35] These TFs play critical roles in cell fate by regulating expression of many genes including those associated with differentiation and cell death.[36,37]

To date, there are several common miR profiling methods including qRT-PCR,[38] oligonucleotide microarrays,[39,40] and northern blotting.[41,42] Northern blot analysis is difficult for routine miR analysis due to low sensitivity, low throughput, and long analysis time.[43] Many array and gel-based sensing methods fail to detect low expression levels of miRs because they are diluted when pooled for analysis. [43] Furthermore, these types of analysis involve extraction of the miR from the cell, which makes them susceptible to loss of detailed information of the location of miRs in cells and tissue. [43] In other words, the differences in miR expression may result from cell- to-cell differences rather than differences within a single cell. Also, some studies of miR expression in cancer have reported a relatively poor correlation between the results from microarray- and qRT-PCR-based analysis. [44,45] In order to truly validate array and gel-based miR expression profiles, logic gates capable of *in situ* analysis are needed.

In situ sensors[46,47] allow visual identification of where small ncRNA are located in cells, subcellular regions, and tissues. The predominate method for *in situ* analysis is fluorescent *in situ* hybridization (FISH). [48,49] However, FISH methods run the risk of washing away potentially

relevant miR due to the combination of low amounts of miRs and the need for copious rinsing steps. *In situ* sensors, such as single molecular beacons[50-53] and others, [54-59] are based on the disruption of a quenching mechanism to increase the fluorescence intensity. However, it is easy to have misleading experimental results from false signal due to nuclease degradation of these sensors during cellular and tissue imaging. Many of these techniques (especially FISH probes) are limited by poor selectivity due to off-analyte interaction with endogenous mRNA, non-target miRs, and intermediates in the biosynthetic pathway. [60] Our group has addressed false signals from poor selectivity and sensor degradation by forcing Förster Resonance Energy Transfer interactions rather than disruption of a quenched state.[61-63] However, none of these methods address simultaneous analysis of miR combinations.

Several groups work on computational DNA algorithmic self-assembly or displacement gates.[64-70] Deiters[71] and Song[72] have applied logic gates for both one and two miR inputs. Weizmann has used programmable oligonucleotide probes for real-time miR21 imaging inside live cells through a cascade hybridization reaction.[73] Deiters has demonstrated DNA computation with AND gates to detect both miR21 and miR122 or each one individually in live cells.[71] Song has shown DNA Origami- based YES or AND gates, respectively for autonomous biosensing of either miR21 or miR195, or both miRs.[72] However, Song's DNA origami is not applicable to intracellular analysis.

To the best of our knowledge, current methods have yet to attempt gate designs that accept more than two miR inputs per sensor. However, to analyze the tens of miRs[60] from each cell of a larger population, it is necessary to develop gates that can accept more than two inputs simultaneously. Such analysis is needed to achieve a statistically relevant understanding of the role miRs play in biology.[60]

Work by Deiters and others have forged the foundation from which we were able to build upon to advance logic gate technology. [71-73] We sought to address the need for logic gates that can accommodate more miR inputs. In addition, we designed the gate to generate Förster Resonance Energy Transfer (FRET) induced signal changes to alleviate false signal issues.[61-63]

Current gate designs use multiple short partially double- stranded sequences that have competitive miR recognition mechanisms. One way to increase the number of miRs is to increase the length of the DNA strands to accommodate more miRs. However, due to DNA's natural tendency to form hairpins, this will likely be a challenge. Instead we chose to take advantage of

DNA's flexibility to control the hairpin structures that are formed. By controlling the DNA's secondary structure, we expect to enable logic gate technology that can accept more than two input miRs.

Here, we present proof-of-principle for a fluorescent-based molecular logic gate, termed a nano-assembly logic gate. The nano-assembly logic gate uses competitive hybridization mechanisms to recognize the miRs. Signal is generated through a FRET mechanism. We will demonstrate the gate's selectivity against off-analyte cocktails and its performance in crude MCF-7 cell lysate. Then the gate's response to one, two, and three miR inputs will be discussed. Finally, a discussion of the gate's predicted chemical and physical properties will reveal how to make improvements for future designs.

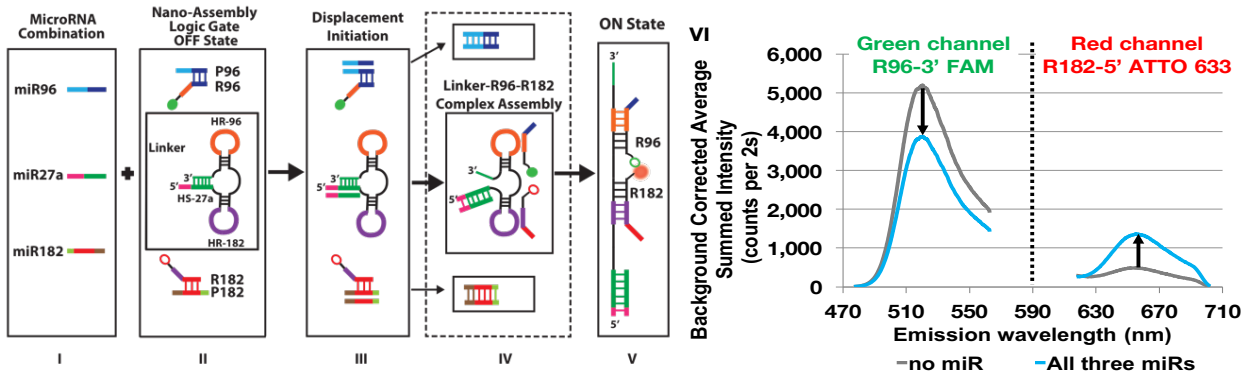

Figure 2.1 Recognition and transduction mechanism of nano-assembly logic gate. The miR combination (I) interacts with the gate's OFF state (II) to initiate competitive displacement (III) and complex assembly (IV) to bring reporters R96 and R182 together for a final ON state (V). The green and red circles represent the donor FAM, and the acceptor ATTO 633, respectively. VI shows the changes in the FRET dye's emission spectra from the nano- assembly logic gate (NA-L3) with and without three miRs. Equimolar 100 nM solutions were excited with 75 mW of power at 935 nm (N = 3).

2.3 Experimental

2.3.1 Instrumentation

All spectra were collected with a custom-built fluorimeter detailed in previous work.[61-63] All samples were excited with 75 mW (average power) at 935 nm from a MaiTai Ultrafast Titanium-Sapphire laser (Spectra Physics, Newport, 100 femtosecond (fs) pulses at a repetition rate of 80 MHz). Emission spectra were collected with an Acton Spectrometer (SP-2356) and Princeton Instruments electron-multiplied charge coupled device camera (512B-eXcelon3-EMCCD). The spectrometer used a grating blazed at 500 nm with 300 grooves per mm. The detector used LightField software with the following parameters for acquisition: 2000 ms exposure

time, 1 exposure averaged per frame, 60 frames (collected to gauge instrumental error), full frame read-out mode, high Analog-to-Digital Conversion Gain (ADC), 100 MHz ADC speed, low noise ADC quality, and the CCD camera was thermoelectrically cooled to −70 °C to minimize dark noise.

2.3.2 Oligonucleotides and Materials

Oligonucleotides were purchased from IDT (Integrated DNA Technologies, Inc., Coralville, Iowa, United States). Two reporters for L0 were biotin-labeled intended for future cell imaging applications. Organic dye modifications attached to all the reporters were chosen based on previous work.[74] Working solution of oligonucleotides were prepared by diluting stock oligonucleotides solutions in a custom buffer that contained: 10 mM Tris buffer (pH 10), 2.5 mM $MgCl_2$, and 0.005% Tween-20 in PBS at room temperature (about 25 °C), all were obtained from Fisher Scientific. The final pH of the buffer solution was approximately 8.

Oligonucleotide concentrations diluted to 2 μM were verified using a Nanodrop spectrometer (Thermo Scientific, ND-1000 UV-VIS spectrophotometer). The Nanodrop loses accuracy below a concentration of 2 μM. The oligonucleotides were hybridized at 37 °C. All of the experimental solutions contained oligonucleotides at a final concentration of 100 nM. The error bars in all figures represented the sample preparation errors.

2.3.3 Oligonucleotides design

The nano-assembly logic gate was designed in Matlab. The Matlab program used Watson–Crick type base pairing. A five-step design process was used and mapped out in Figure A1.1 In step one of the design process, the miR analyte sequences (miR27a, miR96, and miR182) were converted into DNA sequences. DNA was used for proof-of-principle tests because it is less susceptible to nuclease degradation than RNA. In step two, three probe strands P27a, P96, and P182 were designed to be fully complementary to miR27a, miR96, and miR182, respectively. In step three, potential cross-reactivity of miRs with non-corresponding probe strands was addressed by changing the Triple-A tails of P96 and P182 to Triple-T tails (tails highlighted in black). In step four, reporter strands (R96 and R182) were designed to be partially complementary to probe strands (P96 and P182). In step five, a linker strand (L) was designed to bind R96, R182, and miR27a.

The Matlab program produced hundreds to thousands of potential reporters and linker sequences. These candidate reporters and linkers had to go through a complicated filtration

process. The filtration process is thoroughly discussed in A1.1 This filtration process was evaluated based mainly on the estimated thermodynamic data.

Six linkers (L0–6), two reporters for L0, and two reporters for L1 to L5 were chosen for further tests. The sequences of these oligonucleotides are listed in the Tables A1.1–A1.3 and Tables A1.4–A1.8 compare the predicted thermodynamic data and formed hydrogen bonds amongst different sequences. Open-source software available on the DINAMelt Web Server[75] was used to estimate all thermodynamic data. The various assumptions and details of DINAMelt have been addressed in another publication[63] and A1.1.

2.3.4 Crude cell lysate protocol

To obtain the crude MCF-7 cell lysate, a freeze–thaw cell lysate protocol was adapted from Doyle and co-workers.[76] The MCF-7 cells were a gift from Dr. Emily Ho's lab at Oregon State University. We cultured the MCF-7 cells in RPMI 1640 medium (GibcoTM) with 10% FBS (GibcoTM) and 1% of 100× Glutamax (GibcoTM). Cells were incubated under 5.0% CO_2 at 37 °C. The MCF-7 cells with a concentration off 3.3×10^6 cells per mL were lysed by 90 min incubation at 55 °C in 1× Tris-EDTA (TE) buffer with 0.5% Tween-20 (v/v) and 2% (w/v) Sodium Dodecyl Sulfate (SDS). Then, the lysate was stored at −20 °C. The TE buffer was obtained from Quality Biological Inc. and the SDS was from Avantor Performance Materials. The frozen lysate was thawed at room temperature prior to further oligonucleotides testing. Using the same hybridization methods discussed above, the oligonucleotides were pre-hybridized in aqueous solution, and then added into the crude lysate for further testing.

2.4 Results and Discussion

2.4.1 Recognition and transduction mechanism

We designed six nano-assembly logic gates (NA-L0 to NA-L5) to detect multiple miRs simultaneously. As will be revealed throughout the discussion, NA-L3 proved to have the best attributes and will be the focus of the results and discussion. For proof-of-principle we started with a gate that only responded to all three miRs: miR27a, miR96, and miR182 (Figure 2.1, I). The gate was designed and characterized for future two-photon fluorescence imaging in cells and tissue. Fluorescence can also be achieved with single-photon sources, making the gate applicable to both techniques.

The gate's transduction mechanism relies on FRET enhancement of ATTO 633 (acceptor

dye) when FAM (donor dye) is stimulated. Response from the gate was indicated by the change in fluorescence signal from ATTO 633's OFF to ON state (Figure 2.1, II–VI). To observe FRET enhancement from ATTO 633, 935 nm was found to be the best wavelength to selectively excite FAM (Figure A1.2). The maximum signal from FAM and ATTO 633 were seen at ~520 nm (green channel) and 660 nm (red channel), respectively. To establish the extent of FRET enhancement a red to green signal intensity ratio (R/G ratio) was calculated.

Figure 2.1 (II) shows the nano-assembly logic gate's OFF state structure consists of three independent parts. The first part is a miR96 selective reporter–probe complex (RP96). Reporter, R96, is labeled with FAM and is partially bound to a probe strand (P96). The second part is a miR182 selective reporter–probe complex (RP182). Reporter, R182, is labeled with ATTO 633 and is partially bound to another probe strand (P182). Each reporter–probe complex is designed so the probe is more selective for the miR than the reporter. The third part of the gate is a linker strand (L) that contains a miR27a selective hybridization site (HS-27a) and two hairpin regions HR-96 and HR-182 that are selective for R96 and R182, respectively. HR-96 and HR-182 are located in the hairpin's loop and part of the stem (see Table A1.1 for the binding sequences of L for miR27a, R96, and R182).

The gate's recognition mechanism is comprised of five competitive strand displacement reactions (Figure 2.1, III and IV). Each strand displacement reaction is facilitated by toe-hold mediated branch migration. These five competitive reactions create five equilibriums. The purpose of these competitive based equilibriums is to impart selectivity for each miR and each reporter. Three equilibriums enable selective binding to each miR. Two equilibriums involve selective binding of the linker to each reporter. The competitive displacement reactions are achieved by over- coming the interactions between: (1) the two reporter–probe complexes, (2) the linker's 3′ end and HS-27a, and (3) the two stem regions of L's HR-96 and HR-182 (Figure 2.1, II–IV).

In order for the gate to work, miR96 and miR182 must dis- place R96 and R182 from their respective RP96 and RP182 complexes (Figure 2.1, III–IV). To displace the 3′ end of the linker, miR27a must bind with full complementarity to HS-27a (Figure 2.1, III). Once miR27a binds HS-27a the linker partially opens so the reporters can access the hairpin regions to initiate binding (Figure 2.1, IV). In a mixture of just miR96 and miR182, R96 and R182 (which are conjugated to FAM and ATTO 633, respectively) will get displaced from their respective reporter–probe complexes. Once free, these reporters may bind to the linker and create a false signal. To avoid the

false signal, the green part of the linker's HS-27a region was designed to keep the multi-hairpin structure intact.

In the ON state, the complex is assembled through the binding of miR27a, R96, and R182 to the linker. Figure 2.1 (V) shows the complex assembly that brings two dyes within the FRET distance. Figure 2.1 (VI) shows that the signal from R96 decreased as R182's signal increased when all 3 miRs are present. This result confirmed that the FRET-based transduction element was activated by 935 nm excitation of FAM to induce ATTO 633's FRET enhancement.

2.4.2 Performance of nano-assembly logic gate against off-analytes and in crude MCF-7 cell lysate

The selectivity of nano-assembly logic gate-L3 (NA-L3) was tested against an off-analyte cocktail in buffer. The off-analyte cocktail contained five miRs that were at an equivalent concentration as the gate. The five off-analytes were: mmu-miR29b-1- 5p, mmu-miR26a-2-3p, hsa-miR146a-3p, hsa-miR146a-5p, hsa-miR146b-5p. The off-analyte sequences are listed in Table A1.3. The sequence similarity between analytes and off-analytes ranged from 3/22 to 6/22 bases (or 13 to 27%).

Figure 2.2 (A) shows the results for the selectivity against the off-analyte cocktail. A positive control with all three analyte miRs added to NA-L3 gave an average R/G ratio of 0.3607 ± 0.0174 AU (arbitrary units). A blank control of NA-L3 without any miRs was used to establish the baseline R/G ratio. The baseline R/G was 0.0972 ± 0.0030 AU. Off-analytes had an average R/G ratio of 0.1005 ± 0.0006 AU for NA-L3. There was no statistical difference ($p < 0.025$) between the low R/G ratios from no analytes and off-analyte miRs. This result shows the gate had good selectivity against mismatched sequences with at least 27% similarity. Future work will evaluate gates with 90 to 96% (up to one base change out of 24) sequence similarity.

Figure 2.2 (B) demonstrated NA-L3 was able to differentiate OFF and ON states in crude MCF-7 cell lysate. In this case, to estab- lish the baseline R/G ratio a blank control in cell lysate only contained reporter–probe complexes. For a negative control no miR was added to NA-L3. For a positive control all three miRs were added to NA-L3. Blank control containing only reporter–probe complexes showed an average R/G ratio of 0.0582 ± 0.0007 AU. The no miR control for NA-L3 gave an average R/G ratio of 0.0775 ± 0.0023 AU. With all three miRs the average R/G ratio was 0.3045 ± 0.0085 AU. There was a statistically sig- nificant increase in signal ($p < 0.025$) from the no miR to all three miRs controls.

The positive control in buffer and cell lysate both showed a R/G ratio that increased ~3.5 times compared to the respective negative or blank controls. The similar factor changes in R/G ratio of NA-L3 in aqueous buffer solution or crude cell lysate showed its robust performance.

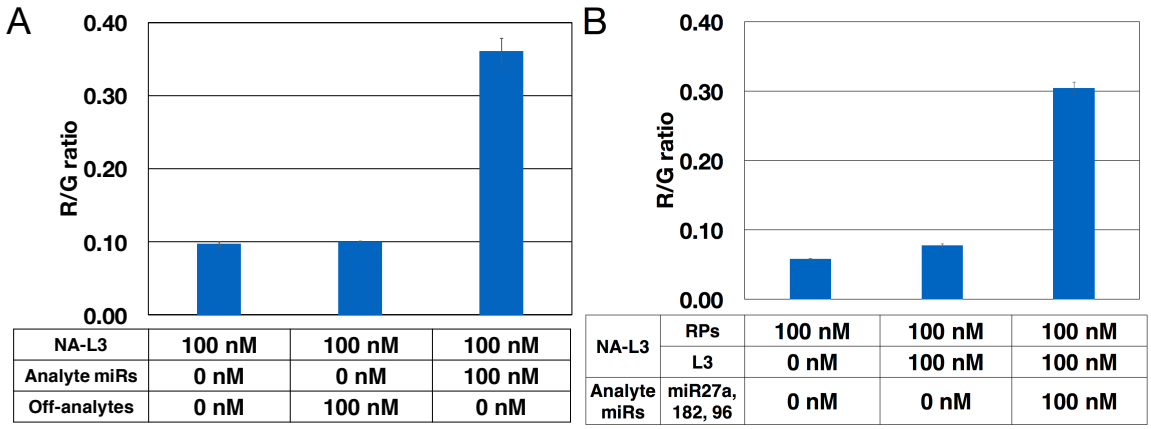

NA-L3	100 nM	100 nM	100 nM
Analyte miRs	0 nM	0 nM	100 nM
Off-analytes	0 nM	100 nM	0 nM

NA-L3	RPs	100 nM	100 nM	100 nM
	L3	0 nM	100 nM	100 nM
Analyte miRs	miR27a, 182, 96	0 nM	0 nM	100 nM

Figure 2.2 Performance of nano-assembly logic gate against off-analytes and in crude MCF-7 cell lysate. (A) Shows the nano-assembly logic gate-L3's (NA-L3) ability to resist binding off-analytes (N = 3). The off-analyte cocktail included equivalent amounts of five miRs: mmu-miR29b-1-5p, mmu-miR26a-2- 3p, hsa-miR146a-3p, hsa-miR146a-5p, hsa-miR146b-5p. (B) Shows NA-L3's ability to differentiate between OFF and ON states in crude MCF-7 cell lysate (N = 3). The error bars are too small to see. The relative standard deviation ranges from 0.627% to 4.826%.

2.4.3 Nano-assembly logic gate's sensitivity in cell lysate

The sensitivity of nano-assembly logic gate-L3 (NA-L3) in crude MCF-7 cell lysate was determined from three independent calibration curves. The miR concentration was increased from 0 to 100 nM in 25 nM steps. The sensitivity and limit of detection (LOD) from each calibration curve was then averaged. The sensitivity was $2.138 \pm 0.098 \times 10^{-3}$ AU per nM (N = 3). The LOD was 1.017 ± 0.236 nM (N = 3).

The logic gate's LOD is at the upper end of the biologically relevant fM to nM range. To improve the detection limit, lower concentrations of the logic gate or longer integration times can be used.

Figure 2.3 shows the logic gate's R/G ratio increased as the concentration of all three miRs increased. In a biological sample there will likely be disproportionate relative concentrations among the miR. However, this is not a problem, as the gate will respond to the lowest concentration miR in the combination. Such a gate will help determine whether the miR combination can be correlated to a change in protein synthesis when one of the miR concentrations is limiting. Furthermore, we envision combining multiple logic gates to create logic circuits that will reveal the disproportionate concentrations in more detail.

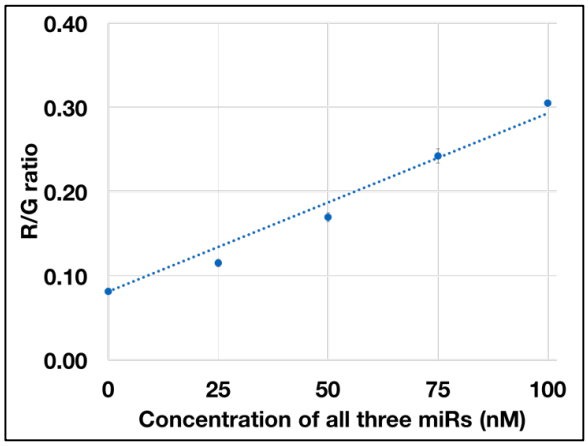

Figure 2.3 Nano-assembly logic gate-L3's (NA-L3) average response from the addition of three analyte miRs (N = 3). For each concentration, equivalent amounts of three miRs were added. The error bars were too small to see. The relative standard deviation ranged from 1.555 to 6.585%.

2.4.4 Nano-assembly logic gate response

The R/G ratios for nano-assembly logic gates-L1 and -L3 (NA-L1 and NA-L3) when challenged with individual and multiple miRs are shown in Figure 2.4 (A) and (B), respectively. The only difference in NA-L1 and NA-L3 was the linker's sequence (Table A1.1). A blank control established the baseline R/G ratio from NA-L1 and NA-L3 when no miR was present. The blank control consisted of the linker (L1 or L3), RP96, and RP182. The ability of each gate's linker to resist unintentional binding between the reporter and linker in the absence of all three miRs was systematically tested by adding individual and combinations of two miRs.

For the blank control group, the R/G ratio from NA-L1 and NA-L3 were not statistically different ($p < 0.025$). A similar result between NA-L1 and NA-L3 was found for the addition of all three miRs. For the blank control group, the average R/G ratio from gates NA-L1 and NA-L3 was 0.0975 ± 0.0039 AU. For the addition of all three miRs the average R/G ratio from NA-L1 and NA-L3 was 0.3553 ± 0.0119 AU. Both NA-L1 and NA-L3 showed the largest changes in R/G ratio when all three miRs were added. Compared to the blank control group the addition of all 3 miRs increased the R/G ratio by a factor of about 3.6 ($p < 0.025$).

The low R/G ratio was associated with the fact the dyes were calculated to be about 6.0 nm apart based on a FRET efficiency of about 27% and a Förster distance, R_0, of 5.1 nm[77] (A1.2). Future designs will evaluate the optimal FRET distance by changing the number of nucleotide bases in-between the reporter binding domains along the linker.

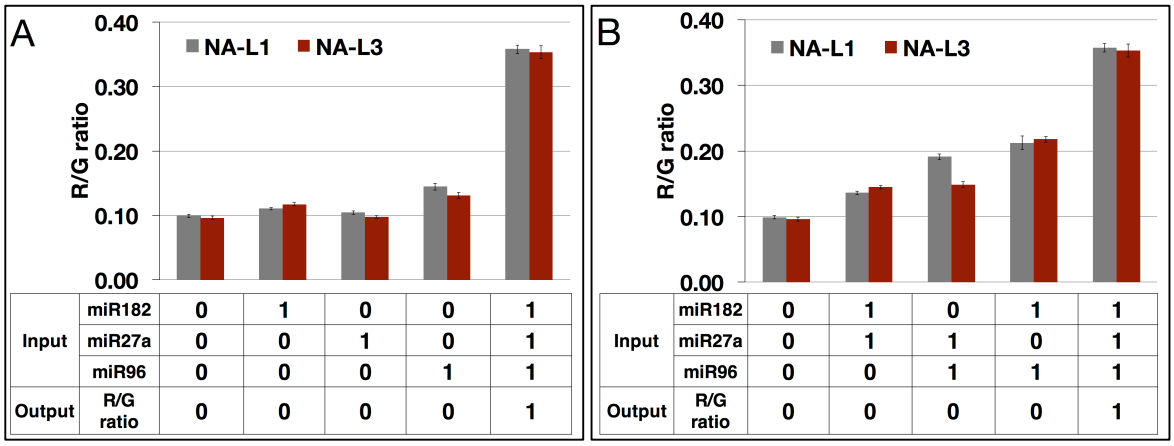

Figure 2.4 Nano-assembly logic gates' (NA-L1 and NA-L3) response to one, two, and three miR inputs. (A) Demonstrated NA-L1 and NA-L3's selectivity against single miR (N = 3). (B) Showed NA-L1 and NA-L3's selectivity against combinations of two miRs (N = 3). Truth table shows expected output based on the inputs. The error bars are too small to see. The relative standard deviation ranges from 1.740% to 4.871%.

Addition of single and combinations of two miRs showed statistical increases in the R/G ratio from the blank control group. Tables 2.1 and 2.2 quantitated the percent change in R/G ratio caused by single and double miR additions. The following equation was used:

$$\%\Delta R = 100 \times \frac{(R_{XmiR} - R_0)}{(R_{3miR} - R_0)} \qquad (Eq\ 1)$$

where R is the R/G ratio in general, R_{XmiR} is the ratio for single or double miR addition, R_0 is the ratio for no miRs added, and R_{3miR} is the ratio for all three miRs added. False signals from each gate were considered relevant if they were larger than the limit of quantitation (LOQ). Each gate's LOQ was defined as it's average R_0 value plus ten times its standard deviation.

Table 2.1 Limit of Quantitation (LOQ) thresholds and percent ratio change from single miR additions

	NA-L1	NA-L3
LOQ threshold	0.1249 AU	0.1259 AU
miR182	4.5%	8.1%
miR27a	2.1%	0.6%
miR96	17.7%	13.5%

Table 2.2 Limit of Quantitation (LOQ) thresholds and percent ratio change from double miR additions

	NA-L1	NA-L3
LOQ Threshold	0.1249 AU	0.1259 AU
miR27a/miR182	14.5%	19.0%
miR27a/miR96	35.7%	20.4%
miR96/miR182	43.9%	47.3%

The percent change in R/G ratio listed in Table 2.1 for addition of miR27a to either NA-L1 or NA-L3 was less than the LOQ. This meant miR27a did not cause any false signals. Although miR182 addition to NA-L1 had a 4.5% change in R/G ratio, the change did not rise above the LOQ threshold to con- tribute false signal. However, miR182 did cause false signals for NA-L3. Addition of single miR96 caused the largest percent change in R/G ratio and false signals for both gates.

In order to observe false signals from single miR additions, some of the reporters, R96 with FAM, and R182 with ATTO 633, must have been on the linker. Compared to controls, the emission spectra in Figure A1.3 showed the FAM signal went down and the ATTO 633 signal went up when only miR96 was added to gate NA-L1 and NA-L3. Similar spectra were observed for addition of miR182 to NA-L1 and NA-L3 (no data shown). These observations supported a situation where both reporters were on the linker even in the presence of just miR96 or miR182.

In the case of miR96 addition, the false signal result was interpreted to mean the displaced R96 bound HR-96 in the linker. Binding to the linker changed the overall energy of the structure in such a way it destabilized HR-182. With HR-182 destabilized the linker's reporter binding domain was able to outcompete RP182 for R182. These events would have caused a fraction of R182 to bind the linker and cause enough of an increase in the R/G ratio to rise above the LOQ false signal threshold value. A similar event must have occurred - to a lesser extent - in the case of miR182 addition to the gates.

Although the hairpin region with the R182 binding domain was weaker than the hairpin region with the R96 binding domain, free R96 showed a larger percent change in R/G ratio. Thermodynamics between closed linker, reporter–probe complex, and linker–reporter complex helped explain why miR96 showed a larger change in R/G ratio than miR182 since they both released respective reporters.

Figure 2.5 shows RP96 to L3-R96 was exothermic, but RP182 to L3-R182 was endothermic. In other words, without miR182 to free the R182, it took energy to disrupt the RP182 complex and form the L-R182 complex. The overall Gibbs energy of RP182 was less stable than the linker by about 0.6 kcal mol^{-1}. Thus in the presence of miR96, R96 was freed and bound to the linker such that HR-182 was destabilized. R182 would rather compete with the destabilized HR-182 stem for binding to L3 and reach a more stable energy with L3-R182 than remain in the linker hairpin or RP182 complex. On the other hand, the Gibbs energy of RP96 was more stable than the

linker hairpin by about 0.5 kcal mol^{-1}, so R96 would rather stay in the RP96 complex than compete with HR-96 stem. Taking the Gibbs energies and enthalpic contributions into account helped explain why the addition of miR96 showed more false signals than that of miR182.

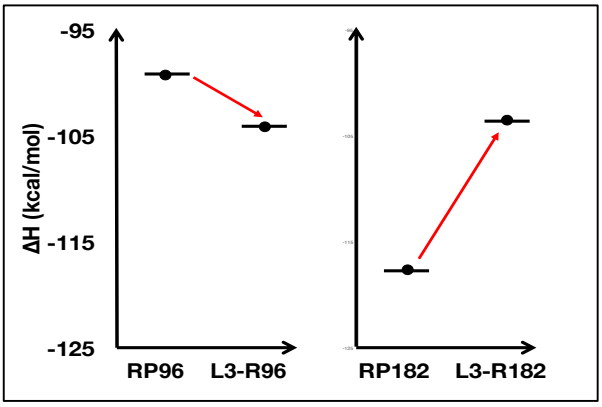

Figure 2.5 Enthalpy diagram of reporter–probe complex to reporter–linker complex for L3.

From Figure 2.4 (A) and (B) and Tables 2.1 and 2.2, any combination of two miRs showed larger percent change in R/G ratio than the single miR additions. For the double miR additions, Table 2.2 revealed the largest percent change in R/G ratio was observed when miR96 and either miR27a or miR182 were added to the gates. The miR96 and miR182 combination showed the largest percent change in R/G ratio (about 45%) and thus the worst false signals for both NA-L1 and NA-L3. This meant that in the absence of miR27a, L1 and L3 were able to bind the freed reporters. These results were expected based on results from single miR analysis any time one of the miRs freed its respective reporter.

There were many nuanced statistical similarities and differ- ences in the false signals between NA-L1 and NA-L3 from single and double miR additions. Most of the false signals from NA-L1 and NA-L3 were only different by 2 to 5 percentage points. The one relevant statistical difference between the two gates was the false signal when miR27a and miR96 were added to NA-L1 and NA-L3. The false signal from NA-L3 was about 15 percentage points less than that of NA-L1.

Although there were some false positives, the R/G ratio output from all three miRs were more than 2 to 3 times greater than that of single miRs and more than 1.5 times greater than that of the two miR combinations. The linker's reporter binding domains did a reasonable job preventing binding of single reporters, and fair job resisting binding of two reporters.

Although the gate was designed as a 3 miR input AND logic, it serves as AND logic for two or three miRs. Such a logic allows for differentiation of miR96 AND miR182 from miR96, miR182, AND miR27a. In some biological situations this information may be relevant. In this case, any of our previously developed NOT[61–63] gates could be added to validate the absence of miR27a.

2.4.5 Linker design considerations and attributes

Since the linker is a key part of the nano-assembly logic gate, its sequence plays a big role in the response to single and multiple analyte inputs. This section will discuss how the linker's sequence and binding interactions alter its stability and ultimate functionality.

After the Matlab program and filtration process, six linkers (L0–L5) and four reporters (R96 and R182 for L0, R96 and R182 for L1–L5) were chosen for analysis. These six linkers and their corresponding reporters (R96 and R182), as well as the common probes (P96 and P182), formed six nano-assembly logic gates (NA-L0–5). A true three input AND gate should only increase the R/G ratio from baseline when all three inputs are present. The underlying hypothesis for the linker's design was that HS-27a, HR-96, and HR-182 would keep the multi-hairpin structure intact until all three miRs were present. A secondary hypothesis was that the HS-27a would keep HR-96 and HR-182 intact to resist R96 and R182 from binding to the linker in the absence of miR27a.

Keeping the reporter binding domains' sequence on L1–L5 constant we altered the HS-27a stem's stability from −4.93 to −12.99 kcal mol^{-1} and from 22 to 33 hydrogen bonds. For HR-182, there were some nuanced differences between the stem's sequence and thermodynamics amongst L1–L5. However, for HR-96 the stem's sequence and thermodynamics were the same for L1–L5. A1. 3 and Table A1.5 contain a detailed comparison between linkers L1 to L5.

Figure A1.4 shows that all linker variants had false signals in the presence of just the two reporters. This result provided evidence that no level of stability in the HS-27a stem was able to keep the HR regions fully intact when both reporters were free from the probe.

In another linker design, L0, the hairpin region's stems were very different and more thermodynamically stable than those of L1–L5. The sequences for the reporter binding domains were slightly different from those of L1–L5. The linker–reporter binding interactions were weaker for L0 than those for L1–L5. The HS-27a did have a similar stability to L4, and both were more

stable than any other linker. The A1.3 and in Table A1.5 contain a detailed comparison between linkers L0 and L1–L5.

L0 was an attractive choice because in thermodynamic pre- dictions for the binding of either one or both reporters to the linker; the processes were endothermic and had positive changes in Gibbs energy. An endothermic process with a positive change in Gibbs energy was expected to be unfavorable. Thus we expected the logic gate to stay in the OFF state if just two inputs were present. In a prediction with both reporters and the miR27a binding to L0, the process was exothermic and had a negative Gibbs energy. From this prediction the L0 was expected to generate signal. However, constant temperature, thermal cycling, and salt adjustment attempts to bind L0 to both reporters and miR27a all failed.

L3, on the other hand, was predicted to have an endothermic process for addition of just R182 but an exothermic process with the addition of R96 or both R182 and R96. The addition of just one or both reporters showed a negative Gibbs energy. Negative Gibbs energies are indicative of favorable reaction conditions only limited by kinetics. The fact a statistically significant increase in the R/G ratio was observed when L3 was in the presence of R182 and R96 provides evidence the favorable reaction occurred.

The fact L0 did not show any change in R/G ratio suggests two probable situations: (1) the complex between the linker, reporters, and miR27a did not form or was incomplete and/or (2) the dyes were outside the FRET distance needed to see changes in donor and acceptor signal. As for L3, a R/G ratio below one indicates two probable situations: (1) the equilibrium to form a complex between the linker, reporters, and miR27a was incomplete, and (2) the dyes were within the FRET distance but far apart.

In a titration experiment the FRET ratio was monitored as increasing amounts of L3 were added to a constant amount of reporters and miR27a (data not shown). The FRET ratio stabilized when equimolar concentrations of linker, reporters, and miR27a were present. This result provided evidence that the R/G ratio of ~0.35 corresponded to complete binding of linkers to reporters and miR27a. Future single molecule experiments will help determine if the observed intensity from each dye in the FRET pair was due to the FRET distance or due to an incomplete reaction.

Predicted chemical and physical boundary conditions were investigated to understand how a linker sequence should be designed so it would: (1) bind both reporters and miR27a, and (2) stay intact in the absence of any one of the miRs in a combination. To identify the chemical and physical

boundary conditions for a functional gate, the predicted thermodynamics, chemical interactions, and molecular structures of L0 were compared to L3. Figure 2.6 compares the molecular structures and thermodynamics of L0 to L3.

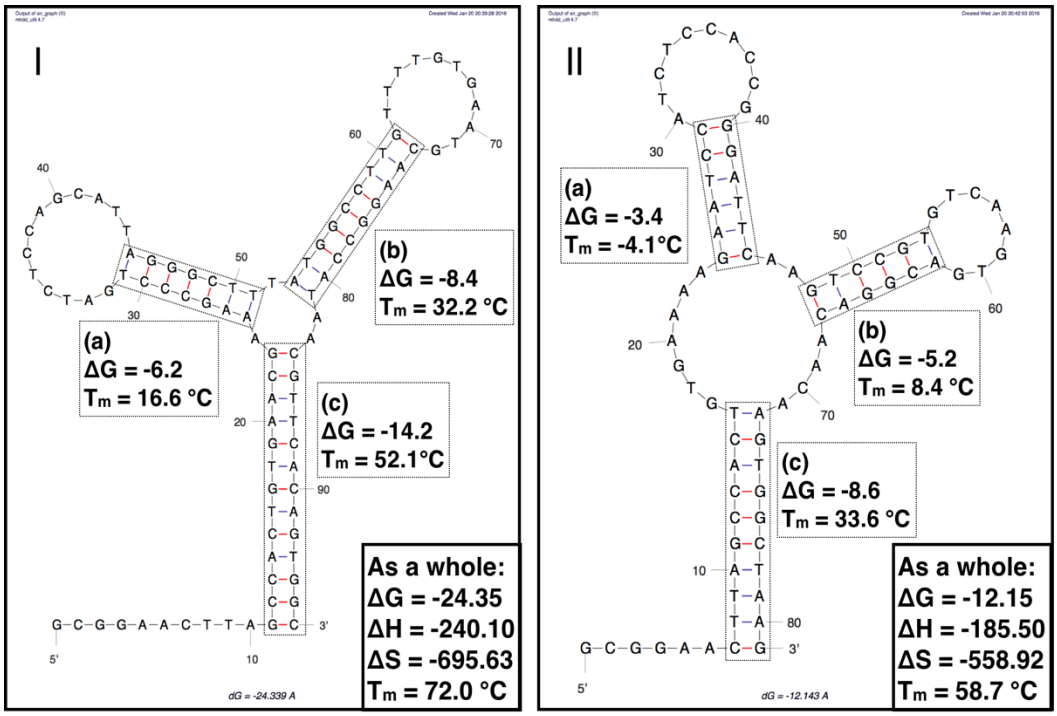

Figure 2.6 Predicted multi-hairpin structures of (I) L0 and (II) L3 from "Quikfold" of DINAMelt Web Server. L3 successfully sensed miR combinations due to its reasonable stability in the folded state and three stable stem parts (a, b, and c). Here, a, b, and c represented HR-182, HR-96, and HS-27a, respectively. The units for Gibbs free energy and enthalpy were kcal mol^{-1}, and for entropy is cal $(mol\ K)^{-1}$.

There are several other factors in addition to enthalpic, entropic, and toe-hold contributions that govern the linker's ability to form a complex and display a signal change. These additional factors include: (1) branch migration, (2) gains in hydrogen bonds, (3) molar fraction of complex formed, and (4) homodimer thermodynamic values and structure probabilities. Table 2.3 compares some key boundary conditions for L0 and L3.

The predicted structure in Figure 2.6, thermodynamic analysis and discussion of Figure 2.5, and molar fractions along with several experiments provided evidence that the multi-hairpin structure in Figure 2.1 likely formed. First, the fact that L0 did not work and L3 did not respond well to single miR inputs sup- ports the formation of a hairpin structure. Furthermore, the fact that presence of both reporters did not change L3's signal by the full dynamic range, but adding miR27a did, supports a multi-modal structure. The observed signal changes were in agreement with the expected results if the structure depicted in Figure 2.1 formed.

Table 2.3 Key predicted chemical and physical boundary conditions defined by L0 and L3

L0	L3
R182 only bind loop of HR182, no branch migration to disrupt HR182's stem	R182 binds stem and loop in HR182, branch migration can disrupt HR182's stem.
dG(HR-182) = -4.18 kcal/mol	dG(HR-182) = -1.92 kcal/mol
dG(HR-96) = -6.98 kcal/mol	dG(HR-96) = -3.3 kcal/mol
dG(L) = -24.35 kcal/mol	dG(L) = -12.13 kcal/mol
dG(R96,R182) = -17.9 kcal/mol	dG(R96,R182) = -23.8 kcal/mol
ddG(L to LR96R182) = +6.45 kcal/mol (not favorable)	ddG(L to LR96R182) = -11.67 kcal/mol (favorable)
L to LR182 gain 7 H-bonds	L to LR182 gain 17 H-Bonds
L to LR96 gain 6 H-Bonds	L to LR96 gain 15 H-Bonds
High probability for a homodimer	Low probability for a homodimer
Homodimer more stable than hairpin by 12.15 kcal/mol	Homodimer less stable than hairpin by 2.35 kcal/mol

Based on the fact R182 only bound to HR-182's loop region in L0 and the lack of an observed change in R/G ratio suggested that there was no branch migration to open HR-182's stem. The lack of branch migration coupled with thermodynamic stability of HR-182 meant either: (1) the reporter was unable to bind the loop region or (2) the reporter R182 partially bound HR-182 but kept L0's overall structure such that the two dyes were outside the FRET distance. If the dyes were outside the FRET distance, then no changes in donor and acceptor dye intensities would be observed. Either explanation was supported by the fact no changes in signal were observed for L0. There is literature precedence for the observed FRET changes to be sensitive to nano-assembly conformational (structural) states.[78]

In contrast, L3's HR-182 had two nucleotides in the stem and several in the loop that bind R182. As for HR-96, four nucleotides in the stem bound R96. The two nucleotides in HR-182's stem and the four in HR-96's stem that facilitate branch migration must have been enough to open the HRs and bring the two dyes within the FRET distance to observe changes in the dyes' signal. The fact that only two nucleotides bound R182 suggests the branch migration may not have been enough to open all the linker's HR-182s. Thus the equilibrium had trouble to fully complex every R182. Alternatively, the incomplete branch migration may have permitted the R182 to bind HR-182, but in such away the linkers structure did not open HR-182's stem. This would force the dyes to be farther apart causing less FRET efficiency. Both incomplete reaction and large FRET distance account for the R/G ratio that was less than one.

Gains in hydrogen bonds are fundamental to the thermodynamics that drive strand displacement mechanisms. There were far fewer hydrogen bonds gained when the reporters for L0

bound their respective domains in the hairpin region compared to hydrogen bonds gained for L3. L0 only gained 7 hydro- gen bonds compared to the 17 gained by L3 when R182 disrupted HR-182's stem to complex the linker's reporter binding domain. As for the R96 binding domain in L0, only 6 hydrogen bonds were gained compared to 15 gained by L3 when R96 bound HR-96. Pi-stacking interactions are also fundamental to strand displacement thermodynamic driving forces. As expected from the discussion on gains in hydrogen bonds, twice as many pi-stacking interactions were gained in L3 than L0 for both R96 and R182 interacting with their respective reporter binding domains. The low number of hydrogen bonds and pi-stacking interactions gained by L0 compared to L3 supported the idea that the branch migration and strand displacement was limited in L0. As a result, the linker–reporter complexes needed to observe FRET did not form in L0.

The molar fraction of complex formed between each linker (L0 and L3), both reporters, and miR27a was predicted by concatenating the R96, R182, and miR27a sequences *in silico*. L3 was predicted to form 100% (Figure A1.5 I), but L0 was only predicted to form 2.82% at 37 °C (Figure A1.6 I). Experimental results showed that L0 failed to respond to R96, R182, and miR27a, but L3 succeeded. Thus, the method of predicted molar fraction was a good metric to gauge if a complex would form or not.

Typically, homodimers are not predicted to form between single DNA strands that can form hairpins. The basis for this assumption is that intramolecular interactions occur over shorter distances than intermolecular interactions. Thus, the hairpin will form prior to the homodimer.[63] However, L0 was predicted to form with an equivalent probability as the hairpin. Furthermore, the Gibbs energy of the homodimer was more stable than the hairpin by 12.15 kcal mol^{-1}. Taken together these metrics predict a favorable probability and energy landscape to form homodimers. The reaction to disrupt L0's homodimer and form a complex with both reporters and miR27a was endothermic and had a positive Gibbs energy. These thermodynamic values indicated that the complex formation was not favorable. A potential reason no change in signal was observed when the reporters and miR27a were added to L0 was the inability to disrupt the homodimer.

In contrast, L3's probability to form a homodimer was less than the probability for a hairpin structure. In addition, the Gibbs energy to form a homodimer was less stable than the hairpin by 2.35 kcal mol^{-1}. Taken together these metrics predict a probability and energy landscape that was not favorable to form a homodimer. Even if a L3 homodimer did form, the change in energy to

form a complex between the linker, both reporters, and miR27a was exothermic and the Gibbs energy was less than zero. Thus, the thermodynamics were favorable to bind reporters and demonstrate signal change. Experimental evidence supported the signal from FRET pairs did change.

2.5 Conclusion

The ability to use a multi-hairpin linker with reporter–probe complexes to serve as a nano-assembly based molecular Boolean logic gate was demonstrated. The description "logic" means the gate is selective for a specific combination of short ncRNA. As a model system, three microRNAs were used as inputs for an AND Boolean logic gate. Differences in the gate's OFF and ON states were seen in aqueous buffer and crude cell lysate. NA-L3 showed selectivity against off-analyte miRs. NA-L3 also showed a consistent 3.5 factor change in R/G ratio between the OFF and ON states in both buffer and crude cell lysate.

In aqueous buffers, slight issues with false signals from single and double analyte miR additions were seen. These issues will be resolved by fine-tuning the thermodynamics and types of base pairing in the various regions of the linker strand as well as the reporter–probe complexes. The gate in this work serves as an AND logic for two or three miRs. In some biological situations this information will be relevant.

Future work will involve optimization of current NA-L3 for only three miRs in breast cancer cell lines. In the next design the linker will be modified to incorporate attributes from L0 with those of L1–L5. FRET distances of reporters will be adjusted to improve the FRET efficiency. In addition to thermodynamic considerations, we will account for: number of sequences to support branch migration, the molar fraction, gains in hydrogen bonds and pi-stacking, and homodimer probability and thermodynamics.

For future cell imaging applications an internal standard dye on the multi-hairpin motif will be needed to observe differential expression of miRs in cells. We also envision combining logic gates to reach the goal of multiplexing the tens[60] of miRs that describe biological processes. For example, two logic gates can create a circuit for six miRs. With an alternative transduction mechanism, a logic circuit made of three to four gates would permit detection of nine to twelve miRs. The development of this nano-assembly logic gate has great potential for far reaching single-cell applicability and other applications, including cellular computing, analysis of

biological microenvironments, and disease therapeutic analysis.

2.6 Acknowledgements

We would like to thank Oregon State University for supporting this research.

2.7 References

(1) S. Choudhuri, Small noncoding RNAs: biogenesis, function, and emerging significance in toxicology, J. Biochem. Mol. Toxicol., 2010, 24(3), 195–216.
(2) V. Benes and M. Castoldi, Expression profiling of microRNA using real-time quantitative PCR, how to use it and what is available, Methods, 2010, 50(4), 244–249.
(3) S. Fleige and M. W. Pfaffl, RNA integrity and the effect on the real-time qRT-PCR performance, Mol. Aspects Med., 2006, 27(2–3), 126–139.
(4) K. E. Resnick, H. Alder, J. P. Hagan, D. L. Richardson, C. M. Croce and D. E. Cohn, The detection of differentially expressed microRNAs from the serum of ovarian cancer patients using a novel real-time PCR platform, Gynecol. Oncol., 2009, 112(1), 55–59.
(5) J. Krützfeldt, M. N. Poy and M. Stoffel, Strategies to deter- mine the biological function of microRNAs, Nat. Genet., 2006, 38(6s), S14–S19.
(6) L. F. Sempere, M. Christensen, A. Silahtaroglu, M. Bak, C. V. Heath, G. Schwartz, W. Wells, S. Kauppinen and C. N. Cole, Altered MicroRNA Expression Confined to Specific Epithelial Cell Subpopulations in Breast Cancer, Cancer Res., 2007, 67(24), 11612–11620.
(7) C. L. Bockmeyer, M. Christgen, M. Müller, S. Fischer, P. Ahrens, F. Länger, H. Kreipe and U. Lehmann, MicroRNA profiles of healthy basal and luminal mammary epithelial cells are distinct and reflected in different breast cancer subtypes, Breast Cancer Res. Treat., 2011, 130(3), 735–745.
(8) R. C. Lee and V. Ambros, An Extensive Class of Small RNAs in Caenorhabditis elegans, Science, 2001, 294(5543), 862–864.
(9) L. He and G. J. Hannon, MicroRNAs: small RNAs with a big role in gene regulation, Nat. Rev. Genet., 2004, 5(7), 522–531.
(10) M. Lagos-Quintana, R. Rauhut, W. Lendeckel and T. Tuschl, Identification of novel genes coding for small expressed RNAs, Science, 2001, 294(5543), 853–858.
(11) N. C. Lau, L. P. Lim, E. G. Weinstein and D. P. Bartel, An abundant class of tiny RNAs with probable regulatory roles in Caenorhabditis elegans, Science, 2001, 294(5543), 858–862.
(12) A. J. Hamilton and D. C. Baulcombe, A Species of Small Antisense RNA in Posttranscriptional Gene Silencing in Plants, Science, 1999, 286(5441), 950–952.
(13) D. P. Bartel, MicroRNAs: genomics, biogenesis, mecha- nism, and function, Cell, 2004, 116(2), 281–297.
(14) S. Yekta, I.-H. Shih and D. P. Bartel, MicroRNA-Directed Cleavage of HOXB8 mRNA, Science, 2004, 304, 594–596.
(15) J. E. Abrahante, A. L. Daul, M. Li, M. L. Volk, J. M. Tennessen, E. A. Miller and A. E. Rougvie, The Caenorhabditis elegans hunchback-like gene lin-57/hbl-1 controls developmental time and is regulated by microRNAs, Dev. Cell, 2003, 4(5), 625–637.
(16) N. Bushati and S. M. Cohen, microRNA Functions, Annu. Rev. Cell Dev. Biol., 2007, 23, 175–205.
(17) S.-Y. Lin, S. M. Johnson, M. Abraham, M. C. Vella, A. Pasquinelli, C. Gamberi, E. Gottlieb and F. J. Slack, The C. elegans hunchback homolog, hbl-1, controls temporal patterning and is a probable microRNA target, Dev. Cell, 2003, 4(5), 639–650.
(18) F. J. Slack, M. Basson, Z. Liu, V. Ambros, H. R. Horvitz and G. Ruvkun, The lin-41 RBCC gene acts in the C. elegans heterochronic pathway between the let-7 regulatory RNA and the LIN-29 transcription factor, Mol. Cell, 2000, 5(4), 659–669.
(19) S. K. Shenouda and S. K. Alahari, MicroRNA function in cancer: oncogene or a tumor suppressor? Cancer Metastasis Rev., 2009, 28(3–4), 369–378.
(20) H.-C. Chen, G.-H. Chen, Y.-H. Chen, W.-L. Liao, C.-Y. Liu, K.-P. Chang, Y.-S. Chang and S.-J. Chen, MicroRNA deregu- lation and pathway alterations in nasopharyngeal carci- noma, Br. J. Cancer, 2009,

100(6), 1002–1011.
(21) P. Moskwa, F. M. Buffa, Y. Pan, R. Panchakshari, P. Gottipati, R. J. Muschel, J. Beech, R. Kulshrestha, K. Abdelmohsen, D. M. Weinstock, M. Gorospe, A. L. Harris, T. Helleday and D. Chowdhury, miR-182-Mediated Downregulation of BRCA1 Impacts DNA Repair and Sensitivity to PARP Inhibitors, Mol. Cell, 2011, 41(2), 210–220.
(22) S. U. Mertens-Talcott, S. Chintharlapalli, X. Li and S. Safe, The Oncogenic microRNA-27a Targets Genes That Regulate Specificity Protein Transcription Factors and the G2 M Checkpoint in MDA-MB-231 Breast Cancer Cells, Cancer Res., 2007, 67(22), 11001–11011.
(23) S. F. Tavazoie, C. Alarcón, T. Oskarsson, D. Padua, Q. Wang, P. D. Bos, W. L. Gerald and J. Massagué, Endogenous human microRNAs that suppress breast cancer metastasis, Nature, 2008, 451(7175), 147–152.
(24) C. M. Croce, Causes and consequences of microRNA dysregulation in cancer, Nat. Rev. Genet., 2009, 10(10), 704–714.
(25) M. V. Iorio, M. Ferracin, C.-G. Liu, A. Veronese, R. Spizzo, S. Sabbioni, E. Magri, M. Pedriali, M. Fabbri, M. Campiglio, S. Ménard, J. P. Palazzo, A. Rosenberg, P. Musiani, S. Volinia, I. Nenci, G. A. Calin, P. Querzoli, M. Negrini and C. M. Croce, MicroRNA Gene Expression Deregulation in Human Breast Cancer, Cancer Res., 2005, 65(16), 7065–7070.
(26) C.-H. Chiang, M.-F. Hou and W.-C. Hung, Up-regulation of miR182 by β-catenin in breast cancer increases tumorigenicity and invasiveness by targeting the matrix metalloproteinase inhibitor RECK, Biochim. Biophys. Acta, Gen. Subj., 2013, 1830(4), 3067–3076.
(27) J. Lu, G. Getz, E. A. Miska, E. Alvarez-Saavedra, J. Lamb, D. Peck, A. Sweet-Cordero, B. L. Ebert, R. H. Mak, A. A. Ferrando, J. R. Downing, T. Jacks, H. R. Horvitz and T. R. Golub, MicroRNA expression profiles classify human cancers, Nature, 2005, 435(7043), 834–838.
(28) G. A. Calin and C. M. Croce, MicroRNA signatures in human cancers, Nat. Rev. Cancer, 2006, 6(11), 857–866.
(29) N. Yang, G. Coukos and L. Zhang, MicroRNA epigenetic alterations in human cancer: One step forward in diagnosis and treatment, Int. J. Cancer, 2008, 122(5), 963–968.
(30) T. Paranjape, F. J. Slack and J. B. Weidhaas, MicroRNAs: tools for cancer diagnostics, Gut, 2009, 58(11), 1546–1554.
(31) C. Corcoran, A. M. Friel, M. J. Duffy, J. Crown and L. O'Driscoll, Intracellular and Extracellular MicroRNAs in Breast Cancer, Clin. Chem., 2011, 57(1), 18–32.
(32) A. Eijkelenboom and B. M. T. Burgering, FOXOs: signaling integrators for homeostasis maintenance, Nat. Rev. Mol. Cell Biol., 2013, 14(2), 83–97.
(33) I. K. Guttilla and B. A. White, Coordinate Regulation of FOXO1 by miR27a, miR96, and miR182 in Breast Cancer Cells, J. Biol. Chem., 2009, 284(35), 23204–23216.
(34) J.-H. Paik, R. Kollipara, G. Chu, H. Ji, Y. Xiao, Z. Ding, L. Miao, Z. Tothova, J. W. Horner, D. R. Carrasco, S. Jiang, D. G. Gilliland, L. Chin, W. H. Wong, D. H. Castrillon and R. A. DePinho, FoxOs Are Lineage-Restricted Redundant Tumor Suppressors and Regulate Endothelial Cell Homeostasis, Cell, 2007, 128(2), 309–323.
(35) D. N. Gross, A. P. J. van den Heuvel and M. J. Birnbaum, The role of FoxO in the regulation of metabolism, Oncogene, 2008, 27(16), 2320–2336.
(36) T. Obsil and V. Obsilova, Structure/function relationships underlying regulation of FOXO transcription factors, Oncogene, 2008, 27(16), 2263–2275.
(37) Z. Fu and D. J. Tindall, FOXOs, cancer and regulation of apoptosis, Oncogene, 2008, 27(16), 2312–2319.
(38) C. Becker, A. Hammerle-Fickinger, I. Riedmaier and M. W. Pfaffl, mRNA and microRNA quality control for RT- qPCR analysis, Methods, 2010, 50(4), 237–243.
(39) H.-H. Liu, X. Tian, Y.-J. Li, C.-A. Wu and C.-C. Zheng, Microarray-based analysis of stress-regulated microRNAs in Arabidopsis thaliana, RNA, 2008, 14(5), 836–843.
(40) J. L. Abell, J. D. Driskell, R. A. Dluhy, R. A. Tripp and Y.-P. Zhao, Fabrication and characterization of a multiwell array SERS chip with biological applications, Biosens. Bioelectron., 2009, 24(12), 3663–3670.
(41) B. M. Beckmann, A. Grunweller, M. H. W. Weber and R. K. Hartmann, Northern blot detection of endogenous small RNAs (14 nt) in bacterial total RNA extracts, Nucleic Acids Res., 2010, 38(14), e147.
(42) S. W. Kim, Z. Li, P. S. Moore, A. P. Monaghan, Y. Chang, M. Nichols and B. John, A sensitive non-radioactive north- ern blot method to detect small RNAs, Nucleic Acids Res., 2010, 38(7), e98.
(43) B. N. Johnson and R. Mutharasan, Biosensor-based microRNA detection: techniques, design, performance, and challenges, Analyst, 2014, 139(7), 1576–1588.

(44) J. Koshiol, E. Wang, Y. Zhao, F. Marincola and M. T. Landi, Strengths and Limitations of Laboratory Procedures for MicroRNA Detection, Cancer Epidemiol., Biomarkers Prev., 2010, 19(4), 907–911.
(45) M. Avissar, B. C. Christensen, K. T. Kelsey and C. J. Marsit, MicroRNA Expression Ratio Is Predictive of Head and Neck Squamous Cell Carcinoma, Clin. Cancer Res., 2009, 15(8), 2850–2855.
(46) B. Bohunicky and S. A. Mousa, Biosensors: the new wave in cancer diagnosis, Nanotechnol., Sci. Appl., 2010, 4, 1–10.
(47) S. Catuogno, C. L. Esposito, C. Quintavalle, L. Cerchia, G. Condorelli and V. De Franciscis, Recent Advance in Biosensors for microRNAs Detection in Cancer, Cancers, 2011, 3(2), 1877–1898.
(48) E. Lécuyer, H. Yoshida, N. Parthasarathy, C. Alm, T. Babak, T. Cerovina, T. R. Hughes, P. Tomancak and H. M. Krause, Global Analysis of mRNA Localization Reveals a Prominent Role in Organizing Cellular Architecture and Function, Cell, 2007, 131(1), 174–187.
(49) E. Bertrand, P. Chartrand, M. Schaefer, S. M. Shenoy, R. H. Singer and R. M. Long, Localization of ASH1 mRNA particles in living yeast, Mol. Cell, 1998, 2(4), 437– 445.
(50) S. Tyagi and F. R. Kramer, Molecular Beacons: Probes that Fluoresce upon Hybridization, Nat. Biotechnol., 1996, 14(3), 303–308.
(51) S. A. Marras, F. R. Kramer and S. Tyagi, Efficiencies of fluo- rescence resonance energy transfer and contact-mediated quenching in oligonucleotide probes, Nucleic Acids Res., 2002, 30(21), e122.
(52) G. Bonnet, S. Tyagi, A. Libchaber and F. R. Kramer, Thermodynamic basis of the enhanced specificity of struc- tured DNA probes, Proc. Natl. Acad. Sci. U. S. A., 1999, 96(11), 6171–6176.
(53) K. He, R. Liao, C. Cai, C. Liang, C. Liu and X. Chen, Y-shaped probe for convenient and label-free detection of microRNA-21 in vitro, Anal. Biochem., 2016, 499, 8–14.
(54) H. Cao, S. Liu, W. Tu, J. Bao and Z. Dai, A carbon nano- tube/quantum dot based photoelectrochemical biosensing platform for the direct detection of microRNAs, Chem. Commun., 2014, 50(87), 13315–13318.
(55) G.-J. Zhang, J. H. Chua, R.-E. Chee, A. Agarwal and S. M. Wong, Label-free direct detection of MiRNAs with silicon nanowire biosensors, Biosens. Bioelectron., 2009, 24(8), 2504–2508.
(56) H. Vaisocherová, H. Šípová, I. Víšová, M. Bocková, T. Špringer, M. Laura Ermini, X. Song, Z. Krejčík, L. Chrastinová, O. Pastva, K. Pimková, M. D. Merkerová, J. E. Dyr and J. Homola, Rapid and sensitive detection of multiple microRNAs in cell lysate by low-fouling surface plasmon resonance biosensor, Biosens. Bioelectron., 2015, 70, 226–231.
(57) W.-J. Yang, X.-B. Li, Y.-Y. Li, L.-F. Zhao, W.-L. He, Y.-Q. Gao, Y.-J. Wan, W. Xia, T. Chen, H. Zheng, M. Li and S.-Q. Xu, Quantification of microRNA by gold nanoparticle probes, Anal. Biochem., 2008, 376(2), 183–188.
(58) X. Ding, Y. Yan, S. Li, Y. Zhang, W. Cheng, Q. Cheng and S. Ding, Surface plasmon resonance biosensor for highly sensitive detection of microRNA based on DNA super-sand- wich assemblies and streptavidin signal amplification, Anal. Chim. Acta, 2015, 874, 59–65.
(59) K. E. Sapsford, T. Pons, I. L. Medintz and H. Mattoussi, Biosensing with luminescent semiconductor quantum dots, Sensors, 2006, 6(8), 925–953.
(60) R. M. Graybill and R. C. Bailey, Emerging Biosensing Approaches for microRNA Analysis, Anal. Chem., 2016, 88(1), 431–450.
(61) N. E. Larkey, C. K. Almlie, V. Tran, M. Egan and S. M. Burrows, Detection of miRNA Using a Double-Strand Displacement Biosensor with a Self-Complementary Fluorescent Reporter, Anal. Chem., 2014, 86(3), 1853– 1863.
(62) N. E. Larkey, C. N. Brucks, S. S. Lansing, S. D. Le, N. M. Smith, V. Tran, L. Zhang and S. M. Burrows, Molecular structure and thermodynamic predictions to create highly sensitive microRNA biosensors, Anal. Chim. Acta, 2016, 909, 109–120.
(63) C. K. Almlie, N. E. Larkey and S. M. Burrows, Fluorescent microRNA biosensors: a comparison of signal generation to quenching, Anal. Methods, 2015, 7(17), 7296–7310.
(64) C. G. Evans and E. Winfree, DNA sticky end design and assignment for robust algorithmic Self-assembly, in Proceedings of the 19th International Conference on DNA Computing and Molecular Programming – Vol. 8141 (DNA 19), ed. D. Soloveichik and B. Yurke, Springer International Publishing, New York, 2013, pp. 61–75.
(65) P. Wu, Y. Tu, Y. Qian, H. Zhang and C. Cai, DNA strand- displacement-induced fluorescence enhancement for highly sensitive and selective assay of multiple microRNA in cancer cells, Chem. Commun., 2014, 50(8), 1012–1014.

(66) M. Teichmann, E. Kopperger and F. C. Simmel, Robustness of Localized DNA Strand Displacement Cascades, ACS Nano, 2014, 8(8), 8487–8496.
(67) D. Y. Zhang and G. Seelig, Dynamic DNA nanotechnology using strand-displacement reactions, Nat. Chem., 2011, 3(2), 103–113.
(68) H.-Z. He, D. S.-H. Chan, C.-H. Leung and D.-L. Ma, G-quad- ruplexes for luminescent sensing and logic gates, Nucleic Acids Res., 2013, 41(8), 4345–4359.
(69) D.-L. Ma, H.-Z. He, D. S.-H. Chan and C.-H. Leung, Simple DNA-based logic gates responding to biomolecules and metal ions, Chem. Sci., 2013, 4(9), 3366–3380.
(70) P. Zhang, Z. He, C. Wang, J. Chen, J. Zhao, X. Zhu, C.-Z. Li, Q. Min and J.-J. Zhu, In Situ Amplification of Intracellular MicroRNA with MNAzyme Nanodevices for Multiplexed Imaging, Logic Operation, and Controlled Drug Release, ACS Nano, 2015, 9(1), 789–798.
(71) J. Hemphill and A. Deiters, DNA Computation in Mammalian Cells: MicroRNA Logic Operations, J. Am. Chem. Soc., 2013, 135(28), 10512–10518.
(72) D. Wang, Y. Fu, J. Yan, B. Zhao, B. Dai, J. Chao, H. Liu, D. He, Y. Zhang, C. Fan and S. Song, Molecular Logic Gates on DNA Origami Nanostructures for MicroRNA Diagnostics, Anal. Chem., 2014, 86(4), 1932–1936.
(73) Z. Cheglakov, T. M. Cronin, C. He and Y. Weizmann, Live Cell MicroRNA Imaging Using Cascade Hybridization Reaction, J. Am. Chem. Soc., 2015, 137(19), 6116–6119.
(74) N. E. Larkey, L. Zhang, S. S. Lansing, V. Tran, V. L. Seewaldt and S. M. Burrows, Förster resonance energy transfer to impart signal-on and -off capabilities in a single microRNA biosensor, Analyst, 2016, 141(22), 6239–6250.
(75) http://unafold.rna.albany.edu/?q=DINAMelt.
(76) H. Lee, S. J. Shapiro, S. C. Chapin and P. S. Doyle, Encoded Hydrogel Microparticles for Sensitive and Multiplex microRNA Detection Directly from Raw Cell Lysates, Anal. Chem., 2016, 88(6), 3075–3081.
(77) http://www.atto-tec.com/index.php?id=65&L=1.
(78) A. H. Buck, C. J. Campbell, P. Dickinson, C. P. Mountford, H. C. Stoquert, J. G. Terry, S. A. G. Evans, L. M. Keane, T.-J. Su, A. R. Mount, A. J. Walton, J. S. Beattie, J. Crain and P. Ghazal, DNA Nanoswitch as a Biosensor, Anal. Chem., 2007, 79(12), 4724–4728.

Chapter 3.

Structural and thermodynamic principles influencing nanoscale molecular-logic-based measurement systems

Lulu Zhang, Annie M. Bluhm, Kuo-Fu Tseng, and Sean M. Burrows

Submitted to Analytical Chemistry. This manuscript is under review.

3.1 Abstract

Nanoscale measurement systems known as molecular logic sensors respond to specific combinations of chemical or biological inputs. However, scaling-up the multiplex abilities of these sensors face challenges differentiating between an incomplete and a complete set of inputs. Here, we present on the development of a three-input AND logic sensor that was theoretically predicted to better differentiate input numbers by tuning the thermodynamics and moving hybridizing sites. Although the new designs were able to better resist binding two inputs, the response to three inputs was retarded. As a result, the ability to differentiate input numbers was not improved. Based on the theoretical and experimental data, we will reveal the limits in the accuracy of predictive tools. We found that the predictive tools on thermodynamic-related design metrics and structural stability must be collectively considered. Our findings provide a noteworthy improvement to the design process of logic sensors for measurement science. Furthermore, the results presented here will contribute to the nanoscale systems and structures as well as the selectivity phases of analytical operation. Finally, by providing design guidelines and highlighting pitfalls our work will advance the field of molecular logic nanoscale measurement systems in general.

3.2 Introduction

Molecular sensors are emerging to compute specific patterns of biomolecules and carry out cellular computations[1,2]. One type of molecular sensors is known as DNA-based logic gates or circuits. Logic circuits combine one or more logic gate (*e.g.* AND, OR, and NOT) to interact with chemicals and biomolecules to perform various functions[3–7]. The Watson-Crick base pairing is central to the way DNA-based sensors maintain and alter their structure to recognize and respond to inputs.

Logic gates typically consist of gate strands and output strands[8]. The biomolecules of interest are the inputs. The gates are designed to be more complementary to the inputs than to the outputs[9]. The outputs can be labelled with fluorescent dyes to report on the occurrence of the biophysical interactions between the gates and the inputs. The inputs bind to the gates and displace the outputs through a toehold-initiated strand displacement reaction[10–13]. A toehold (around 3 to 6 nucleotides long) is a DNA segment in a gate that recognizes the complementary nucleotides of an input.

We are just beginning to learn how small RNA biomolecules work in groups to perform

biological functions[14–19]. Logic gates and circuits will play a central role to progress our understanding of how small RNA biomolecules shape biology. For example, molecular logic gates have great potential to assess a cell's small non-coding RNA signature. One type of small non-coding RNA known as microRNA (miR) are around 22 nucleotides long[20–22]. They are of interest due to the discovery of key roles in the maintenance of homeostasis and disease[23–35].

Recent activity around logic gates and circuits has focused on advancing design strategies and innovating designs for unique applications[36–43]. For instance, Seelig combined AND with OR gates to demonstrate a complex chemical circuit for sensing synthetic RNA inputs[44]. Li *et al.* presented three-input Majority logic gate and multiple-input logic circuit for sensing three synthetic DNA inputs (42 nts to 63 nts long) at ~20 ℃.[45] However such logic gates or circuits were not ready for intracellular analysis of small non-coding RNAs because (1) small non-coding RNAs have short sequences (*e.g.* microRNAs are ~22nts), (2) logic gates that function at ~20℃ doesn't mean they can work as 37 ℃(the biological temperature), and (3) Li's logic devices were susceptible to false-positive signals from nuclease degradation during biological study since their design relied on the disruption of fluoreohore-quencher pair as the transduction mechanism. In addition, many published DNA-based logic gates or circuits either rely on several different output signals to perform multiplex analysis, or rely on single-output signal to compute output from one or two inputs[46–52]. Single-output sensors capable of recognizing multiple inputs will benefit cell-based analysis due to the noisy molecular environment of cells and cell lysates.

Designing DNA-based logic gates or circuits is challenging due to the lack of a solid and complete design process. Dirks[53] *et al.* established several criteria for designing nucleic acid sequences to adopt desired secondary structures, such as energy minimization. Later, Dirks established an algorithm for analyzing strand complex formation from the thermodynamic and equilibrium properties of interacting nucleic-acid strands[54]. Building upon this foundational work, synthesizing the data generated from these thermodynamic, structural, and equilibrium algorithms will help advance the development of DNA- and logic-based sensors.

Our previous work on a three-input nano-assembly AND logic gate (NALG) demonstrated the ability to generate a single-output signal from three inputs[55]. The single-output signaling mechanism relied on Förster Resonance Energy Transfer (FRET) enhancement. One unresolved issue with NALG was a noticeable FRET enhancement from only two inputs. NALG's signal response to both two and three inputs are not ideal for cases where a signature expression of two

miR inputs versus three miR inputs is related to different cellular processes or diseases.

In this paper, we focus on the theoretical and experimental functionality of a multi-hairpin motif in the presence of two (R96 and R182) or three inputs (R96, R182, and miR27a). The purpose of our study is to address the issue of DNA-based sensors not strictly responding to the desired number of inputs. We will discuss the gap between the theoretical predictions and the experimental results in terms of the motifs' biophysical interactions, structural change, and signal response in the presence of two or three inputs. We will discuss the accuracy and limits of two open-source web servers (DINAMelt[56,57] and NUPACK[58]) for theoretical prediction. We will outline the key predictive metrics and summarize their boundary values. Our findings provide noteworthy improvement to the design process to achieve better multiplexing abilities for molecular logic sensors.

3.3 Experimental

3.3.1 Instrumentation

All spectra were collected with a custom-built fluorimeter detailed in previous work[39,40,52,59]. Briefly, a MaiTai Ultrafast Titanium-Sapphire laser (Spectra Physics, Newport, 100 femtosecond (fs) pulses at a repetition rate of 80 MHz) delivered source radiation to excite all samples with average power of 75 mW at 935 nm. Emission spectra were collected with an Acton Spectrometer (SP-2356) coupled to an electron-multiplied charge coupled device camera (Princeton Instruments, 512B-eXcelon3-EMCCD). The spectrometer had a 300 groove per mm grating blazed at 500 nm to collect the emission spectra. The data was acquired from the detector with LightField software. The following parameters were set in LightField: 2 000 ms exposure time, 1 exposure averaged per frame, 60 frames (collected to gauge instrumental error), full frame read-out mode, high Analog-to-Digital Conversion Gain (ADC), 100 MHz ADC speed, low noise ADC quality, and the EMCCD chip was thermoelectrically cooled to - 70 °C to minimize dark noise.

3.3.2 Oligonucleotides and materials

All oligonucleotides were purchased from IDT and used as received (Integrated DNA Technologies, Inc., Coralville, Iowa, United States). All oligonucleotide sequences are listed in Table A2.1. The stock oligonucleotides solutions were diluted with a custom buffer at room

temperature[55]. The custom buffer solution with final pH of around 8 contained 0.005% Tween-20 in PBS, 2.5 mM $MgCl_2$, and 10 mM Tris, and all components were from Fisher Scientific.

A stock solution of 20 μM oligonucleotides were diluted to 2 μM and verified with a Nanodrop spectrometer (Thermo Scientific, ND-1000 UV-VIS spectrophotometer). Then the diluted oligonucleotides were hybridized at 37 °C. All experimental solutions were prepared to contain a final concentration of 100 nM oligonucleotides.

3.4 Results and discussion

3.4.1 Design theory on biophysical properties and sensing mechanism of multi-hairpin motifs

Building upon our published multi-hairpin motif (Type 1 Motif, T1M[55]), we designed two new types referred as Type 2 and Type 3 Motif (T2M and T3M). T1Ms and T2Ms have two subtypes: T1M-1 and T1M-2[55] for T1Ms, and T2M-1 and T2M-2 for T2Ms. T3M has no subtypes.

As seen in Figure 3.1, all motif types conform to the general structures having two hairpin (HP) regions (red and green boxes), an internal loop (black curved line not boxed), and one double-stranded (DS) region (blue box). DS region includes the 3-prime and 5-prime tails. The arrows on the motifs indicate the 3-prime ends. A HP region contains a loop and an internal double-stranded stem.

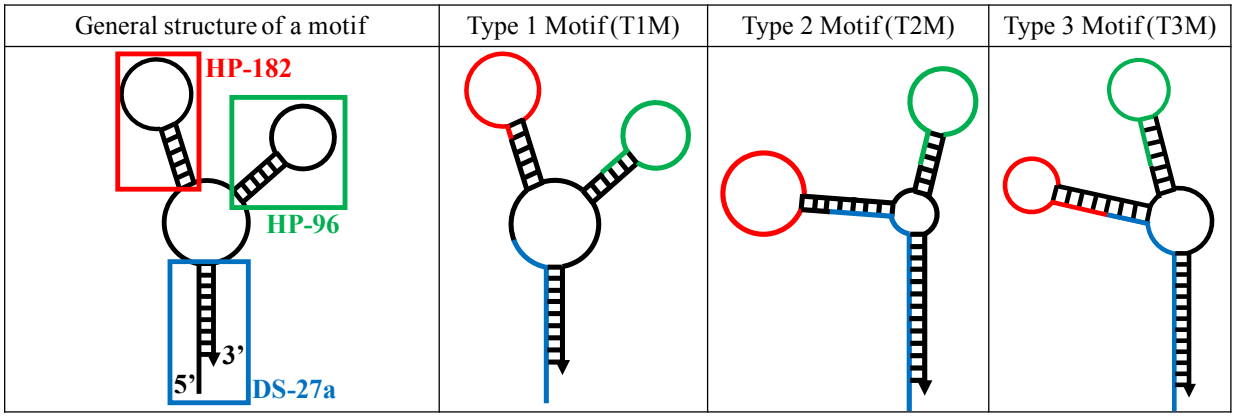

Figure 3.1 The theoretical multi-hairpin structure of three motif types and different locations for the inputs' complementary sequence in each motif type. The parts of the motif colored in red, green, and blue represent the complementary sequences for inputs R182, R96, or miR27a, respectively. Based on the predicted structure, motifs' size and shape are drawn on a relative scale to each other. The arrows indicate the 3-prime ends of the motifs. Black short bars represent base pairs.

The red boxed hairpin region is HP-182 containing the complementary sequence for R182. Similarly, the green boxed hairpin region is HP-96 and the blue boxed double-stranded region is DS-27a. HP-96 and DS-27a contain the complementary sequences for R96 and miR27a,

respectively. In Figure 3.1, the colored parts in each motif type highlight the locations of each inputs' complementary sequence.

The motif undergoes both self- and directed- assembly of nucleic-acid strands to report on inputs[55]. In theory, the motif only responds to three inputs and exhibits a two-step structural change.[55] First, miR27a must be present to bind DS-27a, thereby partially destabilizing the motif. Then the toehold in each loop enables the interaction with R182 and R96 through the corresponding HP-182 and HP-96. Reporters' binding continues to disrupt HP regions' stems through strand displacement, thereby changing motif's structure.

The 3-prime end of R96 is labeled with FAM as a donor. R182 were labeled with ATTO633 at the 5-prime end. From previous work under two-photon conditions, we observed the largest FRET signal from ATTO633 when FAM was excited at 935 nm[55]. The maximum emission signal from FAM and ATTO 633 were seen at ~520 nm (green channel) and 660 nm (red channel), respectively. The extent of FRET enhancement was assessed by a red to green intensity ratio (R/G ratio).

The motif as a multi-hairpin is defined as the OFF state when the R/G ratio is low. The motif with three inputs is defined as the ON state and is expected to have a higher R/G ratio than the OFF state. We assessed each motifs' differentiating-input-number ability by testing if motif stays in the OFF state when two inputs are present, and turns ON when three inputs are present. We created a quantitative index with Equation 1:

$$\text{Differentiating} - \text{Input} - \text{number Index (DIN index)} = \frac{(R/G)_{3-input}}{(R/G)_{2-input}} \qquad \text{Equation 1}$$

where $(R/G)_{2\text{-input}}$ and $(R/G)_{3\text{-input}}$ are R/G ratios of the motif in the presence of two and three inputs, respectively. A high DIN index indicates the motifs are able to precisely differentiate a specific number of inputs. To improve the DIN index, we can either try to decrease $(R/G)_{2\text{-input}}$, or improve $(R/G)_{3\text{-input}}$, or both. New motifs were predicted to have higher DIN indexes than T1Ms through the evaluation of (1) the inputs' complementary sequence location, (2) the number of Hydrogen-bonds (H-bonds), and (3) the molarity percentage of complex formed after reaction with either two or three inputs (see detail in the discussion below).

We hypothesized that modifying the location of each input's complementary sequence in the motif would affect the motif's biophysical interactions with each input. As the motif interacts with a different number of inputs resulting in dissimilar structural changes and thus different R/G

ratios were expected. To test our hypothesis, we developed T2Ms and T3M. Figure 3.1 shows that all motif types had R96's complementary sequence (green) in the loop and stem of HP-96. For T1Ms, around 84% (10 out of 12 nts) of R182's complementary sequence (red) was in the loop of HP-182, as a toehold, and the rest in HP-182's stem. In T2Ms, R182's complementary sequence was only in the loop of HP-182. For T3M, half of R182's complementary sequence was in the loop of HP-182, as a toehold, and half in HP-182's stem. The complementary sequence for miR27a (blue) in T1Ms was located in the 5-prime tail of DS-27a and part of the internal loop. Both T2Ms and T3Ms had miR27a's complementary sequence in part of HP-182 stem, part of the internal loop, and the 5-prime tail of DS-27a.

T2Ms were expected to experience less overall structural changes than T1Ms after interacting with two reporters, thereby a lower R/G ratio. There were two reasons for such expectations: first, when T2Ms react with two reporters only the stem of HP-96 was expected to be disrupted; second, in T2Ms the R182 complementary sequence was confined to HP-182 loop. Thus, R182's interaction with T2Ms would only occur in the loop thereby keeping HP-182 stem intact. Compared to T1Ms, the T3Ms were expected to have a harder time interacting with R182 due to a smaller exposed interacting area from (1) a shorter toehold and (2) a smaller HP-182 loop. As a result, we expected T3M to have a lower R/G ratio in the presence of two inputs than T1Ms.

In the presence of three inputs, miR27a's interaction was expected to destabilize T2Ms' and T3M's structures more than T1Ms. After miR27a's interacting and disrupting DS-27a, miR-27a could continue to disrupt HP-182 stem in new motifs. Thus, we expected new motifs having a higher response to three inputs and a larger DIN index.

Next, we considered the number of Hydrogen-bonds (H-bonds) in the motif as another design metric. We found more total H-bonds formed in the new motifs (Table A2.2 and appendix section A2.1). Since H-bonds add the thermodynamic stability, we expected more stability from the new motifs and thus better resistance to structural changes when the motifs interact with two inputs.

Our previous molarity percentage analysis (DINAMelt) successfully predicted T1Ms would have a higher R/G ratio for three inputs than for two inputs[54] (Figure 3.2). Thus, molarity percentage analysis was considered as another valuable predictive tool for motif design. A high molarity percentage suggested favorable complex formation. Figure 3.2 shows the predicted molarity percentage of each motif type forming complexes with two (Rs) or three (Rs+miR27a)

inputs. The inputs had to be concatenated because DINAMelt only analyzes two strands interacting. More detail about concatenating the inputs can be found in the appendix section A2.2.

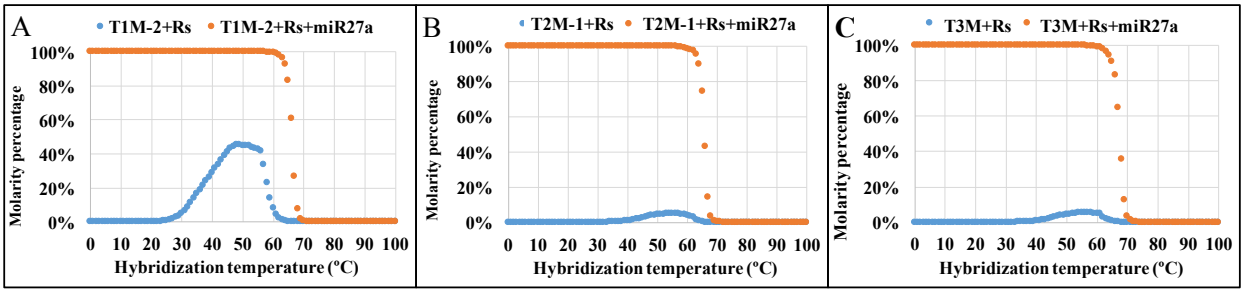

Figure 3.2 The DINAMelt molarity percentage analysis of three motif types bound to either the *in silico* concatenated two reporters (Rs, blue dots) or two reporters and miR27a (Rs+miR27a, orange dots). (A) At 37 ºC, T1M-2 was predicted to form a complex with both Rs and Rs+miR27a. (B) T2M-1 and (C) T3M were predicted to form a negligible amount of complex with two reporters, but would form a complex with three inputs at 37 ºC.

At 37 ºC, the molarity percentage analysis suggested that T2Ms and T3M would form less stable complexes with two inputs compared to T1Ms (Blue dots in Figure 3.2). Figure 3.2A shows that T1M-2 was predicted to form 22% complexes with Rs. However, T2Ms and T3M were predicted to form only 0.3% complex with Rs (Figures 3.2B and 3.2C). All motif types were estimated to complex 100% with Rs+miR27a (orange dots in Figure 3.2). These predictions indicated that the new motifs would form stable complexes with three inputs but not with two inputs. Therefore, the predicted molarity percentage results supported our hypothesis that changing the inputs' complementary sequence locations in new motif types would improve motif's differentiating-input-number ability.

3.4.2 Experimental results of motif response and ability to differentiate input number

We compared the three motifs types' ability to stay OFF in the presence of two inputs, and turn ON with the addition of three inputs based on the experimental R/G ratios. 10% Native polyacrylamide gel electrophoresis (PAGE) confirms motifs form complex with two and three inputs (see appendix Figure A2.1). A more sensitive fluorescence analysis was carried out and presents results in Figure 3.3. To establish a baseline R/G ratio and have a control for the OFF state, we measured a solution with an equivalent amount of uncomplexed R96 and R182 (black line in Figure 3.3). The baseline R/G ratio was 0.090 ± 0.001 AU (N=3) and used to inform if adding two inputs to the motifs would cause undesired responses.

Figure 3.3A shows compared to the baseline R/G ratio, adding R96 and R182 to T1Ms, T2Ms, and T3M increased the average R/G ratios by factors of about 2.7, 1.8, and 1.8, respectively

(relative standard deviations ranging from 1.1 to 2.5%, $p < 0.025$). The smaller change in R/G ratio for T2Ms and T3Mt than T1Ms was evidence that the new motifs mitigated undesired responses from two inputs.

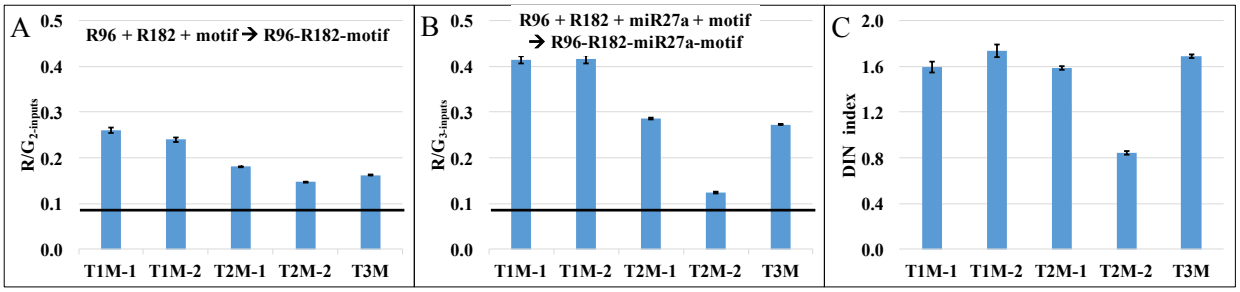

Figure 3.3 Signal change and differentiating-input-number index from three motif types. The motifs' signal change in the presence of two inputs of R96 and R182 (N=3, A) and three inputs of R96, R182, and miR27s (N=3, B)). (C) The differentiating-input-number (DIN) index of three inputs against two inputs for each motif (N=3). In some graphs the error bars are too small to be seen.

To establish the ON state signal ratio, we measured the R/G ratio of each motif type after adding three inputs. Figure 3.3B shows that in the presence of three inputs, the average R/G ratios of T1Ms, T2Ms, and T3Ms increased respectively by factors of about 4.6, 2.3, and 3.0 compared to the baseline R/G ratio (relative standard deviations ranged from 1.1 to 2.3%, $p < 0.025$). The new motifs' smaller R/G ratios upon adding three inputs suggested that new motifs were not as responsive as T1Ms to three inputs.

To evaluate motifs' response towards three versus two inputs, we calculated a differentiating-input-number index (DIN index) from the data in Figure 3.3A and 3.3B. We plotted the DIN index in Figure 3.3C and found no statistical difference in the DIN index among T1Ms, T2M-1, and T3M ($p < 0.025$). As seen in Figure 3.3, even though new motif types' response toward two inputs was lower than T1Ms, their response to three inputs were not as high as T1Ms. As a result, all motifs showed similar DIN index, except T2M-2, in disagreement with the theoretical prediction.

3.4.3 The relationship between the experimental results and theoretical prediction

The lower R/G ratio from the new motif types in the presence of two reporters met the theoretical prediction. However, the new motifs reduced signal change towards three inputs and comparable DIN index disagreed with the theoretical prediction.

The fact that the smaller R/G ratio from new motifs reacting with two reporters implies that a complex between the new motifs and two reporters was harder to form than predicted.

However, the same can be applied to three inputs, in disagreement with predictions. To further study the gap between the experimental results and theoretical prediction, we considered other predictive thermodynamic-related metrics including: (1) the number of H-bonds, (2) the thermodynamic values (Gibbs energy and melting point) of the motif as either a multi-hairpin or homodimer, and (3) the change in Gibbs energy from the reaction of the motif with two or three inputs. These predicted data from the thermodynamic-related metrics suggested the critical role the homodimer plays to diminish the new motifs' response to inputs.

The effect of H-bonds on the motif stability was discussed in the previous section and in appendix section A2.1. Due to the increased number of H-bonds formed in the motif stems, new motifs were predicted to be more structurally stable than T1Ms. As expected, there was a decrease in the motif's response to two inputs. However, we did not expect the increased stability would affect motif's interaction with three inputs. Instead, we expected the presence of three inputs to destabilize the motifs through the collective interactions between each input and its corresponding binding locations. In particular, the miR27a's complementary sequence was strategically placed to destabilize the whole motif upon miR27a binding and overcome the increased stability. The decreased signal suggested that a small increase in H-bonds likely contributed a lot to the structural stability of the new motifs leading to lower accessibility to either two or three inputs. Other reasons for the low signal change might be explained by the stability difference between the multi-hairpins and homodimers of each motif. Such stability difference was evaluated from the predictive analysis of the molarity percentage and thermodynamic values.

The molarity percentage analysis from DINAMelt suggested that the new motif types would be better at differentiating input numbers than T1Ms (Figure 3.2). However, the prediction from the molarity percentage analysis did not exactly match with the experimental results (see Figure 3.2 and 3.3). The experimental result shows T2Ms' and T3M's R/G ratio to three inputs was statistically lower ($p < 0.025$) than T1Ms (Figure 3.3B). However, the molarity percentage analysis predicted that all motif types would form complex with three inputs. The disagreement likely resulted from the limitations of DINAMelt. As discussed earlier, the sequence of multiple oligonucleotide-inputs had to be concatenated *in silico* (appendix section A2.2) to predict the molarity percentage of a motif form a complex with multiple inputs. Such treatment overestimated the cumulative number of H-bonds and pi-stacking resulting in falsely estimating the stability of

formed complex. Therefore, this limitation was considered as one of the causes leading to the inaccurate molarity percentage prediction.

Another predicative online tool, NUPACK, its molarity percentage prediction of motif-inputs complexes agreed better with the experiment (Table 3.1). NUPACK allows the analysis of more than two oligonucleotides. The predicted molarity percentages from NUPACK were much smaller than from DINAMelt. The data shown in the Table 3.1 suggests that the molarity percentage predicted from NUPACK mostly agrees with the motifs' signal response to inputs (Figure 3.3). For example, the higher predicted molarity percentage of T1M with R96-R182-miR27a (5.3 - 5.4%) than R96-R182 (0.15 - 0.65%) matched with the experimental results that T1Ms responded more to three inputs than to two inputs. The lower predicted molarity percentage of new motif-two inputs complex agreed with the experimental results that new motifs responded less to two reporters than T1Ms. However, the highest molarity percentage of (T2M-1)-R96-R182-miR27a (5.9%) did not agree with T2M-1's lower R/G ratio for three inputs demonstrating the gap between the theoretical and experimental results.

Table 3.1 NUPACK molarity percentage analysis of three motif types forming complex with either two reporters or two reporters and miR27a.

Complex	Motif-R96-R182	Motif-R96-R182-miR27a
T1M-1	0.65%	5.4%
T1M-2	0.15%	5.3%
T2M-1	0.00%	5.9%
T2M-2	0.00%	0.00%
T3M	0.00%	0.36%

* See A2.2 for details on the analysis.

Although NUPACK's prediction did not completely agree with the experimental results, we found that NUPACK was still better at predicting the molarity percentages between multiple oligonucleotides. The most likely reason was that both NUPACK and DINAMelt do not predict homodimers as part of molarity percentages analysis.

The existence of the homodimers was another probable cause for the lower R/G ratio in the presence of either two or three inputs. If forming the homodimer was more favorable, then fewer multi-hairpin motifs would be available to perform molecular logic. The stabilities of a homodimer and a multi-hairpin were assessed through the Gibbs energy (ΔG) and melting temperature (T_m) prediction from DINAMelt. The predictive temperature was set at 37 ℃, the typical temperature for cellular analysis and for hybridizing the motif with the inputs (see SI

section 3). A structure was considered stable if (1) T_m was predicted to be higher than 37 ℃ and (2) ΔG was estimated to be negative.

Table 3.2 shows that the T_m of T1Ms's homodimers were below 37 °C and T_m of its multi-hairpins were over 37 °C, thus we expected T1Ms would form multi-hairpins preferentially. Different from T1Ms, although new motifs' multi-hairpins have T_m predicted higher than 37 °C, the T_m of their homodimers were also higher than 37 °C. These predicted T_m of new motifs suggests that new motifs formed an appreciable amount of both the homodimers and multi-hairpins thus existed as a mixture. 10% Native PAGE confirms more homodimers were formed in new motifs than in T1Ms (appendix Figure A2.1). Because of only considering the multi-hairpin formation, the predictive tools did not accurately predict the molarity percentage of the new motifs complexing with inputs.

Table 3.2 The melting point of motifs as multi-hairpins or homodimers

	T_m of motif as multi-hairpins (℃)	T_m of motif as homodimers (℃)
T1M-1	56.8	33.6
T1M-2	58.7	36.6
T2M-1	62.0	44.5
T2M-2	63.9	50.3
T3M	64.2	47.7

Table 3.3 The Gibbs energy of motifs as multi-hairpins or homodimers

	ΔG of motif as multi-hairpins	ΔG of motif as homodimers
T1M-1	-10.16 kcal/mol	-8.70 kcal/mol
T1M-2	-12.15 kcal/mol	-9.80 kcal/mol
T2M-1	-14.96 kcal/mol	-16.40 kcal/mol
T2M-2	-15.32 kcal/mol	-21.70 kcal/mol
T3M	-16.37 kcal/mol	-21.00 kcal/mol

Table 3.3 shows that ΔG of T1Ms' multi-hairpins were more negative than T1Ms' homodimers by around 2 kcal/mol. In contrast, ΔG of new motifs' homodimers were more negative than multi-hairpins by 0.6 to 6.38 kcal/mol. Table 3.3 shows that ΔG of new motifs' homodimers were more negative than T1Ms' homodimers by around 8 to 11 kcal/mol. Combining with the native PAGE results (appendix Figure A2.1), these predictions suggest that (1) T1Ms' multi-hairpins were more favorably formed than T1Ms' homodimers and (2) new motifs' homodimers were more favorably formed than T1Ms' homodimers. Therefore, T1Ms most likely existed with a majority of the motifs in multi-hairpin structure and were able to perform molecular

logic. The new motifs existed as a mixture of both homodimers and multi-hairpins and had more homodimers than T1Ms had. As seen experimentally (Figure 3.3, above), such a mixture would lower the ability of new motifs to respond to either two or three inputs. For example, T2M-2 with the highest T_m and most negative ΔG of homodimers showed the lowest R/G ratio to either two or three inputs. Such a conclusion is further supported by our previous work showing that homodimers between reporter hairpins lead to similar difficulties in having a functional sensor.[52]

To further study how multi-hairpins and homodimers affect the motifs' reaction favorability and R/G ratios, we predicted the (1) Gibbs energy (ΔG) of the motif complexing with the concatenated two or three inputs, and (2) Gibbs energy change (ddG) of the motif reacting with the concatenated two or three inputs (Figure 3.4). Figure 3.4A shows that complexes formed by each motif bound to two reporters (motif-R96-R182) had similar negative ΔG around -23 kcal/mol. Each motif forming a complex with three inputs (motif-R96-R182-miR27a) were predicted to have a negative ΔG around -43 kcal/mol. The ΔG of each motif-R96-R182-miR27a was more negative than that of motif-R96-R182 by around -20 kcal/mol. The more negative ΔG of motif-R96-R182-miR27a provide evidence to explain why all motifs had larger R/G ratios for three versus two inputs.

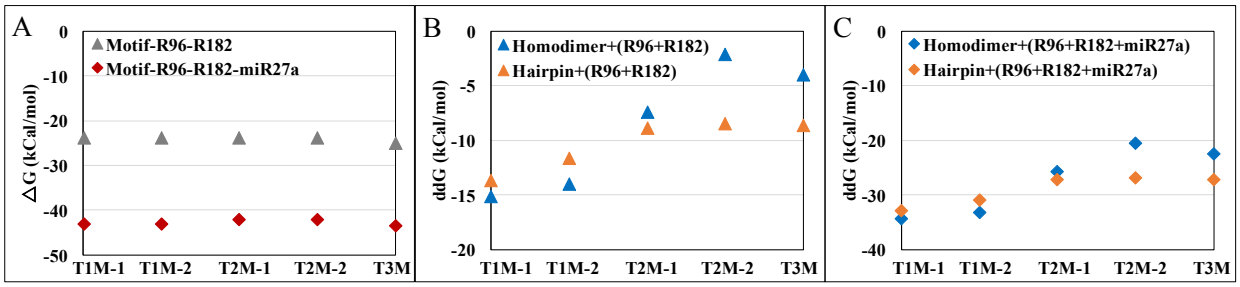

Figure 3.4 Predicted Gibbs energy (ΔG) and Gibbs energy change (ddG) of motifs complexing with inputs. (A) ΔG of motif complexing with concatenated two inputs (R96 and R182, gray triangle), and concatenated three inputs (R96, R182, and miR27a, red diamond). ddG from motif reacting with (B) R96 and R182, and (C) R96, R182, and miR27a. For (B) and (C), the blue points represent the motif starting in the homodimer. Similarly, the orange points represent the multi-hairpin. Since these are predicted values there are no error bars.

Figure 3.4B shows the ddG from the biophysical interaction of R96 and R182 with the motif as homodimers (Homodimer+two-inputs) and multi-hairpins (Hairpin+two-inputs). More negative ddG indicated a more favorable reaction. As seen in Figure 3.4B, two inputs reacting with T1Ms demonstrated more negative ddG than with the new motifs in either form (multi-hairpins or homodimers). The more positive ddG from new motifs' homodimers reacting with two inputs indicated that Homodimer+two-inputs reaction was less favorable than the Hairpin+two-inputs

reaction. The existence of new motifs in the homodimers form (previous T_m and ΔG discussion) and the low favorability of new motifs' homodimers reacting with two inputs are plausible reasons why the new motifs had a lower R/G ratio from two inputs compared to T1Ms.

Figure 3.4C shows the ddG from the reaction of R96, R182, and miR27a with a motif as homodimers (Homodimer+three-inputs) and multi-hairpins (Hairpin+three-inputs). T1Ms as either multi-hairpins or homodimers showed the most negative ddG (-31 kcal/mol) from reacting with three inputs thus suggesting the most reaction favorability. New motifs' homodimers were predicted to have less favorability to react with three inputs than their multi-hairpins due to the more positive ddG. Among all new motifs, T2M-2 was estimated to be the least favorable to react with inputs since the most positive ddG of Homodimer+two-inputs and Homodimer+three-inputs reactions. Such prediction matched with T2M-2's lowest R/G ratio from two or three inputs in Figure 3.3. Considering the discussed T_m, ΔG, and ddG, the reaction of the new motifs with either two or three inputs was predicted to be less favorable as seen experimentally the lower R/G ratio. These results show that the lower favorability of new motifs' homodimers reacting with three inputs contributed to the observed lower R/G ratio.

From our analysis of the theory and experiment, we have learned it is critical to collectively consider the following design metrics in order to create functional molecular logic. Important design metrics for DNA-based sensors are: (1) the number of H-bonds formed in each hairpin and double-stranded regions, (2) NUPACK-based molarity percentage analysis, and (3) DINAMelt-predicted thermodynamic-related parameters (T_m, ΔG, and ddG).

Since T1Ms' had the largest R/G ratios and comparable DIN indexes to the new motifs, we established boundary values for the design metrics based on T1Ms' predicted data. A boundary value for molarity percentage ratio (MPR) was 10 and calculated by dividing the NUPACK molarity percentage of T1M-R96-R182-miR27a by that of T1M-R96-R182 (Table 3.1). A motif with larger MPR (10) is expected to show a higher DIN index.

For a motif preferentially forming multi-hairpins, homodimers' T_m should be lower than 37 °C and multi-hairpin's T_m over 37 °C. Based on the theory, T1Ms' multi-hairpins were expected to form preferentially because the predicted T_m of homodimers were lower than multi-hairpins; and the Gibbs energy of the multi-hairpins were averagely 2 kcal/mol more negative than homodimers (Table 3.3). Thus, a difference in ΔG of 2 kcal/mol was set as boundary value for predicting multi-hairpins and homodimers formation. ΔG of all motif-R96-R182-miR27a

complexes was found to be 20 kcal/mol more negative than motif-R96-R182 complexes, indicating the more stable motif-R96-R182-miR27a complexes (Figure 3.4A). Thus, in order to form a more stable motif-R96-R182-miR27a complex, the boundary value of ΔG difference was set at 20 kcal/mol. ddG of T1Ms' multi-hairpins reacting with three inputs was around 20 kcal/mol more negative than with two inputs (Figure 3.3B and 3.3C). Thus, the boundary value for the ddG difference was set to 20 kcal/mol. Although H-bonds were important for stability, the data was not conclusive to how many H-bonds lead to adequate stability, thus no boundary values were reported.

Here we summarize the predicted numerical values a molecular logic biosensor should satisfy to strictly function AND logic:

(1) $\frac{\text{NUPACK−based molarity percentage (motif−3 inputs complex)}}{\text{NUPACK−based molarity percentage (motif−2 inputs complex)}} > 10$

(2) T_m (Motif as homodimer) <37 °C < T_m (Motif as multi-hairpin)

(3) ΔG (Motif as multi-hairpin) $-$ ΔG (Motif as homodimer) < -2 kcal/mol

(4) ΔG (motif-3 inputs complex) $-$ ΔG (motif-2 inputs complex) < -20 kcal/mol

(5) ddG (Multi-hairpin + three inputs reaction) $-$ ddG (Multi-hairpin + two inputs reaction) < -20 kcal/mol

3.5 Conclusion

We expect our findings will contribute to filling the gap between theory and experiment. In doing so we expect to help guide and advance future single-/multi-hairpin-structure-based logic sensor design. Fully considering the structural and thermodynamic metrics helps to achieve more accurate interpretation of the estimated results and pushes forward the design process of nucleic-acid-based logic sensors. However, trial and error is still required to fine-tune molecular logic's nanostructural features and improve the DIN index. As the molecular logic field progresses, we envision an algorithm that can synthesize design metrics and boundary values established by this and other works. Such an algorithm will benefit future studies by identifying ideal predictive metrics to inform on design for DNA-based sensor.

To understand the interplay between molecules in complex systems, molecular logic devices that operate strictly as designed for will be powerful tools. In this work, strict AND logic means only response to a certain number of inputs (here 3), but not to any other number of inputs (here 2). In the future, we plan to apply the multi-hairpin motif as a subunit to build larger nano-

structures to accommodate even more biological inputs. More broadly, the design strategy and parameters will be vital to create other types of nanoscale logic systems (*e.g.* OR, NOR, and NAND). Future work will demonstrate the feasibility of our molecular logic sensor designs to work in cells to revolutionize the amount and accuracy of information gained to better understand biology in general.

3.6 Acknowledgements

We would like to thank Oregon State University for supporting this research.

3.7 References

(1) Zhang, D. Y.; Seelig, G. Dynamic DNA Nanotechnology Using Strand-Displacement Reactions. *Nat. Chem.* **2011**, *3* (2), 103–113.
(2) Chen, Y.-J.; Groves, B.; Muscat, R. A.; Seelig, G. DNA Nanotechnology from the Test Tube to the Cell. *Nat. Nanotechnol.* **2015**, *10* (9), 748–760.
(3) Goodman, R. P.; Heilemann, M.; Doose, S.; Erben, C. M.; Kapanidis, A. N.; Turberfield, A. J. Reconfigurable, Braced, Three-Dimensional DNA Nanostructures. *Nat. Nanotechnol.* **2008**, *3* (2), 93–96.
(4) Lu, Y.; Liu, J. Functional DNA Nanotechnology: Emerging Applications of DNAzymes and Aptamers. *Curr. Opin. Biotechnol.* **2006**, *17* (6), 580–588.
(5) Pinheiro, A. V.; Han, D.; Shih, W. M.; Yan, H. Challenges and Opportunities for Structural DNA Nanotechnology. *Nat. Nanotechnol.* **2011**, *6* (12), 763–772.
(6) Qian, L.; Winfree, E.; Bruck, J. Neural Network Computation with DNA Strand Displacement Cascades. *Nature* **2011**, *475* (7356), 368–372.
(7) Zhang, F.; Nangreave, J.; Liu, Y.; Yan, H. Structural DNA Nanotechnology: State of the Art and Future Perspective. *J. Am. Chem. Soc.* **2014**, *136* (32), 11198–11211.
(8) Chen, X.; Ellington, A. D. Shaping up Nucleic Acid Computation. *Curr. Opin. Biotechnol.* **2010**, *21* (4), 392–400.
(9) Teichmann, M.; Kopperger, E.; Simmel, F. C. Robustness of Localized DNA Strand Displacement Cascades. *ACS Nano* **2014**, *8* (8), 8487–8496.
(10) Phillips, A.; Cardelli, L. A Programming Language for Composable DNA Circuits. *J. R. Soc. Interface* **2009**, *6* (Suppl_4), S419–S436.
(11) Zhu, J.; Zhang, L.; Li, T.; Dong, S.; Wang, E. Enzyme-Free Unlabeled DNA Logic Circuits Based on Toehold-Mediated Strand Displacement and Split G-Quadruplex Enhanced Fluorescence. *Adv. Mater.* **2013**, *25* (17), 2440–2444.
(12) Srinivas, N.; Ouldridge, T. E.; Sulc, P.; Schaeffer, J. M.; Yurke, B.; Louis, A. A.; Doye, J. P. K.; Winfree, E. On the Biophysics and Kinetics of Toehold-Mediated DNA Strand Displacement. *Nucleic Acids Res.* **2013**, *41* (22), 10641–10658.
(13) Zhang, D. Y.; Winfree, E. Control of DNA Strand Displacement Kinetics Using Toehold Exchange. *J AM CHEM SOC* **2009**, *131*, 17303–17314.
(14) Lu, J.; Getz, G.; Miska, E. A.; Alvarez-Saavedra, E.; Lamb, J.; Peck, D.; Sweet-Cordero, A.; Ebert, B. L.; Mak, R. H.; Ferrando, A. A.; et al. MicroRNA Expression Profiles Classify Human Cancers. *Nature* **2005**, *435* (7043), 834–838.
(15) Esteller, M. Non-Coding RNAs in Human Disease. *Nat. Rev. Genet.* **2011**, *12*, 861.
(16) Sassen, S.; Miska, E. A.; Caldas, C. MicroRNA—Implications for Cancer. *Virchows Arch.* **2008**, *452* (1), 1–10.
(17) Kantharidis, P.; Wang, B.; Carew, R. M.; Lan, H. Y. Diabetes Complications: The MicroRNA Perspective. *Diabetes* **2011**, *60* (7), 1832–1837.
(18) Romaine, S. P. R.; Tomaszewski, M.; Condorelli, G.; Samani, N. J. MicroRNAs in Cardiovascular Disease: An Introduction for Clinicians. *Heart* **2015**, *101* (12), 921–928.

(19) Jabri, E. Non-Coding RNA: Small, but in Control. *Nat. Rev. Mol. Cell Biol.* **2005**, *6*, 361.
(20) Picuri, J. M.; Frezza, B. M.; Ghadiri, M. R. Universal Translators for Nucleic Acid Diagnosis. *J. Am. Chem. Soc.* **2009**, *131* (26), 9368–9377.
(21) He, H.-Z.; Chan, D. S.-H.; Leung, C.-H.; Ma, D.-L. G-Quadruplexes for Luminescent Sensing and Logic Gates. *Nucleic Acids Res.* **2013**, *41* (8), 4345–4359.
(22) Fan, D.; Zhu, J.; Zhai, Q.; Wang, E.; Dong, S. Cascade DNA Logic Device Programmed Ratiometric DNA Analysis and Logic Devices Based on a Fluorescent Dual-Signal Probe of a G-Quadruplex DNAzyme. *Chem Commun* **2016**, *52* (19), 3766–3769.
(23) Bloomston, M.; Frankel, W. L.; Petrocca, F.; Volinia, S.; Alder, H.; Hagan, J. P.; Liu, C.-G.; Bhatt, D.; Taccioli, C.; Croce, C. M. MicroRNA Expression Patterns to Differentiate Pancreatic Adenocarcinoma from Normal Pancreas and Chronic Pancreatitis. *Jama* **2007**, *297* (17), 1901–1908.
(24) Kulshreshtha, R.; Ferracin, M.; Wojcik, S. E.; Garzon, R.; Alder, H.; Agosto-Perez, F. J.; Davuluri, R.; Liu, C.-G.; Croce, C. M.; Negrini, M.; et al. A MicroRNA Signature of Hypoxia. *Mol. Cell. Biol.* **2007**, *27* (5), 1859–1867.
(25) Sempere, L. F.; Christensen, M.; Silahtaroglu, A.; Bak, M.; Heath, C. V.; Schwartz, G.; Wells, W.; Kauppinen, S.; Cole, C. N. Altered MicroRNA Expression Confined to Specific Epithelial Cell Subpopulations in Breast Cancer. *Cancer Res.* **2007**, *67* (24), 11612–11620.
(26) Place, R. F.; Li, L.-C.; Pookot, D.; Noonan, E. J.; Dahiya, R. MicroRNA-373 Induces Expression of Genes with Complementary Promoter Sequences. *Proc. Natl. Acad. Sci.* **2008**, *105* (5), 1608–1613.
(27) Tavazoie, S. F.; Alarcón, C.; Oskarsson, T.; Padua, D.; Wang, Q.; Bos, P. D.; Gerald, W. L.; Massagué, J. Endogenous Human MicroRNAs That Suppress Breast Cancer Metastasis. *Nature* **2008**, *451* (7175), 147–152.
(28) Avissar, M.; Christensen, B. C.; Kelsey, K. T.; Marsit, C. J. MicroRNA Expression Ratio Is Predictive of Head and Neck Squamous Cell Carcinoma. *Clin. Cancer Res.* **2009**, *15* (8), 2850–2855.
(29) Chen, H.-C.; Chen, G.-H.; Chen, Y.-H.; Liao, W.-L.; Liu, C.-Y.; Chang, K.-P.; Chang, Y.-S.; Chen, S.-J. MicroRNA Deregulation and Pathway Alterations in Nasopharyngeal Carcinoma. *Br. J. Cancer* **2009**, *100* (6), 1002–1011.
(30) Croce, C. M. Causes and Consequences of MicroRNA Dysregulation in Cancer. *Nat. Rev. Genet.* **2009**, *10* (10), 704–714.
(31) Shenouda, S. K.; Alahari, S. K. MicroRNA Function in Cancer: Oncogene or a Tumor Suppressor? *Cancer Metastasis Rev.* **2009**, *28* (3–4), 369–378.
(32) Chen, Z.; Li, Y.; Huang, P.; Luthra, R. Hypoxia-Regulated MicroRNA-210 Modulates Mitochondrial Function and Decreases ISCU and COX10 Expression. *Oncogene* **2010**, *29*, 4362–4368.
(33) Krutilina, R.; Sun, W.; Sethuraman, A.; Brown, M.; Seagroves, T. N.; Pfeffer, L. M.; Ignatova, T.; Fan, M. MicroRNA-18a Inhibits Hypoxia-Inducible Factor 1α Activity and Lung Metastasis in Basal Breast Cancers. *Breast Cancer Res.* **2014**, *16* (4), 1.
(34) Qin, X.; Wang, X.; Wang, Y.; Tang, Z.; Cui, Q.; Xi, J.; J. Li, Y.-S.; Chien, S.; Wang, N. MicroRNA-19a Mediates the Suppressive Effect of Laminar Flow on Cyclin D1 Expression in Human Umbilical Vein Endothelial Cells. *Proc. Natl. Acad. Sci.* **2010**, *107* (7), 3240–3244.
(35) Lai, N.; Dong, Q.; Ding, H.; Miao, Z.; Lin, Y. MicroRNA-210 Overexpression Predicts Poorer Prognosis in Glioma Patients. *J. Clin. Neurosci.* **2014**, *21* (5), 755–760.
(36) Buck, A. H.; Campbell, C. J.; Dickinson, P.; Mountford, C. P.; Stoquert, H. C.; Terry, J. G.; Evans, S. A. G.; Keane, L. M.; Su, T.-J.; Mount, A. R.; et al. DNA Nanoswitch as a Biosensor. *Anal. Chem.* **2007**, *79* (12), 4724–4728.
(37) Lubrich, D.; Lin, J.; Yan, J. A Contractile DNA Machine. *Angew. Chem. Int. Ed.* **2008**, *47* (37), 7026–7028.
(38) Hemphill, J.; Deiters, A. DNA Computation in Mammalian Cells: MicroRNA Logic Operations. *J. Am. Chem. Soc.* **2013**, *135* (28), 10512–10518.
(39) Larkey, N. E.; Almlie, C. K.; Tran, V.; Egan, M.; Burrows, S. M. Detection of MiRNA Using a Double-Strand Displacement Biosensor with a Self-Complementary Fluorescent Reporter. *Anal. Chem.* **2014**, *86* (3), 1853–1863.
(40) Almlie, C. K.; Larkey, N. E.; Burrows, S. M. Fluorescent MicroRNA Biosensors: A Comparison of Signal Generation to Quenching. *Anal Methods* **2015**, *7* (17), 7296–7310.
(41) Cheglakov, Z.; Cronin, T. M.; He, C.; Weizmann, Y. Live Cell MicroRNA Imaging Using Cascade Hybridization Reaction. *J. Am. Chem. Soc.* **2015**, *137* (19), 6116–6119.

(42) Wu, P.; Tu, Y.; Qian, Y.; Zhang, H.; Cai, C. DNA Strand-Displacement-Induced Fluorescence Enhancement for Highly Sensitive and Selective Assay of Multiple MicroRNA in Cancer Cells. *Chem Commun* **2014**, *50* (8), 1012–1014.

(43) Deng, R.; Tang, L.; Tian, Q.; Wang, Y.; Lin, L.; Li, J. Toehold-Initiated Rolling Circle Amplification for Visualizing Individual MicroRNAs In Situ in Single Cells. *Angew. Chem. Int. Ed.* **2014**, *53* (9), 2389–2393.

(44) Seelig, G.; Soloveichik, D.; Zhang, D. Y.; Winfree, E. Enzyme-Free Nucleic Acid Logic Circuits. *Science* **2006**, *314* (5805), 1585–1588.

(45) Li, W.; Yang, Y.; Yan, H.; Liu, Y. Three-Input Majority Logic Gate and Multiple Input Logic Circuit Based on DNA Strand Displacement. *Nano Lett.* **2013**, *13* (6), 2980–2988.

(46) Tyagi, S.; Kramer, F. R. Molecular Beacons: Probes That Fluoresce upon Hybridization. *Nat. Biotechnol.* **1996**, *14*, 303–306.

(47) Marras, S. A.; Kramer, F. R.; Tyagi, S. Efficiencies of Fluorescence Resonance Energy Transfer and Contact-Mediated Quenching in Oligonucleotide Probes. *Nucleic Acids Res.* **2002**, *30* (21), e122–e122.

(48) Vaisocherová, H.; Šípová, H.; Víšová, I.; Bocková, M.; Špringer, T.; Laura Ermini, M.; Song, X.; Krejčík, Z.; Chrastinová, L.; Pastva, O.; et al. Rapid and Sensitive Detection of Multiple MicroRNAs in Cell Lysate by Low-Fouling Surface Plasmon Resonance Biosensor. *Biosens. Bioelectron.* **2015**, *70*, 226–231.

(49) He, K.; Liao, R.; Cai, C.; Liang, C.; Liu, C.; Chen, X. Y-Shaped Probe for Convenient and Label-Free Detection of MicroRNA-21 in Vitro. *Anal. Biochem.* **2016**, *499*, 8–14.

(50) Yang, W.-J.; Li, X.-B.; Li, Y.-Y.; Zhao, L.-F.; He, W.-L.; Gao, Y.-Q.; Wan, Y.-J.; Xia, W.; Chen, T.; Zheng, H.; et al. Quantification of MicroRNA by Gold Nanoparticle Probes. *Anal. Biochem.* **2008**, *376* (2), 183–188.

(51) Ding, X.; Yan, Y.; Li, S.; Zhang, Y.; Cheng, W.; Cheng, Q.; Ding, S. Surface Plasmon Resonance Biosensor for Highly Sensitive Detection of MicroRNA Based on DNA Super-Sandwich Assemblies and Streptavidin Signal Amplification. *Anal. Chim. Acta* **2015**, *874*, 59–65.

(52) Larkey, N. E.; Brucks, C. N.; Lansing, S. S.; Le, S. D.; Smith, N. M.; Tran, V.; Zhang, L.; Burrows, S. M. Molecular Structure and Thermodynamic Predictions to Create Highly Sensitive MicroRNA Biosensors. *Anal. Chim. Acta* **2016**, *909*, 109–120.

(53) Dirks, R. M. Paradigms for Computational Nucleic Acid Design. *Nucleic Acids Res.* **2004**, *32* (4), 1392–1403.

(54) Dirks, R. M.; Bois, J. S.; Schaeffer, J. M.; Winfree, E.; Pierce, N. A. Thermodynamic Analysis of Interacting Nucleic Acid Strands. *SIAM Rev.* **2007**, *49* (1), 65–88.

(55) Zhang, L.; Bluhm, A. M.; Chen, K.-J.; Larkey, N. E.; Burrows, S. M. Performance of Nano-Assembly Logic Gates with a DNA Multi-Hairpin Motif. *Nanoscale* **2017**, *9* (4), 1709–1720.

(56) Markham, N. R.; Zuker, M. DINAMelt Web Server for Nucleic Acid Melting Prediction. *Nucleic Acids Res.* **2005**, *33* (Web Server), W577–W581.

(57) Markham, N. R.; Zuker, M. *UNAFold: Software for Nucleic Acid Folding and Hybridization*; Humana Press, Totowa, NJ; Vol. II.

(58) Zadeh, J. N.; Steenberg, C. D.; Bois, J. S.; Wolfe, B. R.; Pierce, M. B.; Khan, A. R.; Dirks, R. M.; Pierce, N. A. NUPACK: Analysis and Design of Nucleic Acid Systems. *J. Comput. Chem.* **2011**, *32* (1), 170–173.

(59) Larkey, N. E.; Zhang, L.; Lansing, S. S.; Tran, V.; Seewaldt, V. L.; Burrows, S. M. Förster Resonance Energy Transfer to Impart Signal-on and -off Capabilities in a Single MicroRNA Biosensor. *The Analyst* **2016**, *141* (22), 6239–6250.

Chapter 4.

Molecular logic nanosensor with cascading-toeholds for error-robust small RNA combinatorial analysis

Lulu Zhang, Susmitha Matlapudi, Annie M. Bluhm, and Sean M. Burrows

Manuscript in preparation for publication

4.1 Abstract

Two types of implicit measurement errors associated with intracellular multiplexing analysis of biomolecules are: (1) distinguishing between a complete and an incomplete combinations of biomolecules, and (2) difficulty in delivering equivalent amounts of each subunit from a sensing device into a biological system. To address these implicit measurement errors, we introduce an innovative DNA-based molecular logic nanosensor called an autowalk AND logic operator (AALO). Groups of small non-coding RNAs were selected as the model system to assess the sensing value of AALO. AALO is assembled to be a single-entity nanosensor in order to address the issue of unequal delivery of subunits. To better differentiate a complete from an incomplete combinations of biomolecules, AALO relies on a cascading toehold-initiated strand displacement reactions to inhibit recognition process until all analyte biomolecules are present. We will show how AALO's design impacts the dynamic range, sensing ability, and differentiating-input-number ability. The findings include: (1) nanomolar-range detection limit, (2) selectivity against off-analyte miRs with up to 95 % sequence similarity to analyte miRs, and (3) improved differentiating-input-number ability by 30 % compared to our previously published three-input logic design.

4.2 Introduction

Nucleic acids are regarded as natural building blocks that enable the construction of programmable logic devices[1–10] for computing chemical and molecular patterns in a sample. An exciting area for intracellular molecular pattern analysis that biologists are becoming interested in are microRNAs[11–15]. MicroRNAs (miRs) are a class of small non-coding RNA with approximately 22 nucleotides in length.[16,17] Multiple miRs have been found to work in groups regulating gene expression transcriptionally and post-transcriptionally in both healthy and diseased cells.[18–21] The fluctuations of miR expression levels and changes in miR patterns are observed numerous cellular processes, such as cell divisions and differentiation.[20,22–25] The ability to track such change will help reveal the biological roles of miRs might play in these cellular processes. In this work, we are interested in a combination of miR27a, miR24, and miR210 as a model system. We chose these miR because their expression levels were found to be increased by two to four times in MCF-7 cells after incubating in a hypoxic environment for 48 hours.[26]

In order to achieve multiplexed detection of unique miR combinations, a DNA-based logic

device capable of performing AND logic is desired. DNA-based logic devices recognize analtyes through predictable Watson-Crick base pairing interaction.[27] AND logic sensors usually consists of a gate strand and an output strand. The gate strand is designed to be more complementary to inputs than to outputs.[28] The recognition mechanism typically relies on toehold-mediated strand displacement reaction (TMSDR).[29–33] Strand displacement is the process of a incoming strand displacing a pre-bound strand. A toehold is a short sequence (~ 3-6 nucleotides long) in the GS that initiates binding of the incoming strand.

In a majority of logic designs for imaging or measurement science, the gate strand is labeled with a quencher. The output strands typically are labeled with a fluorescent dye to indicate binding events.[11] In the absence of inputs, output strands bind to the gate making the fluorophore close to quencher thus quenching the fluorescent signal. In the presence of inputs, a strand displacement reaction dislodges the output from the gate.[34,35] As the output (with a fluorescent dye) moves away from the quencher the fluorescent signal increases. However, logic devices relying on quencher-fluorophore disruption as the transduction mechanism are susceptible to false signals in most biological study.[36] False signals arise because endogenous nucleases in cells degrade the logic devices such that the fluorophore-quencher pair get separated causing the signal to increase[37,38,36]

Another limitation of current logic devices is the low input-to-output ratio. To the best of our knowledge, most logic devices have low input-to-output ratio ranging from one-to-one to two-to-one.[39,40] Logic devices with higher input-to-output ratio is desired in order to improve the sensing capability to detect more inputs.

Our previous work presented a nano-assembly logic gate (NALG) that responded to three miR inputs with signal transduced through the Förster Resonance Energy Transfer (FRET).[41,42] However, NALG showed a noticeable signal response towards two miR inputs, thus lowering NALG's ability to accurately differentiate input numbers. Furthermore, the design of NALG comprised of three parts made it difficult to deliver the gate as a whole to cell or tissue samples.

Here, we demonstrate proof-of-principle for an innovative AND logic device called autowalk AND logic operator (AALO) that respond to three inputs: miR27a, miR24, and miR210. To sense this specific miR combination, AALO relies on a cascading toehold-mediated strand displacement reaction to generate an increased acceptor intensity. We will present on the sensitivity, selectivity, differentiating-input-number ability analysis of AALO, as well as the preliminary cellular imaging of AALO in HEK 293T cells.

4.3 Materials and Methods

4.3.1 Instrumentation for spectroscopy setup

The fluorescence spectra were collected with a custom-built fluorimeter described previously.[46] Two laser sources excited the samples: (1) a Titanium:Sapphire and (2) an Argon-ion laser. When applying the Titanium:Sapphire laser, samples were excited at 935 nm with an average power of 75 mW. We previously found this wavelength to give the highest FRET enhancement.[42] When applying the Argon-ion laser, samples were excited at 488 nm with average power of 0.100 μW. Emission spectra were collected with an Acton spectrometer (SP-2356, Princeton Instruments) paired with an electron-multiplied charge coupled device camera (512B-eXcelon3-EMCCD, Princeton Instruments). LightField software was used to acquire the emission spectra. The parameters used in the LightField were shown in the appendix A3.1.

4.3.2 Oligonucleotides and materials

All oligonucleotides were purchased from IDT (Integrated DNA Technologies, Inc., United States). The miR sequences were converted to DNA analogues because DNA is more stable against nuclease degradation. All oligonucleotides were diluted in a custom buffer (see appendix A3.2) and then hybridized at 37 °C. The design process of autowalk AND logic operator design process was shown in the appendix A3.3. the selection process of blocking strand was shown in A3.4 of the appendix. The experimental process of assembling autowalk AND logic operator was shown in the appendix A3.5.

4.3.3 Sensitivity study in crude MCF-7 cell lysate

A freeze–thaw protocol to lyse MCF-7 cells was adapted from Doyle et al.[43] and described in our previous publication.[42] To test the sensitiviey of AALO, aliquots of pre-assembled AALOs were added to micro-centrifuge tubes containing increasing amounts of all three analyte miRs in the crude MCF-7 cell lysate (1.2×10^7 cells/mL). Each tube was prepared to contain a final AALO concentration of 100 nM and all three miR analyte concentrations ranged from 0–100 nM.

4.3.4 Sequence similarities between analyte and off-analyte miRs

An online miR database (miRBase[57-59]) found off-analyte miRs (miR-27b-3p, miR-6804-5p, and miR-4921-5p) that respectively correspond with analyte inputs miR27a, miR210, and miR24. The approach to search for off-analyte miRs in miRBase was described in the appendix A3.6. The sequence similarity of off-analytes against analytes ranged from 41% to 95% (Table 4.1). As seen in the Table 4.1 the similar sequences are highlighted in red. We used those to count

the number of similar bases between analyte and off analyte. We then divided the number of similar bases by total number of bases in the strand to calculate the sequence similarity.

Table 4.1 The off-analyte miR sequences and their sequence similarity to the given analyte miRs. The nucleotides in red are mismatched nucleotides compared to the given analyte miR sequence.

Off-analyte name	Off-analyte miR sequences	Sequence similarity to analyte miRs
miR-6804-5p	5'-TGAGGGTGTCAGCAGGTGACG-3'	10/22= 45% similar to miR210
miR-4921-5p	5'-TTCAGCAGGAACAGCT-3'	14/22= 64% similar to miR24
miR-27b-3p	5'-TTCACAGTGGCTAAGTTCTGC-3'	20/21= 95% similar to miR7a

4.3.5 Cellular imaging of autowalk AND logic operator

HEK 293T cells were a generous gift from Dr. Siva Kolluri's lab at Oregon State University. A nucleofactor (Lonza) transfected the HEK 293T cells with the pre-hybridized forced "ON" AALOs (see A3.5 in the appendix for details on the nucleofaction process). The nucleofacted cells were fixed with 4% paraformaldehyde (Electron Microscopy Sciences) and imaged with an Axio Observer Z1 objective-type TIRF microscope (Zeiss). Details on the filter setting for the TIRF microscope are available in the appendix A3.5.

4.4 Results and discussion

4.4.1 Sensing mechanism of autowalk AND logic operator

Autowalk AND logic operator (AALO) is a single-entity nanosensor that consists of four single-stranded DNAs: one gate strand (GS), two reporters (R27a and R24) as output strands, and a blocking strand (BS). AALO can exist in either one of two states depending on where the two reporter strands bind along AALO's gate strand: (1) "OFF" state and (2) "ON" state. In the absence of any miR inputs, two reporters can bind to either the 5' end of GS leading to the donor-acceptor dye pair outside the FRET distance (low acceptor intensity), or the 3' end of GS resulting in the dye pair within the FRET distance (high acceptor intensity).

Since the two reporters can bind to either the 5' or 3' end of GS, we designed a blocking strand to keep AALO in the "OFF" state until all inputs are present. AALO's signal change with and without a blocking strand was shown in the appendix A3.8. BSs with different sequences bound to GS can form loops in GS. The toeholds for R24 and R27a can be located in these loops thus their accessibilities were constrained.

Only the presence of all three miR inputs are able to change AALO from "OFF" state to

"ON" state through a five-step toehold-mediated strand displacement reaction (TMSDR). The cascading TMSDRs only expose one toehold per reaction and trigger the following strand displacement reaction, therefore preventing acceptor signal increase due to the presence of only one or two inputs. AALO is designed to have only one exposed toehold (miR27a's toehold) that initiates the first TSMDR along the GS and subsequent displacement of R27a (Figure 4.1). First TSMDR not only frees R27a, but exposes miR24's hidden toehold to mediate the second TSMDR with miR24. Analogously, the interaction of GS with miR24 displaces R24 and reveals miR210's toehold to start the third TSMDR. After the third TSMDR from miR210's binding, BS is partially displaced from the GS. Consequently, the constrained toehold for R24 is made accessible to R24 to continue the fourth TSMDR. The fourth TSMDR allows R24 bind to the 3' end of GS further displaces BS to make R27a's toehold accessible for mediating R27a's binding. R27a's binding not only ultimately frees BS, but also brings the donor-acceptor dye pair within the FRET distance. Energy transfer from donor to the acceptor occurs when dyes are within the FRET distance leading to the increased acceptor intensity.

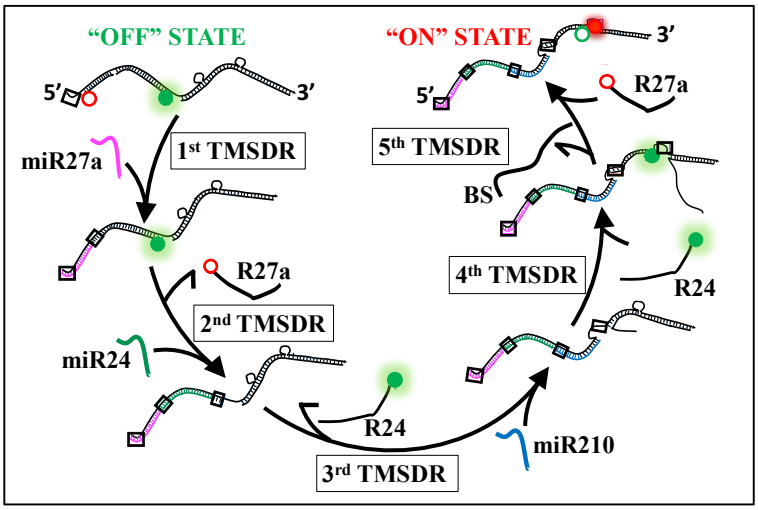

Figure 4.1 Sensing mechanism of autowalk AND logic operator to recognize a miR combination (miR27a, miR24, and miR210). The mechanism relies on a five-step toehold-mediated strand displacement reaction (TMSDR). Toeholds are indicated in the black boxes.

4.4.2 Signal metric determination to evaluate FRET event

To determine the signal metric to accurately evaluate FRET efficiency, we compared the donor and acceptor intensities from a two-reporter control, AALO's "OFF" and "ON" state. We established a control (Rs) containing the equivalent amounts of R24 and R27a for the "OFF" state. Figure 4.2A shows the donor intensity from Rs was statistically lower than AALO's "OFF" state

by a factor of around 0.8 ($p < 0.001$). There was no statistical difference between the acceptor intensity of Rs and AALO's "OFF" ($p < 0.025$) in Figure 4.2B.

Comparing the donor intensities of Rs and "OFF", we would conclude that FRET event occurred in Rs. However, the similar low acceptor intensity of Rs and "OFF" suggests that the FRET event did not occur in either Rs control or the "OFF" state. The conclusion based on acceptor intensity is considered reasonable and matches with our hypothesis that both donor and acceptor intensity of Rs and "OFF" were not statistically different. The hypothesis is made based on two facts: (1) R24 and R27a were mixed in Rs but there was no interaction between them to produce FRET, and (2) the donor and acceptor of the "OFF" were outside the FRET distance thus no FRET. In addition, the acceptor intensity was strictly controlled by the FRET distance, whereas the donor intensity can be influenced by many known and unknown factors, such as reporters' self intercalation leading to donor fluorescence quenching. Thus, we focused on the acceptor intensity as signal metric for the more accurate assessment of the FRET event.

What's more learned from Figure 4.2B is that the acceptor intensity of AALO's "ON" state was approximately five times higher than the "OFF" ($p < 0.001$). The increased acceptor intensity of the "ON" indicated that AALO was capable of sensing the presence of three miR inputs and induce FRET enhancement. To quantitatively compare the recognizing capability of different AALOs, we defined a new metric 'sensing window' that is the acceptor intensity difference of each AALO in its "OFF" (without the presence of any miR) and "ON" (with the addition of all three miRs) state (Equation 1):

$$\text{Sensing window} = I^{A}_{3\,miRs} - I^{A}_{0\,miRs} \qquad \text{Equation 1}$$

Where I^{A} is the acceptor intensity in general, $I^{A}_{0\,miRs}$ and $I^{A}_{3\,miRs}$ are the acceptor intensities for the addition of no miRs (0) and three miRs (3). In addition, we tested the effect of FRET distance and nucleotide types on FRET efficiency (details are in SI section A3.9). AALO with 7 adenine nucleotides as FRET distance showed the highest sensing window with ~70, 000 counts (details are in Appendix Figure A3.3). Therefore, 7 adenine nts was used for AALO design.

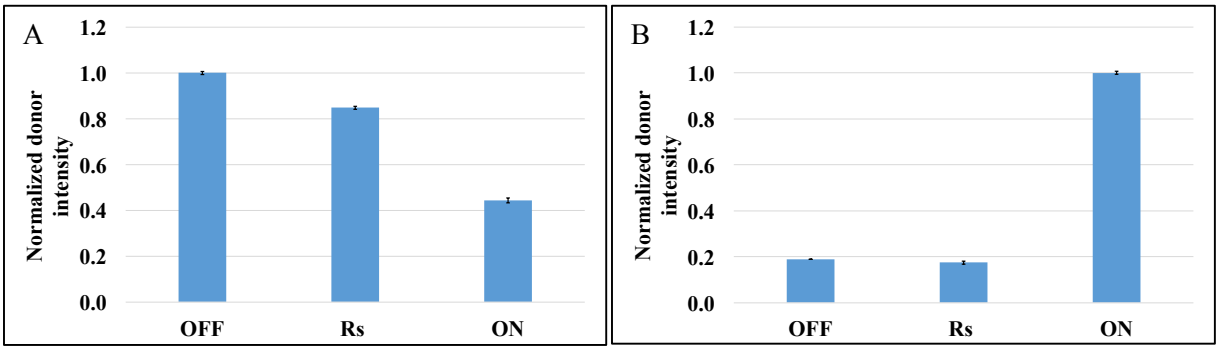

Figure 4.2 Signal metric determination to evaluate FRET event. (A) The donor and (B) acceptor intensities of the control (Rs), AALO's "OFF", and "ON" states (N=3). The control consisted of R24 and R27a.

4.4.3 Sensing ability and blocking strength study

As discribed in the previosu section, a blocking strand was able to keep AALO in the "OFF" state without any miRs and turn AALO "ON" in the presecne of all three miRs. However, we have found different AALOs showed the increased acceptor intensity not only in the presence of three miRs but also of two miRs (Figure 4.3). The only differences among these AALOs are the BSs with different sequences. Different BSs bound to GS resulted in the diverse toehold lengths and toehold locations for miR210 and two reporters (see details in Appendix Tables A3.7 and A3.8). In this whole section, the discussed toeholds for reporters are the ones located at binding sites for "ON" state, thus in the 3' end of GS. We hypothesized that AALOs' signal response to inputs were impacted greatly by the various toehold lengths and toehold locations.

AALO's sensing ability to three inputs was quantitatively evaluated by the dynamic range (DR). Dynamic range was gauaging the difference in AALO's acceptor intensity before ("OFF") and after ("ON") adding three miR inputs. An AALO with a large DR indicated a high signal response toward three miR inputs. DR was calculated based on Equation 2:

$$Dynamic\ range\ (DR) = \frac{I^A_{3\ miRs} - I^A_{0\ miRs}}{I^A_{3\ miRs}} \qquad \text{Equation 2}$$

where I^A, $I^A_{0\ miR}$, and $I^A_{3\ miRs}$ were defined in equation 1.

AALO's ability to keep low acceptor intensity in the repsence of two miR inputs was defined as the blocking strength of AALO. The blocking strength was evaluated throuth the AALO's acceptor intensity change (AIC) in the presence of two miRs: (1) miR27a and miR24, (2) miR27a and miR210, and (3) miR24 and miR210. Too strong blocking strength reduces AALO's dynamic range. Too weak blocking strength increases the chance of responding to an incomplete miR combination, such as two miR inputs. AIC was calculated based on Equation 3.

$$Acceptor\ intensity\ change\ (AIC\%) = \frac{I^A_{2\ miRs-X} - I^A_{0\ miRs}}{I^A_{3\ miRs} - I^A_{0\ miR}} \times 100\% \qquad \text{Equation 3}$$

where I^A, $I^A_{0\ miR}$, and $I^A_{3\ miRs}$ were defined in Equation 1, $I^A_{2\ miRs-X}$ is the acceptor intensity from the addition of two miRs and X is the specific combination of two miRs.

Figure 4.3 illustrates the sensing ability and blocking strength of fourteen AALOs in terms of the dynamic range (DR) and acceptor intenstity change (AIC) in the presence of two miR inputs. Figure 4.3A shows that in the presence of three miR inputs, most ALLOs had DRs larger than 0.3 except AALO-6 through AALO-10. The low and even negative DR values of AALO-6 through AALO-10 most likley reuslted from all three toeolds being less than 3 nts. Reducing R24's toehold from 3 nts (AALO-3) to 0 nts (AALO-8) reduced by 0.5 arbitrary DR units. Such short toeholds make initiating binding difficult. AALO-6 through AALO-9 had only two toeholds (details are in Appendix Table A3.7). AALO-10 did not have toeholds for R24 and R27a. Low DR of AALO-6 through AALO-10 demonstrated that the blocking strength of the BSs for these AALOs was too strong thus rendered the ALLOs non-functional. Therefore, we did not further pursue evaluating the blocking strength of AALOs with BS-6 through BS-10.

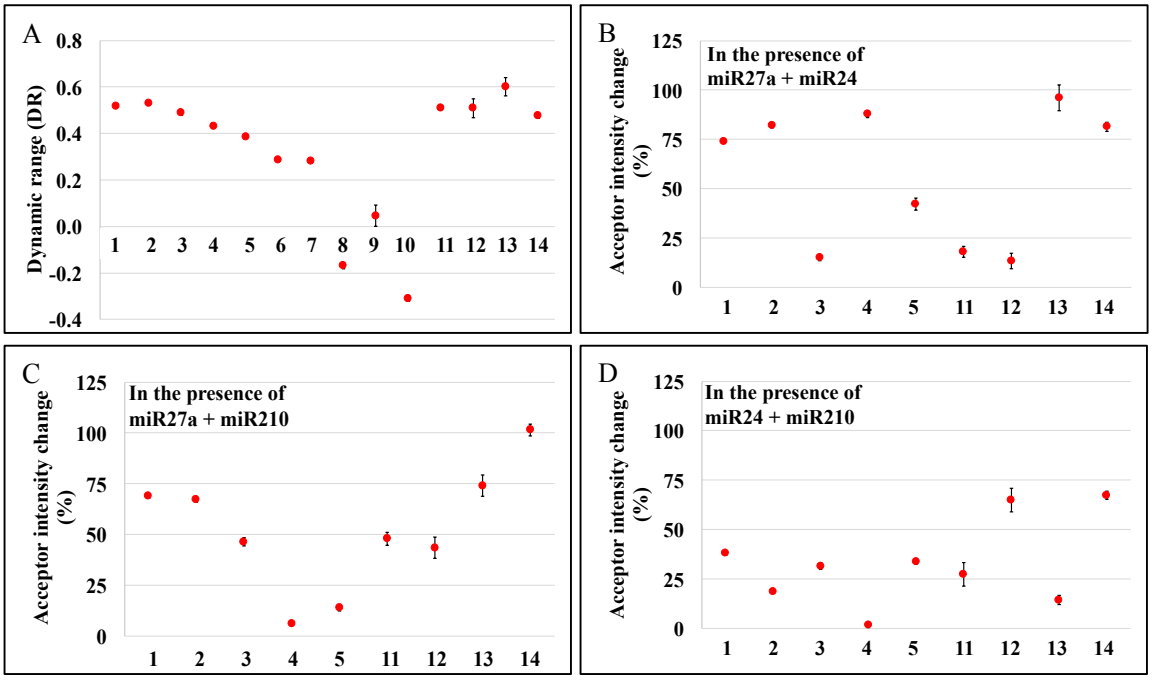

Figure 4.3 Sensing ability and blocking strength comparison of fourteen autowalk AND logic operators. (A) The dynamic range of AALOs in the presence of all three miRs. The acceptor intensity change (AIC) in the presence of (B) miR27a and miR24, (C) miR27a and miR210, and (D) miR24 and miR210. Some standard deviations are too small to be seen (N = 3). Data was accuired by Titanium:Sapphire laser.

Figure 4.3B shows that in the presence of miR27a and miR24, only AALO-3, -5, -11, -12 had AICs lower than 50%. A value less than 50% represents lower reponse towards an incomplete combination of two miR inputs. The AIC of AALO-11 was about 80% lower than AALO-13. Similar observations were made for AALO-12 and AALO-14. The major difference between AALO-11 and AALO-13 (or AALO-12 and AALO-14) was R24's toehold location. Taking the pair of AALO-13 and AALO-11 as an example, R24's toehold was moved from 5' (AALO-13) to 3' (AALO-11) end in R24's "ON" binding site. Such results suggested R24's toehold located in the 5' end made it more accessible to R24 than in the 3' end. AALO-3 and AALO-5 showed lower AIC than AALO-2 and AALO-4. Comparing the pair of AALO-2 and AALO-3, or AALO-4 and AALO-5, we have found both R27a's and R24's toeholds were located in the middle of the corresponding binding sits, but their lengths were 1 nt shorter. The signal and toehold lengths difference of AALO-2 through AALO-5 indicated longer toehold promoted reporters binding to ALLOs leading to higher AIC. There was no statistical association was found between the AIC and R27a's toehold location.

Figure 4.3C showed five AALOs (-3, -4, -5, -11, and -12) had AICs lower than 50% with the addition of miR27a and miR210. AALO-2's AIC was statically higher than AALO-4 by 60% ($p < 0.001$). Similar observation was seen in AALO-3 and AALO-5. Comparing AALO-2 and AALO-4, or AALO-3 and AALO-5, miR210's toehold (*i.e.* AALO-2) was 2 nts longer (*i.e.* AALO-4). This fact indicated that longer miR210's toehold would better assist miR210's binding to partially release BS, thus allow the interaction of GS with freed R27a and R24. Here freed R27a was from miR27a's binding. Freed R24 was probably unbound from incomplete assembled AALOs. AALO-13 and AALO-14 had the highest AIC of 75 to 100%. As we discussed earlier, R24's toeholds in AALO-13 and AALO-14 located in the 5' end made it more accessible to freed R24 thus increased AIC to incomplete combinations of two miRs: (1) miR27a and miR24, and (2) miR27a and miR210. Thus AIC of AALOs from the addition of miR27a and miR210 was believed to be associated with the miR210's toehold length and R24's toehold location.

The additon of miR24 and miR210 showed the least AIC in Figure 4.3D. Most AALOs demonstrated AICs lower than 40% except AALO-12 and AALO-14. R27a's toehold at the overhang 3' end of GS largely initiated the binding to the unbound R27a. Unbound reporters (R27a and R24) was from incomplete assembled AALOs. R27a' binding weakened the hybridization between BS and GS to allow GS's interaction with unbound R24 thus result in the increased AIC

in AALO-12 and AALO-14. No conclusive evidence was found to explain the association of toehold length and AIC from the addition of miR24 and miR210.

Balancing the toehold length and toehold location is critical to gain high DR to three inputs and low AIC to two inputs. Appropriate toehold length in AALO would keep a high sensing ability to analyte miRs and achieve a desired blocking strength to reduce AIC. Having R24's toehold located in the middle or 3' end of the R24's "ON" binding site was a benefit because those locations were able to keep AIC low in the presence of two miR inputs: miR27a and miR24, or miR27a and miR210. R27a's toehold located in the middle or 5' end was found to decrease AIC from the addition of miR24 and miR210.

Among all the AALOs tested, AALO-11 showed the lowest average AIC around 27% in the presence of two miR inputs, as well as a high DR. To further reduce AIC, we fine-tuned the toeholds for R24's and R27a's in AALO-11 leading to six more AALOs, AALO-15 through AALO-20 (details are in Appendix Table A3.8). Their AIC results when in the presence of two miRs are listed in Table 4.2. The only difference between AALO-15 and AALO-16, or AALO-17 and AALO-18, or AALO-19 and AALO-2 was the radom bases added in the BS. The added radom bases was to enlarge the loop in GS formed by BS bound to GS. Thus the contrained toeholds for reporters were expected to be more accessible. AALO-16 having higher AIC than AALO-15 provides evidence that adding random bases weakens the binding between BS and GS thus increasing AIC towards two miRs. Compared to AALO-11, the toeholds for R24 and R27a in AALO-19 were decreased to 3nts and 4 nts, respectively. Besides, in AALO-19 a second toehold (2 nts) for R24 was added to the 5' end of R24's "ON" binding site. AALO-19 showed the highest dynamic range and the lowest average AIC in the presence of two miRs ranging from 16% to 20% (Table 4.2). These results indicate that having shorter toehold for R27a and two short toeholds for R24 in both ends of R24's "ON" binding site in the GS decreased AALO-19's response towards two miRs, but kept DR high to three miRs.

Table 4.2 AALOs' dynamic range and acceptor intensity changes (AIC%) in the presence of two miRs (N=3). Data of AALO-11, AALO-15 through AALO-20 was accuired by Argon-ion laser.

	Dynamic range	AIC% from miR24+miR210	AIC% from miR27a+miR210	AIC% from miR27a+miR24
AALO-11	0.45±0.03	26.3%±1.2%	28.5%±1.5%	26.5%±1.1%
AALO-15	0.43±0.02	34.6%±1.8%	39.6%±2.0%	30.1%±1.6%
AALO-16	0.37±0.01	46.6%±1.7%	28.0%±1.3%	19.5%±1.0%
AALO-17	0.70±0.01	20.6%±0.5%	29.2%±0.6%	18.5%±0.4%
AALO-18	0.46±0.02	43.0%±1.9%	36.9%±1.6%	20.4%±1.1%
AALO-19	0.70±0.03	15.9%±0.9%	19.1%±0.9%	17.6%±0.8%
AALO-20	0.52±0.02	23.9%±1.1%	14.9%±0.8%	7.8%±0.5%

4.4.4 Sensitivity analysis of autowalk AND logic operators in cell lysate

The sensitivity of AALO-19 in crude MCF-7 cell lysate was determine from three calibration curves. Appendix Figure A3.4 shows the acceptor intensity increased linearly with the concentration of three miRs. Three calibration curves were constructed over the concentration dynamic range of 0 to 100 nM. The average limit of detection (LOD) was determined the LOD from each calibration curve. The average LOD was 3.3 ± 0.3 nM (N=3). The nanomolar LOD of AALO-19 is at the upper end of miRs' biologically relevant concentration. In a biological sample there will likely be disproportionate relative concentrations of three miRs. Thus we mimicked this situation and found ALLO-19 showed response to the lowest concentration miR in the combination (appendix Figure A3.5).

4.4.5 Selectivity analysis against off-analyte miRs with similar sequence

Selectivity of AALO-19 was tested against three off-analyte miRs. The off-analytes were miR-6804-5p (OA1) miR-4921-5p (OA2), and miR-27b-3p (OA3). The sequence similarity between the analytes and off-analytes ranged from 9/22 to 20/21 bases (or 41% to 95%). Figure 4.4 shows AALO-19's selectivity against single, double, all three (equal molar or sixty times excess) off-analytes. A blank control of AALO-19 without any miRs (OFF) was established the baseline normalized acceptor intensity of 1.00 ± 0.07 AU. There was no statistical difference ($p < 0.0001$) between the acceptor intensity from no analytes and off-analyte miRs. The result shows that AALO-19 had excellent selectivity against mismatched sequences with 41% to 95% similarity.

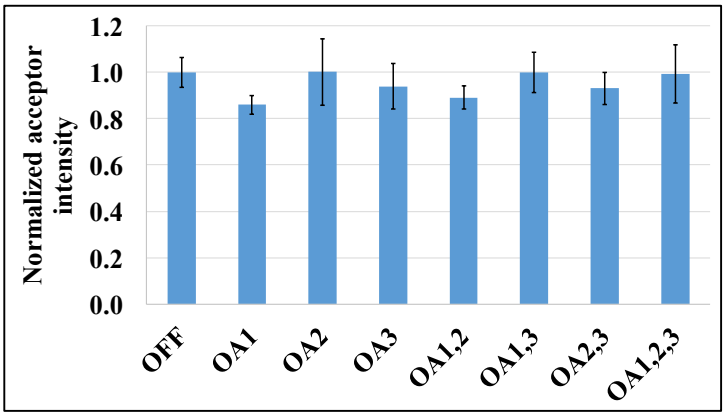

Figure 4.4 Selectivity study of ALLO-19 against three off-analyte miRs (N = 3). The off-analytes included miR-6804-5p (OA1), miR-4921-5p (OA2), and miR-27b-3p (OA3). The sequence similarity between analytes and off-analytes ranged from 9/22 to 20/21 bases (or 41% to 95%). Data was accuired by Argon-ion laser.

4.4.6 Differentiating-input-number ability evaluation

To evaluate the differentiating-input-number ability, the acceptor intensity change of AALO-19 was studied when challenged with individual and multiple miRs (Figure 4.5). A blank control established the baseline acceptor intensity of AALO-19 when no miR was present. The blank control was an assembled AALO without any miR (OFF). The acceptor intensity was normalized based on the highest value from the addition of all three miRs to AALO-19.

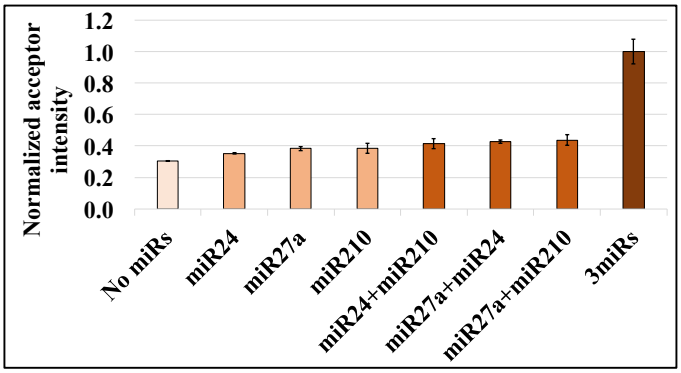

Figure 4.5 Acceptor intensity for ALLO-19 challenged with individual and multiple miRs (N=3). Compared to the no miRs control, the acceptor intensity increased the most from the addition of all three miR inputs, then with two miR inputs, and the least with single miR input. Data was accuired by Argon-ion laser.

The blank control had the average normalized acceptor intensity of 0.30 ± 0.01 AU. After adding all three miRs the average acceptor intensity was 1.00 ± 0.08 AU. Compared to the blank, the addition of all 3 miRs increased the acceptor intensity by about 3.3 times ($p < 0.0001$). Figure 4.5 shows statistical increases in the acceptor intensity from the blank after adding single and combinations of two miRs.

In order to evaluate the differentiating-input-number ability, we calculated the acceptor intensity difference between the addition of an incomplete (single or double miRs) and a complete (three miRs) miR combinations with Equation 4 and listed in Table 4.3:

$$\Delta I^A = \frac{I^A_{XmiRs} - I^A_{3\,miRs}}{I^A_{3\,miRs} - I^A_{0\,miR}} \times 100\% \qquad \text{Equation 4}$$

where I^A_{XmiRs} is the normalized acceptor intensity for the addition of single or double miRs, and the rest were defined in Equation 1. The ΔI^A from the addition of single miR was around 88% to 93%. With the addition of double miRs, ΔI^A of AALO-19 was lower to around 80%. These results indicated that AALO-19 is better at differentiating the presence of single miR than double miRs from three miRs. However, compared to our published nano-assembly logic gate-3 (NALG-3, Chapter 2), AALO-19 showed the improved differentiating-input-number ability by around 30%, especially in the case of two miRs. As in the presence of two miRs (miR96 and miR182), NALG-3[44] showed the lowest ΔI^A of 47% indicating its low differentiating-input-number ability (appendix Table A3.9).

Table 4.3 Differentiating acceptor intensity of autowalk AND logic operator (AALO-19) caused by single and double miR additions. Data was accuired by Argon-ion laser.

AALO-19	miR inputs	ΔI^A
Signal change from single-miR addition	miR24	93.2±0.8%
	miR27a	88.5±0.8%
	miR210	88.5±0.8%
Signal change from double-miR addition	miR24+miR210	84.1±0.9%
	miR24+miR27a	82.4±0.8%
	miR27a+miR210	80.9±0.9%

4.4.7 Intracellular Imaging of autowalk AND logic operator

Prior to imaging of the targeted combination of miRs, the cellular uptake of the forced "ON" autowalk AND logic operator was explored. Figure 4.6 shows a forced "ON" AALO-19 was successfully transfected into HEK293T cells. Figure 4.6c shows the bright yellow dots indicating the colocalization of the donor dye-FAM in the green channel (Figure 4.6a) and the acceptor - Texas red in the red channel (Figure 4.6b). Texas red displaced ATTO 633 and used as an acceptor due to the microscope constrains of not allowing to detect the signals from ATTO633. The spatial overlap of the FRET dye pairs indicated that forced "ON" AALO was against degradation after 24 hours' intracellular incubation. However, the signal of the FRET red channel was low. The complicated cellular matrixes could compromise the FRET red signal to further reduce it to be

lower than the microscope's detection of limit.

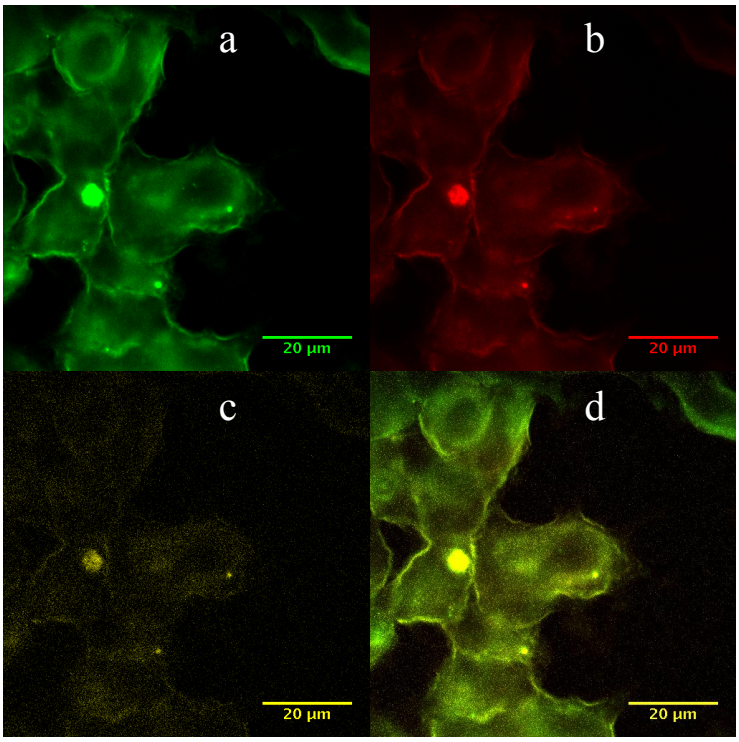

Figure 4.6 Engineered autowalk AND logic operator in HEK293T cells. HEK293T cells were transfected with the forced "ON" AALO. (a) Green channel: donor excitation/emission at 488/520 nm, related to FAM fluorescent dye. (b) Red channel: acceptor excitation/emission at 560/615 nm, related to Texas Red dye. (c) FRET channel (excitation at 488 nm and emission at 615 nm, FRET). (d) Merged images a, b, c. Scale bar indicates 20 μm.

4.5 Conclusions

The blocking strand was critical to prevent false-positive acceptor signal resulted from two reporters bound to the secondary binding regions in the gate strand. Such implicit measurement error would falsely indicate the presence of analyte miRs resulting in autowalk AND logic operator failed to function as a strict logic sensor. Compared to our previously published nano-assembly logic gate (NALG), autowalk AND logic operator 19 (AALO-19 with BS-19) showed an excellent selectivity of differentiating the highly sequence-similar off-analytes (up to 95%) from the analyte miRs and an improved differentiating-input-number ability. Different from NALG's low to 46.9% the acceptor intensity difference between the addition of an incomplete (double miRs) and a complete (three miRs) miR combinations, AALO-19 showed a statistically higher value to 80%. The improvement in selectivity and the differentiating-input-number ability was believed to be resulted from the blocking strand design. We believe AALO holds the potential to distinguish all

off-analytes with single nucleotide polymorphism and perform robust sensing only to a complete combination of inputs.

Future research direction of AALO includes 1) expanding its throughput ability to accommodate up to 10 miRs, 2) lowering the limit of detection to fulfill the needs of detecting miRs with pM concentration range, and 3) locating the analyte miRs through AALO's binding imaged in the cell or tissue samples. For its application in biological study, the cross-talk issue of three channels should be addressed through single molecules control study. More work needs to be done to improve the FRET signal in cells.

4.6 Acknowledgements

I would like to thank Milton Harris Summer Fellowship for sponsoring this research.

4.7 References

(1) Seeman, N. C. Nucleic Acid Junctions and Lattices. *J. Theor. Biol.* **1982**, *99* (2), 237–247.
(2) Adleman, L. Molecular Computation of Solutions to Combinatorial Problems. *Science* **1994**, *266* (5187), 1021-1024.
(3) Rothemund, P. W. K.; Papadakis, N.; Winfree, E. Algorithmic Self-Assembly of DNA Sierpinski Triangles. *PLoS Biol.* **2004**, *2* (12), e424.
(4) Seelig, G.; Soloveichik, D.; Zhang, D. Y.; Winfree, E. Enzyme-Free Nucleic Acid Logic Circuits. *Science* **2006**, *314* (5805), 1585–1588.
(5) Couny, F.; Benabid, F.; Roberts, P. J.; Light, P. S.; Raymer, M. G. Generation and Photonic Guidance of Multi-Octave Optical-Frequency Combs. *Science* **2007**, *318* (5853), 1118–1121.
(6) Frezza, B. M.; Cockroft, S. L.; Ghadiri, M. R. Modular Multi-Level Circuits from Immobilized DNA-Based Logic Gates. *J. Am. Chem. Soc.* **2007**, *129* (48), 14875–14879.
(7) Lubrich, D.; Lin, J.; Yan, J. A Contractile DNA Machine. *Angew. Chem. Int. Ed.* **2008**, *47* (37), 7026–7028.
(8) Goodman, R. P.; Heilemann, M.; Doose, S.; Erben, C. M.; Kapanidis, A. N.; Turberfield, A. J. Reconfigurable, Braced, Three-Dimensional DNA Nanostructures. *Nat. Nanotechnol.* **2008**, *3* (2), 93–96.
(9) Chen, X.; Ellington, A. D. Shaping up Nucleic Acid Computation. *Curr. Opin. Biotechnol.* **2010**, *21* (4), 392–400.
(10) He, H.-Z.; Chan, D. S.-H.; Leung, C.-H.; Ma, D.-L. G-Quadruplexes for Luminescent Sensing and Logic Gates. *Nucleic Acids Res.* **2013**, *41* (8), 4345–4359.
(11) Chen, A. K.; Davydenko, O.; Behlke, M. A.; Tsourkas, A. Ratiometric Bimolecular Beacons for the Sensitive Detection of RNA in Single Living Cells. *Nucleic Acids Res.* **2010**, *38* (14), e148–e148.
(12) Hemphill, J.; Deiters, A. DNA Computation in Mammalian Cells: MicroRNA Logic Operations. *J. Am. Chem. Soc.* **2013**, *135* (28), 10512–10518.
(13) Deng, R.; Tang, L.; Tian, Q.; Wang, Y.; Lin, L.; Li, J. Toehold-Initiated Rolling Circle Amplification for Visualizing Individual MicroRNAs In Situ in Single Cells. *Angew. Chem. Int. Ed.* **2014**, *53* (9), 2389–2393.
(14) Wu, P.; Tu, Y.; Qian, Y.; Zhang, H.; Cai, C. DNA Strand-Displacement-Induced Fluorescence Enhancement for Highly Sensitive and Selective Assay of Multiple MicroRNA in Cancer Cells. *Chem Commun* **2014**, *50* (8), 1012–1014.
(15) Cheglakov, Z.; Cronin, T. M.; He, C.; Weizmann, Y. Live Cell MicroRNA Imaging Using Cascade Hybridization Reaction. *J. Am. Chem. Soc.* **2015**, *137* (19), 6116–6119.
(16) Bartel, D. P. MicroRNAs: Genomics, Biogenesis, Mechanism, and Function. *cell* **2004**, *116* (2), 281–297.

(17) Dinger, M. E.; Pang, K. C.; Mercer, T. R.; Mattick, J. S. Differentiating Protein-Coding and Noncoding RNA: Challenges and Ambiguities. *PLoS Comput. Biol.* **2008**, *4* (11), e1000176.
(18) Camps, C.; Saini, H. K.; Mole, D. R.; Choudhry, H.; Reczko, M.; Guerra-Assunção, J. A.; Tian, Y.-M.; Buffa, F. M.; Harris, A. L.; Hatzigeorgiou, A. G.; et al. Integrated Analysis of MicroRNA and MRNA Expression and Association with HIF Binding Reveals the Complexity of MicroRNA Expression Regulation under Hypoxia. *Mol. Cancer* **2014**, *13* (1), 1.
(19) Abrahante, J. E.; Daul, A. L.; Li, M.; Volk, M. L.; Tennessen, J. M.; Miller, E. A.; Rougvie, A. E. The Caenorhabditis Elegans Hunchback-like Gene Lin-57/Hbl-1 Controls Developmental Time and Is Regulated by MicroRNAs. *Dev. Cell* **2003**, *4* (5), 625–637.
(20) Bloomston, M.; Frankel, W. L.; Petrocca, F.; Volinia, S.; Alder, H.; Hagan, J. P.; Liu, C.-G.; Bhatt, D.; Taccioli, C.; Croce, C. M. MicroRNA Expression Patterns to Differentiate Pancreatic Adenocarcinoma from Normal Pancreas and Chronic Pancreatitis. *Jama* **2007**, *297* (17), 1901–1908.
(21) Bockmeyer, C. L.; Christgen, M.; Müller, M.; Fischer, S.; Ahrens, P.; Länger, F.; Kreipe, H.; Lehmann, U. MicroRNA Profiles of Healthy Basal and Luminal Mammary Epithelial Cells Are Distinct and Reflected in Different Breast Cancer Subtypes. *Breast Cancer Res. Treat.* **2011**, *130* (3), 735–745.
(22) Carleton, M.; Cleary, M. A.; Linsley, P. S. MicroRNAs and Cell Cycle Regulation. *Cell Cycle* **2007**, *6* (17), 2127–2132.
(23) Lal, A.; Navarro, F.; Maher, C. A.; Maliszewski, L. E.; Yan, N.; O'Day, E.; Chowdhury, D.; Dykxhoorn, D. M.; Tsai, P.; Hofmann, O.; et al. MiR-24 Inhibits Cell Proliferation by Targeting E2F2, MYC, and Other Cell-Cycle Genes via Binding to "Seedless" 3′UTR MicroRNA Recognition Elements. *Mol. Cell* **2009**, *35* (5), 610–625.
(24) Ivey, K. N.; Srivastava, D. MicroRNAs as Regulators of Differentiation and Cell Fate Decisions. *Cell Stem Cell* **2010**, *7* (1), 36–41.
(25) Smith-Vikos, T.; Slack, F. J. MicroRNAs and Their Roles in Aging. *J. Cell Sci.* **2012**, *125* (1), 7–17.
(26) Kulshreshtha, R.; Ferracin, M.; Wojcik, S. E.; Garzon, R.; Alder, H.; Agosto-Perez, F. J.; Davuluri, R.; Liu, C.-G.; Croce, C. M.; Negrini, M.; et al. A MicroRNA Signature of Hypoxia. *Mol. Cell. Biol.* **2007**, *27* (5), 1859–1867.
(27) Zhang, D. Y.; Seelig, G. Dynamic DNA Nanotechnology Using Strand-Displacement Reactions. *Nat. Chem.* **2011**, *3* (2), 103–113.
(28) Teichmann, M.; Kopperger, E.; Simmel, F. C. Robustness of Localized DNA Strand Displacement Cascades. *ACS Nano* **2014**, *8* (8), 8487–8496.
(29) Li, W.; Yang, Y.; Yan, H.; Liu, Y. Three-Input Majority Logic Gate and Multiple Input Logic Circuit Based on DNA Strand Displacement. *Nano Lett.* **2013**, *13* (6), 2980–2988.
(30) Fan, D.; Zhu, J.; Zhai, Q.; Wang, E.; Dong, S. Cascade DNA Logic Device Programmed Ratiometric DNA Analysis and Logic Devices Based on a Fluorescent Dual-Signal Probe of a G-Quadruplex DNAzyme. *Chem Commun* **2016**, *52* (19), 3766–3769.
(31) Zhang, D. Y.; Winfree, E. Control of DNA Strand Displacement Kinetics Using Toehold Exchange. *J AM CHEM SOC* **2009**, *131*, 17303–17314.
(32) Zhu, J.; Zhang, L.; Dong, S.; Wang, E. Four-Way Junction-Driven DNA Strand Displacement and Its Application in Building Majority Logic Circuit. *ACS Nano* **2013**, *7* (11), 10211–10217.
(33) Srinivas, N.; Ouldridge, T. E.; Sulc, P.; Schaeffer, J. M.; Yurke, B.; Louis, A. A.; Doye, J. P. K.; Winfree, E. On the Biophysics and Kinetics of Toehold-Mediated DNA Strand Displacement. *Nucleic Acids Res.* **2013**, *41* (22), 10641–10658.
(34) Qian, L.; Winfree, E.; Bruck, J. Neural Network Computation with DNA Strand Displacement Cascades. *Nature* **2011**, *475* (7356), 368–372.
(35) Larkey, N. E.; Almlie, C. K.; Tran, V.; Egan, M.; Burrows, S. M. Detection of MiRNA Using a Double-Strand Displacement Biosensor with a Self-Complementary Fluorescent Reporter. *Anal. Chem.* **2014**, *86* (3), 1853–1863.
(36) Almlie, C. K.; Larkey, N. E.; Burrows, S. M. Fluorescent MicroRNA Biosensors: A Comparison of Signal Generation to Quenching. *Anal Methods* **2015**, *7* (17), 7296–7310.
(37) Marras, S. A.; Kramer, F. R.; Tyagi, S. Efficiencies of Fluorescence Resonance Energy Transfer and Contact-Mediated Quenching in Oligonucleotide Probes. *Nucleic Acids Res.* **2002**, *30* (21), e122–e122.
(38) Chen, A. K.; Behlke, M. A.; Tsourkas, A. Avoiding False-Positive Signals with Nuclease-Vulnerable Molecular Beacons in Single Living Cells. *Nucleic Acids Res.* **2007**, *35* (16), e105–e105.

(39) Zhang, P.; He, Z.; Wang, C.; Chen, J.; Zhao, J.; Zhu, X.; Li, C.-Z.; Min, Q.; Zhu, J.-J. *In Situ* Amplification of Intracellular MicroRNA with MNAzyme Nanodevices for Multiplexed Imaging, Logic Operation, and Controlled Drug Release. *ACS Nano* **2015**, *9* (1), 789–798.

(40) Larkey, N. E.; Zhang, L.; Lansing, S. S.; Tran, V.; Seewaldt, V. L.; Burrows, S. M. Förster Resonance Energy Transfer to Impart Signal-on and -off Capabilities in a Single MicroRNA Biosensor. *The Analyst* **2016**, *141* (22), 6239–6250.

(41) Chakraborty, B.; Sha, R.; Seeman, N. C. A DNA-Based Nanomechanical Device with Three Robust States. *Proc. Natl. Acad. Sci.* **2008**, *105* (45), 17245–17249.

(42) Zhang, L.; Bluhm, A. M.; Chen, K.-J.; Larkey, N. E.; Burrows, S. M. Performance of Nano-Assembly Logic Gates with a DNA Multi-Hairpin Motif. *Nanoscale* **2017**, *9* (4), 1709–1720.

(43) Lee, H.; Shapiro, S. J.; Chapin, S. C.; Doyle, P. S. Encoded Hydrogel Microparticles for Sensitive and Multiplex MicroRNA Detection Directly from Raw Cell Lysates. *Anal. Chem.* **2016**, *88* (6), 3075–3081.

(44) Zhang, L.; Bluhm, A. M.; Chen, K.-J.; Larkey, N. E.; Burrows, S. M. Performance of Nano-Assembly Logic Gates with a DNA Multi-Hairpin Motif. *Nanoscale* **2017**.

Chapter 5.
Summaries and Conclusions

5.1. Summaries and Conclusions

AND logic gates described herein were designed to overcome some limitations of the current *in situ* logic sensors. This work has contributed new designs and key innovations that will benefit the field of *in situ* logic sensors for multiplexing analysis. The iteration of the nano-assembly logic gate (NALG, Chapter 2[1]) and autowalk AND logic operator (AALO, Chapter 4) was designed for simultaneous detection for three miR inputs and showed reduced false signals against nuclease degradation when compared to molecular beacons. The works that followed the first iteration enhanced AND logic gate by optimizing: (1) multiplex ability for various miR analytes (Chapter 2[1], 3, and 4), (2) structural and thermodynamic features that influence molecular-based logic measurement systems in the nanotechnology field (Chapter 3), (3) design alterations to increase differentiating-input-number ability by enlarging the differentiating response to incomplete (one or two) and complete miR combinations (Chapter 4), and (4) selectivity against off-analyte miRs that have up to 95% similar sequence compared to analyte miRs (Chapter 4), (5) transfection methods to delivery autowalk AND logic opeartor into cells (Chapter 4).

There are still many potential issues that we need to work on to improve the logic gate to achieve the intracellular multiplexing analysis. Some of the issues include hybridization kinetics between logic gate and analyt miRs, stability against enzyme degradation, sensitivity, selectivity, signal reposne to the disproportionate miR concentrations, differentiating-input-number ability, and multiplex capability.

Logic sensors with faster hybridization kinetics to bind the analyte miRs are more competitive with regard to reveal the spatial and temporal fluctuations of combinatorial miRs within a living cell. In comparison to DNA probes, 2′O-Methyl (2′OMe) RNA modification in DNA probes demonstrated faster hybridization kinetics and the ability to bind analyte miRs.[2] Faster hybridization between logic sensors and analyte miRs may decrease response time.

Although both logic sensors (NALG and AALO) demonstrated no false-positive signal from enzyme digestion, the logic sensor itself is still susceptible to be degraded leading to the increased background noise and decreased output signal.[3] Logic gates modification could potentially protect them from nuclease degradation[4], such as the addition of locked nucleic acids

(LNAs)[5,6], 2‘fluoro-modefied RNA (2’F RNA)[7], or polyethylene glycol (PEG)[8–10] as spacers in non-complementary regions, morpholino oligomer[11–13], and peptide nucleic acids (PNAs).[14–16]

The concentration of miRs has been reported low in cells and ranges from the picomolar to nanomolar. NALG and AALO have demonstrated the limit of detection (LOD) of 1 nanomolar to a particular combination of three miR inputs in concentration. In order to detect the lower end (picomolar) of miRs concentration range, we need to improvise the logic gate to lower the established nanomolar LOD. To improve the detection limit, lower concentrations of the logic gate or longer integration times can be used. We can also amplify the FRET signal to increase the sensitivity of the FRET-based logic gates. Further FRET enhancement can be achieved by finding a better FRET donor-acceptor pair and a more reasonable FRET distance. Additionally, increasing the ratio of donor-acceptor molecules labeled in the logic gates has been reported to show a high FRET enhancement factor of 40.[17]

As for the disproportionate relative concentrations among the multiple miRs, the lowest concentration miR in the combination is regarded as the limiting agent. Preliminary results showed AALO-19 responded to the lowest concentration miR in the combination (Figure A3.5). To further evaluate the relationship of logic gate’s signal response and miR concentration, a calibration curve with disproportionate concentration miRs can be analyzed. Additionally, we envision combining multiple logic gates to create logic circuits that most likely reveal the disproportionate concentrations in more detail.

The differentiating-input-number ability of logic gates is an issue during multiplex miR analysis. We have decreased logic gates’ undesirable response to an incomplete combination of miR inputs through different structural design, such as from NALG to AALO. AALO’s ability to differentiate input numbers can be further improved by continuing the blocking strand sequence design and modify the DNA nucleotides in the blocking strand. Inserting LNAs to the blocking strand may increase binding affinity with the gate strand leading to the stronger blocking strength. Non-canonical bases can be incorporated to a certain region of the blocking strand; its corresponding non-canonical pair can also be inserted to the gate strand where target miR or reporter strands will not bind. The binding of non-canonical bases pairs will increase the binding affinity of the gate and blocking strand.

The multiplex capability of the logic gates needs to be enhanced to fulfill the requirement of detecting the tens’ and more miRs simultaneously.[18] Instead of using FRET-based logic gates,

multiplex miRs analysis can be achieved through the method of coupling several single-input sensors.[19] Each sensor is labeled with one fluorescent dye and targets one specific miR. However, the usage of multiple fluorescent dyes involves two issues: one is cross-talk between dyes, and the other is low transfection efficiency of all these separate sensors or logic gates into the same cells. The cross-talk between dyes can be decreased by using the dye-specific offsets with the continually variable filters.[20] Many data process methods combining experimental design such as Matlab code with single fluorescent dye control group can be used reduce the cross-talk issue.

Besides, DNA-based logic sensor can be in cooperated with molecules having smaller emission profiles, such as quantum dots.[21] FRET-based DNA logic gates can be combined as circuits allowing the multiplexing analysis.[22]

The relative change in multiple miRs as a whole is more indicative of the cell state than a individual miR.[23] The logic gates have the potential to a specific miRs combination as biomarkers to learn about the underlying mechanisms of biological process,[24–29] such as cellular regulatory pathways. The work that I have done designing the logic gates for multiple miRs will assist researchers to better consider the structural, predicted thermodynamics, and FRET-based transduction mechanism when they developing their own DNA-based analytical tools to detect miRs. The biological work involving the transfection and the cellular imaging of these logic gates will aid researchers to transfect the nano-sized fluorescent-labeled DNA devices into cells for cellular imaging.

5.2 References

(1) Zhang, L.; Bluhm, A. M.; Chen, K.-J.; Larkey, N. E.; Burrows, S. M. Performance of Nano-Assembly Logic Gates with a DNA Multi-Hairpin Motif. *Nanoscale* **2017**, *9* (4), 1709–1720.

(2) Majlessi, M. Advantages of 2'-O-Methyl Oligoribonucleotide Probes for Detecting RNA Targets. *Nucleic Acids Res.* **1998**, *26* (9), 2224–2229.

(3) Larkey, N. E.; Almlie, C. K.; Tran, V.; Egan, M.; Burrows, S. M. Detection of MiRNA Using a Double-Strand Displacement Biosensor with a Self-Complementary Fluorescent Reporter. *Anal. Chem.* **2014**, *86* (3), 1853–1863.

(4) Borgatti, M.; Romanelli, A.; Saviano, M.; Pedone, C.; Lampronti, I.; Breda, L.; Nastruzzi, C.; Bianchi, N.; Mischiati, C.; Gambari, R. Resistance of Decoy PNA-DNA Chimeras to Enzymatic Degradation in Cellular Extracts and Serum. *Oncol. Res.* **2003**, *13* (5), 279–287.

(5) Wang, L.; Yang, C. J.; Medley, C. D.; Benner, S. A.; Tan, W. Locked Nucleic Acid Molecular Beacons. *J. Am. Chem. Soc.* **2005**, *127* (45), 15664–15665.

(6) Martinez, K.; Estevez, M.-C.; Wu, Y.; Phillips, J. A.; Medley, C. D.; Tan, W. Locked Nucleic Acid Based Beacons for Surface Interaction Studies and Biosensor Development. *Anal. Chem.* **2009**, *81* (9), 3448–3454.

(7) Li, J.; Li, X.; Li, Y.; Yang, H.; Wang, L.; Qin, Y.; Liu, H.; Fu, L.; Guan, X.-Y. Cell-Specific Detection of MiR-375 Downregulation for Predicting the Prognosis of Esophageal Squamous Cell Carcinoma by MiRNA In Situ Hybridization. *PLoS ONE* **2013**, *8* (1), e53582.

(8) Lee, M.; Kim, S. W. Polyethylene Glycol-Conjugated Copolymers for Plasmid DNA Delivery. *Pharm. Res.* **2005**, *22* (1), 1–10.
(9) Mao, H.-Q.; Roy, K.; Troung-Le, V. L.; Janes, K. A.; Lin, K. Y.; Wang, Y.; August, J. T.; Leong, K. W. Chitosan-DNA Nanoparticles as Gene Carriers: Synthesis, Characterization and Transfection Efficiency. *J. Controlled Release* **2001**, *70* (3), 399–421.
(10) Rumney IV, S.; Kool, E. T. DNA Recognition by Hybrid Oligoether–Oligodeoxynucleotide Macrocycles*. *Angew. Chem. Int. Ed. Engl.* **1992**, *31* (12), 1617–1619.
(11) Hudziak, R. M.; Barofsky, E.; Barofsky, D. F.; Weller, D. L.; Huang, S. B.; Weller, D. D. Resistance of Morpholino Phosphorodiamidate Oligomers to Enzymatic Degradation. *Antisense Nucleic Acid Drug Dev.* **1996**, *6* (4), 267–272.
(12) Hudziak, R. M.; Baerofsky, E.; Baerofsky, D. F.; Weller, D. L.; Huang, S.-B. Resistance of Morpholino Phosphorodiamidate Oligomers to Enzymatic Degradation. *Antisense Nucleic Acid Drug Dev.* **1996**, *6* (4).
(13) Blum, M.; De Robertis, E. M.; Wallingford, J. B.; Niehrs, C. Morpholinos: Antisense and Sensibility. *Dev. Cell* **2015**, *35* (2), 145–149.
(14) Demidov, V. V.; Potaman, V. N.; Frank-Kamenetskil, M. D.; Egholm, M.; Buchard, O.; Sönnichsen, S. H.; Nlelsen, P. E. Stability of Peptide Nucleic Acids in Human Serum and Cellular Extracts. *Biochem. Pharmacol.* **1994**, *48* (6), 1310–1313.
(15) Nielsen, P. E.; Egholm, M. An Introduction to Peptide Nucleic Acid. 17.
(16) Gray, G. D.; Basu, S.; Wickstrom, E. Transformed and Immortalized Cellular Uptake of IOligodeoxynucleoside Phosphorothioates, 3'-Alkylamino Oligodeoxynucleotides, Z'cO-Methyl Oligoribonucleotides, Oligodeoxynucleoside MethLylphosphonates, and Peptide Nucleic Acids. 12.
(17) Buckhout-White, S.; Spillmann, C. M.; Algar, W. R.; Khachatrian, A.; Melinger, J. S.; Goldman, E. R.; Ancona, M. G.; Medintz, I. L. Assembling Programmable FRET-Based Photonic Networks Using Designer DNA Scaffolds. *Nat. Commun.* **2014**, *5*.
(18) Graybill, R. M.; Bailey, R. C. Emerging Biosensing Approaches for MicroRNA Analysis. *Anal. Chem.* **2016**, *88* (1), 431–450.
(19) Ryoo, S.-R.; Lee, J.; Yeo, J.; Na, H.-K.; Kim, Y.-K.; Jang, H.; Lee, J. H.; Han, S. W.; Lee, Y.; Kim, V. N.; et al. Quantitative and Multiplexed MicroRNA Sensing in Living Cells Based on Peptide Nucleic Acid and Nano Graphene Oxide (PANGO). *ACS Nano* **2013**, *7* (7), 5882–5891.
(20) Almlie, C. K.; Hsiao, A.; Burrows, S. M. Dye-Specific Wavelength Offsets to Resolve Spectrally Overlapping and Co-Localized Two-Photon Induced Fluorescence. *Anal. Chem.* **2016**, *88* (2), 1462–1467.
(21) Gliddon, H. D.; Howes, P. D.; Kaforou, M.; Levin, M.; Stevens, M. M. A Nucleic Acid Strand Displacement System for the Multiplexed Detection of Tuberculosis-Specific MRNA Using Quantum Dots. *Nanoscale* **2016**, *8* (19), 10087–10095.
(22) Zhang, L.; Bluhm, A. M.; Chen, K.-J.; Larkey, N. E.; Burrows, S. M. Performance of Nano-Assembly Logic Gates with a DNA Multi-Hairpin Motif. *Nanoscale* **2017**.
(23) Mogilyansky, E.; Rigoutsos, I. The MiR-17/92 Cluster: A Comprehensive Update on Its Genomics, Genetics, Functions and Increasingly Important and Numerous Roles in Health and Disease. *Cell Death Differ.* **2013**, *20* (12), 1603–1614.
(24) Iorio, M. V.; Ferracin, M.; Liu, C.-G.; Veronese, A.; Spizzo, R.; Sabbioni, S.; Magri, E.; Pedriali, M.; Fabbri, M.; Campiglio, M.; et al. MicroRNA Gene Expression Deregulation in Human Breast Cancer. *Cancer Res.* **2005**, *65* (16), 7065–7070.
(25) Calin, G. A.; Croce, C. M. MicroRNA Signatures in Human Cancers. *Nat. Rev. Cancer* **2006**, *6* (11), 857–866.
(26) Yang, N.; Coukos, G.; Zhang, L. MicroRNA Epigenetic Alterations in Human Cancer: One Step Forward in Diagnosis and Treatment. *Int. J. Cancer* **2007**, *122* (5), 963–968.
(27) Tavazoie, S. F.; Alarcón, C.; Oskarsson, T.; Padua, D.; Wang, Q.; Bos, P. D.; Gerald, W. L.; Massagué, J. Endogenous Human MicroRNAs That Suppress Breast Cancer Metastasis. *Nature* **2008**, *451* (7175), 147–152.
(28) Corcoran, C.; Friel, A. M.; Duffy, M. J.; Crown, J.; O'Driscoll, L. Intracellular and Extracellular MicroRNAs in Breast Cancer. *Clin. Chem.* **2011**, *57* (1), 18–32.
(29) Chiang, C.-H.; Hou, M.-F.; Hung, W.-C. Up-Regulation of MiR-182 by β-Catenin in Breast Cancer Increases Tumorigenicity and Invasiveness by Targeting the Matrix Metalloproteinase Inhibitor RECK. *Biochim. Biophys. Acta BBA - Gen. Subj.* **2013**, *1830* (4), 3067–3076.

Bibliography

(1) Jabri, E. Non-Coding RNA: Small, but in Control. *Nat. Rev. Mol. Cell Biol.* **2005**, *6*, 361.

(2) Kaikkonen, M. U.; Lam, M. T. Y.; Glass, C. K. Non-Coding RNAs as Regulators of Gene Expression and Epigenetics. *Cardiovasc. Res.* **2011**, *90* (3), 430–440.

(3) Esteller, M. Non-Coding RNAs in Human Disease. *Nat. Rev. Genet.* **2011**, *12*, 861.

(4) Lal, A.; Navarro, F.; Maher, C. A.; Maliszewski, L. E.; Yan, N.; O'Day, E.; Chowdhury, D.; Dykxhoorn, D. M.; Tsai, P.; Hofmann, O.; et al. MiR-24 Inhibits Cell Proliferation by Targeting E2F2, MYC, and Other Cell-Cycle Genes via Binding to "Seedless" 3′UTR MicroRNA Recognition Elements. *Mol. Cell* **2009**, *35* (5), 610–625.

(5) Loayza-Puch, F.; Yoshida, Y.; Matsuzaki, T.; Takahashi, C.; Kitayama, H.; Noda, M. Hypoxia and RAS-Signaling Pathways Converge on, and Cooperatively Downregulate, the RECK Tumor-Suppressor Protein through MicroRNAs. *Oncogene* **2010**, *29* (18), 2638–2648.

(6) Trapnell, C. Defining Cell Types and States with Single-Cell Genomics. *Genome Res.* **2015**, *25* (10), 1491–1498.

(7) Hemphill, J.; Deiters, A. DNA Computation in Mammalian Cells: MicroRNA Logic Operations. *J. Am. Chem. Soc.* **2013**, *135* (28), 10512–10518.

(8) Tagore, S.; Bhattacharya, S. DNA Computation: Applications and Perspectives. *J. Proteomics Bioinform.* **2010**, *03* (07).

(9) He, L.; Hannon, G. J. MicroRNAs: Small RNAs with a Big Role in Gene Regulation. *Nat. Rev. Genet.* **2004**, *5* (7), 522–531.

(10) Bartel, D. P. MicroRNAs: Genomics, Biogenesis, Mechanism, and Function. *cell* **2004**, *116* (2), 281–297.

(11) Chen, A. K.; Behlke, M. A.; Tsourkas, A. Avoiding False-Positive Signals with Nuclease-Vulnerable Molecular Beacons in Single Living Cells. *Nucleic Acids Res.* **2007**, *35* (16), e105–e105.

(12) Zhang, L.; Bluhm, A. M.; Chen, K.-J.; Larkey, N. E.; Burrows, S. M. Performance of Nano-Assembly Logic Gates with a DNA Multi-Hairpin Motif. *Nanoscale* **2017**, *9* (4), 1709–1720.

(13) Rinn, J. L.; Kertesz, M.; Wang, J. K.; Squazzo, S. L.; Xu, X.; Brugmann, S. A.; Goodnough, L. H.; Helms, J. A.; Farnham, P. J.; Segal, E.; et al. Functional Demarcation of Active and Silent Chromatin Domains in Human HOX Loci by Noncoding RNAs. *Cell* **2007**, *129* (7), 1311–1323.

(14) Kim, D. H.; Saetrom, P.; Snove, O.; Rossi, J. J. MicroRNA-Directed Transcriptional Gene Silencing in Mammalian Cells. *Proc. Natl. Acad. Sci.* **2008**, *105* (42), 16230–16235.

(15) Chen, Z.; Li, Y.; Huang, P.; Luthra, R. Hypoxia-Regulated MicroRNA-210 Modulates Mitochondrial Function and Decreases ISCU and COX10 Expression. *Oncogene* **2010**, *29*, 4362–4368.

(16) Srivastava, N.; Manvati, S.; Srivastava, A.; Pal, R.; Kalaiarasan, P.; Chattopadhyay, S.; Gochhait, S.; Dua, R.; Bamezai, R. N. MiR-24-2 Controls H2AFX Expression Regardless of Gene Copy Number Alteration and Induces Apoptosis by Targeting Antiapoptotic Gene BCL-2: A Potential for Therapeutic Intervention. *Breast Cancer Res.* **2011**, *13* (2), 1.

(17) Abrahante, J. E.; Daul, A. L.; Li, M.; Volk, M. L.; Tennessen, J. M.; Miller, E. A.; Rougvie, A. E. The Caenorhabditis Elegans Hunchback-like Gene Lin-57/Hbl-1 Controls Developmental Time and Is Regulated by MicroRNAs. *Dev. Cell* **2003**, *4* (5), 625–637.

(18) Blackshaw, S.; Harpavat, S.; Trimarchi, J.; Cai, L.; Huang, H.; Kuo, W. P.; Weber, G.; Lee, K.; Fraioli, R. E.; Cho, S.-H.; et al. Genomic Analysis of Mouse Retinal Development. *PLoS Biol.* **2004**, *2* (9), e247.

(19) Smith-Vikos, T.; Slack, F. J. MicroRNAs and Their Roles in Aging. *J. Cell Sci.* **2012**, *125* (1), 7–17.

(20) Croce, C. M. Causes and Consequences of MicroRNA Dysregulation in Cancer. *Nat. Rev. Genet.* **2009**, *10* (10), 704–714.

(21) Mertens-Talcott, S. U.; Chintharlapalli, S.; Li, X.; Safe, S. The Oncogenic MicroRNA-27a Targets Genes That Regulate Specificity Protein Transcription Factors and the G2-M Checkpoint in MDA-MB-231 Breast Cancer Cells. *Cancer Res.* **2007**, *67* (22), 11001–11011.

(22) Faghihi, M. A.; Modarresi, F.; Khalil, A. M.; Wood, D. E.; Sahagan, B. G.; Morgan, T. E.; Finch, C. E.; St. Laurent III, G.; Kenny, P. J.; Wahlestedt, C. Expression of a Noncoding RNA Is Elevated in Alzheimer's Disease and Drives Rapid Feed-Forward Regulation of β-Secretase. *Nat. Med.* **2008**, *14* (7), 723–730.

(23) Romaine, S. P. R.; Tomaszewski, M.; Condorelli, G.; Samani, N. J. MicroRNAs in Cardiovascular Disease: An Introduction for Clinicians. *Heart* **2015**, *101* (12), 921–928.

(24) da Silva Oliveira, K. C.; Thomaz Araújo, T. M.; Albuquerque, C. I.; Barata, G. A.; Gigek, C. O.; Leal, M. F.; Wisnieski, F.; Rodrigues Mello Junior, F. A.; Khayat, A. S.; de Assumpção, P. P.; et al. Role of MiRNAs and Their Potential to Be Useful as Diagnostic and Prognostic Biomarkers in Gastric Cancer. *World J. Gastroenterol.* **2016**, *22* (35), 7951.

(25) Reis, E. M.; Nakaya, H. I.; Louro, R.; Canavez, F. C.; Flatschart, Á. V. F.; Almeida, G. T.; Egidio, C. M.; Paquola, A. C.; Machado, A. A.; Festa, F.; et al. Antisense Intronic Non-Coding RNA Levels Correlate to the Degree of Tumor Differentiation in Prostate Cancer. *Oncogene* **2004**, *23* (39), 6684–6692.

(26) Bloomston, M.; Frankel, W. L.; Petrocca, F.; Volinia, S.; Alder, H.; Hagan, J. P.; Liu, C.-G.; Bhatt, D.; Taccioli, C.; Croce, C. M. MicroRNA Expression Patterns to Differentiate Pancreatic Adenocarcinoma from Normal Pancreas and Chronic Pancreatitis. *Jama* **2007**, *297* (17), 1901–1908.

(27) Bockmeyer, C. L.; Christgen, M.; Müller, M.; Fischer, S.; Ahrens, P.; Länger, F.; Kreipe, H.; Lehmann, U. MicroRNA Profiles of Healthy Basal and Luminal Mammary Epithelial Cells Are Distinct and Reflected in Different Breast Cancer Subtypes. *Breast Cancer Res. Treat.* **2011**, *130* (3), 735–745.

(28) Chiang, C.-H.; Hou, M.-F.; Hung, W.-C. Up-Regulation of MiR-182 by β-Catenin in Breast Cancer Increases Tumorigenicity and Invasiveness by Targeting the Matrix Metalloproteinase Inhibitor RECK. *Biochim. Biophys. Acta BBA - Gen. Subj.* **2013**, *1830* (4), 3067–3076.

(29) Rupaimoole, R.; Ivan, C.; Yang, D.; Gharpure, K. M.; Wu, S. Y.; Pecot, C. V.; Previs, R. A.; Nagaraja, A. S.; Armaiz-Pena, G. N.; McGuire, M.; et al. Hypoxia-Upregulated MicroRNA-630 Targets Dicer, Leading to Increased Tumor Progression. *Oncogene* **2016**, *35* (33), 4312–4320.

(30) Hui, A.; How, C.; Ito, E.; Liu, F.-F. Micro-RNAs as Diagnostic or Prognostic Markers in Human Epithelial Malignancies. *BMC Cancer* **2011**, *11* (1), 1.
(31) Paranjape, T.; Slack, F. J.; Weidhaas, J. B. MicroRNAs: Tools for Cancer Diagnostics. *Gut* **2009**, *58* (11), 1546–1554.
(32) Liu, H.-H.; Tian, X.; Li, Y.-J.; Wu, C.-A.; Zheng, C.-C. Microarray-Based Analysis of Stress-Regulated MicroRNAs in Arabidopsis Thaliana. *RNA* **2008**, *14* (5), 836–843.
(33) Abell, J. L.; Driskell, J. D.; Dluhy, R. A.; Tripp, R. A.; Zhao, Y.-P. Fabrication and Characterization of a Multiwell Array SERS Chip with Biological Applications. *Biosens. Bioelectron.* **2009**, *24* (12), 3663–3670.
(34) Mitchell, P. S.; Parkin, R. K.; Kroh, E. M.; Fritz, B. R.; Wyman, S. K.; Pogosova-Agadjanyan, E. L.; Peterson, A.; Noteboom, J.; O'Briant, K. C.; Allen, A.; et al. Circulating MicroRNAs as Stable Blood-Based Markers for Cancer Detection. *Proc. Natl. Acad. Sci.* **2008**, *105* (30), 10513–10518.
(35) Becker, C.; Hammerle-Fickinger, A.; Riedmaier, I.; Pfaffl, M. W. MRNA and MicroRNA Quality Control for RT-QPCR Analysis. *Methods* **2010**, *50* (4), 237–243.
(36) Heegaard, N. H. H.; Schetter, A. J.; Welsh, J. A.; Yoneda, M.; Bowman, E. D.; Harris, C. C. Circulating Micro-RNA Expression Profiles in Early Stage Nonsmall Cell Lung Cancer. *Int. J. Cancer* **2012**, *130* (6), 1378–1386.
(37) Wang, Z.; Gerstein, M.; Snyder, M. RNA-Seq: A Revolutionary Tool for Transcriptomics. *Nat. Rev. Genet.* **2009**, *10* (1), 57–63.
(38) Seeman, N. C. Nucleic Acid Junctions and Lattices. *J. Theor. Biol.* **1982**, *99* (2), 237–247.
(39) Adleman, L. Molecular Computation of Solutions to Combinatorial Problems. *Science* **1994**, *266* (5187), 1021-1024.
(40) Rothemund, P. W. K.; Papadakis, N.; Winfree, E. Algorithmic Self-Assembly of DNA Sierpinski Triangles. *PLoS Biol.* **2004**, *2* (12), e424.
(41) Seelig, G.; Soloveichik, D.; Zhang, D. Y.; Winfree, E. Enzyme-Free Nucleic Acid Logic Circuits. *Science* **2006**, *314* (5805), 1585–1588.
(42) Couny, F.; Benabid, F.; Roberts, P. J.; Light, P. S.; Raymer, M. G. Generation and Photonic Guidance of Multi-Octave Optical-Frequency Combs. *Science* **2007**, *318* (5853), 1118–1121.
(43) Frezza, B. M.; Cockroft, S. L.; Ghadiri, M. R. Modular Multi-Level Circuits from Immobilized DNA-Based Logic Gates. *J. Am. Chem. Soc.* **2007**, *129* (48), 14875–14879.
(44) Lubrich, D.; Lin, J.; Yan, J. A Contractile DNA Machine. *Angew. Chem. Int. Ed.* **2008**, *47* (37), 7026–7028.
(45) Goodman, R. P.; Heilemann, M.; Doose, S.; Erben, C. M.; Kapanidis, A. N.; Turberfield, A. J. Reconfigurable, Braced, Three-Dimensional DNA Nanostructures. *Nat. Nanotechnol.* **2008**, *3* (2), 93–96.
(46) Chen, X.; Ellington, A. D. Shaping up Nucleic Acid Computation. *Curr. Opin. Biotechnol.* **2010**, *21* (4), 392–400.
(47) He, H.-Z.; Chan, D. S.-H.; Leung, C.-H.; Ma, D.-L. G-Quadruplexes for Luminescent Sensing and Logic Gates. *Nucleic Acids Res.* **2013**, *41* (8), 4345–4359.
(48) Lagendijk, A. K.; Moulton, J. D.; Bakkers, J. Revealing Details: Whole Mount MicroRNA in Situ Hybridization Protocol for Zebrafish Embryos and Adult Tissues. *Biol. Open* **2012**, *1* (6), 566–569.

(49) Markey, F. B.; Ruezinsky, W.; Tyagi, S.; Batish, M. Fusion FISH Imaging: Single-Molecule Detection of Gene Fusion Transcripts In Situ. *PLoS ONE* **2014**, *9* (3), e93488.
(50) Chen, K. H.; Boettiger, A. N.; Moffitt, J. R.; Wang, S.; Zhuang, X. Spatially Resolved, Highly Multiplexed RNA Profiling in Single Cells. *Science* **2015**, *348* (6233), aaa6090–aaa6090.
(51) Moffitt, J. R.; Zhuang, X. RNA Imaging with Multiplexed Error Robust Fluorescence in Situ Hybridization. **2016**, 42.
(52) Moffitt, J. R.; Hao, J.; Bambah-Mukku, D.; Lu, T.; Dulac, C.; Zhuang, X. High-Performance Multiplexed Fluorescence in Situ Hybridization in Culture and Tissue with Matrix Imprinting and Clearing. *Proc. Natl. Acad. Sci.* **2016**, *113* (50), 14456–14461.
(53) Prigodich, A. E.; Randeria, P. S.; Briley, W. E.; Kim, N. J.; Daniel, W. L.; Giljohann, D. A.; Mirkin, C. A. Multiplexed Nanoflares: MRNA Detection in Live Cells. *Anal. Chem.* **2012**, *84* (4), 2062–2066.
(54) Kang, W. J.; Cho, Y. L.; Chae, J. R.; Lee, J. D.; Choi, K.-J.; Kim. Molecular Beacon-Based Bioimaging of Multiple MicroRNAs during Myogenesis. *Biomaterials* **2011**, *32* (7), 1915–1922.
(55) Baker, M. B.; Bao, G.; Searles, C. D. In Vitro Quantification of Specific MicroRNA Using Molecular Beacons. *Nucleic Acids Res.* **2012**, *40* (2), e13–e13.
(56) Buck, A. H.; Campbell, C. J.; Dickinson, P.; Mountford, C. P.; Stoquert, H. C.; Terry, J. G.; Evans, S. A. G.; Keane, L. M.; Su, T.-J.; Mount, A. R.; et al. DNA Nanoswitch as a Biosensor. *Anal. Chem.* **2007**, *79* (12), 4724–4728.
(57) Chen, A. K.; Davydenko, O.; Behlke, M. A.; Tsourkas, A. Ratiometric Bimolecular Beacons for the Sensitive Detection of RNA in Single Living Cells. *Nucleic Acids Res.* **2010**, *38* (14), e148–e148.
(58) Fan, D.; Zhu, J.; Zhai, Q.; Wang, E.; Dong, S. Cascade DNA Logic Device Programmed Ratiometric DNA Analysis and Logic Devices Based on a Fluorescent Dual-Signal Probe of a G-Quadruplex DNAzyme. *Chem Commun* **2016**, *52* (19), 3766–3769.
(59) Johnson, B. N.; Mutharasan, R. Biosensor-Based MicroRNA Detection: Techniques, Design, Performance, and Challenges. *The Analyst* **2014**, *139* (7), 1576.
(60) Barad, O.; Meiri, E.; Avniel, A.; Aharonov, R.; Barzilai, A.; Bentwich, I.; Einav, U.; Gilad, S.; Hurban, P.; Karov, Y.; et al. MicroRNA Expression Detected by Oligonucleotide Microarrays: System Establishment and Expression Profiling in Human Tissues. *Genome Res.* **2004**, *14* (12), 2486–2494.
(61) Benes, V.; Castoldi, M. Expression Profiling of MicroRNA Using Real-Time Quantitative PCR, How to Use It and What Is Available. *Methods* **2010**, *50* (4), 244–249.
(62) Arroyo, J. D.; Chevillet, J. R.; Kroh, E. M.; Ruf, I. K.; Pritchard, C. C.; Gibson, D. F.; Mitchell, P. S.; Bennett, C. F.; Pogosova-Agadjanyan, E. L.; Stirewalt, D. L.; et al. Argonaute2 Complexes Carry a Population of Circulating MicroRNAs Independent of Vesicles in Human Plasma. *Proc. Natl. Acad. Sci.* **2011**, *108* (12), 5003–5008.
(63) Pritchard, C. C.; Kroh, E.; Wood, B.; Arroyo, J. D.; Dougherty, K. J.; Miyaji, M. M.; Tait, J. F.; Tewari, M. Blood Cell Origin of Circulating MicroRNAs: A Cautionary Note for Cancer Biomarker Studies. *Cancer Prev. Res. (Phila. Pa.)* **2012**, *5* (3), 492–497.
(64) Pritchard, C. C.; Cheng, H. H.; Tewari, M. MicroRNA Profiling: Approaches and Considerations. *Nat. Rev. Genet.* **2012**, *13* (5), 358–369.

(65) Hanna, J.; Wimberly, H.; Kumar, S.; Slack, F.; Agarwal, S.; Rimm, D. Quantitative Analysis of MicroRNAs in Tissue Microarrays by in Situ Hybridization. *BioTechniques* **2012**, *52* (4).
(66) Koshiol, J.; Wang, E.; Zhao, Y.; Marincola, F.; Landi, M. T. Strengths and Limitations of Laboratory Procedures for MicroRNA Detection. *Cancer Epidemiol. Biomarkers Prev.* **2010**, *19* (4), 907–911.
(67) Avissar, M.; Christensen, B. C.; Kelsey, K. T.; Marsit, C. J. MicroRNA Expression Ratio Is Predictive of Head and Neck Squamous Cell Carcinoma. *Clin. Cancer Res.* **2009**, *15* (8), 2850–2855.
(68) Nhuber, W. S.; Fuchs, B.; Juretschko, S.; Amann, R. Improved Sensitivity of Whole-Cell Hybridization by the Combination of Horseradish Peroxidase-Labeled Oligonucleotides and Tyramide Signal Amplification. *APPL Env. MICROBIOL* **1997**, *63*, 6.
(69) Silahtaroglu, A. N.; Nolting, D.; Dyrskjøt, L.; Berezikov, E.; Møller, M.; Tommerup, N.; Kauppinen, S. Detection of MicroRNAs in Frozen Tissue Sections by Fluorescence in Situ Hybridization Using Locked Nucleic Acid Probes and Tyramide Signal Amplification. *Nat. Protoc.* **2007**, *2*, 2520.
(70) Chen, K. H.; Boettiger, A. N.; Moffitt, J. R.; Wang, S.; Zhuang, X. Spatially Resolved, Highly Multiplexed RNA Profiling in Single Cells. *Science* **2015**, *348* (6233), aaa6090–aaa6090.
(71) Moffitt, J. R.; Hao, J.; Bambah-Mukku, D.; Lu, T.; Dulac, C.; Zhuang, X. High-Performance Multiplexed Fluorescence in Situ Hybridization in Culture and Tissue with Matrix Imprinting and Clearing. *Proc. Natl. Acad. Sci.* **2016**, *113* (50), 14456–14461.
(72) Moffitt, J. R.; Hao, J.; Bambah-Mukku, D.; Lu, T.; Dulac, C.; Zhuang, X. High-Performance Multiplexed Fluorescence in Situ Hybridization in Culture and Tissue with Matrix Imprinting and Clearing. *Proc. Natl. Acad. Sci.* **2016**, *113* (50), 14456–14461.
(73) Chinen, A. B.; Guan, C. M.; Ferrer, J. R.; Barnaby, S. N.; Merkel, T. J.; Mirkin, C. A. Nanoparticle Probes for the Detection of Cancer Biomarkers, Cells, and Tissues by Fluorescence. *Chem. Rev.* **2015**, *115* (19), 10530–10574.
(74) Tsourkas, A.; Behlke, M. A.; Xu, Y.; Bao, G. Spectroscopic Features of Dual Fluorescence/Luminescence Resonance Energy-Transfer Molecular Beacons. *Anal. Chem.* **2003**, *75* (15), 3697–3703.
(75) Wang, D.; Fu, Y.; Yan, J.; Zhao, B.; Dai, B.; Chao, J.; Liu, H.; He, D.; Zhang, Y.; Fan, C.; et al. Molecular Logic Gates on DNA Origami Nanostructures for MicroRNA Diagnostics. *Anal. Chem.* **2014**, *86* (4), 1932–1936.
(76) Cheglakov, Z.; Cronin, T. M.; He, C.; Weizmann, Y. Live Cell MicroRNA Imaging Using Cascade Hybridization Reaction. *J. Am. Chem. Soc.* **2015**, *137* (19), 6116–6119.
(77) Almlie, C. K.; Larkey, N. E.; Burrows, S. M. Fluorescent MicroRNA Biosensors: A Comparison of Signal Generation to Quenching. *Anal Methods* **2015**, *7* (17), 7296–7310.
(78) Graybill, R. M.; Bailey, R. C. Emerging Biosensing Approaches for MicroRNA Analysis. *Anal. Chem.* **2016**, *88* (1), 431–450.
(79) Thaxton, C. S.; Georganopoulou, D. G.; Mirkin, C. A. Gold Nanoparticle Probes for the Detection of Nucleic Acid Targets. *Clin. Chim. Acta* **2006**, *363* (1–2), 120–126.
(80) Yang, W.-J.; Li, X.-B.; Li, Y.-Y.; Zhao, L.-F.; He, W.-L.; Gao, Y.-Q.; Wan, Y.-J.; Xia, W.; Chen, T.; Zheng, H.; et al. Quantification of MicroRNA by Gold Nanoparticle Probes. *Anal. Biochem.* **2008**, *376* (2), 183–188.

(81) Yeh, H.-C.; Sharma, J.; Shih, I.-M.; Vu, D. M.; Martinez, J. S.; Werner, J. H. A Fluorescence Light-Up Ag Nanocluster Probe That Discriminates Single-Nucleotide Variants by Emission Color. *J. Am. Chem. Soc.* **2012**, *134* (28), 11550–11558.
(82) Miao, P.; Tang, Y.; Wang, B.; Meng, F. Near-Infrared Ag2S Quantum Dots-Based DNA Logic Gate Platform for MiRNA Diagnostics. *Anal. Chem.* **2016**, *88* (15), 7567–7573.
(83) Cao, H.; Liu, S.; Tu, W.; Bao, J.; Dai, Z. A Carbon Nanotube/Quantum Dot Based Photoelectrochemical Biosensing Platform for the Direct Detection of MicroRNAs. *Chem Commun* **2014**, *50* (87), 13315–13318.
(84) Zhang, W.; Sun, H.; Yin, S.; Chang, J.; Li, Y.; Guo, X.; Yuan, Z. Bright Red-Emitting Polymer Dots for Specific Cellular Imaging. *J. Mater. Sci.* **2015**, *50* (16), 5571–5577.
(85) Mao, L.; Lu, Z.; He, N.; Zhang, L.; Deng, Y.; Duan, D. A New Method for Improving the Accuracy of MiRNA Detection with NaYF4:Yb,Er Upconversion Nanoparticles. *Sci. China Chem.* **2017**, *60* (1), 157–162.
(86) Teichmann, M.; Kopperger, E.; Simmel, F. C. Robustness of Localized DNA Strand Displacement Cascades. *ACS Nano* **2014**, *8* (8), 8487–8496.
(87) Zhang, D. Y.; Seelig, G. Dynamic DNA Nanotechnology Using Strand-Displacement Reactions. *Nat. Chem.* **2011**, *3* (2), 103–113.
(88) Wu, P.; Tu, Y.; Qian, Y.; Zhang, H.; Cai, C. DNA Strand-Displacement-Induced Fluorescence Enhancement for Highly Sensitive and Selective Assay of Multiple MicroRNA in Cancer Cells. *Chem Commun* **2014**, *50* (8), 1012–1014.
(89) Larkey, N. E.; Almlie, C. K.; Tran, V.; Egan, M.; Burrows, S. M. Detection of MiRNA Using a Double-Strand Displacement Biosensor with a Self-Complementary Fluorescent Reporter. *Anal. Chem.* **2014**, *86* (3), 1853–1863.
(90) Markham, N. R.; Zuker, M. DINAMelt Web Server for Nucleic Acid Melting Prediction. *Nucleic Acids Res.* **2005**, *33* (Web Server), W577–W581.
(91) Markham, N. R.; Zuker, M. *UNAFold: Software for Nucleic Acid Folding and Hybridization*; Humana Press, Totowa, NJ; Vol. II.
(92) Zadeh, J. N.; Steenberg, C. D.; Bois, J. S.; Wolfe, B. R.; Pierce, M. B.; Khan, A. R.; Dirks, R. M.; Pierce, N. A. NUPACK: Analysis and Design of Nucleic Acid Systems. *J. Comput. Chem.* **2011**, *32* (1), 170–173.
(93) Ge, L.; Wang, W.; Sun, X.; Hou, T.; Li, F. Versatile and Programmable DNA Logic Gates on Universal and Label-Free Homogeneous Electrochemical Platform. *Anal. Chem.* **2016**, *88* (19), 9691–9698.
(94) Yu, S.; Wang, Y.; Jiang, L.-P.; Bi, S.; Zhu, J.-J. Cascade Amplification-Mediated In Situ Hot-Spot Assembly for MicroRNA Detection and Molecular Logic Gate Operations. *Anal Chem* **2018**, *90* (7), 4544–4551.
(95) Bi, S.; Zhang, J.; Hao, S.; Ding, C.; Zhang, S. Exponential Amplification for Chemiluminescence Resonance Energy Transfer Detection of MicroRNA in Real Samples Based on a Cross-Catalyst Strand-Displacement Network. *Anal. Chem.* **2011**, *83* (10), 3696–3702.
(96) Marras, S. A.; Kramer, F. R.; Tyagi, S. Efficiencies of Fluorescence Resonance Energy Transfer and Contact-Mediated Quenching in Oligonucleotide Probes. *Nucleic Acids Res.* **2002**, *30* (21), e122–e122.
(97) Hussain, S. A. An Introduction to Fluorescence Resonance Energy Transfer (FRET). *ArXiv Prepr. ArXiv09081815* **2009**.

(98) Graybill, R. M.; Bailey, R. C. Emerging Biosensing Approaches for MicroRNA Analysis. *Anal. Chem.* **2016**, *88* (1), 431–450.
(99) Guttilla, I. K.; White, B. A. Coordinate Regulation of FOXO1 by MiR-27a, MiR-96, and MiR-182 in Breast Cancer Cells. *J. Biol. Chem.* **2009**, *284* (35), 23204–23216.
(100) Amaral, P. P.; John S. Mattick. Noncoding RNA in Development. *Mamm. Genome* **2008**, *19* (7–8), 454–492.
(101) Choudhuri, S. Small Noncoding RNAs: Biogenesis, Function, and Emerging Significance in Toxicology. *J. Biochem. Mol. Toxicol.* **2010**, *24* (3), 195–216.
(102) Mattick, J. S.; Makunin, I. V. Non-Coding RNA. *Hum. Mol. Genet.* **2006**, *15* (suppl_1), R17–R29.
(103) Place, R. F.; Li, L.-C.; Pookot, D.; Noonan, E. J.; Dahiya, R. MicroRNA-373 Induces Expression of Genes with Complementary Promoter Sequences. *Proc. Natl. Acad. Sci.* **2008**, *105* (5), 1608–1613.
(104) Khalil, A. M.; Guttman, M.; Huarte, M.; Garber, M.; Raj, A.; Rivea Morales, D.; Thomas, K.; Presser, A.; Bernstein, B. E.; van Oudenaarden, A.; et al. Many Human Large Intergenic Noncoding RNAs Associate with Chromatin-Modifying Complexes and Affect Gene Expression. *Proc. Natl. Acad. Sci.* **2009**, *106* (28), 11667–11672.
(105) Mercer, T. R.; Dinger, M. E.; Sunkin, S. M.; Mehler, M. F.; Mattick, J. S. Specific Expression of Long Noncoding RNAs in the Mouse Brain. *Proc. Natl. Acad. Sci.* **2008**, *105* (2), 716–721.
(106) Furuno, M.; Pang, K. C.; Ninomiya, N.; Fukuda, S.; Frith, M. C.; Bult, C.; Kai, C.; Kawai, J.; Carninci, P.; Hayashizaki, Y.; et al. Clusters of Internally Primed Transcripts Reveal Novel Long Noncoding RNAs. *PLoS Genet.* **2006**, *2* (4), e37.
(107) Kapranov, P. Large-Scale Transcriptional Activity in Chromosomes 21 and 22. *Science* **2002**, *296* (5569), 916–919.
(108) Nakaya, H. I.; Amaral, P. P.; Louro, R.; Lopes, A.; Fachel, A. A.; Moreira, Y. B.; El-Jundi, T. A.; da Silva, A. M.; Reis, E. M.; Verjovski-Almeida, S. Genome Mapping and Expression Analyses of Human Intronic Noncoding RNAs Reveal Tissue-Specific Patterns and Enrichment in Genes Related to Regulation of Transcription. *Genome Biol.* **2007**, *8* (3), R43.
(109) Ravasi, T. Experimental Validation of the Regulated Expression of Large Numbers of Non-Coding RNAs from the Mouse Genome. *Genome Res.* **2005**, *16* (1), 11–19.
(110) Carleton, M.; Cleary, M. A.; Linsley, P. S. MicroRNAs and Cell Cycle Regulation. *Cell Cycle* **2007**, *6* (17), 2127–2132.
(111) Ivey, K. N.; Srivastava, D. MicroRNAs as Regulators of Differentiation and Cell Fate Decisions. *Cell Stem Cell* **2010**, *7* (1), 36–41.
(112) Kumar, V.; Westra, H.-J.; Karjalainen, J.; Zhernakova, D. V.; Esko, T.; Hrdlickova, B.; Almeida, R.; Zhernakova, A.; Reinmaa, E.; Võsa, U.; et al. Human Disease-Associated Genetic Variation Impacts Large Intergenic Non-Coding RNA Expression. *PLoS Genet.* **2013**, *9* (1), e1003201.
(113) Reis, E. M.; Ojopi, E. P. B.; Alberto, F. L.; Rahal, P.; Tsukumo, F.; Mancini, U. M.; Guimarães, G. S.; Thompson, G. M. A.; Camacho, C.; Miracca, E.; et al. Large-Scale Transcriptome Analyses Reveal New Genetic Marker Candidates of Head, Neck, and Thyroid Cancer. *Cancer Res.* **2005**, *65* (5), 1693–1699.

(114) Iorio, M. V.; Ferracin, M.; Liu, C.-G.; Veronese, A.; Spizzo, R.; Sabbioni, S.; Magri, E.; Pedriali, M.; Fabbri, M.; Campiglio, M.; et al. MicroRNA Gene Expression Deregulation in Human Breast Cancer. *Cancer Res.* **2005**, *65* (16), 7065–7070.
(115) Perez, D. S.; Hoage, T. R.; Pritchett, J. R.; Ducharme-Smith, A. L.; Halling, M. L.; Ganapathiraju, S. C.; Streng, P. S.; Smith, D. I. Long, Abundantly Expressed Non-Coding Transcripts Are Altered in Cancer. *Hum. Mol. Genet.* **2008**, *17* (5), 642–655.
(116) Krutilina, R.; Sun, W.; Sethuraman, A.; Brown, M.; Seagroves, T. N.; Pfeffer, L. M.; Ignatova, T.; Fan, M. MicroRNA-18a Inhibits Hypoxia-Inducible Factor 1α Activity and Lung Metastasis in Basal Breast Cancers. *Breast Cancer Res.* **2014**, *16* (4), 1.
(117) Krol, J.; Loedige, I.; Filipowicz, W. The Widespread Regulation of MicroRNA Biogenesis, Function and Decay. *Nat. Rev. Genet.* **2010**, *11* (9), 597–610.
(118) Yang, N.; Coukos, G.; Zhang, L. MicroRNA Epigenetic Alterations in Human Cancer: One Step Forward in Diagnosis and Treatment. *Int. J. Cancer* **2007**, *122* (5), 963–968.
(119) Mousa, S. Biosensors: The New Wave in Cancer Diagnosis. *Nanotechnol. Sci. Appl.* **2010**, 1.
(120) Mogilyansky, E.; Rigoutsos, I. The MiR-17/92 Cluster: A Comprehensive Update on Its Genomics, Genetics, Functions and Increasingly Important and Numerous Roles in Health and Disease. *Cell Death Differ.* **2013**, *20* (12), 1603–1614.
(121) Camps, C.; Buffa, F. M.; Colella, S.; Moore, J.; Sotiriou, C.; Sheldon, H.; Harris, A. L.; Gleadle, J. M.; Ragoussis, J. Hsa-MiR-210 Is Induced by Hypoxia and Is an Independent Prognostic Factor in Breast Cancer. *Clin. Cancer Res.* **2008**, *14* (5), 1340–1348.
(122) Guttilla, I. K.; White, B. A. Coordinate Regulation of FOXO1 by MiR-27a, MiR-96, and MiR-182 in Breast Cancer Cells. *J. Biol. Chem.* **2009**, *284* (35), 23204–23216.
(123) Corcoran, C.; Friel, A. M.; Duffy, M. J.; Crown, J.; O'Driscoll, L. Intracellular and Extracellular MicroRNAs in Breast Cancer. *Clin. Chem.* **2011**, *57* (1), 18–32.
(124) Gilkes, D. M.; Semenza, G. L. Role of Hypoxia-Inducible Factors in Breast Cancer Metastasis. *Future Oncol.* **2013**, *9* (11), 1623–1636.
(125) Hald, S. M.; Bremnes, R. M.; Al-Shibli, K.; Al-Saad, S.; Andersen, S.; Stenvold, H.; Busund, L.-T.; Donnem, T. CD4/CD8 Co-Expression Shows Independent Prognostic Impact in Resected Non-Small Cell Lung Cancer Patients Treated with Adjuvant Radiotherapy. *Lung Cancer* **2013**, *80* (2), 209–215.
(126) Eilertsen, M.; Andersen, S.; Al-Saad, S.; Richardsen, E.; Stenvold, H.; Hald, S. M.; Al-Shibli, K.; Donnem, T.; Busund, L.-T.; Bremnes, R. M. Positive Prognostic Impact of MiR-210 in Non-Small Cell Lung Cancer. *Lung Cancer* **2014**, *83* (2), 272–278.
(127) Resnick, K. E.; Alder, H.; Hagan, J. P.; Richardson, D. L.; Croce, C. M.; Cohn, D. E. The Detection of Differentially Expressed MicroRNAs from the Serum of Ovarian Cancer Patients Using a Novel Real-Time PCR Platform. *Gynecol. Oncol.* **2009**, *112* (1), 55–59.
(128) O'Connell, R. M.; Rao, D. S.; Baltimore, D. MicroRNA Regulation of Inflammatory Responses. *Annu. Rev. Immunol.* **2012**, *30* (1), 295–312.
(129) Semenza, G. L. TranscriptionalRegulation by Hypoxia-InducibleFactor I Molecular Mechanisms of Oxygen Homeostasis. *Trends Cardiovasc. Med.* **1996**, *6* (5), 151–157.
(130) Lai, N.; Dong, Q.; Ding, H.; Miao, Z.; Lin, Y. MicroRNA-210 Overexpression Predicts Poorer Prognosis in Glioma Patients. *J. Clin. Neurosci.* **2014**, *21* (5), 755–760.
(131) Westholm, J. O.; Lai, E. C. Mirtrons: MicroRNA Biogenesis via Splicing. *Biochimie* **2011**, *93* (11), 1897–1904.

(132) Diederichs, S.; Haber, D. A. Dual Role for Argonautes in MicroRNA Processing and Posttranscriptional Regulation of MicroRNA Expression. *Cell* **2007**, *131* (6), 1097–1108.
(133) Okamura, K.; Phillips, M. D.; Tyler, D. M.; Duan, H.; Chou, Y.; Lai, E. C. The Regulatory Activity of MicroRNA* Species Has Substantial Influence on MicroRNA and 3′ UTR Evolution. *Nat. Struct. Mol. Biol.* **2008**, *15* (4), 354–363.
(134) Yang, J.-S.; Phillips, M. D.; Betel, D.; Mu, P.; Ventura, A.; Siepel, A. C.; Chen, K. C.; Lai, E. C. Widespread Regulatory Activity of Vertebrate MicroRNA* Species. *RNA* **2011**, *17* (2), 312–326.
(135) Rhoades, M. W.; Reinhart, B. J.; Lim, L. P.; Burge, C. B.; Bartel, B.; Bartel, D. P. Prediction of Plant MicroRNA Targets. *Cell* **2002**, *110* (4), 513–520.
(136) Llave, C. Cleavage of Scarecrow-like MRNA Targets Directed by a Class of Arabidopsis MiRNA. *Science* **2002**, *297* (5589), 2053–2056.
(137) Chen, X. A MicroRNA as a Translational Repressor of APETALA2 in Arabidopsis Flower Development. *Science* **2004**, *303* (5666), 2022–2025.
(138) Krek, A.; Grün, D.; Poy, M. N.; Wolf, R.; Rosenberg, L.; Epstein, E. J.; MacMenamin, P.; da Piedade, I.; Gunsalus, K. C.; Stoffel, M.; et al. Combinatorial MicroRNA Target Predictions. *Nat. Genet.* **2005**, *37* (5), 495–500.
(139) Kalsotra, A.; Wang, K.; Li, P. F.; Cooper, T. A. MicroRNAs Coordinate an Alternative Splicing Network during Mouse Postnatal Heart Development. *Genes Dev.* **2010**, *24* (7), 653–658.
(140) Wang, J.; Haubrock, M.; Cao, K.-M.; Hua, X.; Zhang, C.-Y.; Wingender, E.; Li, J. Regulatory Coordination of Clustered MicroRNAs Based on MicroRNA-Transcription Factor Regulatory Network. *BMC Syst. Biol.* **2011**, *5* (1), 199.
(141) Calin, G. A.; Sevignani, C.; Dumitru, C. D.; Hyslop, T.; Noch, E.; Yendamuri, S.; Shimizu, M.; Rattan, S.; Bullrich, F.; Negrini, M.; et al. Human MicroRNA Genes Are Frequently Located at Fragile Sites and Genomic Regions Involved in Cancers. *Proc. Natl. Acad. Sci.* **2004**, *101* (9), 2999–3004.
(142) Camps, C.; Saini, H. K.; Mole, D. R.; Choudhry, H.; Reczko, M.; Guerra-Assunção, J. A.; Tian, Y.-M.; Buffa, F. M.; Harris, A. L.; Hatzigeorgiou, A. G.; et al. Integrated Analysis of MicroRNA and MRNA Expression and Association with HIF Binding Reveals the Complexity of MicroRNA Expression Regulation under Hypoxia. *Mol. Cancer* **2014**, *13* (1), 1.
(143) Kulshreshtha, R.; Ferracin, M.; Wojcik, S. E.; Garzon, R.; Alder, H.; Agosto-Perez, F. J.; Davuluri, R.; Liu, C.-G.; Croce, C. M.; Negrini, M.; et al. A MicroRNA Signature of Hypoxia. *Mol. Cell. Biol.* **2007**, *27* (5), 1859–1867.
(144) Harris, A. L. HYPOXIA — A KEY REGULATORY FACTOR IN TUMOUR GROWTH. *Nat. Rev. Cancer* **2002**, *2* (1), 38–47.
(145) Crosby, M. E.; Kulshreshtha, R.; Ivan, M.; Glazer, P. M. MicroRNA Regulation of DNA Repair Gene Expression in Hypoxic Stress. *Cancer Res.* **2009**, *69* (3), 1221–1229.
(146) Denk, W.; Strickler, J. H.; Webb, W. W.; others. Two-Photon Laser Scanning Fluorescence Microscopy. *Science* **1990**, *248* (4951), 73–76.
(147) helmchen, F.; Denk, W. Deep Tissue Two-Photon Microscope. *Nat. Methods* **2005**, *2* (12), 932–940.
(148) Chen, Y.-J.; Groves, B.; Muscat, R. A.; Seelig, G. DNA Nanotechnology from the Test Tube to the Cell. *Nat. Nanotechnol.* **2015**, *10* (9), 748–760.

(149) Lu, Y.; Liu, J. Functional DNA Nanotechnology: Emerging Applications of DNAzymes and Aptamers. *Curr. Opin. Biotechnol.* **2006**, *17* (6), 580–588.
(150) Pinheiro, A. V.; Han, D.; Shih, W. M.; Yan, H. Challenges and Opportunities for Structural DNA Nanotechnology. *Nat. Nanotechnol.* **2011**, *6* (12), 763–772.
(151) Qian, L.; Winfree, E.; Bruck, J. Neural Network Computation with DNA Strand Displacement Cascades. *Nature* **2011**, *475* (7356), 368–372.
(152) Zhang, F.; Nangreave, J.; Liu, Y.; Yan, H. Structural DNA Nanotechnology: State of the Art and Future Perspective. *J. Am. Chem. Soc.* **2014**, *136* (32), 11198–11211.
(153) Phillips, A.; Cardelli, L. A Programming Language for Composable DNA Circuits. *J. R. Soc. Interface* **2009**, *6* (Suppl_4), S419–S436.
(154) Zhu, J.; Zhang, L.; Li, T.; Dong, S.; Wang, E. Enzyme-Free Unlabeled DNA Logic Circuits Based on Toehold-Mediated Strand Displacement and Split G-Quadruplex Enhanced Fluorescence. *Adv. Mater.* **2013**, *25* (17), 2440–2444.
(155) Srinivas, N.; Ouldridge, T. E.; Sulc, P.; Schaeffer, J. M.; Yurke, B.; Louis, A. A.; Doye, J. P. K.; Winfree, E. On the Biophysics and Kinetics of Toehold-Mediated DNA Strand Displacement. *Nucleic Acids Res.* **2013**, *41* (22), 10641–10658.
(156) Zhang, D. Y.; Winfree, E. Control of DNA Strand Displacement Kinetics Using Toehold Exchange. *J AM CHEM SOC* **2009**, *131*, 17303–17314.
(157) Lu, J.; Getz, G.; Miska, E. A.; Alvarez-Saavedra, E.; Lamb, J.; Peck, D.; Sweet-Cordero, A.; Ebert, B. L.; Mak, R. H.; Ferrando, A. A.; et al. MicroRNA Expression Profiles Classify Human Cancers. *Nature* **2005**, *435* (7043), 834–838.
(158) Sassen, S.; Miska, E. A.; Caldas, C. MicroRNA—Implications for Cancer. *Virchows Arch.* **2008**, *452* (1), 1–10.
(159) Kantharidis, P.; Wang, B.; Carew, R. M.; Lan, H. Y. Diabetes Complications: The MicroRNA Perspective. *Diabetes* **2011**, *60* (7), 1832–1837.
(160) Picuri, J. M.; Frezza, B. M.; Ghadiri, M. R. Universal Translators for Nucleic Acid Diagnosis. *J. Am. Chem. Soc.* **2009**, *131* (26), 9368–9377.
(161) Sempere, L. F.; Christensen, M.; Silahtaroglu, A.; Bak, M.; Heath, C. V.; Schwartz, G.; Wells, W.; Kauppinen, S.; Cole, C. N. Altered MicroRNA Expression Confined to Specific Epithelial Cell Subpopulations in Breast Cancer. *Cancer Res.* **2007**, *67* (24), 11612–11620.
(162) Place, R. F.; Li, L.-C.; Pookot, D.; Noonan, E. J.; Dahiya, R. MicroRNA-373 Induces Expression of Genes with Complementary Promoter Sequences. *Proc. Natl. Acad. Sci.* **2008**, *105* (5), 1608–1613.
(163) Tavazoie, S. F.; Alarcón, C.; Oskarsson, T.; Padua, D.; Wang, Q.; Bos, P. D.; Gerald, W. L.; Massagué, J. Endogenous Human MicroRNAs That Suppress Breast Cancer Metastasis. *Nature* **2008**, *451* (7175), 147–152.
(164) Chen, H.-C.; Chen, G.-H.; Chen, Y.-H.; Liao, W.-L.; Liu, C.-Y.; Chang, K.-P.; Chang, Y.-S.; Chen, S.-J. MicroRNA Deregulation and Pathway Alterations in Nasopharyngeal Carcinoma. *Br. J. Cancer* **2009**, *100* (6), 1002–1011.
(165) Shenouda, S. K.; Alahari, S. K. MicroRNA Function in Cancer: Oncogene or a Tumor Suppressor? *Cancer Metastasis Rev.* **2009**, *28* (3–4), 369–378.
(166) Qin, X.; Wang, X.; Wang, Y.; Tang, Z.; Cui, Q.; Xi, J.; J. Li, Y.-S.; Chien, S.; Wang, N. MicroRNA-19a Mediates the Suppressive Effect of Laminar Flow on Cyclin D1 Expression in Human Umbilical Vein Endothelial Cells. *Proc. Natl. Acad. Sci.* **2010**, *107* (7), 3240–3244.

(167) Deng, R.; Tang, L.; Tian, Q.; Wang, Y.; Lin, L.; Li, J. Toehold-Initiated Rolling Circle Amplification for Visualizing Individual MicroRNAs In Situ in Single Cells. *Angew. Chem. Int. Ed.* **2014**, *53* (9), 2389–2393.
(168) Li, W.; Yang, Y.; Yan, H.; Liu, Y. Three-Input Majority Logic Gate and Multiple Input Logic Circuit Based on DNA Strand Displacement. *Nano Lett.* **2013**, *13* (6), 2980–2988.
(169) Tyagi, S.; Kramer, F. R. Molecular Beacons: Probes That Fluoresce upon Hybridization. *Nat. Biotechnol.* **1996**, *14*, 303–306.
(170) Vaisocherová, H.; Šípová, H.; Víšová, I.; Bocková, M.; Špringer, T.; Laura Ermini, M.; Song, X.; Krejčík, Z.; Chrastinová, L.; Pastva, O.; et al. Rapid and Sensitive Detection of Multiple MicroRNAs in Cell Lysate by Low-Fouling Surface Plasmon Resonance Biosensor. *Biosens. Bioelectron.* **2015**, *70*, 226–231.
(171) He, K.; Liao, R.; Cai, C.; Liang, C.; Liu, C.; Chen, X. Y-Shaped Probe for Convenient and Label-Free Detection of MicroRNA-21 in Vitro. *Anal. Biochem.* **2016**, *499*, 8–14.
(172) Ding, X.; Yan, Y.; Li, S.; Zhang, Y.; Cheng, W.; Cheng, Q.; Ding, S. Surface Plasmon Resonance Biosensor for Highly Sensitive Detection of MicroRNA Based on DNA Super-Sandwich Assemblies and Streptavidin Signal Amplification. *Anal. Chim. Acta* **2015**, *874*, 59–65.
(173) Larkey, N. E.; Brucks, C. N.; Lansing, S. S.; Le, S. D.; Smith, N. M.; Tran, V.; Zhang, L.; Burrows, S. M. Molecular Structure and Thermodynamic Predictions to Create Highly Sensitive MicroRNA Biosensors. *Anal. Chim. Acta* **2016**, *909*, 109–120.
(174) Dirks, R. M. Paradigms for Computational Nucleic Acid Design. *Nucleic Acids Res.* **2004**, *32* (4), 1392–1403.
(175) Dirks, R. M.; Bois, J. S.; Schaeffer, J. M.; Winfree, E.; Pierce, N. A. Thermodynamic Analysis of Interacting Nucleic Acid Strands. *SIAM Rev.* **2007**, *49* (1), 65–88.
(176) Larkey, N. E.; Zhang, L.; Lansing, S. S.; Tran, V.; Seewaldt, V. L.; Burrows, S. M. Förster Resonance Energy Transfer to Impart Signal-on and -off Capabilities in a Single MicroRNA Biosensor. *The Analyst* **2016**, *141* (22), 6239–6250.
(177) Dinger, M. E.; Pang, K. C.; Mercer, T. R.; Mattick, J. S. Differentiating Protein-Coding and Noncoding RNA: Challenges and Ambiguities. *PLoS Comput. Biol.* **2008**, *4* (11), e1000176.
(178) Zhu, J.; Zhang, L.; Dong, S.; Wang, E. Four-Way Junction-Driven DNA Strand Displacement and Its Application in Building Majority Logic Circuit. *ACS Nano* **2013**, *7* (11), 10211–10217.
(179) Zhang, P.; He, Z.; Wang, C.; Chen, J.; Zhao, J.; Zhu, X.; Li, C.-Z.; Min, Q.; Zhu, J.-J. *In Situ* Amplification of Intracellular MicroRNA with MNAzyme Nanodevices for Multiplexed Imaging, Logic Operation, and Controlled Drug Release. *ACS Nano* **2015**, *9* (1), 789–798.
(180) Chakraborty, B.; Sha, R.; Seeman, N. C. A DNA-Based Nanomechanical Device with Three Robust States. *Proc. Natl. Acad. Sci.* **2008**, *105* (45), 17245–17249.
(181) Lee, H.; Shapiro, S. J.; Chapin, S. C.; Doyle, P. S. Encoded Hydrogel Microparticles for Sensitive and Multiplex MicroRNA Detection Directly from Raw Cell Lysates. *Anal. Chem.* **2016**, *88* (6), 3075–3081.
(182) Zhang, L.; Bluhm, A. M.; Chen, K.-J.; Larkey, N. E.; Burrows, S. M. Performance of Nano-Assembly Logic Gates with a DNA Multi-Hairpin Motif. *Nanoscale* **2017**.
(183) Majlessi, M. Advantages of 2'-O-Methyl Oligoribonucleotide Probes for Detecting RNA Targets. *Nucleic Acids Res.* **1998**, *26* (9), 2224–2229.

(184) Larkey, N. E.; Almlie, C. K.; Tran, V.; Egan, M.; Burrows, S. M. Detection of MiRNA Using a Double-Strand Displacement Biosensor with a Self-Complementary Fluorescent Reporter. *Anal. Chem.* **2014**, *86* (3), 1853–1863.
(185) Borgatti, M.; Romanelli, A.; Saviano, M.; Pedone, C.; Lampronti, I.; Breda, L.; Nastruzzi, C.; Bianchi, N.; Mischiati, C.; Gambari, R. Resistance of Decoy PNA-DNA Chimeras to Enzymatic Degradation in Cellular Extracts and Serum. *Oncol. Res.* **2003**, *13* (5), 279–287.
(186) Wang, L.; Yang, C. J.; Medley, C. D.; Benner, S. A.; Tan, W. Locked Nucleic Acid Molecular Beacons. *J. Am. Chem. Soc.* **2005**, *127* (45), 15664–15665.
(187) Martinez, K.; Estevez, M.-C.; Wu, Y.; Phillips, J. A.; Medley, C. D.; Tan, W. Locked Nucleic Acid Based Beacons for Surface Interaction Studies and Biosensor Development. *Anal. Chem.* **2009**, *81* (9), 3448–3454.
(188) Li, J.; Li, X.; Li, Y.; Yang, H.; Wang, L.; Qin, Y.; Liu, H.; Fu, L.; Guan, X.-Y. Cell-Specific Detection of MiR-375 Downregulation for Predicting the Prognosis of Esophageal Squamous Cell Carcinoma by MiRNA In Situ Hybridization. *PLoS ONE* **2013**, *8* (1), e53582.
(189) Lee, M.; Kim, S. W. Polyethylene Glycol-Conjugated Copolymers for Plasmid DNA Delivery. *Pharm. Res.* **2005**, *22* (1), 1–10.
(190) Mao, H.-Q.; Roy, K.; Troung-Le, V. L.; Janes, K. A.; Lin, K. Y.; Wang, Y.; August, J. T.; Leong, K. W. Chitosan-DNA Nanoparticles as Gene Carriers: Synthesis, Characterization and Transfection Efficiency. *J. Controlled Release* **2001**, *70* (3), 399–421.
(191) Rumney IV, S.; Kool, E. T. DNA Recognition by Hybrid Oligoether–Oligodeoxynucleotide Macrocycles*. *Angew. Chem. Int. Ed. Engl.* **1992**, *31* (12), 1617–1619.
(192) Hudziak, R. M.; Barofsky, E.; Barofsky, D. F.; Weller, D. L.; Huang, S. B.; Weller, D. D. Resistance of Morpholino Phosphorodiamidate Oligomers to Enzymatic Degradation. *Antisense Nucleic Acid Drug Dev.* **1996**, *6* (4), 267–272.
(193) Hudziak, R. M.; Baerofsky, E.; Baerofsky, D. F.; Weller, D. L.; Huang, S.-B. Resistance of Morpholino Phosphorodiamidate Oligomers to Enzymatic Degradation. *Antisense Nucleic Acid Drug Dev.* **1996**, *6* (4).
(194) Blum, M.; De Robertis, E. M.; Wallingford, J. B.; Niehrs, C. Morpholinos: Antisense and Sensibility. *Dev. Cell* **2015**, *35* (2), 145–149.
(195) Demidov, V. V.; Potaman, V. N.; Frank-Kamenetskil, M. D.; Egholm, M.; Buchard, O.; Sönnichsen, S. H.; Nlelsen, P. E. Stability of Peptide Nucleic Acids in Human Serum and Cellular Extracts. *Biochem. Pharmacol.* **1994**, *48* (6), 1310–1313.
(196) Nielsen, P. E.; Egholm, M. An Introduction to Peptide Nucleic Acid. 17.
(197) Gray, G. D.; Basu, S.; Wickstrom, E. Transformed and Immortalized Cellular Uptake of IOligodeoxynucleoside Phosphorothioates, 3'-Alkylamino Oligodeoxynucleotides, Z'cO-Methyl Oligoribonucleotides, Oligodeoxynucleoside MethLylphosphonates, and Peptide Nucleic Acids. 12.
(198) Buckhout-White, S.; Spillmann, C. M.; Algar, W. R.; Khachatrian, A.; Melinger, J. S.; Goldman, E. R.; Ancona, M. G.; Medintz, I. L. Assembling Programmable FRET-Based Photonic Networks Using Designer DNA Scaffolds. *Nat. Commun.* **2014**, *5*.
(199) Ryoo, S.-R.; Lee, J.; Yeo, J.; Na, H.-K.; Kim, Y.-K.; Jang, H.; Lee, J. H.; Han, S. W.; Lee, Y.; Kim, V. N.; et al. Quantitative and Multiplexed MicroRNA Sensing in Living

Cells Based on Peptide Nucleic Acid and Nano Graphene Oxide (PANGO). *ACS Nano* **2013**, *7* (7), 5882–5891.

(200) Almlie, C. K.; Hsiao, A.; Burrows, S. M. Dye-Specific Wavelength Offsets to Resolve Spectrally Overlapping and Co-Localized Two-Photon Induced Fluorescence. *Anal. Chem.* **2016**, *88* (2), 1462–1467.

(201) Gliddon, H. D.; Howes, P. D.; Kaforou, M.; Levin, M.; Stevens, M. M. A Nucleic Acid Strand Displacement System for the Multiplexed Detection of Tuberculosis-Specific MRNA Using Quantum Dots. *Nanoscale* **2016**, *8* (19), 10087–10095.

(202) Calin, G. A.; Croce, C. M. MicroRNA Signatures in Human Cancers. *Nat. Rev. Cancer* **2006**, *6* (11), 857–866.

(203) SantaLucia, J. A Unified View of Polymer, Dumbbell, and Oligonucleotide DNA Nearest-Neighbor Thermodynamics. *Proc. Natl. Acad. Sci.* **1998**, *95* (4), 1460–1465.

APPENDICES

Appendix I.
Supplemental Information for Chapter 2

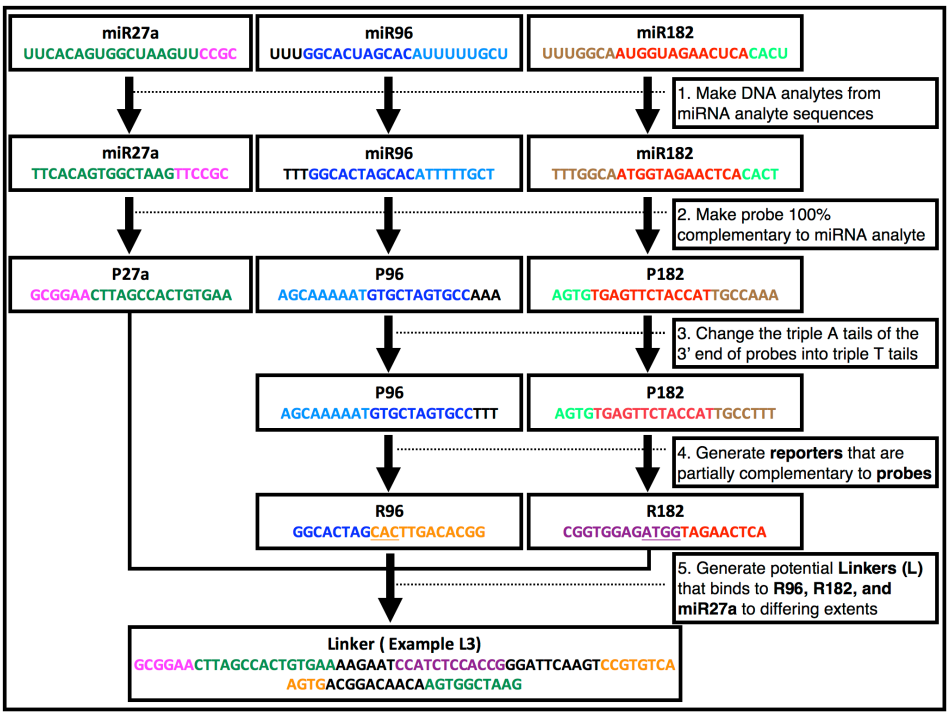

Figure A1.1 The flow chart of the nano-assembly logic gate design process. Matching colors indicate complementary base pairs. Mismatched colors indicate non-complementary base pairs.

A1.1 Reporter and Linker filtration process

The Matlab program produced hundreds to thousands of potential reporters and linkers. These reporter candidates were filtered to rule out those having cross reactivity with off-analyte nucleic acids (other miRs, mRNA, etc.), non-corresponding probes, non-corresponding regions on the linker, and other reporter strands. The evaluation of cross reactivity was based on the thermodynamic estimates by using the "Two-state melting (Hybridization)" (TSM) function from the DINAMelt Web Server.

A similar Matlab filtering process for the reporters was applied to the linkers. To fulfill the many requirements an ideal linker should be, the computer generated linkers had to go through a similar but more complicated filtration process than the reporters did. The linker filtering process includes: 1) estimating the secondary structure and thermodynamics of the multi-hairpin linker through "Quikfold" function (Table A1.5 A), 2) evaluating the off-analyte cross reactivity with the multi-hairpin linker through the TSM function (results in Table A1.6-A1.8), 3) evaluating the analyte (miR27a, R182, and R96) binding thermodynamic data through the TSM function (results

in Table A1.6-A1.8), 4) evaluating the molar fraction of the logic circuits ON state formed when single, double, and all three analytes were present through "Hybridization of two different strands" function (Figure A1.5, A1.6), 5) comparing the probability of forming intramolecular hairpin secondary structure and intermolecular homodimer structure through "Homodimer Stimulations" function (no data shown), and 6) analyzing the number of H-bonds formed in the linker's intramolecular hairpin secondary structure and between linker and analyte/off-analytes (Table A1.5 C-F). All the functions mentioned above were from the DINAMelt Web Server and the following settings were used: hybridization temperature of 37 ℃, Na^+ concentration of 10 mM, Mg^{2+} concentration of 2.5 mM, and strand concentration of 100 nM.

Table A1.1 The linkers' sequences. The sequences (from 5' to 3') in blue, purple, and orange were binding regions for miR27a (HS-27a), R182 (HR-182), and R96 (HR-96) respectively.

L0	GCGGAACTTAGCCACTGTGAACGAAAGCCCTGATCTCCAGCATTAGGGCTTTATGGCCTTGTTTTGTGAATGCAAGGCCATAACGTTCACAGTGGC
L1	GCGGAACTTAGCCACTGTGAAGATATCGCCATCTCCACCGATATCAAGTCCGTGTCAAGTGACGGACAAACAGTGGCTAA
L2	GCGGAACTTAGCCACTGTGAAAAGAATCCATCTCCACCGGGATTCAAGTCCGTGTCAAGTGACGGACAACAAGTGGCTAA
L3	GCGGAACTTAGCCACTGTGAAAAGAATCCATCTCCACCGGGATTCAAGTCCGTGTCAAGTGACGGACAACAAGTGGCTAAG
L4	GCGGAACTTAGCCACTGTGAAGATATCGCCATCTCCACCGATATCAAGTCCGTGTCAAGTGACGGACAACACAGTGGCTAAG
L5	GCGGAACTTAGCCACTGTGAAGATATCGCCATCTCCACCGATATCAAGTCCGTGTCAAGTGACGGACAAACAGTGGCTAAG

Table A1.2 The sequences of analyte miRs, probes, and reporters

miR27a	5'-TTCACAGTGGCTAAGTTCCGC-3'
miR96	5'-TTTGGCACTAGCACATTTTTGCT-3'
miR182	5'-TTTGGCAATGGTAGAACTCACACT-3'
R96 for L1 to L5	5'-GGCACTAGCACTTGACACGG/iSpC3//iSpC3//36-FAM/-3'
R182 for L1 to L5	5'-/5ATTO633N//iSpC3//iSpC3/CGGTGGAGATGGTAGAACTCA-3'
P96	5'-AGCAAAAATGTGCTAGTGCCTTT-3'
P182	5'-AGTGTGAGTTCTACCATTGCCTTT-3'
R96 for L0	5'-/5BiotinTEG/TTTGGCACTAGCACAAAACAAGG/iSpC3//36-FAM/-3'
R182 for L0	5'-/5ATTO633N//iSpC3/AATGCTGGAGGGTAGAACTCACACT/3BioTEG-3'

Table A1.3 The sequences of off-analytes used to make off-analyte cocktail

mmu-miR29b-1-5p	5’-GCTGGTTTCATATGGTGGTTTA-3’
mmu-miR26a-2-3p	5’-CCTGTTCTTGATTACTTGTTTC-3’
hsa-miR146a-3p	5’-CCTCTGAAATTCAGTTCTTCAG-3’
hsa-miR146a-5p	5’-TGAGAACTGAATTCCATGGGTT-3’
hsa-miR146b-5p	5’-TGAGAACTGAATTCCATAGGCT-3’

Table A1.4 Estimated thermodynamic data of cross reactivity between three miRs (A), probes with miRs (B), reporters for L1-5 with miRs (C), and reporters for L1-5 with probes (D), reporters for L0 with miRs (E), reporters for L0 with probes (F). The “Two-State Melting (Hybridization)” (TSM) function from the free online software DINAMelt Server was used to estimate all thermodynamic data. The units for the free energy and enthalpy are kcal/mol, for entropy are cal/(mol*K), for melting temperature is °C

A

miR	miR	ΔG	ΔH	ΔS	T_m
miR27a	miR27a	-3.0	-51.1	-155.1	-0.2
miR96	miR96	-2.5	-32.9	-97.9	-20.0
miR182	miR182	-3.4	-41.3	-122.1	-5.1
miR27a	miR96	-3.3	-32.6	-94.5	-21.0
miR27a	miR182	-3.4	-31.6	-90.9	-21.7
miR96	miR182	-4.3	-72.3	-219.4	11.3

B

Probe	miR	ΔG	ΔH	ΔS	T_m
P96	miR27a	-3.6	-37.8	-110.3	-12.6
P96	miR96	-21.7	-165.3	-463.1	58.9
P96	miR182	-4.3	-43.8	-127.3	-3.0
P182	miR27a	-3.6	-37.8	-110.3	-12.6
P182	miR96	-3.9	-38.5	-111.6	-10.2
P182	miR182	-22.3	-171.1	-479.7	59.4

C

Reporter	miR	ΔG	ΔH	ΔS	T_m
R96	miR27a	-3.3	-32.6	-94.5	-21.0
R96	miR96	-3.0	-32.9	-96.6	-22.7
R96	miR182	-3.6	-42.1	-124.0	-8.1
R182	miR27a	-3.4	-31.6	-90.9	-21.7
R182	miR96	-3.6	-42.1	-124.0	-8.1
R182	miR182	-3.1	-34.0	-99.7	-20.3

D

Reporter	Probe	ΔG	ΔH	ΔS	T_m
R96	P96	-12.6	-99.3	-279.4	42.9
R96	P182	-3.4	-33.6	-97.5	-19.1
R182	P96	-2.1	-25.1	-74.3	-43.1
R182	P182	-11.6	-117.6	-341.6	39.3

E

Reporter	miR	ΔG	ΔH	ΔS	T_m
R96	miR27a	-3.3	-32.6	-94.5	-21.0
R96	miR96	-3.2	-45.9	-137.8	-7.2
R96	miR182	-3.6	-42.1	-124.0	-8.1
R182	miR27a	-3.4	-31.6	-90.9	-21.7
R182	miR96	-3.9	-37.9	-109.5	-10.5
R182	miR182	-2.6	-35.8	-107.0	-20.7

F

Reporter	Probe	ΔG	ΔH	ΔS	T_m
R96	P96	-13.8	-103.8	-290.0	46.4
R96	P182	-3.9	-38.5	-111.6	-10.2
R182	P96	-3.2	-35.7	-104.9	-17.6
R182	P182	-14.9	-120.9	-341.8	47.9

Table A1.5 Linker's estimated thermodynamic data for multi-hairpin structure (A) and intermolecular homodimer structure (B), number of base pairs (total and GC) between reporters for L0 and probes (C), number of base pairs (total and GC) between reporters for L1-5 and probes (D), number of base pairs (total and GC) between reporters/miR27a and linkers (E), and number of base pairs (total and GC) for the stem parts of HR-182, HR-96, and HS-27a of the linkers (F). The "Quikfold" and TSM functions from the free online software DINAMelt Server were used to estimate all thermodynamic data.

A

	Multi-hairpin			
L	ΔG	ΔH	ΔS	T_m
0	-24.35	-240.1	-695.66	72.0
1	-14.14	-194.7	-582.17	61.3
2	-10.16	-169.2	-512.78	56.8
3	-12.15	-185.5	-558.92	58.7
4	-18.5	-228.7	-677.43	64.3
5	-16.13	-211.0	-628.31	62.7

B

	Intermolecular dimer			
L	ΔG	ΔH	ΔS	T_m
0	-36.5	-379.4	-1105.7	60.3
1	-11.6	-284.4	-879.6	38.8
2	-8.7	-109.2	-324.0	33.6
3	-9.8	-78.5	-221.4	36.6
4	-20.5	-317.4	-957.2	47.7
5	-15.6	-317.4	-971.8	42.6

C

	R96		R182	
L0	Total bases	GC pairs	Total bases	GC pairs
P96	12	7	/	/
P182	/	/	15	7

D

	R96		R182	
L1-5	Total bases	GC pairs	Total bases	GC pairs
P96	11	7	/	/
P182	/	/	15	7

E

	R96		R182		miR27a	
L	Total bases	GC pairs	Total bases	GC pairs	Total bases	GC pairs
0	12	5	10	5	21	11
1-5	12	7	12	8	21	11

F

	HR-182		HR-96		HS-27a	
L	Total bases	GC pairs	Total bases	GC pairs	Total bases	GC pairs
0	7	4	9	5	13	8
1	7	3	6	4	11	5
2	6	3	6	4	9	4
3	6	3	6	4	10	5
4	7	3	6	4	13	7
5	7	3	6	4	12	6

Table A1.6 Estimated thermodynamic data of hybridization between L0 and other single-strand DNAs at 37 °C. Two-state melting (Hybridization) (TSM) from the DINAMelt Web Server was used to estimate double-strand hybridization thermodynamic values of the linkers binding with any of the three miRs and two probe strands, finding no favorable binding with the linker. The fact there was no favorable binding meant less cross reactivity between miRs, probes, and linkers.

Estimated thermodynamic data		ΔG	ΔH	ΔS	T_m
GCGGAACTTAGCCACTGTGAACGAAAGCCCTGATCTCCAGCATTAGGGCTT TATGGCCTTGTTTTGTGAATGCAAGGCCATAACGTTCACAGTGGC;					
miR27a	TTCACAGTGGCTAAGTTCCGC;	-23.0	-165.2	-458.4	61.8
R96	TTTGGCACTAGCACAAAACAAGG;	-12.3	-101.8	-288.7	41.6
R182	AATGCTGGAGGGTAGAACTCACACT;	-10.1	-79.9	-225.0	34.4
miR96	TTTGGCACTAGCACATTTTTGCT;	-4.2	-38.0	-109.1	-9.1
miR182	TTTGGCAATGGTAGAACTCACACT;	-4.2	-38.0	-109.1	-9.1
P96	AGCAAAAATGTGCTAGTGCCTTT;	-4.8	-35.1	-97.7	-8.3
P182	AGTGTGAGTTCTACCATTGCCTTT;	-4.8	-35.1	-97.7	-8.3

Table A1.7 Estimated thermodynamic data of hybridization between L1 and other single-strand DNAs at 37 °C. Two-state melting (Hybridization) (TSM) from the DINAMelt Web Server was used to estimate double-strand hybridization thermodynamic values of the linkers binding with any of the three miRs and two probe strands, finding no favorable binding with the linker. The fact there was no favorable binding meant less cross reactivity between miRs, probes, and linkers.

Estimated thermodynamic data		ΔG	ΔH	ΔS	T_m
GCGGAACTTAGCCACTGTGAAGATATCGCCATCTCCACCGATATCAAGTC CGTGTCAAGTGACGGACAAACAGTGGCTAA;					
miR27a	TTCACAGTGGCTAAGTTCCGC;	-23.0	-165.2	-458.4	61.8
R96	GGCACTAGCACTTGACACGG;	-14.0	-104.2	-290.7	47.0
R182	CGGTGGAGATGGTAGAACTCA;	-14.3	-102.8	-285.2	48.1
miR96	TTTGGCACTAGCACATTTTTGCT;	-4.2	-38.0	-109.1	-9.1
miR182	TTTGGCAATGGTAGAACTCACACT;	-4.2	-38.0	-109.1	-9.1
P96	AGCAAAAATGTGCTAGTGCCTTT;	-3.6	-37.8	-110.3	-12.6
P182	AGTGTGAGTTCTACCATTGCCTTT;	-3.8	-37.2	-107.7	-12.0

Table A1.8. Estimated thermodynamic data of hybridization between L3 and other single-strand DNAs at 37 °C. Two-state melting (Hybridization) (TSM) from the DINAMelt Web Server was used to estimate double-strand hybridization thermodynamic values of the linkers binding with any of the three miRs and two probe strands, finding no favorable binding with the linker. The fact there was no favorable binding meant less cross reactivity between miRs, probes, and linkers.

Estimated thermodynamic data		ΔG	ΔH	ΔS	T_m
GCGGAACTTAGCCACTGTGAAAAGAATCCATCTCCACCGGGATTCAAGTC CGTGTCAAGTGACGGACAACAAGTGGCTAAG;					
miR27a	TTCACAGTGGCTAAGTTCCGC;	-23.1	-165.5	-459.9	61.8
R96	GGCACTAGCACTTGACACGG;	-14.0	-104.2	-290.7	47.0
R182	CGGTGGAGATGGTAGAACTCA;	-13.7	-103.5	-289.5	46.0
miR96	TTTGGCACTAGCACATTTTTGCT;	-4.2	-38.0	-109.1	-9.1
miR182	TTTGGCAATGGTAGAACTCACACT;	-4.2	-38.0	-109.1	-9.1
P96	AGCAAAAATGTGCTAGTGCCTTT;	-3.6	-37.8	-110.3	-12.6
P182	AGTGTGAGTTCTACCATTGCCTTT;	-3.8	-37.2	-107.7	-12.0

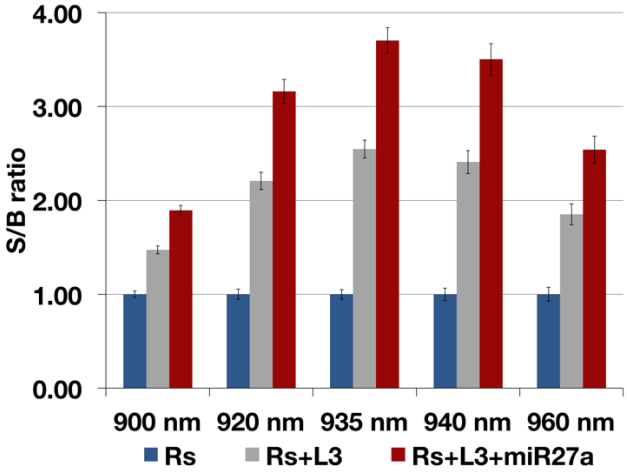

Figure A1.2 The excitation wavelength determination. When excited at 935 nm, L3 showed the highest signal to background (S/B) ratio (N = 2). The acquisition settings were the same as described in experimental section except the exposure time was 250 ms.

A1.2 FRET Efficiency and FRET Distance Calculations

The distance between the dyes, FAM and ATTO 633, on two different linkers, L1 and L3 were estimated using the following two equations:

$$E = 1 - \left(\frac{I_{DA}}{I_D}\right) \text{ and } r = R_o \sqrt[6]{\frac{1-E}{E}}.$$

With the first equation, I_{DA} was the emission intensity of FAM when all miRs were added to a solution with RP182, RP96, and the linkers. I_D was the emission intensity of the FAM-RP96 when it was in the presence of ATTO 633-RP182, but in the absence of the linker and all miRs. There

were equal concentrations of FAM-DNA to ATTO 633-DNA in both I_D and I_{DA} samples. All samples were excited at 935 nm.

To ensure the ATTO 633 did not influence the FAM signal we measured FAM signal with and without ATTO 633 present. The emission intensity of FAM alone was similar to that when FAM was mixed with ATTO 633 (no data shown). Thus, the presence of ATTO 633 did not significantly influence the signal from FAM.

The average E value was then used in the second equation to calculate the distance between FAM and ATTO 633. A literature value of the Förster distance, R_0, for the FAM and ATTO 633 pair was not available in the literature. However, an R_0 value of 51 Å for the ATTO 488 and ATTO 633 pair was available. This R_0 value was used because FAM and ATTO 488 have similar emission wavelengths near 520 nm. For L3, E was found to be 0.2647 ± 0.0022. With the estimated R_0 value and the calculated E value for L3, r was calculated to be 60.49 Å. For L1, E was found to be 0.2722 ± 0.0024 and the distance between the FRET pair, r, was found to be 60.08 Å.

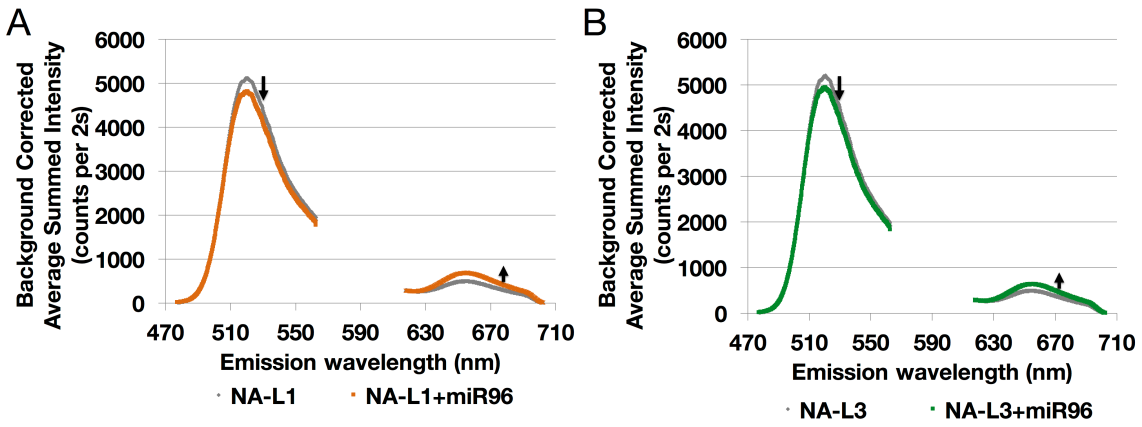

Figure A1.3 The emission spectrum from adding miR96 to NA-L1 (A) and NA-L3 (B) (N = 3).

A1.3 Comparison of Six Linkers: L0 to L5

Figure S4 shows that for each linker, the presence of both reporters caused the R/G ratio to increase by about 3 times (Rs+L, gray bar) compared to the control group of two reporters (Rs, blue bar). When both reporters with miR27a were added to each linker, all the linkers showed the R/G ratio increased by about 5 times (Rs+L+miR27a, red bar) compared to the control group of two reporters (Rs, blue bar).

There were no statistically significant differences between the five linkers as to their responses towards either two reporters, or two reporters with miR27a. L1 and L3 were chosen as representative linkers for further tests.

Amongst L1-L5 there were some nuanced differences between the stem's sequence and thermodynamics for HR-182. However, the stem's sequence and thermodynamics for HR-96 were the same. These nuanced differences in the sequence might be the reason for the similar response toward to the addition of R96 and R182 (Rs) with and without miR27a (Figure S4).

The sequences for L1, L4, and L5 were almost the same except for the last 12-13 nucleotides in the 3' end. L5 has one more guanine base at the 3'end than L1. L4 has one more cytosine base than L5. L2 and L3 had similar sequences, but L3 had one more guanine base at the end of 3', making it more thermodynamically stable than L2. The HR-182 of the five linkers was mostly similar in the stem sequence and energy. L1, L4, and L5 all had the same HR-182 sequences with Gibbs energy of -2.2 kcal/mol. L2 and L3 had the same HR-182 sequences with Gibbs energy of about -1.9 kcal/mole. The hairpin region HR-96 had the same stem sequence for L1 to L5. Thus the stabilities of HR-182 and HR-96 were quite similar for L1 to L5. These similarities in the HRs resulted in the similar response towards to the addition of R96 and R182 (Rs) (Figure S4).

Compared to L1-L5, L0 failed to respond to two Rs with or without miR27a. This result can be explained by the estimated thermodynamic data. For L0, the Gibbs energies for HR-182 and HR-96 were ~4 and ~7 kcal/mole, respectively. The hairpin region's stems in L0 were very different and more thermodynamically stable than those of L1-L5. The linker-reporter complexes' Gibbs energies for linker L0 were ~12 and ~10 for R96 and R182, respectively. Looking at the number of GC base pairs, there were 8 when R182 bound to L1-L5, but only 5 when R182 bound to L0. Also there were two more GC bases paired when R96 bound to L1-L5 than to L0 (Table S5. E). The linker reporter binding interactions were weaker for L0 than those for L1-L5. Even though L0's HS-27a had a similar stability to L4, and both were more stable than any other linker, L0 failed to respond to two Rs with the addition of miR27a.

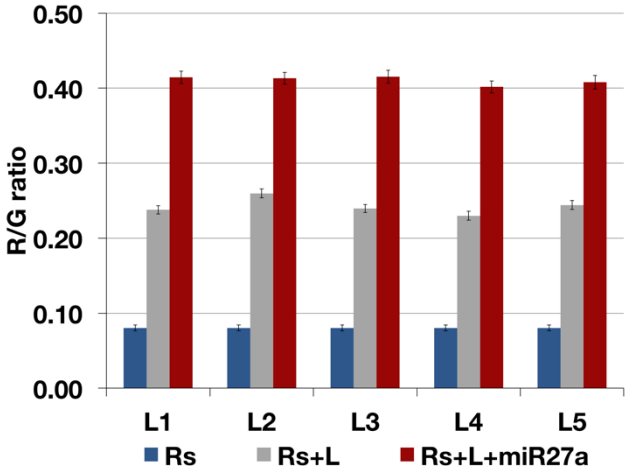

Figure A1.4 All five linkers showed similar response towards the addition of R96 and R182 (Rs) with and without miR27a (N = 2). The acquisition settings were the same as described in experimental section except the exposure time was 250 ms.

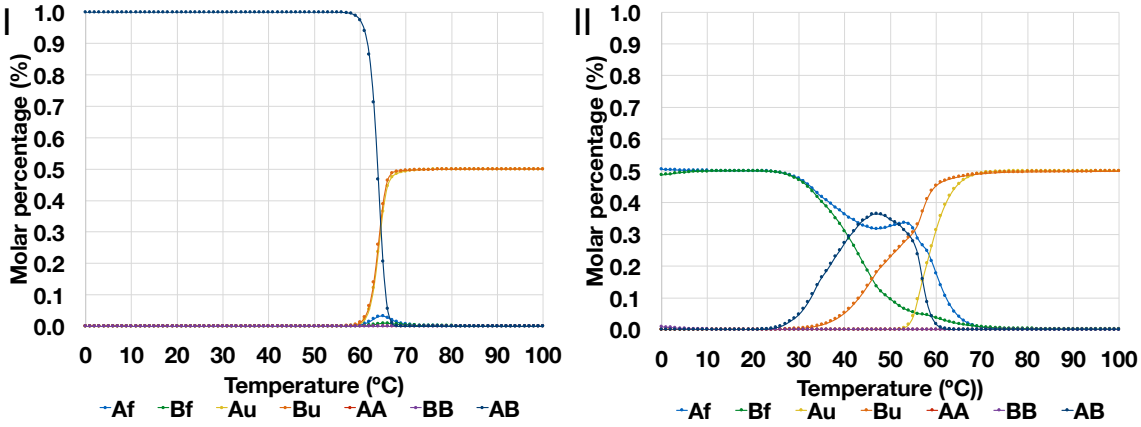

Figure A1.5 Estimated concentrations when two DNA analytes were hybridized at different temperatures. In the figures A was L3 (for I and II), B was either R96-R182-miR27a (for I) or R96-R182 (for II), and the dashed line was the heterodimer concentration between A and B. The subscript f = folded, u = unfolded, AA and BB were homodimers, and AB was the heterodimer. (I) Showed almost 100 % binding of A and B strands when the hybridizing temperature was 37 °C, meaning R96, R182, and miR27a strongly bound to L3 at 37 °C. (II) Showed about 20% binding of A and B strands when the hybridized temperature was around 37 °C, showing R96 and R182 were able to bind to L3 at 37°C and was reflected in the experimental FRET data. The free online software DINAMelt was used to estimate all thermodynamic data; the function used here was "Hybridization of two different DNA strands" (model: Energy minimization).

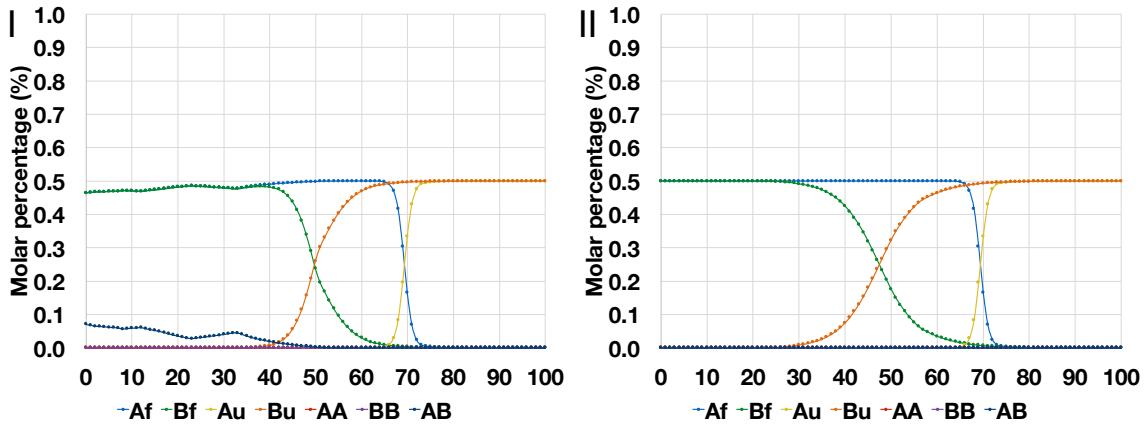

Figure A1.6 Estimated concentrations when two DNA analytes were hybridized at different temperatures. In the figures A was L0 (for I and II), B was either R96-R182-miR27a (for I) or R96-R182 (for II), and the dashed line was the heterodimer concentration between A and B. The subscript f = folded, u = unfolded, AA and BB were homodimers, and AB was the heterodimer. (I) Showed 2.82 % binding of A and B strands when the hybridizing temperature was 37 °C, meaning R96, R182, and miR27a barely bound to L0 at 37 °C. (II) Showed 0 % binding of A and B strands when the hybridized temperature was around 37 °C, showing R96 and R182 were not able to bind to L0 at 37°C. The fact L0 failed to bind both reporters and miR27a was reflected in the FRET data. The free online software DINAMelt was used to estimate all thermodynamic data; the function used here called "Hybridization of two different DNA strands" (model: Energy minimization).

Appendix II.
Supplemental Information for Chapter 3

Table A2.1 The sequences of motifs, reporter96 (R96), reporter182 (R182), and miR27a. The colored bases represent complementary sequence for miR27a (blue), R182 (red), and R96 (green). *5p* and *3p* indicated the 5-prime and 3-prime ends of the oligonucleotides.

T1M-1	*5p*GCGGAACTTAGCCACTGTGAAAAGAATCCATCTCCACCGGGATTCAAGTCCGTGTCAAGTGACGGACAACAAGTGGCTAA*3p*
T1M-2	*5p*GCGGAACTTAGCCACTGTGAAAAGAATCCATCTCCACCGGGATTCAAGTCCGTGTCAAGTGACGGACAACAAGTGGCTAAG*3p*
T2M-1	*5p*GCGGAACTTAGCCACTGTGAACCTCCATCTCCACCGGGTTCACTGTCCGTGTCAAGTGACGGACTTGTGGCTAAGTT*3p*
T2M-2	*5p*GCGGAACTTAGCCACTGTGAACCTCCATCTCCACCGGGTTCACAGTCCGTGTCAAGTGACGGACTGTGGCTAAGTT*3p*
T3M	*5p*GCGGAACTTAGCCACTGTGAACCATCTCCACCGATGGTTCCGTCCGTGTCAAGTGACGGACGTTCAAGTGGCTAAG*3p*
R96	*5p*GGCACTAGCACTTGACACGG*3p*-FAM
R182	ATTO633-*5p*CGGTGGAGATGGTAGAACTCA*3p*
miR27a	*5p*TTCACAGTGGCTAAGTTCCGC*3p*

Table A2.2 The number of Hydrogen bonds formed in the HP-182 stem, HP-96 stem, and double-stranded part of DS-27a in each motif.

	T1M-1	T1M-2	T2M-1	T2M-2	T3M
HP-182 stem	15	15	18	20	20
HP-96 stem	16	16	16	16	19
DS-27a double-stranded part	22	25	27	27	25

A2.1 The impact of Hydrogen-bonds number on motif stability

The HP-182 stems in T2Ms and T3M were considered to be more stable than those in T1Ms due to an additional 3 to 5 H-bonds (see Table S-2). HP-96 stem was regarded as more stable in T3M than in T1Ms due to an extra 3 H-bonds. DS-27a in T2Ms had 2 more H-bonds compared to T1M-2 and thus, was deemed to be more stable. T3M's DS-27a was considered to be more stable than T1M-1's because of an extra 3 H-bonds. Due to more total H-bonds formed in the new motifs, we expected that the new motif types would be more stable than T1Ms and show a lower response (R/G ratio) towards two reporters, thus an improved DIN index.

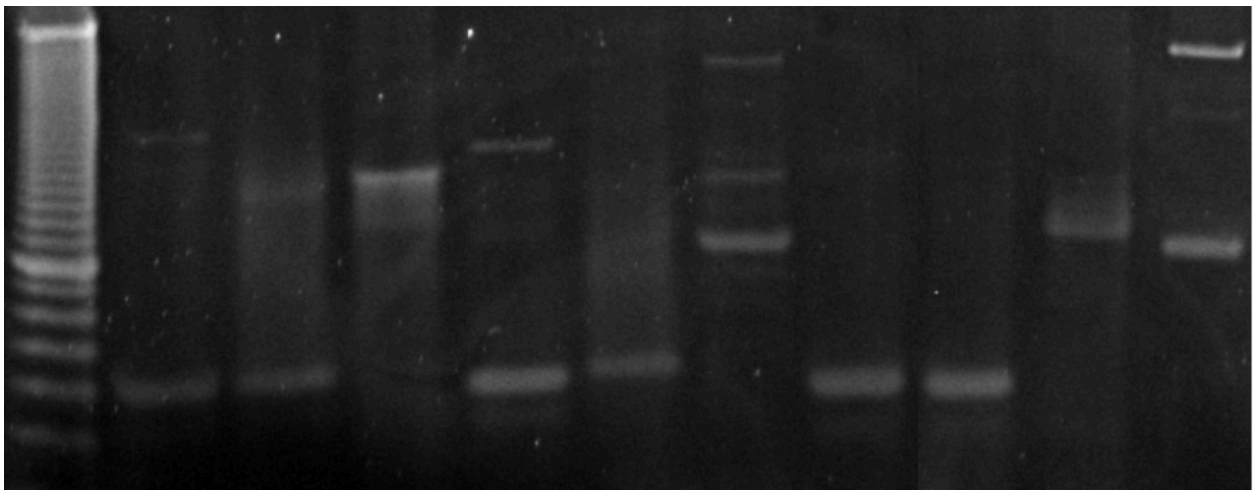

Figure A2.1 10% Native polyacrylamide gel electrophoresis confirming the motif forming complex with two inputs (two reporters, Rs) and three inputs (two reporters and miR27a). Lane 1: 10 bp DNA ladder. Lane 11 (the most right lane): 100 bp DNA ladder. The intense bands in the middle positions of lane 1 and 11 are 100 bps. Lane 2, 5, 8: Type 1 motif-2 (T1M-2), Type 2 motif-2 (T2M-2), Type 3 motif (T3M), respectively. Lanes 3, 6, 9: motif with two inputs, T1M-2+2 inputs, T2M-2+2 inputs, and T3M+2 inputs, respectively. Lanes 4, 7, 10: motif with three inputs, T1M-2+3 inputs, T2M-2+3 inputs, and T3M+3 inputs, respectively. The dim thin bands in the higher position (lane 2, 5 ,8) support the formation of homodimers by two motifs bound together. In the presence of two reporters, only T1M-2 (lane 3) formed complex with reporters but other motifs did not (T2M-2 in lane 6, T3M lane 9). However, fluorescence study showed the slight signal increase from T2M-2 and T3M hybridizing with two reporters, indicating fluorescence is more sensitive analytical technique. In addition, native PAGE results matched with experimental results that different motifs did form complex with two reporters and miR27a and T1M-2 formed more complex than the other two motif types (T1M-2 in lane 4, T2M-2 in lane 7, and T3M in lane 10). This process of motif reacting with three inputs may result in species with retarded mobility as shown in Lanes 4, 7, and 10. The smear around that bands supports the existence of incomplete complexes such as motifs only bind to single input, or two inputs instead of all three miRs.

A2.2 Molarity percentage analysis

The molarity percentage of a motif interacting with inputs was predicted with two online resources: DINAMelt[1,2] and NUPACK[3]. The molarity percentage analysis from both online resources relied on the DNA energy parameters from a study by SantaLucia in 1998[4]. To predict complex formation, the DINAMelt software only allowed assessment of interactions between two nucleic acid strands. To overcome this limitation, we concatenated the inputs' sequence *in silico* to make two single-stranded DNA: one ssDNA was from R96 and R182 (referred as Rs), and the other was from R96, R182, and miR27a (known as Rs+miR27a). We then predicted molarity percentage for complexes formed between each motif type with either Rs or Rs+miR27a. The following hybridization parameters were defined in the algorithm: model: energy minimization, 37 ºC, 10 mM Na^+, 2.5 mM Mg^{2+}, 100 nM motif, 100 nM Rs, and 100 nM Rs+miR27a. These values reflected the experimental conditions. The molarity percentage of the subtype motifs from the same type (*e.g.* T1M-1 and T1M-2) were the same (Data not shown). Thus T1M-2, T2M-1,

and T3M were chosen as representatives to show the molarity percentage of each corresponding motif type (Figure 1).

The advantage of NUPACK is the ability to analyze more than two single strands complexing. The molarity percentage predictions in NUPACK were evaluated at 37 ºC, 50 mM Na^+, 2.5 mM Mg^{2+}, dangle treatment of "none", and 100 nM of motif, R96, R182, and miR27a (all DNA were equimolar). The lowest concentration of Na^+ can be defined was 50 mM. Thus, we increased the concentration of Na^+ from 10 (used in DINAMelt) to 50 mM. The other parameters for the molarity percentage analysis include the 'number of strand species' and 'the maximum complex size'. The number of strand species is the number of oligonucleotides analyzed by the NUPACK. The 'maximum complex size' is the number of oligonucleotides will bind to form a complex. The 'number of strand species' and the 'maximum complex size' were set at 3 and 4 to analyze the molarity percentage of the motif with two and three inputs, respectively.

A2.3 The prediction of the thermodynamic-related metrics

The molecular logic design process for the T1Ms and two reporters (R96 and R182) was detailed in the supplementary information of our published work[5]. The DINAMelt software predicted several thermodynamic-related values as metrics to assess the motifs' biophysical interactions with two or three inputs. These thermodynamic-related metrics included the Gibbs energy (ΔG) and melting point (T_m) of the motif as either multi-hairpins or homodimers, and the Gibbs energy change (ddG) from the reaction of the motif with two or three inputs.

The application of 'two-state melting (hybridization)' in DINAMelt predicted ΔG and T_m of motif as multi-hairpins and homodimers, the complex formed by motif bound to the concatenated R96 and R182 (motif-R96-R182), and complex formed by motif bound to the concatenated R96, R182, and miR27a (motif-R96-R182-miR27a). The following hybridization parameters were defined in DINAMelt: 37 ºC, 10 mM Na^+, 2.5 mM Mg^{2+}, 100 nM motif, 100 nM concatenated R96 and R182, and 100 nM concatenated R96, R182, and miR27a.

The ddG of the reaction between the motif as homodimers and two inputs was calculated by subtracting the ΔG of homodimer-R96-R182 from the ΔG of homodimers. The same mathematical method applied to the ddG for the reaction between (1) the motifs' multi-hairpins and two inputs, (2) the motifs' multi-hairpins and three inputs, and (3) the motifs' homodimers and three inputs.

Reference:

(1) Markham, N. R.; Zuker, M. DINAMelt Web Server for Nucleic Acid Melting Prediction. *Nucleic Acids Res.* **2005**, *33* (Web Server), W577–W581.

(2) Markham, N. R.; Zuker, M. UNAFold: Software for Nucleic Acid Folding and Hybridization. *Bioinformatics, Volume II. Structure, Function and Applications*, number 453 in *Methods in Molecular Biology*, **2008,** chapter 1, pages 3–31. Humana Press, Totowa, NJ. ISBN 978-1-60327-428-9

(3) Zadeh, J. N.; Steenberg, C. D.; Bois, J. S.; Wolfe, B. R.; Pierce, M. B.; Khan, A. R.; Dirks, R. M.; Pierce, N. A. NUPACK: Analysis and Design of Nucleic Acid Systems. *J. Comput. Chem.* **2011**, *32* (1), 170–173.

(4) SantaLucia, J. A Unified View of Polymer, Dumbbell, and Oligonucleotide DNA Nearest-Neighbor Thermodynamics. *Proc. Natl. Acad. Sci.* **1998**, *95* (4), 1460–1465.

(5) Zhang, L.; Bluhm, A. M.; Chen, K.-J.; Larkey, N. E.; Burrows, S. M. Performance of Nano-Assembly Logic Gates with a DNA Multi-Hairpin Motif. *Nanoscale* **2017**, *9* (4), 1709–1720.

Appendix III.
Supplemental Information for Chapter 4

A3.1 Instrumentation detail

An ultrafast tunable Titanium-Sapphire laser (MaiTai, Spectra Physics, Newport) was the main light source. An alternative light source was Argon-ion laser (LASOS, Germany). The Acton spectrometer had a grating blazed at 500 nm with 300 grooves per mm.

LightField software was used to acquire the emission spectra. When Titanium:Sapphire laser was used the light source, the LightFiled software used the following parameters to acquire the data: 2 000 ms exposure time, 1 exposure averaged per frame, 60 frames, full frame read-out mode, high Analog-to-Digital Conversion Gain (ADC), 100 MHz ADC speed, low noise ADC quality, 1 000 μm slit width. The CCD camera was thermoelectrically cooled to −70 °C to minimize dark noise. For solutions containing reporters The grating was centered at either 520 nm for R24 where 5-prime (5') end was labeled with Fluorescein FAM (spectral range: 477.3–562.7 nm), or 660 nm for R27a where 3-prime (3') end o was labeled with ATTO 633 (spectral range: 617.6–702.3 nm).

When Argon-ion laser was used the light source, the data was acquired with different settings in the LightFiled software: 0.1 ms exposure time, 1 exposure averaged per frame, and 20 frames. The other parameters were same as used with the Titanium-Sapphire laser.

A3.2 Oligonucleotides and materials

A custom buffer was prepared to dilute the stock oligonucleotides solutions (at about 25 °C). The buffer solution had a final pH around 8 and contained the following components (all from Fisher Scientific): 0.005% Tween-20 in Phosphate Buffered Saline (PBS), 2.5 mM $MgCl_2$, and 10 mM Tris buffer (pH 10). All oligonucleotides were diluted to a concentration of 2 μM. The diluted concentrations were verified with a Nanodrop spectrometer (Thermo Scientific, ND-1000 UV-VIS spectrophotometer). Measuring below 2 μM was not possible because below that concentration the Nanodrop loses accuracy.

A3.3 Autowalk AND logic operator design process

The autowalk AND logic operator (AALO) consists of four single-stranded DNA sub-units: one gate strand (GS), two reporters (R27a and R24) as output strands, and a blocking strand

(BS). The design of AALO is shown in Figure A3.1. The predicted thermodynamic data of GS interacting with two reporters, BS-19, and three miR inputs are shown in Table A3.1. A custom Matlab program generated a pool of BS candidates. From the pool, BS candidates that did not cross hybridize with other non-target oligonucleotides were selected based on the predicted thermodynamic values. The predicted thermodynamic data evaluating cross-hybridizing of BS with other oligonucleotides are available in Table A3.2 through Table A3.5. A more detailed selection process of candidate blocking strands are described below. All selected oligonucleotide sequences are listed in Table A3.6. Open-source software (DINAMelt Web Server) predicted all thermodynamic data.[1,2]

A3.4 Blocking strand selection process.

The Matlab program produced hundreds to thousands of potential blocking strands that are complementary to the gate strand. These blocking strand candidates were filtered to rule out those having cross reactivity with off-analyte nucleic acids including three miR inputs, two reporters, and themselves as homodimers. The evaluation of cross reactivity was based on the thermodynamic estimates by using the "Two-state melting (Hybridization)" (TSM) function from the DINAMelt Web Server.

The blocking strand filtering process includes: 1) estimating the secondary structure (no data shown) and thermodynamics through "Quikfold" function (Table A3.2), 2) evaluating the cross reactivity with two reporters and three miR inputs (Table A3.3), 3) predicting the stability of themselves as homodimers (Table A3.4) through the TSM function, 4) evaluating secondary structure (Figure S3.2) and thermodynamics of binding to the gate strand through the TSM function (Table A3.5). All the functions mentioned above were from the DINAMelt Web Server and the following settings were used: hybridization temperature of 37 ℃, Na^+ concentration of 10 mM, Mg^{2+} concentration of 2.5 mM, and strand concentration of 100 nM.

A3.5 Assembly of autowalk AND logic operator

To assemble the autowalk AND logic operator, the gate strands were hybridized with an equimolar amount of blocking strands at 80 °C for 2 mins then at 37°C for 90 mins. Treating GS-BS mixture at 80 °C was to melt all possible homodimers (i.e. complexes between two identical ssDNAs). Homodimers run the risk of lowering the amount of GS-BS duplex thus reducing the chance of forming functional AALOs. Next, equimolar amounts of each reporter (R24 and R27a) were added to the GS-BS duplex and hybridized at 37°C for 120 mins.

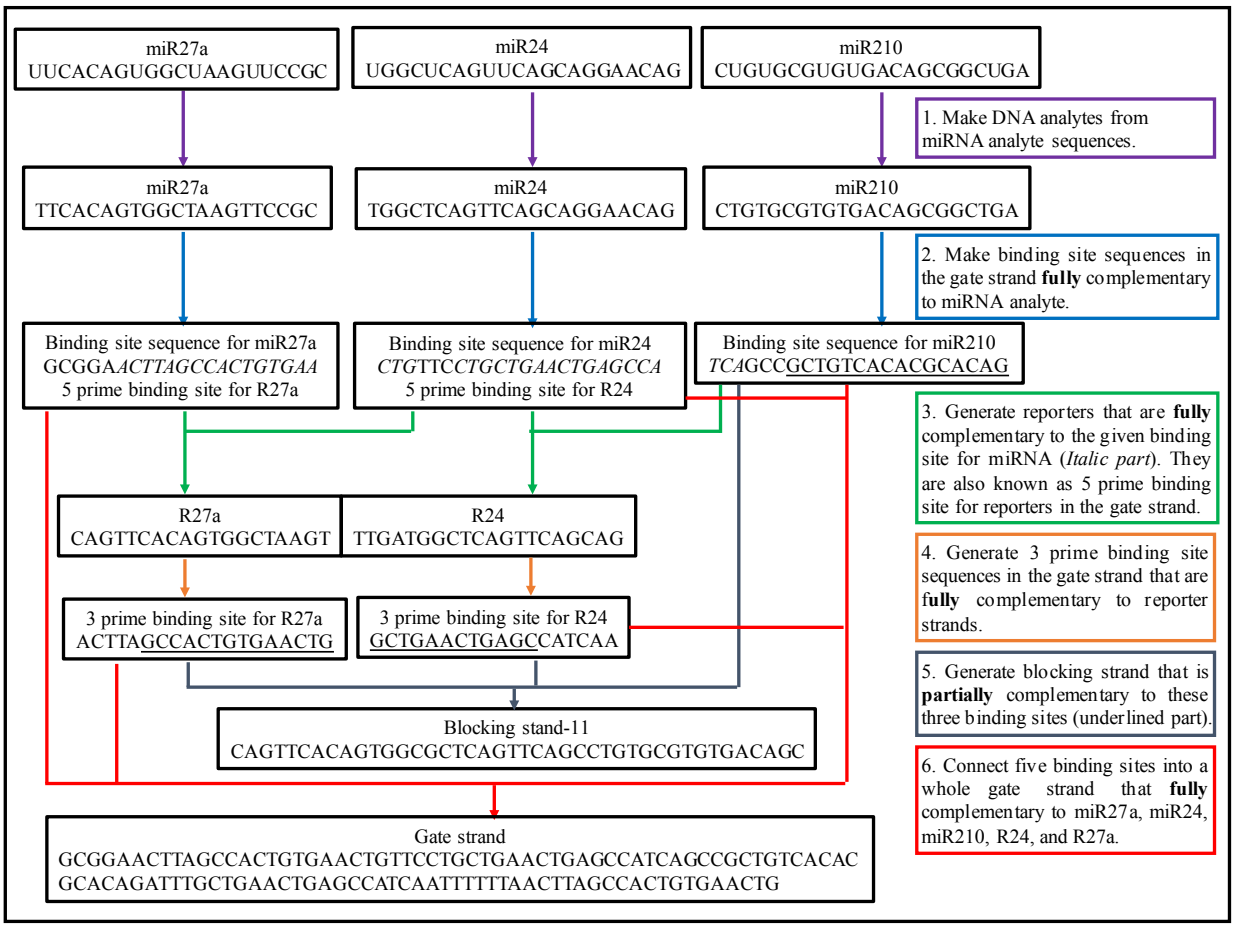

Figure A3.1 The flow chart of autowalk AND logic operator design.

Table A3.1 Estimated thermodynamic data of hybridization between gate strand and other single-strand DNAs at 37 °C. Two-state melting (Hybridization) (TSM) from the DINAMelt Web Server was used to estimate double-strand hybridization thermodynamic values of the gate strand binding with any of three miRs and two reporters, finding favorable binding with the gate. Gate-5' means the hybridization happens in the 5 prime binding site in the gate strand. Similarly, Gate-3' means the hybridization happens in the 3 prime binding site in the gate strand.

	ΔG (kcal/mol)	ΔH (kcal/mol)	ΔS (cal/mol/K)	T_m (°C)
Gate-5' + R27a	-19.7	-149.6	-418.8	56.7
Gate-5' + R24	-20.8	-155.9	-435.7	58.2
Gate + BS-19	-43.1	-377.7	-1079.0	66.0
Gate + miR27a	-23.0	-165.2	-458.4	61.8
Gate + miR24	-25.3	-182.7	-507.5	63.7
Gate + miR210	-28.8	-185.6	-505.5	70.4
Gate-3' + R27a	-19.5	-145.2	-405.4	56.7
Gate-3' + R24	-20.0	-149.4	-417.2	57.4

Table A3.2 Estimated thermodynamic data of twenty blocking strands forming the secondary structures. The "Quikfold" function from the DINAMelt Web Server was used. The units for Gibbs energy (ΔG) and enthalpy change (ΔH) are kcal/mol. The unit for entropy change (ΔS) is cal/K/mol.

BS-1	ΔG = -0.12	ΔH = -21.6	ΔS = -69.26	T_m = 38.7°C
BS-2	ΔG = -3.53	ΔH = -52.90	ΔS = -159.18	T_m = 59.2°C
BS-3	ΔG = -2.31	ΔH = -33.00	ΔS = -98.95	T_m = 60.4°C
BS-4	ΔG = -3.53	ΔH = -52.90	ΔS = -159.18	T_m = 59.2°C
BS-5	ΔG = -2.31	ΔH = -33.00	ΔS = -98.95	T_m = 60.4°C
BS-6	ΔG = -2.31	ΔH = -33.00	ΔS = -98.95	T_m = 60.4°C
BS-7	ΔG = -2.31	ΔH = -33.00	ΔS = -98.95	T_m = 60.4°C
BS-8	ΔG = -1.90	ΔH = -36.20	ΔS = -110.59	T_m = 54.2°C
BS-9	ΔG = -1.90	ΔH = -36.20	ΔS = -110.59	T_m = 54.2°C
BS-10	ΔG = -1.90	ΔH = -36.20	ΔS = -110.59	T_m = 54.2°C
BS-11	ΔG = -3.52	ΔH = -75.7	ΔS = -232.73	T_m = 52.1°C
BS-12	ΔG = -1.50	ΔH = -38.30	ΔS = -118.65	T_m = 49.6°C
BS-13	ΔG = -2.20	ΔH = -39.70	ΔS = -120.91	T_m = 55.2°C
BS-14	ΔG = -2.20	ΔH = -39.70	ΔS = -120.91	T_m = 55.2°C
BS-15	ΔG = -1.90	ΔH = -36.20	ΔS = -110.59	T_m = 54.2°C
BS-16	ΔG = -1.08	ΔH = -90.30	ΔS = -287.67	T_m = 40.8°C
BS-17	ΔG = -3.43	ΔH = -58.00	ΔS = -175.95	T_m = 56.5°C
BS-18	ΔG = -0.41	ΔH = -39.70	ΔS = -126.68	T_m = 40.2°C
BS-19	ΔG = -3.63	ΔH = -58.00	ΔS = -175.30	T_m = 57.7°C
BS-20	ΔG = -0.58	ΔH = -44.40	ΔS = -141.29	T_m = 41.1°C

Table A3.3 Estimated thermodynamic data of hybridization of the blocking strand (BS-19 was used as an example) with two reporters, and three miR inputs at 37 °C. Two-state melting (Hybridization) (TSM) from the DINAMelt Web Server was used to estimate the cross reactivity with off-analyte single-stranded DNAs. The data shows unfavorable reaction. The units for Gibbs energy (ΔG) and enthalpy change (ΔH) are kcal/mol. The unit for entropy change (ΔS) is cal/K/mol.

BS-19 + R24	ΔG = -3.8	ΔH = -39.7	ΔS = -115.6	T_m = -9.1°C
BS-19 + R27a	ΔG = -6.8	ΔH = -62.0	ΔS = -178.0	T_m = 18.2°C
BS-19 + miR210	ΔG = -5.0	ΔH = -44.4	ΔS = -126.9	T_m = 1.4°C
BS-19 + miR24	ΔG = -3.8	ΔH = -39.7	ΔS = -115.6	T_m = -9.1°C
BS-19 + miR27a	ΔG = -6.8	ΔH = -62.0	ΔS = -178.0	T_m = 18.2°C

Table A3.4 Estimated thermodynamic data of twenty blocking strands forming the homodimers at 37 °C. Two-state melting (Hybridization) (TSM) from the DINAMelt Web Server was used to estimate the thermodynamic data. The units for Gibbs energy (ΔG) and enthalpy change (ΔH) are kcal/mol. The unit for entropy change (ΔS) is cal/K/mol.

BS-1	ΔG = -3.1	ΔH = -21.0	ΔS = -57.7	T_m = -39.0°C
BS-2	ΔG = -7.0	ΔH = -105.6	ΔS = -318.0	T_m = 28.5°C
BS-3	ΔG = -3.9	ΔH = -55.0	ΔS = -164.8	T_m = 6.3°C
BS-4	ΔG = -7.0	ΔH = -105.6	ΔS = -318.0	T_m = 28.5°C
BS-5	ΔG = -3.9	ΔH = -55.0	ΔS = -164.8	T_m = 6.3°C
BS-6	ΔG = -4.1	ΔH = -50.7	ΔS = -150.1	T_m = 5.2°C
BS-7	ΔG = -4.1	ΔH = -50.7	ΔS = -150.1	T_m = 5.2°C
BS-8	ΔG = -3.9	ΔH = -55.0	ΔS = -164.8	T_m = 6.3°C
BS-9	ΔG = -3.9	ΔH = -55.0	ΔS = -164.8	T_m = 6.3°C
BS-10	ΔG = -4.1	ΔH = -50.7	ΔS = -150.1	T_m = 5.2°C
BS-11	ΔG = -6.4	ΔH = -151.2	ΔS = -466.7	T_m = 30.0°C
BS-12	ΔG = -4.0	ΔH = -33.4	ΔS = -94.9	T_m = -10.1°C
BS-13	ΔG = -7.9	ΔH = -84.0	ΔS = -245.5	T_m = 29.6°C
BS-14	ΔG = -7.9	ΔH = -84.0	ΔS = -245.5	T_m = 29.6°C
BS-15	ΔG = -4.1	ΔH = -50.7	ΔS = -150.1	T_m = 5.2°C
BS-16	ΔG = -6.2	ΔH = -77.2	ΔS = -228.8	T_m = 22.8°C
BS-17	ΔG = -6.4	ΔH = -62.0	ΔS = -179.4	T_m = 20.1°C
BS-18	ΔG = -3.7	ΔH = -46.0	ΔS = -136.3	T_m = 0.1°C
BS-19	ΔG = -6.4	ΔH = -62.0	ΔS = -179.4	T_m = 20.1°C
BS-20	ΔG = -3.7	ΔH = -46.0	ΔS = -136.3	T_m = 0.1°C

Table A3.5 Estimated thermodynamic data of hybridization between gate strand and twenty different blocking strands at 37 °C. Two-state melting (Hybridization) (TSM) from the DINAMelt Web Server was used to estimate the hybridization thermodynamic values. The units for Gibbs energy (ΔG) and enthalpy change (ΔH) are kcal/mol. The unit for entropy change (ΔS) is cal/K/mol.

BS-1	ΔG = -30.5	ΔH = -324.4	ΔS = -947.7	T_m = 57.0°C
BS-2	ΔG = -32.3	ΔH = -332.2	ΔS = -967.2	T_m = 58.5°
BS-3	ΔG = -36.0	ΔH = -352.8	ΔS = -1021.3	T_m = 60.9°C
BS-4	ΔG = -36.3	ΔH = -352.1	ΔS = -1018.2	T_m = 61.2°
BS-5	ΔG = -40.0	ΔH = -372.5	ΔS = -1071.9	T_m = 63.4°C
BS-6	ΔG = -44.4	ΔH = -386.0	ΔS = -1101.5	T_m = 66.6°C
BS-7	ΔG = -48.4	ΔH = -405.7	ΔS = -1152.2	T_m = 68.7°C
BS-8	ΔG = -44.1	ΔH = -385.1	ΔS = -1099.6	T_m = 66.3°C
BS-9	ΔG = -48.0	ΔH = -404.8	ΔS = -1150.2	T_m = 68.4°C
BS-10	ΔG = -56.4	ΔH = -438.0	ΔS = -1230.5	T_m = 73.0°C
BS-11	ΔG = -40.0	ΔH = -335.3	ΔS = -952.2	T_m = 66.6°C
BS-12	ΔG = -39.2	ΔH = -330.2	ΔS = -938.2	T_m = 66.2°C
BS-13	ΔG = -38.3	ΔH = -328.5	ΔS = -935.8	T_m = 65.3°C
BS-14	ΔG = -38.2	ΔH = -325.7	ΔS = -927.0	T_m = 65.5°C
BS-15	ΔG = -45.3	ΔH = -370.3	ΔS = -1047.8	T_m = 68.9°C
BS-16	ΔG = -44.1	ΔH = -389.2	ΔS = -1112.6	T_m = 66.1°C
BS-17	ΔG = -44.2	ΔH = -392.1	ΔS = -1121.7	T_m = 65.9°C
BS-18	ΔG = -42.1	ΔH = -418.6	ΔS = -1214.0	T_m = 62.1°C
BS-19	ΔG = -43.1	ΔH = -377.7	ΔS = -1079.0	T_m = 66.0°C
BS-20	ΔG = -40.7	ΔH = -406.0	ΔS = -1177.8	T_m = 61.7°C

Table A3.6 The sequences of gate strand, reporters (R27a and R24), miR inputs (miR27a, miR24, and miR210), and blocking strands (BS) oligonucleotides. Underlined nucleotides in BS-16, BS-18, and BS-20 are random bases added between the complementary sequence for miR210's, R24's "ON", and R27a's "ON" binding sites in the GS.

Name	Sequence (5'-3')
Gate strand	GCGGAACTTAGCCACTGTGAACTGTTCCTGCTGAACTGAGCCATCAGCCGCTGTCAC ACGCACAGATTTGCTGAACTGAGCCATCAATTTTTTAACTTAGCCACTGTGAACTG
R27a	CAGTTCACAGTGGCTAAGT-3ATTO633N
R24	/56-FAM/-TTGATGGCTCAGTTCAGCAG
miR27a	TTCACAGTGGCTAAGTTCCGC
miR24	TGGCTCAGTTCAGCAGGAACAG
miR210	CTGTGCGTGTGACAGCGGCTGA
BS-1	CAGTTCAGCTAAGTTTGATGGGTTCAGCCTGTGCGTGTGACAG
BS-2	CAGTTCAGGCTAAGTTTGATGGGTTCAGCCTGTGCGTGTGACAGC
BS-3	CAGTTCACGGCTAAGTTTGATGGCGTTCAGCCTGTGCGTGTGACAGC
BS-4	CAGTTCAGGCTAAGTTTGATGGGTTCAGCCTGTGCGTGTGACAGCGG
BS-5	CAGTTCACGGCTAAGTTTGATGGCGTTCAGCCTGTGCGTGTGACAGCGG
BS-6	CAGTTCACAGTGGCTAAGTTTGATGGCGTTCAGCCTGTGCGTGTGACAGC
BS-7	CAGTTCACAGTGGCTAAGTTTGATGGCGTTCAGCCTGTGCGTGTGACAGCGG
BS-8	CAGTTCACGGCTAAGTTTGATGGCTCAGTTCAGCCTGTGCGTGTGACAGC
BS-9	CAGTTCACGGCTAAGTTTGATGGCTCAGTTCAGCCTGTGCGTGTGACAGCGG
BS-10	CAGTTCACAGTGGCTAAGTTTGATGGCTCAGTTCAGCCTGTGCGTGTGACAGCGG
BS-11	CAGTTCACAGTGGCGCTCAGTTCAGCCTGTGCGTGTGACAGC
BS-12	ACAGTGGCTAAGTTGCTCAGTTCAGCCTGTGCGTGTGACAGC
BS-13	CAGTTCACAGTGGCTTGATGGCTCAGCTGTGCGTGTGACAGC
BS-14	ACAGTGGCTAAGTTTTGATGGCTCAGCTGTGCGTGTGACAGC
BS-15	CAGTTCACAGTGGCTAATGGCTCAGTTCAGCCTGTGCGTGTGACAGC
BS-16	CAGTTCACAGTGGCTAATG<u>TGCAAAACGGTTG</u>GCTCAGTTCAGC<u>TTTC</u>CTGTGCGTG TGACAGC
BS-17	CAGTTCACAGTGGCTATAAAAAAATGGCTCAGTTCACTGTGCGTGTGACAGC
BS-18	CAGTTCACAGTGGCTAT<u>TCT</u>AAAAAA<u>GTT</u>ATGGCTCAGTTCA<u>TGTTTC</u>CTGTGCGTG TGACAGC
BS-19	CAGTTCACAGTGGCTAAAAAAATGGCTCAGTTCACTGTGCGTGTGACAGC
BS-20	CAGTTCACAGTGGCT<u>CCTGG</u>AAAAAA<u>GTT</u>ATGGCTCAGTTCA<u>TGTTTC</u>CTGTGCGTG TGACAGC

A3.6 Discover off-analyte miRs

To start the off-analyte miR search, we entered the sequence of a given analyte miR (*e.g.* hsa-miR27a-3p: 5'- UUCACAGUGGCUAAGUUCCGC-3') to an online miR database (miRBase).[3] The miRBase database is operated by the University of Manchester. We selected the 'search by sequence' option and then chose the search method of 'BLASTN' for 'mature miRNA' sequence. The other parameters included the 'E-value cutoff' set as '2000', and the 'maximum number of hits' set at '100'.

A3.7 Cell nucleofection and filter settings in TIRF microscope

HEK 293T cells were seeded at ~500 000 cells into 25 cm^2 culture flask (VWR) and subcultured for 48 hrs in DMEM growth media (37 °C, 5% CO_2, 10% FBS, Gibco™). About 1 000 000 cells were harvested and resuspended in 100 µL of SF 4D-NucleofectorTM X Solution (Lonza) at room temperature for Nucleofection. Then cell-X solution mixture was transferred to a 100 µl Nucleocuvette where the pre-hybridized forced "ON" AALOs were added therefore diluting the concentration of AALOs to 1 µM. The forced "ON" was assembled by hybridizing GS with three miR inputs first, then with two reporters. CM-130 program in the Nucleofactor (Lonza) was used to perform the transfection. After that, the nucleofactored solution were transferred to a 3.5 mm petri dish (10 mm microwell, MatTek) and cultured with 2 mL fresh DMEM growth media (10% FBS, 37 °C, 5% CO_2) for 24 hrs.

Then the cells were fixed with 4% paraformaldehyde (Electron Microscopy Sciences) and imaged with an Axio Observer Z1 objective-type TIRF microscope (Zeiss) equipped with a ×100 oil-immersion objective with 1.46 NA. To detect the green and red fluorescence, we used a filter set including a triple-band-pass excitation filter (483 nm, 564 nm, 642 nm), a triple-color beam-splitter (506 nm, 582 nm, 659 nm), and a triple-band-pass emission filter (526 nm, 601 nm, 688 nm). For FRET imaging, a custom filter set contained a band-pass filter 488/10 for excitation, beam splitter 500, and a 620/60 band-pass emission filter. Fixed cells were excited with 488 nm, 560 nm, and 488 nm to obtain images from the green, red, and FRET detector channels, respectively.

A3.8 Importance of a blocking strand

Figure A3.2 shows the critical role that blocking strand (BS) plays in directing two

reporters to the "OFF" sites in the gate strand (GS) and achieving a large sensing window. Two control groups established the baseline and the maximum acceptor intensity. The baseline control (Rs) included two free reporters (R24 and R27a). A forced "ON" state of AALO (GS+3miRs+Rs) was used to determine the maximum acceptor intensity. As mentioned earlier, a forced "ON" was assembled by hybridizing GS with three miR inputs first, then with two reporters. Different from the previously defined AALO's "ON" state, the forced "ON" state did not need a blocking strand. We expected an increased acceptor intensity of forced "ON" AALO because three miRs would bind to GS on the 5' end thus forcing the following added reporters bind to the "ON" sites.

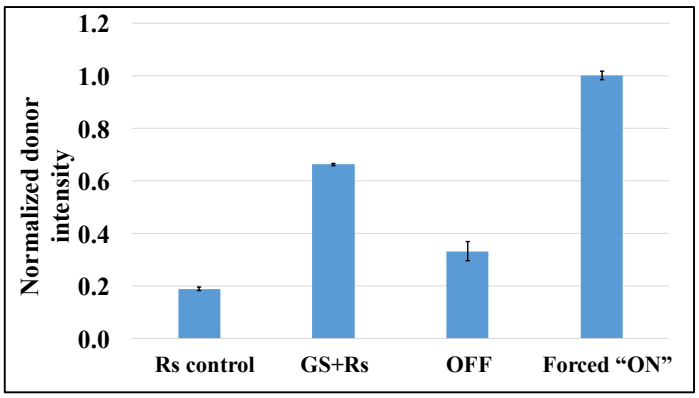

Figure A3.2 Acceptor intensity of the baseline control (Rs), gate strands bound to two reporters without a blocking strand (GS+Rs), "OFF" state of AALO (GS+BS-3+Rs), and forced "ON" state of AALO (GS+3miRs+Rs, N=3).

Figure A3.2 shows that the maximum acceptor signal intensity from the forced "ON" AALO (GS+3miRs+Rs) was five times higher than the baseline from Rs ($p < 0.001$). The acceptor intensity of gate strands bound to two reporters (GS+Rs) was around 3.5 folds higher than the baseline ($p < 0.001$) but lower than the forced "ON" AALO. The acceptor intensity of [gate strands]-reporters (GS+Rs) suggests three possible binding: (1) both reporters bound to "OFF" sites (low acceptor intensity), (2) both reporters bound to "ON" sites (high acceptor intensity), and (3) one reporter bound to "OFF" and the other to "ON" sites (low acceptor intensity).

Different from GS+Rs, "OFF" state of AALO (GS+BS-3+Rs) having GS react with BS first (BS-3 in Figure A3.2) then with two reporters. Compared to GS+Rs, the acceptor intensity of the "OFF" state decreased by 2 times ($p < 0.001$). The lower acceptor intensity for the "OFF" indicated that BS helps direct two reporters to the "OFF" sites to keep the acceptor intensity low and close to the baseline thus enlarging the sensing window. A large sensing window allows ALLOs compensate the high background noises from the complicated matrix (*e.g.* cell lysate),

thus widens AALO's application for good molecular logic.

A3.9 Effect of FRET distance and nucleotide types on FRET efficiency

Förster resonance energy transfer (FRET) efficiency between the donor and acceptor dyes was impacted by the FRET distance and the nucleotide types. FRET distance suggests the donor-acceptor distance and is defined by the number of nucleotides (nts) between R24's (donor) and R27a's (acceptor) "ON" sites in GS. Bao et al reported that increasing the FRET distance between a dye pair (e.g. Cy3 and FAM) from three to six nts would slightly increase FRET efficiency.[58] To determine the best FRET distance for dye pair FAM-ATTO 633, we tested the FRET distances of 5, 7, and 10 nts. As for nucleotide types, we focused on thymine (T) and adenine (A) nucleotides since T and A quench fluorescence the least.[3]

Figure A3.3 demonstrates that different FRET distance and nucleotide types did not cause statistically differences in the acceptor intensity of AALO in either the "OFF" or "ON" state ($p < 0.025$). Additionally, AALO with 7-adenine nts showed the highest sensing window with ~70, 000 counts.

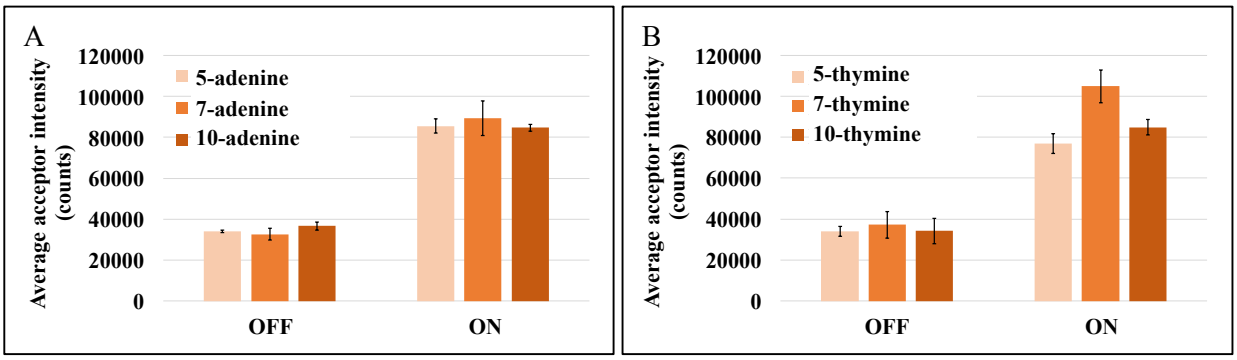

Figure A3.3 The effect of FRET distance and nucleotide types on the acceptor intensity of AALO in "OFF" and "ON" state (N=3). FRET distance from 5-, 7-, and 10 nts with (A) Adenine and (B) thymine nucleotides were tested.

Table A3.7 Exposed toehold lengths and toehold locations in miR210's binding site, R24's and R27a's "ON" binding sites from fourteen autowalk AND logic operators (AALO-1 through AALO-14). Bold number indicates the toehold length. 5', 3', and M indicate the toehold locations: 5-prime end, 3-prime end, and middle of the binding site, respectively.

AALO	1	2	3	4	5	6	7	8	9	10	11	12	13	14
miR210's toehold	**3**, 5'	**3**, 5'	**3**, 5'	**1**, 5'	**1**, 5'	**3**, 5'	**1**, 5'	**3**, 5'	**1**, 5'	**1**, 5'	**3**, 5'	**3**, 5'	**3**, 5'	**3**, 5'
R24's toehold	**4**, M	**4**, M	**3**, M	**4**, M	**3**, M	**3**, M	**3**, M	**0**, M	**0**, M	**0**, M	**6**, 3'	**6**, 3'	**6**, 5'	**6**, 5'
R27a's toehold	**5**, M	**4**, M	**3**, M	**4**, M	**3**, M	**0**, M	**0**, M	**3**, M	**3**, M	**0**, M	**5**, 5'	**6**, 3'	**4**, 5'	**6**, 3'

Table A3.8 Exposed toehold length and toehold location of miR210's binding site, R24's and R27a's "ON" binding sites from six autowalk AND logic operators (ALLO-15 through AALO-20). Bold number indicates the toehold length. 5', 3', and M indicate the toehold locations: 5-prime end, 3-prime end, and middle of the binding site, respectively.

AALO	15	16	17	18	19	20
miR210's toehold	**3**, 5'	**3**, 5'	**3**, 5'	**3**, 5'	**3**, 5'	**3**, 5'
R24's toehold	**4**, 3'	**4**, 3'	(**2,** 5') (**3**, 3')	(**2,** 5') (**3**, 3')	(**2,** 5') (**3**, 3')	(**2,** 5') (**3**, 3')
R27a's toehold	**2**, 5'	**2**, 5'	**3**, 5'	**3**, 5'	**4**, 5'	**4**, 5'

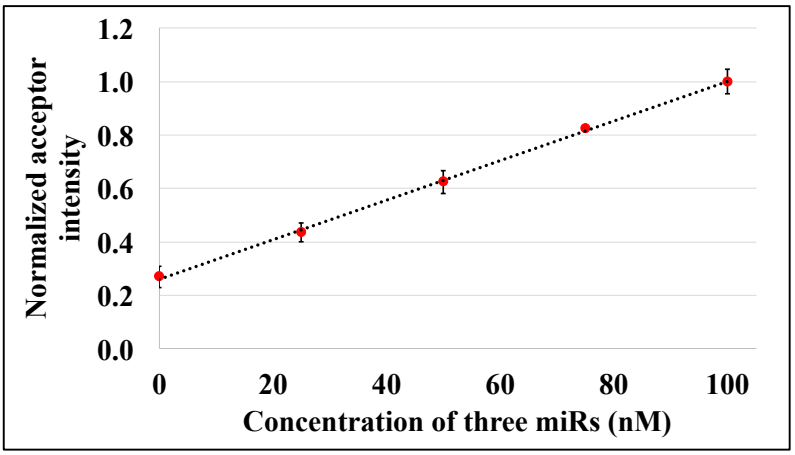

Figure 3.4 Sensitivity, concentration dynamic range, and limit of detection of ALLO-19 in the crude MCF-7 cell lysate (N=3). A calibration curve was constructed over miR concentration ranged from 0 to 100 nM. Data was accuired by Argon-ion laser.

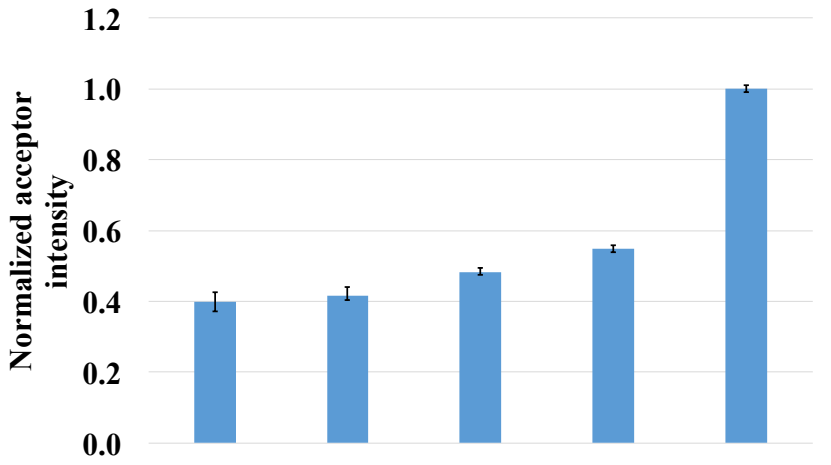

AALO-19	100 nM	100 nM	100 nM	100 nM	100 nM
miR24	0 nM	100 nM	50 nM	25 nM	100 nM
miR210	0 nM	50 nM	25 nM	100 nM	100 nM
miR27a	0 nM	25 nM	100 nM	50 nM	100 nM

Figure A3.5 AALO-19's signal response to the disproportionate relative concentrations of three miRs (N=2). Compared to the group of no miR added, AALO-19 showed statistical higher response to the miR combination where miR24 had the lowest concentration miR ($p < 0.0025$).

Table A3.9 Percent change in acceptor intensity of nano-assembly logic gate-3 (NALG-3) caused by single and double miR additions (N=3).

NALG-3	miR inputs	ΔI^A
Signal change from single-miR addition	miR27a	$100.0 \pm 0.2\%$
	miR182	$89.1 \pm 0.1\%$
	miR96	$83.2 \pm 0.1\%$
Signal change from double-miR addition	miR27a+miR182	$75.6 \pm 0.1\%$
	miR27a+miR96	$70.8 \pm 0.1\%$
	miR96+miR182	$46.9 \pm 0.1\%$

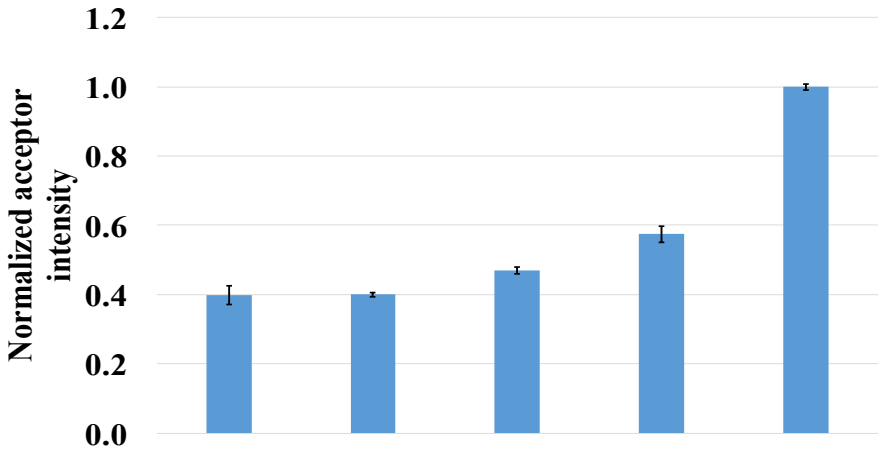

100 nM AALO-19	100 nM AALO-19	100 nM AALO-19	100 nM AALO-19	100 nM AALO-19
0 nM	100 nM OA1	100 nM miR210	100 nM miR210	100 nM miR210
0 nM	100 nM miR24	100 nM OA2	100 nM miR24	100 nM miR24
0 nM	100 nM miR27a	100 nM miR27a	100 nM OA3	100 nM miR27a

Figure A3.6 AALO-19's signal response to the mixture of the equivalent amounts of two analyte miRs and one off-analyte miR (N=2). Compared to the group of no miR added, AALO-19 showed statistical higher response to the miR mixture where off-analyte OA3 was mixed with analyte miRs of miR24 and miR210 ($p < 0.0025$).

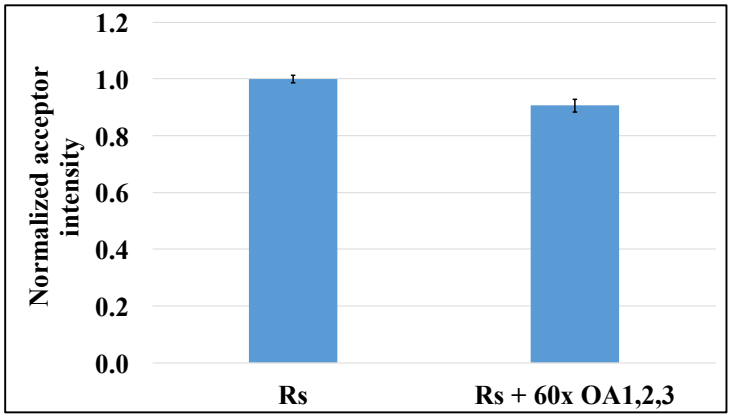

Figure A3.7 The fluorescence quenching effects of high concentration of nucleic acids. The acceptor intensity of 100 nM two reporters (R24 and R27a, Rs) with 600 nM three off-analytes was significantly lower than that of 100 nM two reporters ($p<0.025$).

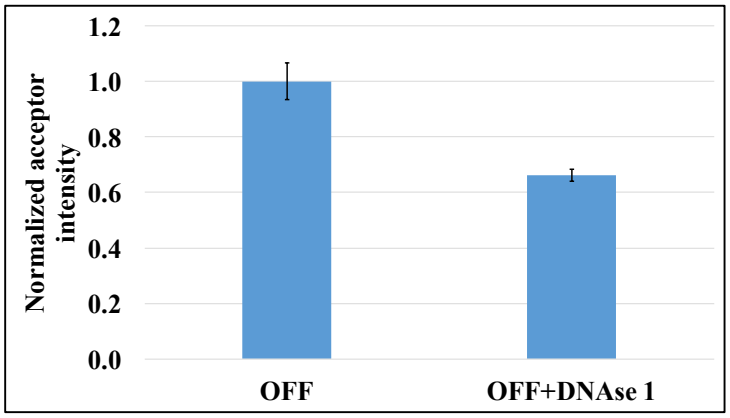

Figure A3.8 False-positive signal test of AALO-19 challenged with deoxyribonuclease (N=2). There was no false-positive signal observed after AALO-19 was treated with enzyme DNase I.

Section A3.10 The differentiating-input-number ability test of AALO-11

To evaluate the differentiating-input-number ability, the acceptor intensity change of AALO-11 was studied when challenged with individual and multiple miRs (Figure A3.9). A blank control established the baseline acceptor intensity of AALO-11 when no miR was present. The blank control consisted of the probe, blocking strand, two reporters (R24 and R27a). The acceptor intensity was normalized with the highest value from the addition of all three miRs to the AALO-11.

For the blank control group, the average normalized acceptor intensity was 0.38 ± 0.04 AU. For the addition of all three miRs the average acceptor intensity was 1.00 ± 0.03 AU. AALO-11 showed the largest changes in acceptor signal when all three miRs were added. Compared to the blank the addition of all 3 miRs increased the acceptor signal by a factor of about 2.5 ($p < 0.0001$). Figure A3.9 shows the addition of single and combinations of two miRs showed statistical increases in the acceptor intensity from the blank control group.

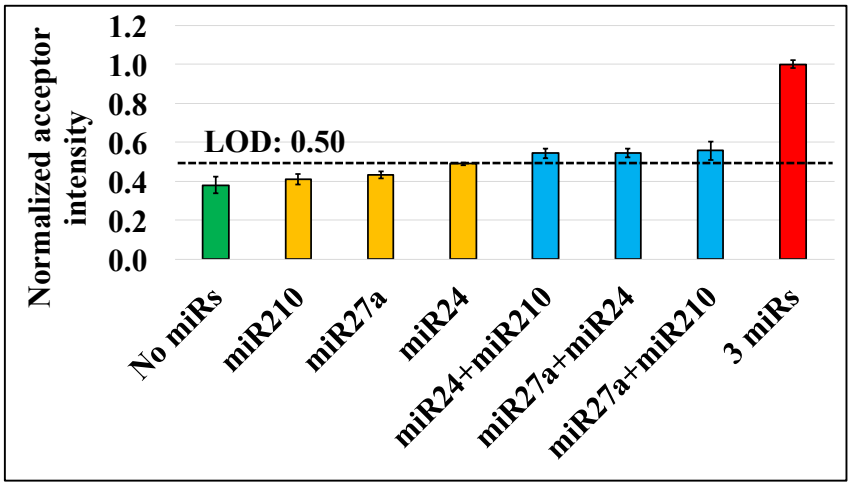

Figure A3.9 The acceptor intensity for AALO-11 challenged with individual and multiple miRs (N=3). Compared to the no miRs control group (green bar) where no miRs were added to the AALO-11, the acceptor intensity increased the most with the addition of all three miR inputs (red bar), then with two miR inputs (blue bar), and the least with single miR input (yellow bar). The black dash line indicates the LOD of AALO-11.

Tables A3.10 quantitated the percent change in acceptor intensity caused by single and double miR additions. The following equation was used:

$$\%\Delta A = 100\times\frac{A_{XmiR} - LOD}{A_{3miR} - LOD}$$

where A is the normalized acceptor intensity in general, A_{XmiR} is the normalized acceptor intensity for single or double miR addition, and A_{3miR} is the normalized acceptor intensity for all three miRs added. False signals from AALO were considered relevant if they were larger than the limit of detection (LOD). AALO-11's LOD was defined as it's average normalized A_{0miR} value plus three times its standard deviation, and with a value of 0.50.

The change in normalized acceptor intensity listed in Table A3.10 for addition of single miR to AALO-11 was less than the LOD. This meant single miR did not cause any false signals. With the addition of double miRs to AALO-11, the change in normalized acceptor intensity was higher than the LOD by 6 to 10% (Table A3.8). This meant double miRs did cause the false signals.

Table A3.10 The percent change in acceptor intensity of four-entities AND connector-11 (AALO-11) caused by single and double miR additions.

AALO-11	%Δ*A*
LOD	0.50
miR24	-5.0
miR27a	-16.3
miR210	-21.2
miR24+miR210	6.3
miR24+miR27a	6.6
miR27a+miR210	9.0

Reference:

(1) Markham, N. R.; Zuker, M. DINAMelt Web Server for Nucleic Acid Melting Prediction. *Nucleic Acids Res.* **2005**, *33* (Web Server), W577–W581.

(2) Zuker, M. Mfold Web Server for Nucleic Acid Folding and Hybridization Prediction. *Nucleic Acids Res.* **2003**, *31* (13), 3406–3415.

(3) Tsourkas, A.; Behlke, M. A.; Xu, Y.; Bao, G. Spectroscopic Features of Dual Fluorescence/Luminescence Resonance Energy-Transfer Molecular Beacons. *Anal. Chem.* **2003**, *75* (15), 3697–3703.